



**Department of Biomedical and Clinical Sciences  
Università degli Studi di Milano**

**Doctoral Program in Translational Medicine  
Department of Clinical Science and Community Health  
XXXVI Cycle**

**Nanotechnological approaches for cancer diagnosis,  
treatment and management: implementation of  
Ferritin protein nanoparticles for tumor targeting**

**PhD candidate: Marta Sevieri  
Registration number: R12980**

**Tutor: Dr. Serena Mazzucchelli  
Coordinator: Prof.ssa Chiarella Sforza**

**ACADEMIC YEAR 2023/2024**

# Table of contents

<b>1. ABSTRACT</b>	<b>3</b>
<b>2. GENERAL INTRODUCTION</b>	<b>8</b>
<b>2.1 Breast Cancer</b>	<b>8</b>
2.1.1 Classification of Breast Cancer	8
2.1.2 Treatment options for Breast Cancer	10
<b>2.2 Nanotechnology and Nanomedicine</b>	<b>15</b>
2.2.1 Nanomedicine: lights and shadows	16
2.2.2 Applications of nanomedicine	21
2.2.3 Nanoparticles for cancer treatment	24
<b>2.3 Ferritin nanoparticles</b>	<b>29</b>
2.3.1 Structure and properties of Fn	29
2.3.2 Fn nanocages as delivery systems	31
2.3.3 Novel strategies to improve bioavailability and <i>in vivo</i> circulation of HFfn	32
<b>3. STUDY 1: ICG-LOADED HFfn NANOCAGES FOR IMAGE-GUIDED SURGERY APPLICATIONS</b>	<b>34</b>
<b>3.1 Introduction</b>	<b>34</b>
3.1.1 Fluorescence guided surgery in oncology	34
3.1.2 Indocyanine green	36
3.1.3 New ICG-based strategies	37
<b>3.2 Aim of the study one</b>	<b>39</b>
<b>3.3 Materials and methods</b>	<b>40</b>
<b>3.4 Results</b>	<b>49</b>
3.4.1 Production and purification of HFfn and HFfn-PAS	49
3.4.2 Purification of HFfn and HFfn-PAS from endotoxin contamination	50
3.4.3 <i>In vitro</i> characterization of HFfn and HFfn-PAS nanocages	51
3.4.4 <i>In vitro</i> binding assay	54
3.4.5 Development of HFfn-ICG and HFfn-PAS-ICG	55
3.4.6 <i>In vivo</i> evaluation of HFfn-ICG biodistribution and tumor targeting	55
3.4.7 Mass spectrometry analysis on organs homogenates	57
3.4.8 Evaluation of HFfn-PAS-ICG tumor accumulation in a breast cancer murine model	61
<b>3.5 Discussion and conclusion</b>	<b>64</b>
<b>4. STUDY 2: FERRITIN NANOCAGES LOADED WITH DOXORUBICIN: A STRATEGY TO PRESERVE ANTITUMOR IMMUNITY FROM DOXORUBICIN TOXICITY</b>	<b>66</b>
<b>4.1 Introduction</b>	<b>66</b>
<b>4.2 Aim of the study two</b>	<b>67</b>

<b>4.3 Materials and Methods</b>	<b>67</b>
<b>4.4 Results and Discussion</b>	<b>72</b>
4.4.1 Human Peripheral Blood Mononuclear Cells internalized DOX in a dose and time-dependent manner	72
4.4.2 DOX internalization affects the proliferative potential of human Peripheral Blood Mononuclear Cells	73
4.4.3 DOX treatment predominantly targets CD8 <sup>+</sup> T cells	76
4.4.4 DOX formulation in ferritin nanocages (FerOX) preserve DOX activity in a panel of Patient-derived organoids	78
4.4.5 FerOX reduces DOX internalization in Peripheral Blood Mononuclear Cells	79
4.4.6 FerOX displays a reduced uptake in T cells, sparing central memory, effector memory and naive subpopulations	80
4.4.7 FerOX suitability in cancer patients by preserving PBMC proliferative potential	81
<b>4.5 Conclusions</b>	<b>84</b>
<b>5. STUDY 3: FERRITIN-TRASTUZUMAB NANOCONJUGATES: A STRATEGY TO VEHICLE TRASTUZUMAB TO THE BRAIN AND TACKLE HER2-POSITIVE BREAST CANCER BRAIN METASTASIS</b>	<b>85</b>
5.1 Aim of the study three	85
<b>6. CONCLUSIONS</b>	<b>100</b>
<b>7. REFERENCES</b>	<b>101</b>

# 1. Abstract

Despite the efforts performed in the field of cancer research, data concerning the incidence of this pathology in North America and Europe reveal that tumors still represent the second cause of death. In fact, the effectiveness of many drugs is often seriously affected by lack of specificity in hitting the therapeutic target, determining the onset of toxicity issues.

In this context, Nanomedicine aims to make a decisive contribution. Nanoparticle (NPs)-based drug delivery systems can enhance the physicochemical properties of a wide variety of drugs used in oncology to limit off-site side effects and improve their therapeutic efficacy, increasing drug accumulation in target tissue. Thus, through the development of nanocarriers capable of selectively recognizing and interacting with tumor cells and/or tissues, potential groundbreaking applications in the diagnosis, treatment and prevention of cancer could become feasible.

In my PhD project, I exploited the unique features of a NPs based on recombinant heavy-chain ferritin nanocages (HF<sub>n</sub>). HF<sub>n</sub> nanocages represent a promising protein-based class of NPs for drug delivery widely investigated by virtue of (1) their natural tumor homing and limited accumulation in off-target organs which leads to reduced off-target toxicity; (2) their biocompatibility; (3) their structure that allows the encapsulation of different types of drugs or fluorescent tracers; (4) their versatility to be modified at the surface both exploiting chemical and genetical strategies.

My work has been divided into three main studies aimed at implementing innovative strategies based on HF<sub>n</sub> nanocages both for diagnostic and therapeutic approaches in oncology.

In **Study 1**, I presented the exploitation of HF<sub>n</sub> nanocages as nanodevices for fluorescence image-guided surgery (FGS). This technique is gaining interest due to its potential to improve tumor margin visualization and real-time identification of tumor deposits, maximizing the benefits for patients. However, no tumor-targeted probe effectively capable of localizing tumor tissue is available to date. For this reason, we proposed a HF<sub>n</sub>-based nanotracer for the delivery of indocyanine green (ICG), which is the main fluorescent dye currently used in clinics for FGS. A novel variant of HF<sub>n</sub> was developed, extensively characterized *in vitro* and loaded with ICG for *in vivo* experiments demonstrating potentiality as tumor-targeted nanotracers for the identification of tumors.



In **Study 2**, HF<sub>n</sub> nanocages were exploited for the encapsulation of a chemotherapeutic drug, doxorubicin (DOX) obtaining FerOX nanoformulation. FerOX has been investigated by virtue of its natural tumor homing and limited accumulation in off-target organs which leads to reduced off-target toxicity of drugs herein encapsulated. In particular, the object of this study was to assess the efficacy of FerOX as an alternative formulation capable of preserving the proliferative potential of human lymphocytes and the potential impact in the generation of an adaptive immune response after treatment.

In **Study 3**, we focused on the use of HF<sub>n</sub> nanocages conjugated to the monoclonal anti-HER2 antibody trastuzumab (TZ). By exploiting the ability of HF<sub>n</sub> to cross the blood brain barrier (BBB), we achieved the delivery of TZ as a prophylactic treatment to tackle brain metastasis in HER2-positive advanced breast cancer.

# Abbreviation list

<b>ABD</b>	Albumin Binding Domain
<b>ADC</b>	Antibody-drug conjugates
<b>BBB</b>	Blood Brain Barrier
<b>BC</b>	Breast cancer
<b>BM</b>	Brain metastasis
<b>CD</b>	Circular Dicroism
<b>CEA</b>	Carcinoembryonic antigen
<b>CM</b>	Central memory cells
<b>CRC</b>	Colorectal cancer
<b>CT</b>	Computed tomography
<b>DC</b>	Dendritic cells
<b>DEAE</b>	Diethylaminoethanol
<b>DOX</b>	Doxorubicin
<b>DLS</b>	Dynamic Light Scattering
<b>EGFR</b>	Epidermal growth factor receptor
<b>EM</b>	Effector memory cells
<b>EPR</b>	Enhanced permeability and retention
<b>ER</b>	Estrogen receptor
<b>ERBB2</b>	Human epidermal growth factor
<b>ETX</b>	Endotoxin
<b>ET</b>	Endocrine therapy
<b>EU</b>	Endotoxin units
<b>FC</b>	Flow cytometry
<b>FDA</b>	Food and Drug administration
<b>FerOX</b>	DOX loaded HF <sub>n</sub> nanocages
<b>FGS</b>	Fluorescence Guided Surgery
<b>FISH</b>	Fluorescence In Situ Hybridization test
<b>FMT</b>	Fluorescence molecular tomography
<b>Fn</b>	Ferritin
<b>FPLC</b>	Fast protein liquid chromatography

<b>GMP</b>	Good manufacturing practice
<b>HER2</b>	Human epidermal growth factor receptor
<b>HF<sub>n</sub></b>	H-ferritin nanoparticles
<b>HF<sub>n</sub>-ICG</b>	ICG-loaded HF <sub>n</sub> nanoparticles
<b>HF<sub>n</sub>-PAS</b>	H-ferritin nanoparticles PASylated
<b>ICCD</b>	Immunogenic cancer cell death
<b>ICG</b>	Indocyanine Green
<b>IEC</b>	Ione exchange chromatography
<b>IPTG</b>	Isopropyl-β-D-1-thiogalattopiranoside
<b>i.v.</b>	Intravenous administration
<b>LAL</b>	Limulus Amebocyte Lysate test
<b>LB</b>	Luria Bertani
<b>LF<sub>n</sub></b>	L-ferritin nanoparticles
<b>mAb</b>	Monoclonal antibody
<b>miRNA</b>	miRNA
<b>MFI</b>	Mean fluorescence intensity
<b>MMPs</b>	Matrix metalloproteinases
<b>MRI</b>	Magnetic resonance imaging
<b>NAC</b>	Neoadjuvant chemotherapy
<b>NIR</b>	Near-infrared
<b>NPs</b>	Nanoparticles
<b>OD</b>	Optical density
<b>OI</b>	Optical imaging
<b>PAS</b>	Proline, alanine and serine sequence
<b>PBMC</b>	Peripheral Blood Mononuclear Cells
<b>pCR</b>	Pathologic complete response
<b>PD-L1</b>	Programmed death-ligand 1
<b>PDO</b>	Patient derived organoid
<b>PEG</b>	Polyethylene glycol
<b>PET</b>	Positron emission tomography
<b>PgR</b>	Progesterone receptor
<b>PTX</b>	Paclitaxel

<b>RES</b>	Reticuloendothelial system
<b>SEC</b>	Size exclusion chromatography
<b>SDS-PAGE</b>	Sodium Dodecyl Sulphate - PolyAcrylamide Gel Electrophoresis
<b>siRNA</b>	Small interfering RNA
<b>TEM</b>	Transmission Electron microscopy
<b>TDE</b>	Terminally differentiated effector cells
<b>T-DM1</b>	Trastuzumab Emtansine
<b>T-Dtx</b>	Trastuzumab Deruxtecan
<b>TfR1</b>	Human transferrin receptor 1
<b>TME</b>	Tumor microenvironment
<b>TZ</b>	Trastuzumab
<b>UHPLC/MS-MS</b>	Ultra-high performance liquid chromatography-tandem mass spectrometry
<b>μCT</b>	Micro computed tomography

## 2. General introduction

### 2.1 Breast Cancer

Worldwide, Breast Cancer (BC) represents one of the most life-threatening and common types of cancer affecting women<sup>1</sup>. Female BC has now surpassed lung tumor as the most frequently diagnosed cancer with an approximate number of 287.850 new cases of invasive BC among women in North America in 2022<sup>2</sup>. Although great effort has been made in the early detection and treatment of BC, this malignancy unfortunately continues to have a large impact on the global number of cancer deaths<sup>3</sup>. In the last years, nearly 685.000 deaths were globally attributed to BC, leading to the dramatic facts that one in eight women will develop BC during their lifetime and that about 1 in 39 will die from this disease<sup>1,4</sup>.

Although survival rates have markedly improved over the past two decades, the incidence of this disease continues to rise worldwide. Thus, global efforts are needed to counteract its impacting burden, especially in transitioning countries.

One of the most challenging aspects in tackling BC is attributable to its high heterogeneity<sup>3,5</sup>. BC takes shape as group of neoplasms exhibiting different histological, prognostic, clinical features, and displaying a high degree of diversity, not only among different patients (intertumor heterogeneity) but also within each individual tumor (intratumor heterogeneity). Indeed, BC comprises multiple biological entities which involve genomic alterations, gene expression, and the tumor microenvironment (TME). All these factors together, lead to diverse clinical behavior, different disease trajectories, treatment options, and ultimately can adversely influence patient's outcomes<sup>4</sup>.

#### 2.1.1 Classification of Breast Cancer

BC classification is of paramount importance in guiding therapeutic decisions and finally achieving better patient's responses. Historically, BC are clinically stratified in subtypes according to the immunohistochemical expression of estrogen receptor (ER), progesterone receptor (PgR), and human epidermal growth factor (ERBB2) receptor (HER2)<sup>6,7</sup>.

Based on this classification, four broad clinical groups of BC have been identified: Luminal A, Luminal B, HER2-positive, and triple-negative (TNBC), which is characterized by the lack of expression of any of the above receptors <sup>8,9</sup>.

Luminal A tumors are characterized by ER+ and/or PgR+ ( $\geq 20\%$ ), the absence of HER2 overexpression and a low expression of cell proliferation marker Ki-67 (less than 14%). This subtype accounts for ~40–50% of BC cases and is associated with low grade and proliferation and a comparably good prognosis with less incidence of relapse and higher survival rate.

The second subtype, Luminal B BC, displays an ER+ and/or PgR+ (but generally lower than Luminal A;  $< 20\%$ ) and a higher Ki-67 value (typically  $> 14\%$ ). This subtype accounts for ~30% of cases and may be associated with a poorer prognosis.

The HER2-positive group comprises 10–15% of BC cases and is characterized by ER-, PgR-, and HER2 positive setting and is considered a more aggressive and fast-growing <sup>10</sup>. The two of most common tests for the determination of the HER2 status include immunohistochemistry, which gives a score of 0 to 3+ that measures the amount of HER2 proteins on the surface of cells in a breast cancer tissue sample, and the Fluorescence In Situ Hybridization test (FISH). Accordingly, a score of 3+ and FISH positive testing determine unambiguously the HER2-positive status of a patient. This subtype can be often related to drug resistance and associated with a higher incidence of brain metastasis and worse clinical outcomes <sup>11</sup>.

TNBC, also known as basal-like BC, is characterized by the lack of ER and PgR, and an HER2 scoring of 1+ or 2+, without gene amplification. This subtype, often occurring in women under 40 years of age, constitutes ~15–20% of BC cases and is associated with an aggressive behavior and tendency to recur, leading to a worse prognosis compared to other molecular subtypes of BC <sup>12</sup>.

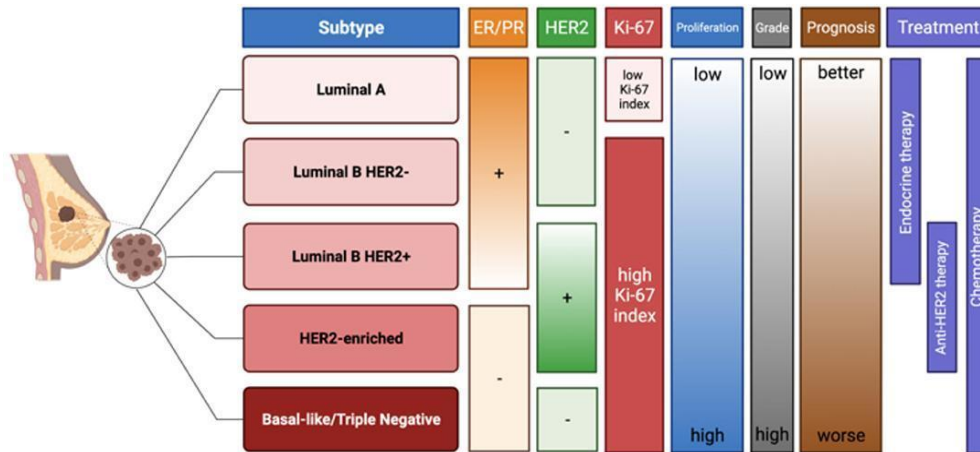


Figure 2.1 Schematic representation of BC subtypes<sup>8</sup>

### 2.1.2 Treatment options for Breast Cancer

Decades of research had a profound impact over the treatment of patients with BC, contributing to a tremendous evolution over the past century. Nowadays, treatment options for BC, originally strictly related to the surgical approach, have moved forward a multidisciplinary treatment which include endocrine therapy, chemotherapy, radiotherapy, targeted therapy, and immunotherapy.

The treatment of BC and the associated therapeutic decisions are mainly determined by stage at diagnosis. For early BC, generally related to stages 0, I, II, and III, the main goal of therapy is to eradicate the tumor from the breast and regional lymph nodes and prevent metastatic spreading. For metastatic BC, therapy is mostly proposed with palliative intent<sup>13</sup>.

To date, the available treatments for nonmetastatic BC include local modalities i.e. surgery and radiotherapy and systemic therapies that can be preoperative (neoadjuvant), postoperative (adjuvant), or both<sup>14</sup>.

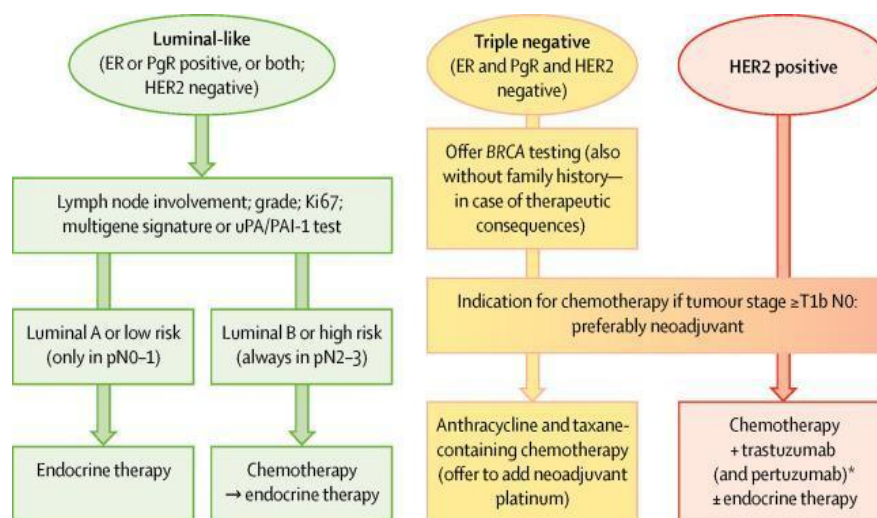


Figure 2.2 Classification of the main BC subtypes and related therapeutic approaches<sup>5</sup>

Among the presented tumor subtypes, Luminal BC are often considered as more treatable by virtue of their lower aggressiveness and intrinsic features. Indeed, about two-thirds of patients with BC present a hormone receptor positive disease (Luminal A and B) and could benefit from endocrine therapy (ET). ET carried out with the use of Tamoxifen and aromatase inhibitors is efficient in counteracting estrogen-promoted tumor growth, however some cases may require the incorporation of chemotherapy (especially in Luminal B subtype) (Figure 2.1) <sup>13</sup>. Standard ET consists in the oral assumption of anti-estrogen medication taken daily for 5 to 10 years that proved to substantially reduce (approximately by 50%) the 5-year risk for recurrence in comparison with no ET <sup>13</sup>.

For what concerns TNBC, chemotherapy is considered the only systemic therapy with demonstrated efficacy and in particular neoadjuvant therapy has become a particularly recommended option. Although TNBC has been traditionally considered a 'targetless' BC for which no targeted therapies are currently approved, intense ongoing research has brought new therapeutic opportunities. Of note, the dose-dense regimens and platinum-based therapies in the neoadjuvant setting have been proposed for TNBC patients <sup>15</sup>. Moreover, new therapies including PARP inhibitors, immune-checkpoint inhibitors and immunotherapy for example for programmed death-ligand 1 (PD-L1) hold great promise <sup>16,17</sup>. Overall, anthracycline and taxane-based chemotherapy are the standard of care followed by surgery but managing the related adverse events while balancing efficacy continues to be a challenge <sup>15,18</sup>.

Very often, in the face of a better pathologic complete response (pCR) after chemotherapy, patients with TNBC are prone to suffer a recurrence which can cause the development of visceral and brain metastases. Indeed, in many cases, mechanisms of resistance may occur during treatment thus making the treatment inadequate in the battle against cancer <sup>19</sup>.

Finally, the development of HER2-targeted therapies for patients with HER2-positive BC represented a milestone for the treatment of BC. The first and most relevant example is the humanized monoclonal antibody (mAb) Trastuzumab (TZ) approved by the Food and Drug Administration (FDA). Its mechanism of action consists in binding the extracellular domain of HER2 receptor to alter its downstream signaling, inhibiting cell cycle progression and consequently arresting tumor growth <sup>20,21</sup>.

The first-line treatment for HER-2-positive BC patients generally includes three steps: first, neoadjuvant chemotherapy is administered to reduce the tumor size before



surgical resection, consisting in a taxane-based chemotherapy and dual HER2 blockade with mAb TZ and Pertuzumab <sup>14</sup>. Subsequently, surgery is performed to remove the tumor, followed by adjuvant therapy which may include chemotherapy, radiation therapy and targeted therapy to ensure the complete elimination of any remaining tumor cell, thus limiting recurrence onset <sup>22,23</sup>. The clinical outcomes of the early and metastatic HER2-positive patients proved the significant effectiveness of targeted therapies for preventing recurrences and death reflected by a pCR rate of 65%-70% and extended rates of event-free survival and disease-free survival. However, very frequently, disease progression and relapse due to the onset of several TZ resistance mechanisms can occur <sup>24</sup>. To limit TZ resistance, the use of the mAb Pertuzumab which is able to target a different domain of the HER2 receptor was proposed. Moreover, an interesting solution employed involves the possibility of directly conjugating TZ with anticancer drugs (antibody-drug conjugates, ADCs), thus conferring an intrinsic HER2-targeting ability to the drug and reducing the toxicity of chemotherapy alone. This is the case of Trastuzumab emtansine (T-DM1, Kadcyla®), one of the commercially available ADCs developed, starting from TZ. T-DM1 was approved for the adjuvant therapy of HER2 positive early BC not in pCR after taxanes and anti-HER2 neoadjuvant therapy <sup>25</sup>. However, patients treated with T-DM1 experienced severe hepatotoxicity, thrombocytopenia and lung toxicity. Similarly, another TZ- based ADC, Trastuzumab Deruxtecan (T-Dxd, DS-8201, Enhertu®) was reported to lead to interstitial lung disease and the adverse reactions caused by its administration are currently under investigation in ongoing clinical trials <sup>26</sup>.

Patients diagnosed with HER2-positive BC are also more commonly affected by brain metastases (BM) which negatively influence survival and quality of life <sup>10,27</sup>. The advent of HER2-targeting agents has prolonged survival in patients with advanced disease, but the prevention and management of BM still represents a clinical challenge <sup>28,29</sup>. Indeed, TZ improves survival of BC patients, but it has low central nervous system penetrance, being ineffective in treating BM. Thus, it is essential to find proper therapies more effective and less toxic to control, and ultimately prevent, brain involvement in HER2-positive BC.

In light of this, despite the tremendous advantage brought by targeted therapies, several challenges limiting HER2-targeted therapy efficacy, i.e. the evolution of drug resistance and the development of BM still need to be addressed. In this context, tumor-targeted drug delivery and tumor-targeted sensitizers are regarded as the most promising approaches to achieve enhanced therapeutic effect of anticancer drugs.

Emerging evidence has pointed out the potential of nanomedicine and nanoparticles (NPs) as valuable tools for these purposes and to solve the major issues commonly emerged in BC treatment.

In this regard, a review including an update on the most promising NPs-based approaches developed in the last decade for HER2-positive BC therapy has been published with the title “**HER-2-Targeted Nanoparticles for Breast Cancer Diagnosis and Treatment**” and provided as Appendix 1.

This review was aimed at providing broad insight into the different types of HER2-targeted NPs developed in the context of HER2-positive BC therapy and diagnosis. Firstly, we focused on the different targeting strategies that have been explored, their relative outcomes and current limitations that still need to be improved.

The first and most relevant example of HER2-targeted therapy is TZ. However, several patients often experience disease progression and relapse due to the onset of TZ resistance and adverse reactions even when treated with recently developed ADCs like T-DM1 and T-DXd. Another HER-2 targeted therapeutic strategy involves the blockade of the main cellular pathways hyperactivated in HER2-positive BC, such as PI3K/AKT/mTOR and MAPK pathways, by using specific inhibitors such as Everolimus. Also, tyrosine kinase inhibitors such as Neratinib, Lapatinib and Tucatinib are employed in HER2-targeted therapy, although mechanisms of resistance often can arise. Recently, an immunotherapeutic approach has been proposed by employing mAb such as, Atezolizumab, Pembrolizumab and Nivolumab, used as Programmed Death-1 (PD-1) inhibitors to restore antitumor immunity. Despite the available HER-2 targeted therapies presented, a significant fraction of patients relapses or progress due to escape or resistance mechanisms.

In this context, nanotechnology promises to overcome some of these clinical challenges combining these therapeutic solutions with the development of novel HER2-guided nanosystems for effective treatment of BC.

Therapeutic antibodies and their derivatives such as nanobodies, antibody-fragments, peptides, aptamers and ankyrins have been used to functionalize different types of NPs to drive tumor recognition, NP accumulation, and internalization, resulting in increased performance (Figure 2.3).

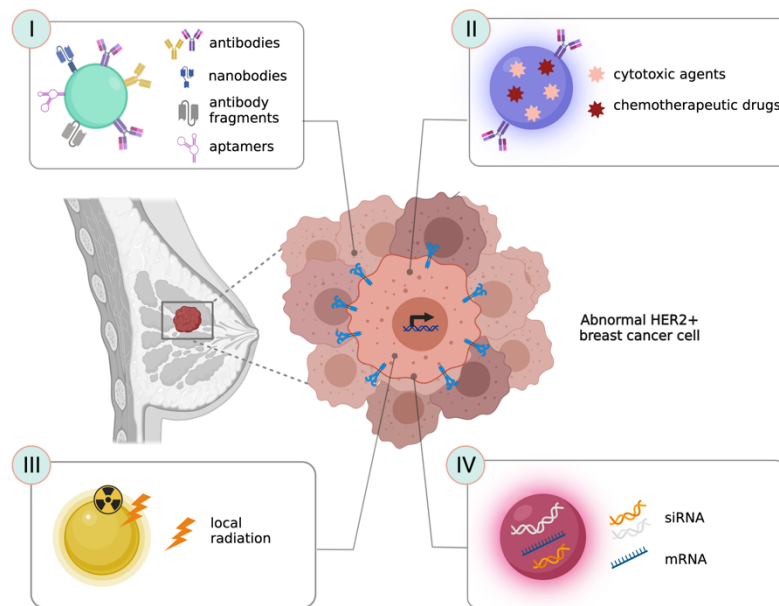


Figure 2.3 Strategies for HER-2+ BC therapy. Reprinted with permission from <sup>23</sup>.

NPs functionalized with the above-mentioned HER2-targeting ligands have been exploited to deliver: (I) different kinds of therapeutic agents (i.e. DOX, Lapatinib and Paclitaxel) or (II) nucleic acids or gene silencing molecules (i.e. siRNA and mRNA). Moreover, NPs have been functionalized with photothermal agents to promote local radiation and achieve tumor ablation.

Several NPs have emerged also as promising candidates for HER2-positive BC detection and screening, as they can be loaded with contrast agents and used as highly sensitive tools for early cancer diagnosis and as theranostic tools if co-loaded with active drugs.

Among all the nanotechnological solutions proposed so far, it is still impossible to identify the winning strategy able to be used as a targeted nanodrug for HER2-positive BC. Indeed, the choice should depend on the final intended application and NP of election. Nevertheless, there is a growing body of evidence indicating that the design of improved NPs is a promising direction in the future and their high translational potential will be explored in depth in the following chapters of this thesis.

## 2.2 Nanotechnology and Nanomedicine

As introduced in the previous paragraph, some innovative therapeutics have been developed exploiting nanotechnology. Before further discussion about these applications in the medical field, it is mandatory to introduce nanotechnology. Nanotechnology represents a multidisciplinary field of research and innovation that deals with materials at the nanoscale. According to the US National Nanotechnology Initiative, nanotechnology can be defined as the understanding and control of matter at a length scale of approximately 1– 100 nanometers <sup>30</sup>.

Indeed, at the nanoscale materials are endowed with unique physical, chemical, and biological properties that differ from those of the same material at a larger size, allowing new and innovative applications.

The concept of nanotechnology was first introduced by the Nobel prize Richard Feynman in 1959, during a famous speech at the California Institute of Technology (Caltech). In his lecture “There’s a plenty of room at the bottom” he theorized the possibility of controlling matter and creating molecular-scale devices, thus anticipating numerous fields of scientific research and technical application <sup>31</sup>. Feynman’s theories achieved concrete meaning a few years later in 1974, thanks to the article “On the Basic Concept of Nano-Technology” published by Norio Taniguchi of Tokyo Science University. Taniguchi defined nanotechnology as the “process of separation, consolidation, and deformation of materials by one atom or one molecule” <sup>32</sup>. The different possible synthesis of nanostructure was described essentially in two approaches: the top-down approach consists in the downsizing of bulk material to get nanosized particles, while the bottom-up approach envisages starting from molecules or atoms to build up nanostructures.

In 2004, the Royal Society and Royal Academy of Engineering defined nanoscience and nanotechnologies as “the study of phenomena and manipulation of materials at atomic, molecular and macromolecular scales, where properties differ significantly from those at a larger scale” and “the design, characterization, production and application of structures, devices and systems by controlling shape and size at nanometer scale”, respectively <sup>33</sup>. Subsequently, the introduction of Transmission Electron Microscopy (TEM), Atomic Force Microscopy and Scanning Tunneling Microscopy made it possible to reach the atomic resolution thus giving a strong impulse in this investigation field.

Research in the nanotechnology field guided the development of NPs which are particles with sizes mainly ranging from 1 nm to 100 nm (Figure 2.4) <sup>34</sup>. Their distinctive size-dependent properties are due to the different ratio between the number of atoms inside the structure and those on the surface. Therefore, the higher surface-to-volume ratio displayed by NPs exponentially increases their chemical and biological reactivity and can be exploited for functionalization. Thus, nanotechnologists have taken advantage of the unique physicochemical and biological properties of nanostructured materials and adapted chemical characteristics, dimensions, shape, structure, morphology and surface properties, for specific purposes.

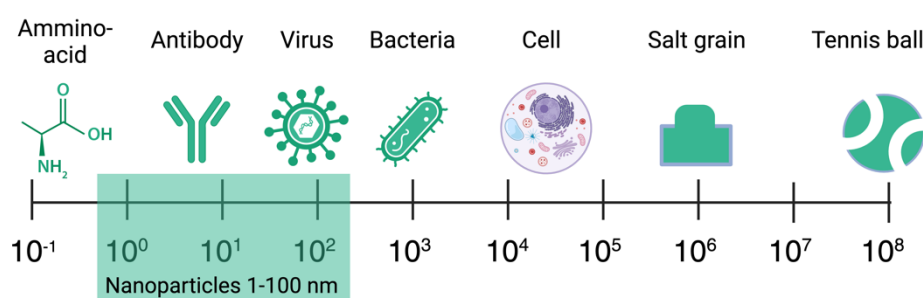


Figure 2.4 Size distribution at the nanoscale.

Nanotechnology research has developed rapidly in the last 20 years with a number of publications exponentially increased, achieving a progressive expansion of the field of investigation, from medicine to mechanics, electronics, energy and the environment. As evidence of this, PubMed research of the keyword “nanoparticle” reports over 31.000 articles related to various aspects of nanotechnology.

The application of nanotechnology in biomedical sciences and healthcare has defined a promising interdisciplinary research field termed as “nanomedicine”, aimed at the application of nanomaterials for diagnosis, monitoring, control, prevention, and treatment of diseases <sup>35</sup>.

### 2.2.1 Nanomedicine: lights and shadows

Nanomedicine research area extends from *in vitro* and *in vivo* diagnostics to therapy, including drug delivery, drug targeting, regenerative medicine and drug discovery, with the aim of improving human health <sup>36</sup>.

Very often nanomedicine takes advantage of NPs which potentially can cross biological barriers and specifically interact with target molecules locally releasing

therapeutic drugs <sup>37</sup>. In addition, certain NPs with therapeutic purpose can be employed also for the diagnosis of diseases, thus becoming theranostic agents.

This field is in great expansion, indeed, according to the recent Trend in Nanomedicine report published by Mordor Intelligence, the nanomedicine market is expected to grow from USD \$219,850 million in 2020 to \$461,252 million by 2026 <sup>38</sup>. Over the past few decades, the FDA has approved commercialization of more than 50 nanomedicine applications and products. Among these products, liposomal drugs and polymeric conjugates are the two dominant classes, which represent more than 80% of the total amount <sup>39</sup>. Moreover, in the last years, due to the global pandemic virus, the coronavirus disease 2019 (COVID-19), the nanomedicine scenario has developed fast. In 2020, Moderna and Pfizer- BioNTech COVID-19 vaccines were authorized for emergency use in the US and they both used lipid nanoparticles as delivery systems. In figure 2.5 which shows the chronological approvals of NPs based on particle type, lipid-based and inorganic NPs emerge as the most clinically authorized NPs. Figure 2.6 reports the approvals in the clinic of NPs based on indication over time. The most represented applications are cancer, anemia and imaging but several new NPs are being introduced for different clinical uses considering the annual raise of the total number of clinical trials <sup>40</sup> (Figure 2.5-2.6).

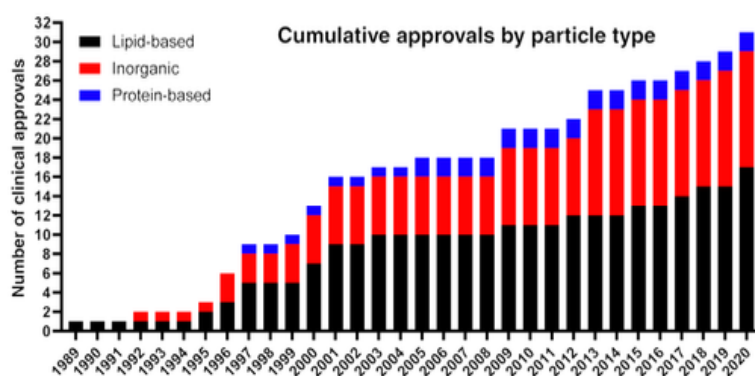


Figure 2.5 Chronological clinical approvals of NPs based on particle type <sup>40</sup>

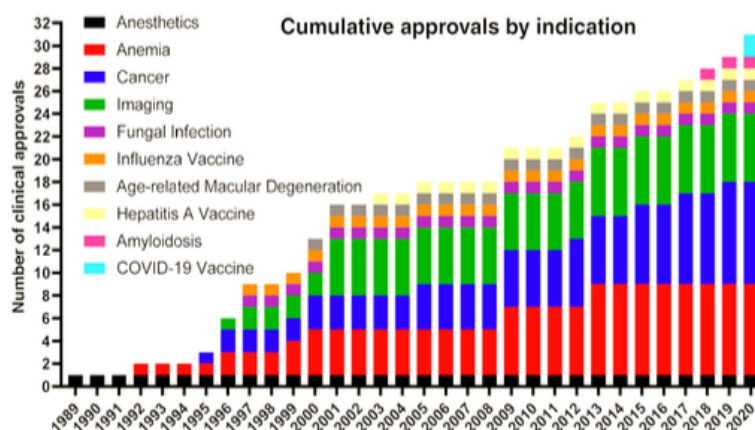


Figure 2.6 Chronological approvals in clinic of nanoparticles based on indication <sup>40</sup>

It is common knowledge that nanomaterials can address some of the most challenging problems of medical diagnosis and therapy and have the potential for improving the quality and duration of life. However, there are still many challenges to be faced in transforming the concept of nanotechnology into a practical and realistic application from which patients can effectively benefit. The adoption of nano-based therapies and diagnostics have been shown to bring significant therapeutic benefits for several biomedical applications. However, their clinical application has not progressed as rapidly as preclinical results and the number of nanomedicines available to patients is below projections for the field.

To fully grasp the opportunities offered by nanomedicines, it is necessary to understand and solve the main issues that may hamper their translation to the commercial sector and ultimately to the clinic. The major challenges that still need to be solved to bring the use of NPs "from the laboratory bench to the patient's bed" include:

- Biological reasons: one hurdle is the discrepancy between the efficacies obtained in preclinical studies and the outcomes from clinical trials, mainly due to the lack of understanding of the differences in physiology and pathology between animal model and humans. Thus, it is important not only to increase the number of *in vivo* studies to better investigate the fate and functionality of nanomedicines in the body, but also to include animal models of pathology. For example, to investigate NPs employed as delivery systems for cancer treatment, animal models that closely recapitulate the heterogeneity and anatomical histology of human cancers are required <sup>42,43</sup>. Added to this, multiple physiological barriers such as tumor penetration, tumor heterogeneity,

relative hypoxia, and endosomal escape represent further impediments for successful oncological applications <sup>44</sup>.

- **Controllable and reproducible production:** the great variability of the main physicochemical characteristics of nanomaterials (structure, composition, size, surface properties, porosity, charge and tendency to aggregation) makes it difficult to carry out an exhaustive characterization of NPs, before and after the administration. For the successful development of therapeutic NPs, it is necessary to have a complete understanding of the characteristics of NPs, including chemical reactivity and stability, and the determination of optimal physicochemical parameters for batch-to-batch reproducibility.
- **Safety challenges and regulatory issues:** it is mandatory to assess potential issues related to toxicity when administering NPs. Currently, no specific regulations for nanomedicine products are available since they have been monitored by applying the same rules as for conventional medicines. However, it is important to consider that the safety evaluation suitable for nanomedicine would be greatly different from bulk drugs due to variation in size and they may react differently according to their properties. This led to the recent development of nanotoxicology with the generation of protocols and procedures for the evaluation of the toxicity of nanostructured materials <sup>38,45,46</sup>. **Scalable manufacturing and cost-effectiveness:** another challenge to clinical development involves the scaling up of nanomaterials. Scalable nanomanufacturing requires the complex balancing of many aspects including scalability, reliability, controllability, efficiency, quality, yield and affordability. Moreover, chemistry, manufacturing, and controls of nanotherapeutics may require the establishment of new good manufacturing practice (GMP) processes with additional modifications of existing unit operations. Overall, large-scale manufacturing is more complicated when NP formulation involves multiple steps or complex technologies. For example, the production of nanoparticles decorated with biological targeting ligands or loaded with two or more therapeutics, comprise multiple functional units and require considerable efforts from the technology-transfer point of view. This could dissuade pharmaceutical companies from investing in large-scale production of nanopharmaceuticals and, more specifically, of nanocarriers. It is therefore essential that the clinical benefits of nanopharmaceuticals should be significant and can justify the huge development and production costs <sup>42,47</sup>.



Considering additional challenges related to the development and clinical translation, to give priority to the development of simpler nanomedicine platforms could be a reasonable decision <sup>44</sup>.

## 2.2 Classification of nanoparticles

To date, a plethora of NPs with different characteristics based on their nature, dimension, shape and specific application have been proposed and investigated. A possible classification of NPs is based on their physical and chemical properties which include organic, inorganic and hybrid NPs <sup>48</sup>.

Organic NPs are characterized for being made up of “soft” or blending materials. Organic NPs developed for drug delivery can be produced from a large variety of substances including lipids (liposomes and micelles) and polymers (polymeric NPs, polymeric micelles and dendrimers). Organic NPs potentially display less toxicity in comparison with metallic NPs and some properties which make them optimal delivery systems and the ideal choice for medical applications. This group of NPs also includes biological NPs which are occurring NPs that can be constituted of organic materials. They are assembled from molecules or atoms synthesized in a biological system. These NPs display structure uniformity, low toxicity, the ability to evade the immune system and the capability to vehiculate pharmaceuticals, which makes them particularly compelling for biomedical applications <sup>49</sup>. Among them, the most broadly studied are exosomes, lipoproteins, viral NPs and ferritin NPs.

Inorganic NPs are more chemically stable and characterized by a higher mechanical strength compared to organic NPs. They include those derived from metals (e.g., gold, silver, copper), semiconductors (e.g., quantum dots), and oxides (e.g., iron oxide). Metallic NPs which are obtained from metal precursors, possess unique opto-electrical properties that make them widely investigated both for diagnostic and therapeutic purposes. For example, gold nanoparticles can exert a thermal heating function or certain inorganic NPs can respond to external stimuli such as magnetic fields or near-infrared (NIR) light to enhance magnetic imaging. Inorganic NPs demonstrated their suitability as contrast agents, fluorescence probes, nanocarriers for drug delivery, and in the energy conversion for photothermal and photodynamic therapies especially in cancer. On the other hand, they are reported to have reduced biocompatibility and there are still many challenges to solve related to their toxicity. Indeed, many issues

such as the accumulation of nanoparticles in organs like the liver and the spleen, for prolonged periods strongly limited their use in clinical trials.

In this context, the development of hybrid nanosystems showing intermediate characteristics between organic and inorganic may allow researchers to develop better carrier systems opening room for new biomedical applications<sup>50</sup>.

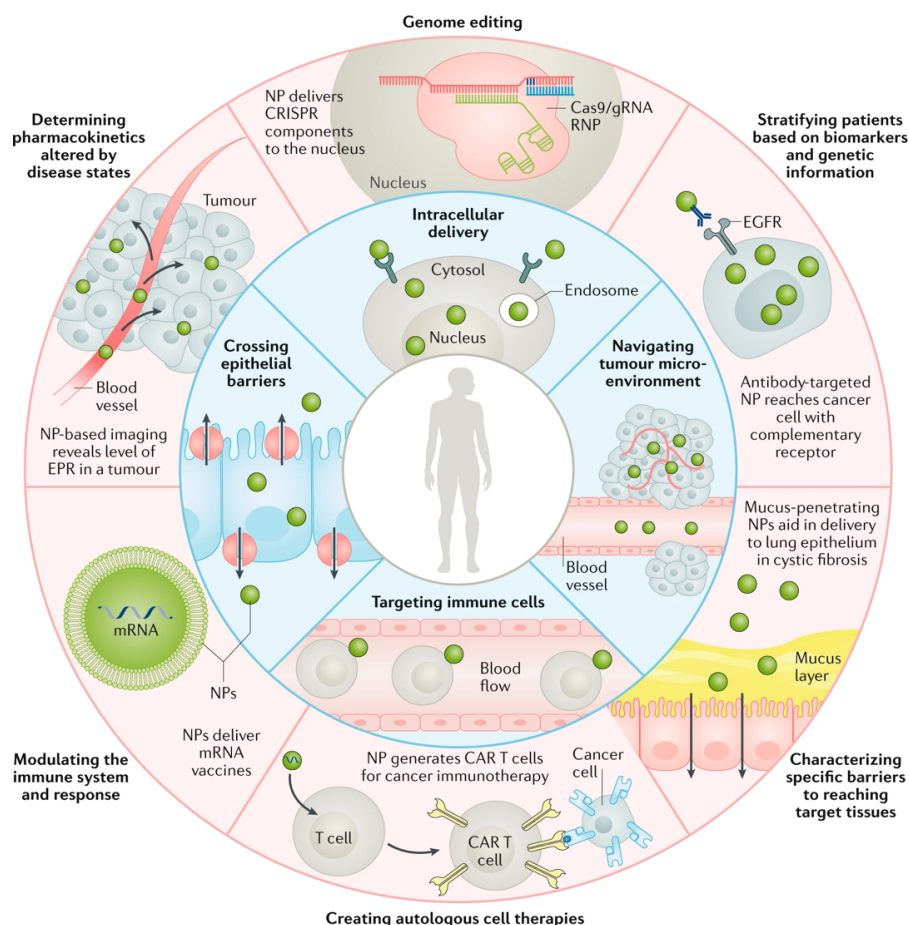


Figure 2.7 Overview highlighting some of the biological barriers that NPs can overcome (inner ring) and precision medicine applications that may benefit from NPs (outer ring). Reprinted with permission from<sup>52</sup>.

## 2.2.2 Applications of nanomedicine

Recently, the implementation of NPs has expanded into a broad range of clinical applications. It is expected that nanomedicine will lead to the development of improved devices, drugs, and other applications, ensuring early diagnoses and/or treatment of many diseases with high efficacy, specificity, and personalization<sup>51</sup>. In particular, NPs hold great promise to overcome the limitations of conventional drug delivery and navigate biological barriers<sup>52</sup>.

The main applications for which NPs have a significant role include:

- Imaging and diagnosis
- Drug delivery
- Vaccine development
- Gene therapy

A key focus in nanomedicine takes advantage of NPs as contrast agents for anatomical imaging and diagnosis. Molecular imaging allows non-invasive visualization of cellular functions and biological processes in the human body for the diagnosis of diseases at early stages. The most representative imaging modalities include computed tomography (CT); magnetic resonance imaging (MRI); positron emission tomography (PET) and optical imaging (OI).

To date, various iron oxide NPs have been developed as contrast agents for MRI due to their high biocompatibility and excellent magnetic properties. NPs probes of high-atomic-number materials like iodine or gold have been extensively investigated to overcome the limitations of current CT contrast agents. In addition, NPs can be functionalized with isotopes for PET applications and with fluorescent dyes or with other compounds for different OI <sup>51,53</sup>. In comparison with conventional probes, NPs possess controllable physical properties, versatility for surface modification and longer circulation time. Moreover, they lend themselves for various combinations also for multimodal imaging and therapy <sup>54</sup>.

NPs have also a strong relevance as drug delivery agents or nanocarriers. Drug delivery using NPs has the potential to overcome many disadvantages of conventional drug delivery by offering improved bioavailability and pharmacokinetics. Overall, they offer enhancement of the pharmaceutical properties (i.e., stability, solubility, *in vivo* half-life and tumor accumulation) of therapeutic molecules.

NPs are often functionalized by exploiting different strategies to minimize clearance and limit the systemic diffusion of the drug. In addition, different functionalization strategies designed to maximize the binding affinity of NPs to the target lesions can facilitate the specific accumulation of the compound accumulation in the target site, with a consequent reduction of side effects and toxicity to off-target organs. Thus, by providing a targeted and sustained drug release, drug-related toxicity could be reduced, limiting frequent dosing and improving patient compliance <sup>55</sup>.

After reaching the target tissue, NPs should have the ability to kill or discriminate diseased from healthy cells, with a controlled release mechanism of the cargo molecule. NPs can also respond to certain stimuli such as changes in pH or temperature, or they can be designed to be slowly degraded in the body (in the case of biodegradable polymers) or eliminated by renal filtration <sup>56</sup>.

Recently, nanotechnology has been incorporated into vaccine development. Indeed, the investigation of the immune responses that can be induced and modulated by NPs led to the study of vaccine formulations based on the use of NPs <sup>61</sup>.

Researchers consider NPs valuable tools both as delivery systems to achieve enhanced antigen processing and as an immunostimulatory adjuvant to induce and boost up immune response. Indeed, thanks to their nano-size and tunable structure they can mimic structural features of pathogens like natural viruses.

Potential nano-systems that work as vaccines to enhance corresponding immune responses and overcome limitations of traditional vaccine adjuvants include polymeric NPs, liposomes, immunostimulatory complexes, virus-like particles, protein NPs and emulsions. Among them, a popular vaccine platform is the protein-based nanocage Ferritin which has been studied to deliver vaccine antigens for various models of infectious diseases such as influenza, HIV, or COVID-19 <sup>62-64</sup>. Based on the antigen loading strategy employed, NPs-based vaccines can encapsulate vaccine antigens or nucleic acid cargos within their core or be functionalized with vaccine antigens on their surface.

Of note, the terrific efforts lavished to obtain vaccines for COVID-19 gave a strong impulse to nano-vaccine development. The first two COVID-19 vaccines introduced in clinics were lipid NPs delivering mRNA encoding engineered viral spike (S) protein developed by Moderna and BioNTech/Pfizer. Both demonstrated efficacy greater than 90% against Wuhan-Hu-1 SARS-CoV-2 after two vaccine doses. To date, more than 26 nanoparticle-based vaccine candidates which encompass diverse formulations have advanced into human clinical trials <sup>65,66</sup>.

NPs have demonstrated remarkable success also as nucleic acid delivery carriers for gene therapy purposes <sup>52</sup>. To date, gene therapy can be achieved by introducing exogenous nucleic acids such as antisense oligonucleotides which delivery is typically carried out by viral vectors with several limitations with respect to safety. On the contrary, by virtue of their tunable features, superior ability to target cells and tissues

and reduced potential adverse effects, NPs could potentially represent a promising solution. NPs have been explored for a wide range of diseases, such as cancer, cystic fibrosis, diabetes, haemophilia and HIV. For systemic delivery of nucleic acid-based therapeutics such as antisense DNA, mRNA, small interfering RNA (siRNA) or microRNA (miRNA), both lipid-based vectors and polymer-based vectors have been intensively investigated in experimental animals and in clinical trials<sup>67,68</sup>. Recently, several nano-delivery approaches integrated with CRISPR–Cas technology have been proposed as a new generation of high-efficiency delivery tools for gene editing<sup>69</sup>.

### 2.2.3 Nanoparticles for cancer treatment

Cancer therapy is one of the applications that could benefit the most from nanotechnology. Cancer nanomedicine seeks to overcome many shortcomings of conventional cancer diagnostics and therapies. Indeed, either conventional chemotherapeutic drugs or immunotherapies are non-tumor-targeted therapeutic approaches, thus not able to accurately discriminate malignant cells from healthy tissues, giving rise to multiple undesired side effects<sup>41</sup>.

Currently, the advances in nanotechnology, together with the improved understanding of cancer biology and nano-bio interactions, have fostered the development of a variety of nanocarriers, designed to improve the therapeutic efficacy while reducing off-target toxicity of the encapsulated anticancer agents through tumor specific targeting.

NPs are usually designed to exert their delivery function for cancer treatment with two different types of targeting: *passive targeting* and *active targeting*<sup>42</sup>.

With passive targeting, the fate of the nanocarrier is determined by their morphological, chemical and physical features and by the anatomical and physiological characteristics of the target site<sup>57</sup>. Generally, nanocarriers are delivered systemically and accumulate in the tumor site as a consequence of the enhanced permeability and retention effect (EPR). This passive targeting phenomenon takes advantage of the abnormal vascularization of the tumoral area, due to both increased number of new vessels which are highly disorganized and dilated (600-800 nm), and the limited lymphatic drainage that facilitates prolonged retention of these NPs in tumors.

From the first nanomedicine approved by FDA, Doxil® (PEGylated liposomal doxorubicin), new nanotherapeutics received approval and have now entered routine clinical use for cancer, all of which rely on EPR-mediated passive tumor targeting.

Nevertheless, it is increasingly known that the EPR effect is highly heterogeneous and characterized by substantial variability among patients, tumor types, and within the same patient between primary tumors and metastases. Hence, several new targeting strategies have been proposed to enhance the accumulation of nanomedicines in low-EPR tumors, including cell-mediated tumor targeting, tumor vasculature targeting and locoregional delivery.

Active targeting instead, is aimed at increasing the binding specificity with target cells or tissues. It involves the functionalization of the surface of NPs by exploiting the reactivity of some end groups for the conjugation with specific proteins, peptides, mAbs and cell-specific ligands. This application typically involves the tuning of surface functionality with one or more targeting moieties able to interact specifically with antigens or receptors that are either uniquely expressed or overexpressed on diseased tissues and cell surfaces<sup>70,71</sup> (Figure 2.8).

It is considered active targeting also the exploitation of physical stimuli such as temperature, pH, and magnetic field<sup>58</sup>. The TME is another key feature that can influence targeting. Hyperproliferative tumor cells are characterized by a high metabolic rate which produces an acidic environment. This hallmark can be exploited by pH-sensitive nanosystems designed to be stable at physiological pH but able to release the drug after degradation in presence of a lower pH. Other unique features of the TME such as the presence of tumor metalloproteinases or higher levels of certain enzymes, can be exploited to achieve a targeted release of the drug<sup>59</sup>.

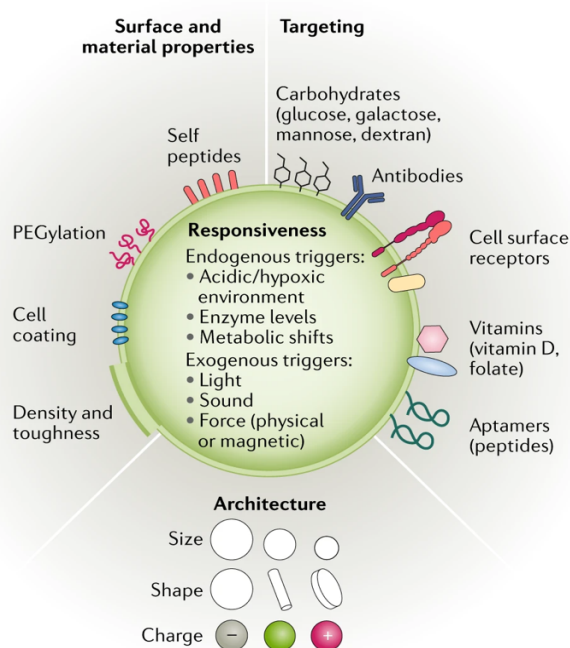


Figure 2.8 Surface and material properties, architecture, targeting moieties and responsiveness are all attributes of nanoparticles (NPs)<sup>52</sup>.

Another promising targeting strategy is the development of biomimetic NPs via cell membrane coating. Indeed, the employment of blood cell or cancer cell membranes is attracting enormous interest to camouflage NPs and extend nanoparticle residence time *in vivo* or to enhance efficient tumor-targeted drug delivery, respectively.

Moreover, once NPs have been internalized into target cells, nanomedicines still need to be accurately delivered to their sites of action inside tumor cells, which are typically located within nucleus, mitochondria, and lysosomes, to maximize therapeutic efficacy while preventing multidrug resistance.

NPs are considered interesting tools for cancer treatment also for their multifunctionality, in fact they can be loaded at the same time with different molecules for both therapeutic and diagnostic purposes. Indeed, theragnostic NPs integrating imaging and therapeutic within one single nano-platform, potentially allow precise diagnosis of disease and concurrent treatment, holding therefore great promise towards personalized nanomedicine <sup>72</sup>.

NPs currently tested for cancer diagnosis and therapy belong to the inorganic or organic category. Regarding inorganic NPs, iron oxide, gold, silica NPs and quantum dots are mainly used for imaging and thermal ablation purposes; while polymeric NPs, liposomes, dendrimers, micelles, and protein-based NPs are more frequently implemented as drug delivery systems <sup>73</sup>.

The first nanomedicine product for cancer approved in 1995 was Doxil, which showed great efficacy in reducing cardiotoxicity compared to free form DOX. Thereafter, several NPs-based anticancer drugs received approval for cancer treatment. More recently, other liposomal formulations entered the clinic such Onivyde (liposomal irinotecan) and Vyxeos (liposomal daunorubicin plus cytarabine) which received FDA approval in 2017 for therapy-related acute myeloid leukemia. Of note, all the formulations approved to date are based on liposomal formulations with the exception of Abraxane® (albumin-bound paclitaxel nanoparticle) approved for lung, breast and pancreatic cancer, and NanoTherm®, an iron oxide nanoparticles formulation approved only in Europe to treat glioblastoma (Table 2.1) <sup>74</sup>.

S. No.	Product	Drug	Nanotechnology platform	Cancer type	Approval
1	Zinostatin stimalamer	Styrene maleic anhydride neocarzinostatin (SMANCS)	Polymer protein conjugate	Primary unresectable hepatocellular carcinoma	1994 (Japan)
2	Doxil (Caelyx)	Doxorubicin hydrochloride	Pegylated liposome	Ovarian cancer and AIDS-related Kaposi's sarcoma	1995 (FDA)
3	DaunoXome	Daunorubicin	Liposome	HIV-related Kaposi sarcoma	1996 (FDA)
4	Lipo-Dox	Doxorubicin	Liposome	Kaposi's sarcoma, breast and ovarian cancer	1998 (Taiwan)
5	Myocet	Doxorubicin	Liposome	Breast cancer	2000 (EMA)
6	Mepact	Muramyl tripeptide phosphatidyl ethanolamine	Liposome	Non-metastatic osteosarcoma	2009 (EMA)
7	Lipusu	Paclitaxel	Liposome	Breast cancer, non-small-cell lung cancer	2013 (EMA)
8	NanoTherm	Fe <sub>3</sub> O <sub>4</sub>	Nanoparticles of superparamagnetic iron oxide coated with amino silane	Glioblastoma, prostate, and pancreatic cancers	2013 (EMA)
9	Ameluz	5-Aminolevulinic acid	Gel containing 5-aminolevulinic acid, E211, SoyPC, and PG	Superficial and/or nodular basal cell carcinoma	2011 (EMA)
10	Depocyt	Cytarabine	Liposome	Lymphomatous malignant meningitis	1999 (FDA)
11	Genexol-PM	Paclitaxel	Polymeric micelle	Non-small cell lung cancer	2006 (South Korea)
12	Nanoxel	Docetaxel	Polymeric micelle	Breast and ovarian cancers, NSCLC, and AIDS-related Kaposi's sarcoma	2006 (India)
13	Marqibo	Vincristine	Liposome	Leukemia	2012 (FDA)
14	Onivyde	Irinotecan	Liposome	Pancreatic cancer	2015 (FDA)
15	Vyxeos	Daunorubicin and cytarabine	Liposome	Acute myeloid leukemia (AML)	2017 (EMA)
16	Oncaspar	L-Asparaginase	PEGylated conjugate	Acute lymphoblastic leukemia	2006 (FDA)
17	DPH107	Paclitaxel	Lipid nanoparticles	Advanced gastric cancer	2016 (Korea)
18	NBTXR3 (Hensify)	Hafnium oxide nanoparticles stimulated with external radiation to enhance tumor cell death via electron production	Hafnium oxide nanoparticles	Locally advanced squamous cell carcinoma	2019 (CE Mark)
19	Apealea	Paclitaxel	Polymeric micelles	Ovarian, peritoneal and fallopian tube cancer	2018 (EMA)
20	Ontak	Denileukin diftitox	Recombinant DNA derived cytotoxic protein	Cutaneous T cell lymphoma	1999 (FDA)
21	Eligard	Leuprolide acetate	Polymeric nanoparticles	Advanced prostate cancer	2002 (FDA)
22	Abraxane	Paclitaxel	Protein carrier	Various cancers including metastatic and pancreatic ci	2005 (FDA)
23	Kadcyla	DM1	Trastuzumab, covalently linked to DM1 via the stable thioether linker MCC	HER2+ breast cancer	2013 (FDA, EMA)
24	Pazenir	Paclitaxel	Paclitaxel formulated as albumin bound nanoparticles. Powder for dispersion for infusion	Metastatic breast cancer, metastatic adenocarcinoma of the pancreas, non-small cell lung cancer	2019 (EMA)

Table 2.1: Approved nanomedicine drugs in the market for cancer treatment <sup>74</sup>

At present, at least 20 cancer nanomedicines are approved worldwide, and more than 80 novel cancer nanomedicines are being tested in over 200 clinical trials. Among them, most clinical-stage anticancer nanotherapeutics are still mainly based on passive targeting tumor accumulation. Indeed, despite the active targeting of NPs may potentially enhance the cellular uptake and lead to increased drug accumulation at the target tumor site, recent results reveal that the actual effect is limited.

The nanomedicine community is wondering about potential reasons for the limited clinical translation of targeted NPs, since none of the actively targeted NPs have advanced past clinical trials despite efforts of successful pre-clinical studies <sup>75</sup>.

A recent survey reported a failure rate for 52% and 86% for Phase II and Phase III trials, respectively. The large part of failures encountered in phase II (71.4%) and phase III (100%) trials were due to insufficient therapeutic efficacy because of the inadequate capacity of nanomedicines to bypass physiological barriers. Among the challenges that strongly affect therapeutic benefit and clinical success of actively targeted NPs, various factors such as tumor heterogeneity, hypoxia, endosomal escape, and other physiological barriers, including clearance by the mononuclear phagocytic system, could be additional obstacles <sup>60</sup>.



Thus, the impressive imbalance between the increasing number of preclinical studies reporting the development of more complex nanomedicines, and the particularly challenging path for the development of nanomedicine products approved for clinical use, has become the focus of intense debate<sup>44,76</sup>. As a consequence, considering that the success rate of clinical translation of many nanomedicine solutions, often too complicated, remains relatively low, the strategy of taking advantage of simpler nanomedicine platforms could be a winning choice. In this context, leveraging biocompatible nanostrategies endowed with high natural tumor homing and efficient drug delivery capacity, could tackle the translational controversies of traditional nanomedicines and close the gap for real clinical application.

Among these nanocarriers and in particular protein-based nanocarriers, ferritin NPs (Fn) stand out by virtue of their capability to specifically target cancer tissues and reduce side effects with a high clinical translational potential and a strong impact in many biomedical applications related to cancer treatment and image-guided surgery. The most relevant aspects regarding the implementation of Fn NPs will be discussed hereafter in this thesis.

## 2.3 Ferritin nanoparticles

In recent years, protein-based NPs have been studied extensively, due to their unique architecture, exceptional biocompatibility, and functionalization versatility<sup>77,78</sup>. In particular, Fn NPs, often referred to as Fn nanocages, are attracting growing interest due to their tremendous potential for targeted delivery of drugs to cancer cells. The most prominent applications that take advantage of Fn as a nanoplatform encompass chemotherapy, immunotherapy, imaging, diagnosis, and vaccine-development. Although there are no currently approved drugs based on Fn, three vaccines against influenza have entered phase I clinical trials, and one has provided positive results<sup>79</sup>. Overall, Fn nanocages stand out from other nanocarriers thanks to their biocompatibility, low toxicity and immunogenicity and natural tumor-homing<sup>80</sup>.

A recent review entitled **“Protein-Based Nanoparticles for the Imaging and Treatment of Solid Tumors: The Case of Ferritin Nanocages, a Narrative Review”**<sup>81</sup>, whose I have been listed as co-author has been published and provided as Appendix 2. This review was aimed at discussing the leading features of Fn and the most recent applications of this promising nanotechnology in oncology, with a particular emphasis on the imaging and treatment of solid tumors.

### 2.3.1 Structure and properties of Fn

Fn describes a family of globular multimeric proteins responsible for the intracellular storage of iron and iron homeostasis. It is ubiquitously expressed in archaea, eubacteria, plants, invertebrates, and mammals, with the only exception of yeasts. Mammalian Fn is mainly localized intracellularly in the cytosol, nucleus and mitochondria, while extracellular ferritin is found in serum, synovial and cerebrospinal fluid. Due to its ability to bind and sequester intracellular iron, Fn ensures intracellular iron concentration maintenance and protection from oxidative stress through the Fenton reaction<sup>82</sup>.

Human Fn is a large protein of 450 kDa constituted by 24 subunits self-assembling in a cage sphere quaternary structure. It defines a highly stable nanocage of 12 nm in diameter, which encloses an internal cavity of 8 nm in diameter. Each cage is assembled from two subunit types, the heavy (H chain; 21 kDa) and light chains (L chain; 19 kDa)<sup>83</sup>. The three-dimensional structure of each ferritin monomers is highly conserved among species and is made up of two couples of antiparallel  $\alpha$ -helices that

fold in a four-helical bundle<sup>84</sup> The H subunit contains the catalytic centers which is involved in the oxidation of  $\text{Fe}^{2+}$  to  $\text{Fe}^{3+}$ , while in the L subunit the amino acid residues of the ferroxidase center are replaced with others that stabilizes further the protein<sup>82,85,86</sup>. The N-terminal ends of each subunit are exposed on the ferritin surface, while the C-terminal ends fold into the inner cavity. The ratio between H and L subunits is determined by Fn's primary role in tissues. For example, in the heart and brain, the H subunit is more abundant for a more pronounced antioxidant activity, while, in the liver and spleen, the presence of L subunits predominantly allows an enhanced iron storage function<sup>87</sup>.

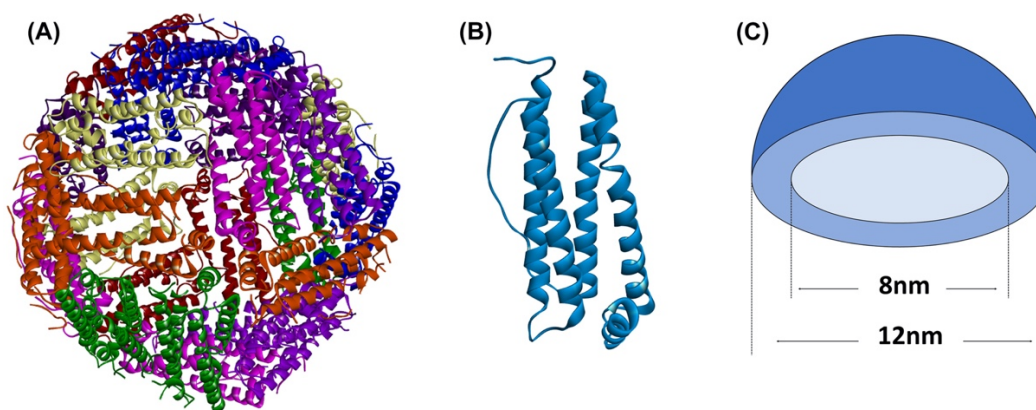


Figure 2.9 The structure of HFn nanocage. A) Structure of human HFn. The 24 subunits were showed in cartoon representations and eight different colors. B) The Fn subunit monomer structure, with five  $\alpha$  helices. (C) The cage-like diagram of Fn, with inner cavity and outer surface of diameter 8 nm and 12 nm, respectively<sup>81</sup>.

Structural features of Fn lead to unique properties, which award it to outstanding properties. The presence of several salt bridges and hydrogen bonds that link subunits, allows it to tolerate pH and temperature variations even far above the physiological ones (temperature  $>80^{\circ}\text{C}$ ; extreme pH values). Moreover, Fn remains stable in presence of denaturing agents such as urea and guanidinium chloride. Consequently, it displays the ability to fold into a quaternary structure in a pH-dependent reversible process. Indeed, nanocages can disassemble in extremely acidic (pH 2-3) or basic (pH 10-12) conditions but reassembles once pH returns to neutrality in a shape memory fashion.

Fn also displays the specific recognition of the human transferrin receptor 1 (TfR1, also named CD71) and subsequent internalization through receptor mediated endocytosis. It has been shown that the expression of TfR1 in proliferating cells, such as cancer cells, may be up to 100-fold higher than in normal cells, awarding Fn to tumor homing capability<sup>88-90</sup>.

### 2.3.2 Fn nanocages as delivery systems

By taking advantage of these unique structural, physicochemical features and versatility, nanotechnologists have exploited nanocages constituted only by H-chains of Fn (HF<sub>n</sub>) as delivery systems especially for cancer applications<sup>78</sup>.

Their cage sphere structure allows the loading of different types of compounds, like chemotherapeutics or fluorescent dyes that have been obtained through different loading strategies. pH or urea-mediated disassembly–reassembly or internalization mediated by metal affinity are biochemical methodologies used to load different cargoes into HF<sub>n</sub>. Moreover, HF<sub>n</sub> nanocages lend themselves also to surface modification with targeting moieties, such as antibodies, fragments of antibodies or peptides to achieve an even more specific tumor interaction. Surface modification can also facilitate drug loading and half-life of HF<sub>n</sub> thus ensuring improved drug release at tumor sites.

To date, a plethora of therapeutic drugs, e.g., paclitaxel, curcumin, daunomycin, epirubicin, etc., have been loaded into the inner cavity of HF<sub>n</sub> nanocages<sup>91,91–93</sup>. Among the HF<sub>n</sub>-based nanoformulates developed, one the most studied in the literature involves the encapsulation DOX. Indeed, it has been extensively demonstrated that DOX nano-formulation in HF<sub>n</sub> is able to improve efficacy and accumulation to the tumor and, above all, is decisive in reducing its cardiotoxicity as well as the serious side effects associated with this type of treatment. Another therapeutic strategy involves the employment of HF<sub>n</sub> as an important carrier for boosting immunity and enhancing treatment effect by blocking immune checkpoint.

In addition, HF<sub>n</sub> are promising candidates for effective brain tumor therapy, due to their intrinsic targeting capability toward TfR1 and ability to cross the BBB<sup>156</sup>.

By taking advantage of their tumor-specific delivery, HF<sub>n</sub> can be useful also for tumor imaging, including MRI and fluorescence-guided oncological surgery. In addition, photodynamic and photothermal therapy in cancer treatment are considered promising fields for HF<sub>n</sub> application. Thus, the opportunity of co-encapsulating different drugs into HF<sub>n</sub> to combine both imaging and therapeutic functionality in a fully biocompatible nanosystem raises even further interest<sup>94</sup>.

Despite their favorable and interesting features, HF<sub>n</sub> nanocarriers still have many limitations. In the first place, it is necessary to provide HF<sub>n</sub> with enhanced circulation time and reduce clearance by the reticuloendothelial system (RES). In this direction,

several modification strategies applicable to HF<sub>n</sub> to provide higher tumor accumulation and enhance its therapeutic effect are currently under investigation.

### 2.3.3 Novel strategies to improve bioavailability and *in vivo* circulation of HF<sub>n</sub>

In the past decade, hundreds of nanodrug delivery systems based on HF<sub>n</sub> have been proposed. Indeed, their versatility and interesting properties put HF<sub>n</sub> ahead of conventional materials in clinical translation for imaging and drug delivery purposes. Several studies demonstrated that HF<sub>n</sub>-based nanocarriers can not only improve the bioavailability of soluble drugs and drive a specific accumulation at the tumor, but also to mitigate the side effects of toxic drugs on healthy tissues<sup>81</sup>. However, some key challenges need to be addressed including the relatively low stability and short *in vivo* half-life of HF<sub>n</sub> for their reliable implementation as drug nanocarriers in the process of clinical translation.

In recent years, several actions have been proposed with the aim of addressing the relatively short half-life that characterizes HF<sub>n</sub> to maximize its intrinsic capability to target specific tumor sites. These strategies, which include chemical and genetical modifications, mainly involve surface functionalization methods to optimize the employment of HF<sub>n</sub> nanosystems<sup>95</sup>.

Chemical modifications of HF<sub>n</sub> nanocages include the conjugation with Polyethylene Glycol (PEG) molecules. Indeed, this strategy, named PEGylation, has been extensively employed to improve systemic circulation time and decrease immunogenicity, thus boosting the efficiency of drug and gene delivery to target tissues. Another strategy via PEG chemical conjugation allowed to obtain HF<sub>n</sub> nano-assemblies which were reported to display improved blood pharmacokinetics and circulation time. Also, a biomineralization method obtained through calcium phosphate coating of HF<sub>n</sub> nanocages has been successfully developed.

Among the genetical modifications of HF<sub>n</sub> nanocages, the PASylation strategy is one of the most compelling. This modification is based on the genetic fusion of biopharmaceuticals such as proteins, peptides, and low-molecular-weight drugs with a sequence rich in proline (P), alanine (A), and serine (S), designed for the first time by Schlapschy. This PAS domain has the property to be unfolded and mimics the activity of polyethylene glycol shell on the nanoparticle surface, making the nanoconstruct stealth for immune system cell, while gaining advantages in biocompatibility and biodegradability as well as in increasing circulation time<sup>66</sup>. This strategy has been applied to HF<sub>n</sub> by genetically fusing PAS sequences to the N-terminal portion of HF<sub>n</sub>

subunits. In the face of relatively easy production, this functionalization strategy is reported to help overcome many of the current difficulties in the use of HF<sub>n</sub>-based assemblies for *in vivo* applications<sup>95</sup>.

Another studied solution was modification of the outer surface of HF<sub>n</sub> with Albumin Binding Domain (ABD), expected to offer an increase in circulation time by exploiting the high affinity of ABD for human serum albumin, the most abundant protein found in plasma. Lastly, a different approach studied to mask the surface of nanocages with the aim of improving their stability is the XTENylation. XTEN represents a class of unstructured polymers that confers larger hydrodynamic volumes to the nanocage, resulting in slower renal clearance.

An overview of the most significant modification strategies explored to improve bioavailability and pharmacokinetics profiles of HF<sub>n</sub>-based nanosystems has been discussed in our Review **“Novel Bioengineering Strategies to Improve Bioavailability and In Vivo Circulation of H-Ferritin Nanocages by Surface Functionalization”** ACS Omega 2023, 8, 8, 7244–7251 and reported as appendix 3.

Starting from the clinical scenario herein described, the present thesis has the objective of investigating innovative strategies based on HF<sub>n</sub> nanocages both for diagnostic and therapeutic approaches in oncology.

In particular, this work is structured into three main studies focused on BC-related applications. In Study 1, we focused on the diagnostic potential of HF<sub>n</sub> as a nanotracer for image guided mammary surgery upon loading with the fluorescent dye indocyanine green (ICG). In Study 2, I expanded the study of HF<sub>n</sub>-based chemotherapeutics considering the impact of FerOX, as a DOX safer nanoformulation for BC treatment to reduce undesired off-target toxicity in BC treatment. Finally, in study 3, we explored *in vivo* the ability of HF<sub>n</sub> to mediate the delivery of the biological drug TZ across the BBB to tackle the development of BM associated with BC.

## 3. Study 1: ICG-loaded HFn nanocages for Image-guided surgery applications

### 3.1 Introduction

The clinical scenario of several types of cancers including BC has profoundly changed recently. Further to the impressive advances in screening programs that allow earlier BC diagnoses, surgeons have changed their approach from an extensive and demolitive surgery to a more conservative one <sup>96,97</sup>. These features, coupled with the fact that cancer surgery is still highly relying on surgeon visual inspection and palpation of the operating field to determine the extent of the tissues to be removed, can lead to a high risk of cancer's misidentification. Indeed, a direct and safe approach to accurately define the tumor and/or metastasis loco-regional extension is not available yet <sup>98</sup>. In this scenario, is emerging the demand of a strategy to provide a tailored and less extensive surgical approach, focused to prevent unnecessary damage to surrounding healthy tissues.

#### 3.1.1 Fluorescence guided surgery in oncology

With the purpose of achieving more accurate surgical approaches, fluorescence guided surgery (FGS) is gaining growing interest in oncology thanks to its potential to radically improve the decision-making on cancer and offer a step towards a tailored surgery <sup>99</sup>. This technique attracted rising attention since it can provide real-time fluorescence images of the operating field, potentially improving tumor visualization and identification of metastatic deposits <sup>100</sup>. Indeed, a more precise anatomic localization of cancer tissues during resection would be crucial for the success of any surgical planning and decisive in maximizing benefits for patients <sup>101</sup>. For example, in BC a lower-than-expected tumor burden might allow to avoid total mastectomy and radiotherapy boost or, on the contrary, a greater tumor mass might imply a less conservative surgical approach or the use of adjuvant strategies.

The clinical application of FGS requires preoperative or intraoperative administration of fluorescent agents to the targeted tissues and the use of a sensitive imaging device. This allows the excitation of the fluorescent agent with a laser beam,

and subsequently the visualization of the fluorescence emission intensity during surgery under a fluorescence camera <sup>102</sup>.

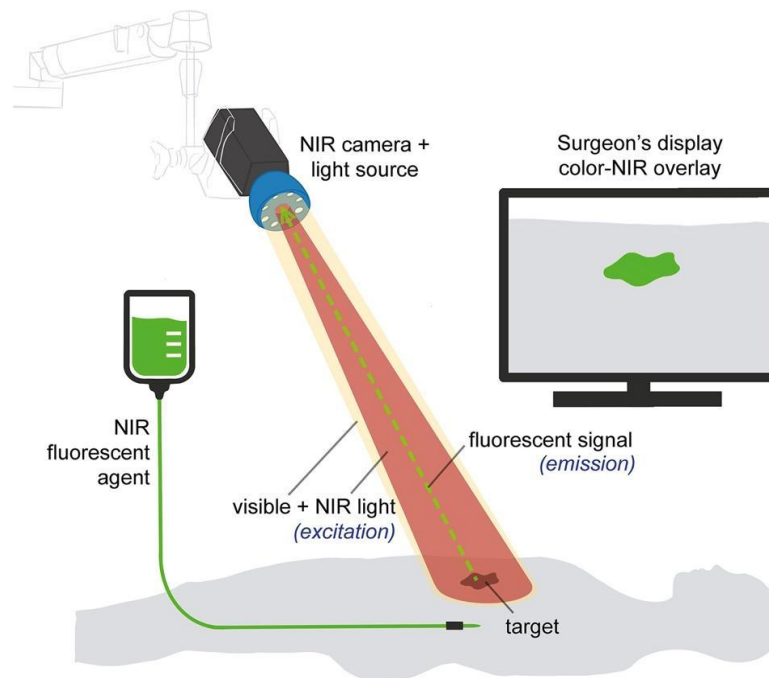


Figure 3.1 The basic principles of fluorescence-guided surgery <sup>103</sup>.

The incorporation of fluorescence-guidance could help navigate tumor margin resection, diagnosis of secondary tumors, and regional lymph node tumor positivity. However, to date, this imaging modality typically provides only qualitative data. Indeed, many factors such as camera-to-target distance, camera angles, and ambient light from the operating room can negatively affect interpretation of images and is prone to large inter-observer variability. Thus, is becoming urgent the need for quantification or at least standardization of reporting criteria, viewing protocols and an objective fluorescence threshold based on the fluorescence signal pattern <sup>104</sup>.

In addition, to address limitations of FGS use in oncology and achieve higher sensitivity and specificity, a homogenous distribution of fluorescence signal deriving from target cells should be accomplished <sup>105</sup>. Indeed, while interventions such as angiography, tissue perfusion assessments and lymphangiography can be performed using non-targeted fluorescent dyes, FGS for solid tumors often demands tumor specific probes to adequately discriminate diseased from healthy tissue.

Different approaches involving fluorescently labeled antibodies, peptides, particles, and other molecules related to cancer hallmarks have been developed for the illumination of target lesions <sup>106</sup>. Well known cancer cell targets, such as carcinoembryonic antigen (CEA), epidermal growth factor receptor (EGFR), vascular endothelial growth factor, epithelial cell adhesion molecule, and integrins could be



exploited for the development tumor-targeted specific probes. An example is the CEA-targeting agent SGM-101 (Surgimab S.A.S., France) investigated in phase III for patients undergoing colorectal cancer (CRC) surgery, after successful detection of malignant lesions in patients undergoing CRC surgery in phase II <sup>107</sup>. Therefore, improving the tumor targeting ability of fluorescent agents is an important step for FGS widespread implementation, with increasing evidence of patient safety and surgical efficiency <sup>103</sup>.

### 3.1.2 Indocyanine green

Among different probes that may assist FGS, the most commonly used is ICG. ICG is a safe, water-soluble organic near-infrared (NIR) fluorescent agent. Since its approval for clinical use obtained by the FDA in 1959, it was introduced as a medical diagnostic tool for NIR fluorescence imaging <sup>108</sup>. ICG emits at 830 nm when excited by a NIR light source at 800 to 810 nm wavelengths and its fluorescence signal can be detected by special devices equipped with cameras sensitive to the NIR-spectrum.

Following intravenous administration (i.v.), ICG interacts with plasma proteins and acts as a vascular agent allowing tissue perfusion and lymphatic drainage assessments. Moreover, thanks to its user-friendly properties and favorable penetration depth <sup>109</sup>, this fluorophore has been widely employed in clinics for angiography and in various surgical fields, including vascular-, gastrointestinal-, and reconstructive surgery. ICG guided FGS is commonly used to reduce complications in visceral surgery such as bile duct injuries in laparoscopic cholecystectomy and the assessment of real-time visceral perfusion <sup>104</sup>.

More recently, ICG has been employed as an optical contrast agent in surgical oncology <sup>110</sup> and reported as a photothermal and photosensitizer agent suitable for photothermal and photodynamic therapy in cancer treatment <sup>111</sup>. More than 150 clinical trials involving the use of ICG have been conducted using ICG for FGS in several types of cancer, including breast, gastric, colon, prostate, skin, and non-small cell lung cancers <sup>112,113</sup>. In addition, ICG has been employed for cancer-related surgical applications, including sentinel lymph node mapping, lymphography, angiography, and anatomical imaging during surgery <sup>114,115</sup>.

Unfortunately, despite its interesting features, ICG suffers from intrinsic issues such as concentration-dependent aggregation and low photostability. Moreover, once i.v. injected, it has a rapid degradation and clearance from the body <sup>34</sup>. In addition, due to

its low contrast, rapid elimination, and poor tumor retention, its optimal usage is still far from being standardized and reliable for the intraoperative detection of tumors and further theranostic applications. Thus, the development of new tumor-specific experimental fluorophores and conjugates based on ICG must be accomplished to fulfill the promises of its employment in FGS <sup>106</sup>.

### 3.1.3 New ICG-based strategies

Considering the above-mentioned major limitations of ICG-guidance, including its lack of tumor specificity, many researchers proposed the exploitation of new ICG-based strategies to boost ICG properties for oncological applications. In this direction, nanotechnology has been widely used for improving ICG's poor stability and *in vivo* half-life to enhance tumor specific accumulation by passive or active targeting features displayed by NPs <sup>116</sup> (Figure 3.2). For instance, ICG has been loaded or conjugated to different types of NPs (polymer-based NPs, lipid-based NPs, silica NPs) <sup>117,118</sup> and also protein-based NPs have been proposed and functionalized for cancer theranostic purposes <sup>119</sup>.

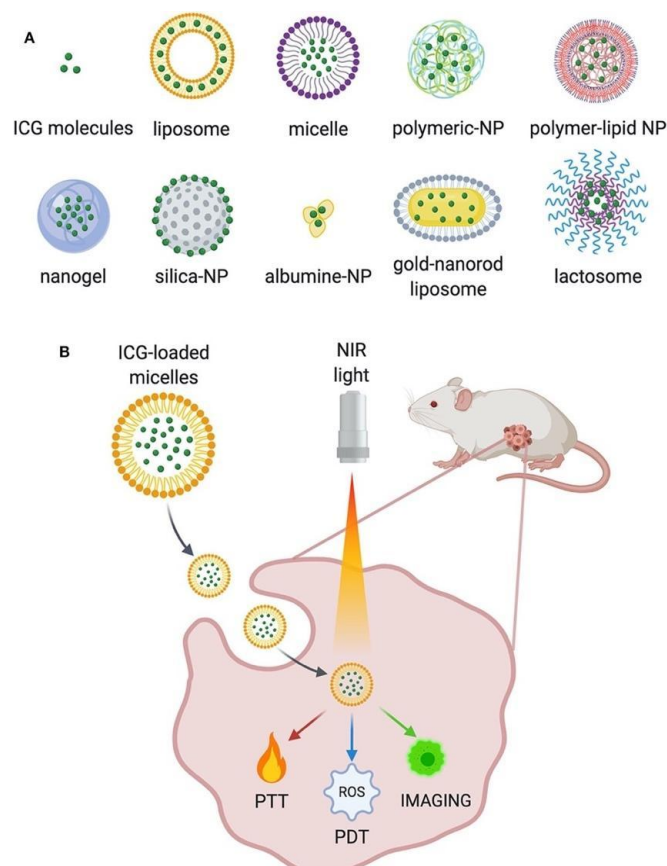


Figure 3.2 A) Some examples of the ICG-NPs obtained with different materials and conjugation techniques. B) Main applications of ICG-NPs in cancer treatment <sup>116</sup>

An assortment of ICG-NPs has been mainly proposed for bioimaging applications as agents for tumor identification. Among them, it is worth highlighting folic acid-conjugated NPs, Hyaluronic acid-conjugated NPs and antibody-conjugated NPs <sup>101</sup>. Two types of NPs, silica-based NPs, named C-Dots, and the pH-activatable ICG-encoded nanosensors, both targeted to  $\alpha v\beta 3$  integrin (which is significantly upregulated in the tumor vasculature), are currently being investigated in clinical trial <sup>120</sup>. In addition, different types of ICG-incorporating liposomes have been assessed by virtue of their fluorescence enhancement contribution for sentinel lymph node imaging.

Aside from NPs, other strategies to deliver ICG have been explored. These include the conjugation of ICG with antibodies. A frequently used antibody is the anti-EGFR mAb, also called panitumumab, thus obtaining panitumumab-ICG conjugate <sup>101</sup>. Another tracer developed for detection of the sentinel lymph node is the hybrid ICG-[<sup>99m</sup>Tc]Tc-albumin nanocolloid which combines the benefits of both technetium-based radiotracer ([<sup>99m</sup>Tc]Tc-albumin nanocolloid) and fluorescence-guidance (ICG) <sup>121</sup>.

Despite the several efforts in this field, different challenges need to be addressed such as non-selective targeting to cancer cells and the poor retention at tumor level <sup>116</sup>. A possible solution to these drawbacks is the implementation of HFn nanocages which combine the specific tumor targeting capability with the potential to improve the properties of ICG <sup>122</sup>.

### 3.2 Aim of the study one

Nanotechnological strategies represent a possible option to solve ICG's issues. In particular, HFn nanocages meet the requirements for a therapeutic application in terms of biocompatibility and tumor targeting. Starting from this, we reasoned to develop a HFn-based tracer suitable for oncological FGS aimed at improving ICG's properties and ensuring tumor specific recognition.

The first aim of this study was the assessment of the feasibility of an ICG-loaded HFn nanoformulation (HFn-ICG) as tumor specific nanotracer for FGS approaches. After developing and characterizing its features *in vitro*<sup>122</sup>, in this study we demonstrated that HFn-ICG acts as an efficient tracer for the identification of the primary tumor mass in comparison to the free dye ICG in a model of murine BC. Moreover, by investigating the accumulation of ICG using mass spectrometry on tumor and organs homogenates, our purpose was to decipher if the major role of nanoformulation could be in driving a tumor specific targeting, or rather in protecting ICG's fluorescence.

The second aim of this study was to obtain a nanotracer proficient in the unambiguous detection of cancer cells even when they are not easily identifiable, like in metastases. Indeed, to also achieve the identification of metastatic deposits, a fine tuning of the nanocage's surface properties become crucial to maintain the already excellent tumor accumulation and retention, while increasing its *in vivo* half-life. To reach this purpose, we proposed the PASylation of HFn already studied in literature<sup>123,124</sup> as an effective strategy to develop a HFn-PAS-ICG nanotracer to also recognize metastasis. Starting from these considerations, we have designed the variant HFn-PAS by genetically inserting at the N-terminus HFn sequence, a PAS sequence of 40 amino acids followed by a cleavable linker recognized by tumor metalloproteinases (MMP)<sup>13,14</sup>. Thus, this strategy is reported to offer enhanced stability to the nanocage thanks to the presence of the PAS shield, but once the nanocage reaches the TME, PAS sequences are selectively removed by MMPs. There, the unmasked HFn can freely interact with TfR1 overexpressed in cancer cells, triggering tumor specific accumulation. After obtaining HFn-PAS nanocages *via* recombinant production in *E. coli* and purification by means of an optimized protocol, my aim was to extensively characterize *in vitro* HFn-PAS. Finally, we focused on investigating their tumor accumulation capability in murine models of BC and CRC, with the purpose of obtaining an *in vivo* ICG-based nanotracer able to universally identify tumor extension for tailored surgical resections.

### 3.3 Materials and methods

#### Production of HFn and HFn-PAS

HFn and HFn-PAS nanocages were produced and purified as recombinant proteins in the *E. coli* strain BL21(DE3) following an established protocol<sup>92</sup>.

The cDNA encoding for HFn was synthesized and subcloned into the vector pET11a by Genescript, obtaining the resulting plasmid pET11a\_HFn.

The variant HFn-PAS has been obtained inserting in the N-terminal portion of HFn monomer (1) a PAS sequence, i.e. a sequence rich in Proline, Alanine and Serine (ASPAAPAPASPAAPAPSAPAASPAAPAPASPAAPAPSAPA) of 40 aminoacids that confers to the nanocage enhanced stability and circulation time *in vivo* and (2) one selective sequences responsive to proteolytic cleavage by different MMPs (Figure 3.3)<sup>123</sup>. Subsequently, the cDNA encoding for HFn-PAS was synthesized and subcloned into the vector pET11a by Genescript, obtaining the resulting plasmid pET11a PAS\_MMPS\_HFn.

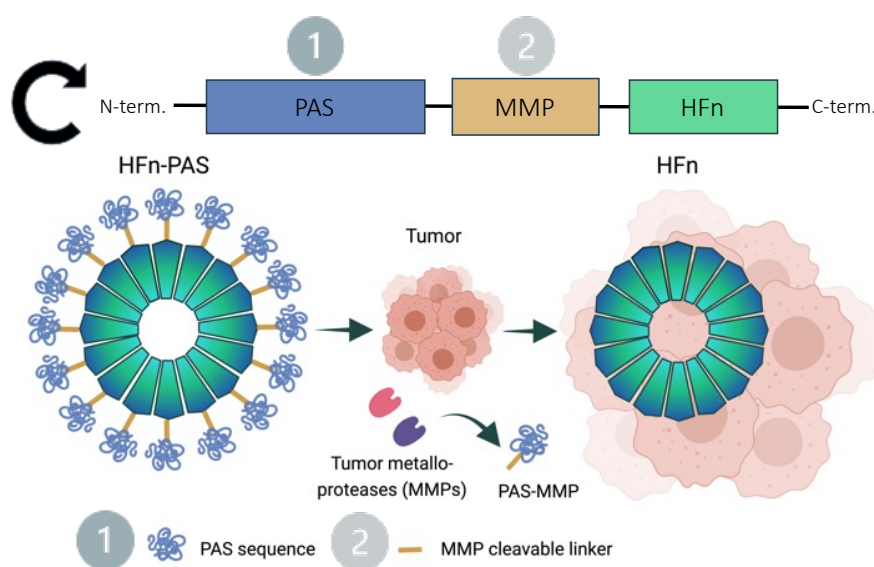


Figure 3.3 Scheme of the novel nanocage HFn-PAS before and after selective proteolytic cleavage by tumor metalloproteinases present in the tumor microenvironment

The obtained plasmids were employed to transform the *E. coli* strain BL21(DE3) by heat-shock method. The transformed strains were then used to produce HFn and HFn-PAS, respectively. Briefly, the transformed strains were grown at 37 °C in Luria–Bertani (LB) medium with Ampicillin (100 µg/mL) until OD (Optical density) 600nm = 0.6. To determine the most suitable induction parameters, different concentrations of isopropyl β-D-1-thiogalactopyranoside (IPTG) and different incubation times have been assessed. For the expression of HFn, IPTG has been added to obtain a final concentration of 0.5 mM for 2.5 h in incubator at 37°C in constant

agitation (100 rpm), while the expression of HF<sub>n</sub>-PAS required the induction with IPTG at 0.5 mM for 3.5 h at 37°C in constant agitation (100 rpm).

At the end of induction time, the cells were collected and centrifuged at 4000 g, for 15 minutes at 4°C. Then, cells were washed and resuspended in lysis buffer (3 mL/g of cells; 20 mM TRIS-HCl pH 8.00, 1 mM PMSF (phenyl-methyl-sulfonyl-fluoride), protease inhibitors complete EDTA free (50 X, 1 tablet in 50 mL), 1 mg/mL lysozyme, 20 mM MgCl<sub>2</sub>). Then, the DNase (40 U/g of cells) was added to the solution and incubated at 4°C in ice for 30 minutes. To prepare the crude extract, cells were sonicated for 6 cycles of 10 seconds applying an ultrasonic output of 50W (Bandelin ultrasonic homogenizer) in an ice bath and centrifuged at 10.000 g for 30 minutes at 4°C. The obtained supernatant was heated for 15 minutes at 70 °C allowing a partial purification by taking advantage of HF<sub>n</sub> stability and then centrifuged at 10.000 g for 30 minutes at 4°C.

### **Purification of HF<sub>n</sub> and HF<sub>n</sub>-PAS**

The purification protocols used for HF<sub>n</sub> and HF<sub>n</sub>-PAS were different. Indeed, for HF<sub>n</sub> the supernatant obtained from the production step (heat treated) was loaded onto a diethylaminoethanol (DEAE) Sepharose anion exchange resin, pre-equilibrated with 2-(N-Morpholino) ethanesulfonic acid potassium salt (K-MES) 20 mM, pH 6.0. The elution for HF<sub>n</sub> purification was carried out with an increasing stepwise gradient of NaCl.

For what concerns the purification of HF<sub>n</sub>-PAS, several modifications have been included, considering its different physico-chemical features in comparison to HF<sub>n</sub>. In the optimized procedure the supernatant was subsequently ultracentrifuged at 35.000 rpm, for 1 h at 6 °C to remove protein aggregates and then precipitated using ammonium sulfate at 65% saturation (w/v) stirring at room temperature (RT) for 2 h. The pellet was resuspended and dialyzed overnight against 20 mM TRIS HCl pH 8.00 to allow solubilization (Figure 3.4 A). Then two different purification methods to obtain the final protein were assessed.

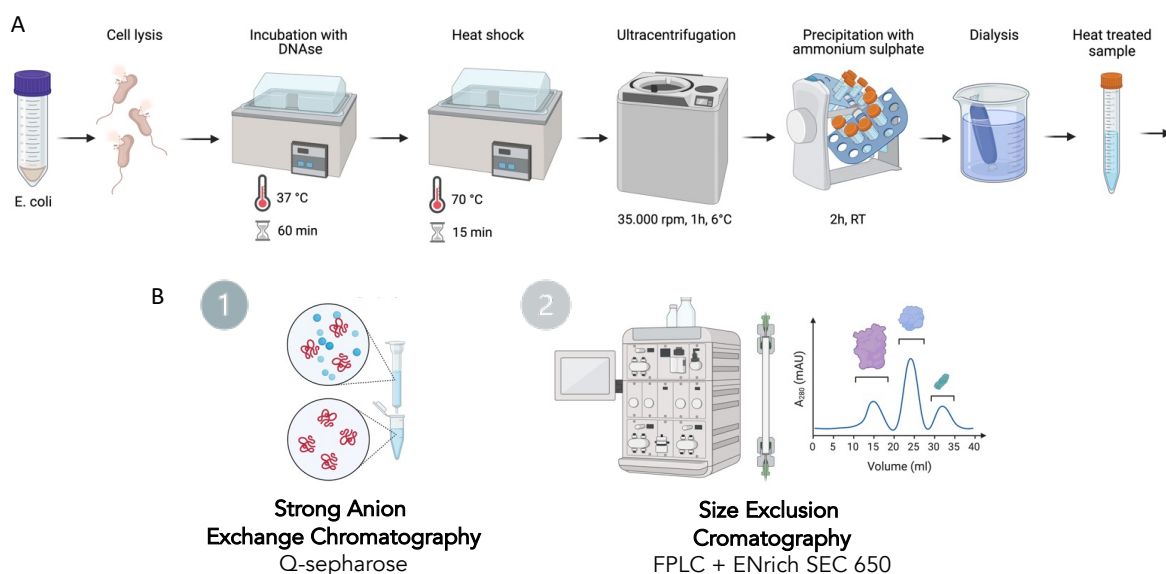


Figure 3.4 A) Scheme of HFN-PAS purification protocol to obtain the heat-treated sample; B) Scheme of the two chromatographic methods assessed to collect the final purified protein

The first purification method involved a strong ion exchange chromatography (IEC) in which the resin HiTrap Q Sepharose High Performance (GE Healthcare) and TRIS-HCl 20 mM pH 8.00 buffer were used (Figure 3.4 B). The resin with 2 mL bed volume was packed in a 1.0 × 10 cm column, using therefore 1 mL of resin for each gram of bacterial pellet. Then, the resin was washed with 10 volumes of mQ water and equilibrated with 20 volumes of 20 mM TRIS HCl pH 8.00.

The supernatant dialyzed in the previous step (heat-treated) was loaded into the column and the flow-through was collected. No washing step was applied since the sample has a very weak interaction with the resin and elutes rapidly through the column. The elution was performed with an increasing stepwise gradient of NaCl. A solution of 20 mM TRIS-HCl pH 8.00 was used to collect Fraction 1 (2 CV). Solutions of 20 mM TRIS-HCl pH 8.00 supplemented with 0.1 M NaCl, 0.2 M NaCl, 0.3 M NaCl, 0.4 M NaCl and 0.5 M NaCl were used to collect respectively Fractions 2, 3, 4, 5 and 6 (2 CV each).

The second chromatographic method applied to the final purification of HFN-PAS, involved the use of size exclusion chromatography (SEC) allowing the separation of proteins according to their size and molecular weight (Figure 3.4 B). The fast protein liquid chromatography system (FPLC NGC 10 Bio- Rad) was coupled with the ENrich 10/300 GL gel-filtration column (Bio-rad) equilibrated with PBS. A volume of 800 µL of heat-treated sample were injected in the loading loop (1 mL) operating the system at the flow rate of 0.5 mL/minute with a maximum pressure of 600 psi. Fractions of

0.5 mL were collected by monitoring the chromatogram from the integrated ChromLab Software (Biorad).

The fractions were analyzed by Sodium Dodecyl Sulphate-PolyAcrylamide Gel Electrophoresis (SDS-PAGE) using 12% (v/v) polyacrylamide gels. Protein concentration was determined by both using the Comassie Plus Protein Assay Reagent (Thermo Fisher Scientific) and measuring absorbance at 280 nm with NanoDrop™ 2000 Spectrophotometer (Thermo Fisher Scientific).

### **Purification of HF<sub>n</sub> and HF<sub>n</sub>-PAS from endotoxin contamination**

An endotoxin (ETX) removal protocol based on the use of 1% Triton X-114 was conceived and performed on HF<sub>n</sub> to obtain injectable formulation for *in vivo* studies<sup>125</sup>. Purified fractions were incubated with 1% Triton X-114 at 4 °C on a tube rotator (20 rpm) for 30 min and then incubated for 10 minutes at 37 °C. Then, the tubes were centrifuged at 17000 g for 15 minutes at 25 °C. The supernatant was collected, and the treatment repeated three times for HF<sub>n</sub> and four times for HF<sub>n</sub>-PAS. Finally, Triton X-114 was removed by gel filtration. To test the ETX content after the purification protocol, the Limulus Amebocyte Lysate (LAL) kinetic turbidimetric assay provided by Charles River Microbial Solutions was performed.

### **In vitro characterization of HF<sub>n</sub> and HF<sub>n</sub>-PAS nanocages: morphology and size**

TEM was used to evaluate the morphology of HF<sub>n</sub> and HF<sub>n</sub>-PAS and to examine their structural integrity. A 20 µL drop of suspension was spotted on the Formvar grid and left drying at RT stained with uranyl-acetate 1% for 30 seconds at RT and dried overnight at RT.

Dynamic Light Scatterin (DLS) measurements of the nanocages produced were also performed using a Zetasizer Nano Instrument (Malvern Panalytical) with a scattering angle of 173°, at 25 °C. A disposable cuvette (optical path length: 1 cm) was used for the measurements of size, while folded capillary zeta cells were used for Z-pot.

Circular Dicroism (CD) analysis was carried out to investigate the characteristics of the secondary- structure contents of HF<sub>n</sub> and HF<sub>n</sub>-PAS. All the CD analysis were conducted in PBS after subtracting the buffer background signal in a 0.1 cm quartz cuvette, using a J-815 CD spectrometer (Jasco). DLS and CD analysis were performed in collaboration with the group of Prof. Francesca Baldelli Bombelli (PoliMi).



**In vitro characterization of HF<sub>n</sub>-PAS nanocages: cleavage of PAS sequences**

To verify the removal of PAS sequences from HF<sub>n</sub>-PAS nanocages in the presence of MMP2/9 proteinases, an enzymatic cleavage assay was performed using three types of collagenase from *Clostridium histolyticum*: collagenase I, collagenase III and collagenase A. HF<sub>n</sub>-PAS solution was mixed with each of the collagenases separately with a ratio 4:1 (HF<sub>n</sub>-PAS:collagenase) and incubated at 37 °C overtime. Samples have been collected at 5 minutes, 15 minutes, 1 h, 2 h and 6 h and analyzed by SDS-PAGE using 12% (v/v) polyacrylamide gel and proteins were detected with Coomassie blue staining.

**In vitro characterization of HF<sub>n</sub>-PAS nanocages: stability after storage**

The stability after storage at -20°C was evaluated until 6 months by thawing the samples after 1, 2, 4 and 6 months and analyzing them by SDS-PAGE.

**In vitro binding assay**

The ability of these HF<sub>n</sub>-PAS to bind 4T1 murine BC cells was assessed by flow cytometry (FC). To assess PAS removal contribution to the binding to BC cells, we performed an in tube-Cell Binding Assay at 4 °C. 4T1 Cells ( $5 \times 10^5$ ) were collected and incubated for 2h at 4 °C in blocking buffer (PBS, 0.3% BSA) supplemented with 20 and 100 µg/mL of FITC-labeled HF<sub>n</sub>-PAS before and after MMPs induced cleavage. After incubation, cells were washed three times with PBS, suspended in 0.5 mL of PBS, and analyzed using a CytoFLEX flow cytometer (Beckman Coulter). 20.000 events were acquired for each analysis, after gating on viable cells and on singlets. A sample of untreated cells was used to set the appropriate gates.

**Development of HF<sub>n</sub>-ICG and HF<sub>n</sub>-PAS-ICG**

ICG has been nanoformulated exploiting the ability of HF<sub>n</sub> to disassemble and reassemble its quaternary structure in response to changes in pH as reported in our previous publication<sup>26</sup>. To accomplish the loading of ICG in HF<sub>n</sub>-PAS nanocages was used the pH gradient. A mixture of HF<sub>n</sub>-PAS (0.5 mg/mL) dissolved in 0.15 M NaCl was brought to pH 2.0 adding HCl 0.5 M, for 15 minutes at RT and 100 rpm shaking, to disassemble the protein cage. Then, the pH was brought back to neutrality (pH 7.5) with the addition of NaOH 0.1 M. In the meantime, ICG powder Verdye (25 mg; Diagnostic Green GmbH) was solubilized in bidistilled deionized water (5 mL; 5 mg/mL) and added to the HF<sub>n</sub> solution at a final dye concentration of 1 mg/mL. The mixture was incubated for 2 h at RT and 180 rpm shaking to allow complete refolding

of the HF<sub>n</sub> quaternary structure. The resulting HF<sub>n</sub>-ICG nanoparticles were then concentrated by means of Amicon Ultra-4 centrifugal filter devices and the non-encapsulated ICG has been removed by gel filtration using a Zeba Spin Desalting column. To quantify the amount of ICG loaded inside HF<sub>n</sub>-PAS an already established procedure was followed <sup>122</sup>.

### ***In vivo* evaluation of HF<sub>n</sub>-ICG biodistribution and tumor targeting**

The animals were managed according to procedures approved by the Italian Ministry of Health (Protocol Number 611/2019-PR, 6 August 2019). All procedures involving animals and their health were conducted in accordance with the 3R principles to minimize the number of mice used and their collateral suffering. The animals were housed in specific pathogen-free conditions and were kept in cages with free access to water and food. Six animals for each experimental time point were recruited. Seven-week-old female BALB/c mice were injected into the mammary fat pad with  $1 \times 10^5$  4T1-Luc cells. Two weeks later, mice were intravenously injected in the tail vein with ICG or HF<sub>n</sub>-ICG at a concentration of 3.8 mg/Kg. Then, mice were sacrificed by cervical dislocation at 6 or 24 h to follow the biodistribution of the two administered formulations. Immediately after the sacrifice, we performed an accurate autopsy by means of the KARL STORZ NIR/ICG endoscopic system (Figure 3.5).

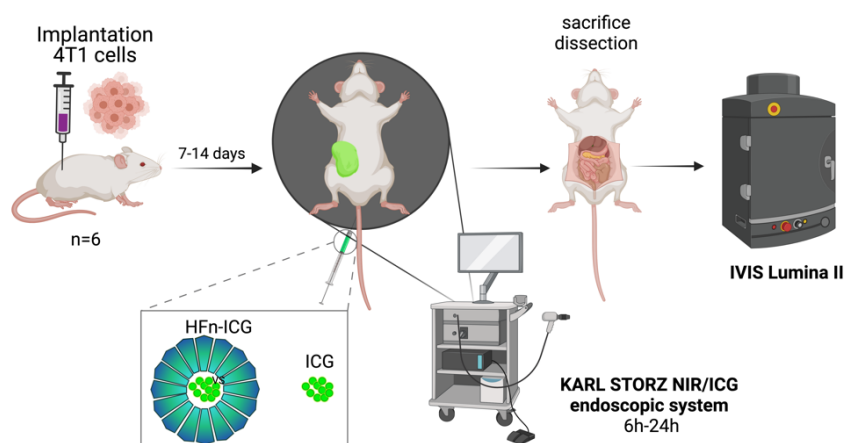


Figure 3.5 Scheme of the experimental design. 4T1-tumor bearing mice were intravenously injected with ICG and HF<sub>n</sub>-ICG at 3.8 mg/Kg. The accumulation at the tumor mass was observed by means of the KARL STORZ NIR/ICG endoscopic system and optical imaging detecting fluorescence with IVIS Lumina II.

This allowed us to detect the fluorescent signal observable in blue in correspondence to ICG or HF<sub>n</sub>-ICG fluorescence accumulation. The tumor and the major organs, i.e., the liver, stomach, gut, kidneys, spleen, heart, lung, brain, and lymph nodes were collected and imaged with an IVIS Lumina II imaging system. *Ex vivo* scans of organs were performed with the following acquisition parameters: Excitation filter: 745 nm,

emission filter: ICG, exposure time: 2 s, binning factor: Medium, f/Stop: 2, Field of View: D<sup>26,30</sup>. The image processing to subtract the tissue autofluorescence background from the ICG signal, and the analysis and quantification of fluorescence signal has been performed with the Living Image Software 4.3.1 (Perkin Elmer) conjugated with the Image Math tool. Acquiring an imaging scan with a background filter (i.e., green fluorescent protein filter), it was possible to separate the ICG signal from the tissue autofluorescence and perform the correct quantification. Finally, all the tumors and the analyzed organs were frozen at  $-80\text{ }^{\circ}\text{C}$  for the preparation of homogenates intended for mass spectrometry analysis.

### **Preparation of organs homogenates**

Organs collected from *in vivo* biodistribution study were homogenized (Glas-Col Tissue Homogenizing System Motor, GLAS-COL) in mQ water (10% w/v), kept in ice-bath during the homogenization process and then stored at  $-80\text{ }^{\circ}\text{C}$  for the mass spectrometry analysis.

### **Mass spectrometry analysis**

The analytical method was developed, and the mass spectrometry analysis performed by the Environmental Research Center at ICS Maugeri (Pavia) in collaboration with Dr. Cristina Sottani. To quantify ICG's content in homogenates of different organs (tumor, liver, kidneys, spleen, lungs, stomach and intestine) a new analytical ultra-high performance liquid chromatography-tandem mass spectrometry (UHPLC-MS/MS) method previously described (Appendix 6). This method, coupled with the quantification of fluorescent signal obtained by *ex vivo* optical imaging, was used as an approach of particular interest for studying the tissue distribution of ICG (Figure 3.6).

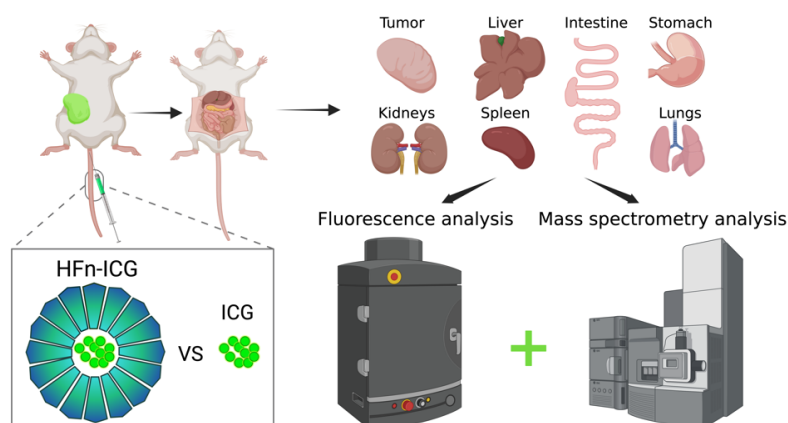


Figure 3.6 Scheme of the experimental design. 4T1-tumor bearing mice were intravenously injected with ICG or HFn-ICG at 3.8 mg/Kg. Tumors and main organs were harvested and observed by optical imaging detecting fluorescence with IVIS Lumina. Then, organs were homogenized and subjected to UHPLC-MS/MS analysis for a comparative and matched analysis with fluorescence determinations.

### Evaluation of HFn-PAS-ICG tumor accumulation in a breast cancer murine model

Animals were managed according to procedures approved by the Italian Ministry of Health (Protocol Number 611/2019-PR) in accordance with the 3R principle. BALB/c mice were injected into the mammary fat pad with  $1 \times 10^5$  4T1-Luc cells. Two weeks later, mice were intravenously injected in the tail vein with ICG, HFn-ICG or HFn-PAS-ICG at the concentration of 3.8 mg/Kg to evaluate the improved performances of HFn-PAS-ICG. The accumulation of the fluorescent signal was monitored *in vivo* every 24 h until one week by means of the IVIS Lumina II imaging system (Perkin Elmer). Then after one week, mice were sacrificed, and tumors collected and imaged with an IVIS Lumina II imaging system (Figure 3.7).

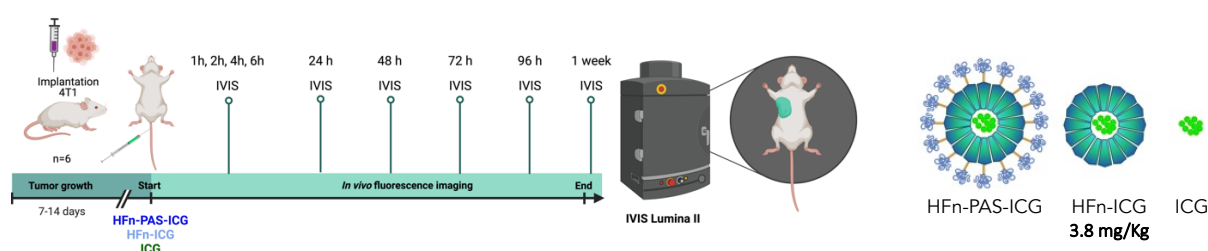


Figure 3.7 Scheme of the experimental design. 4T1-tumor bearing mice were intravenously injected with ICG, HFn-ICG or HFn-PAS-ICG at 3.8 mg/Kg and the accumulation at the tumor mass was observed by optical imaging detecting fluorescence with IVIS Lumina system every 24 h until 1 week.

### Evaluation of HFn-PAS-ICG tumor accumulation in a CRC murine model

An experiment to assess HFn-PAS-ICG performances in a murine model of colorectal cancer was performed at the Institute of Experimental and Molecular Imaging (ExMI) in Aachen, Germany, in collaboration with the group of Prof. Fabian Kiessling. The animals were managed according to procedures approved by the German Law

(Protocol number TV30208G). BALB/cAnNRj mice for each experimental time point were recruited and  $1 \times 10^6$  CT26 cells were injected subcutaneously into the right flank. After one week, HFn-PAS-ICG was injected in each group at the following concentrations: 1.0 mg/Kg, 3.8 mg/Kg and 6 mg/Kg. Mice were subjected to different imaging techniques that include fluorescence molecular tomography (FMT) and microcomputed tomography ( $\mu$ CT) imaging (MiLabs) at 2 h, 4 h, 6 h, 24 h, 48 h, 72 h and 96 h. After 96 h from the injection mice were sacrificed and organs excised for *ex vivo* evaluation using a fluorescence molecular tomography device (Perkin Elmer) (Figure 3.8).

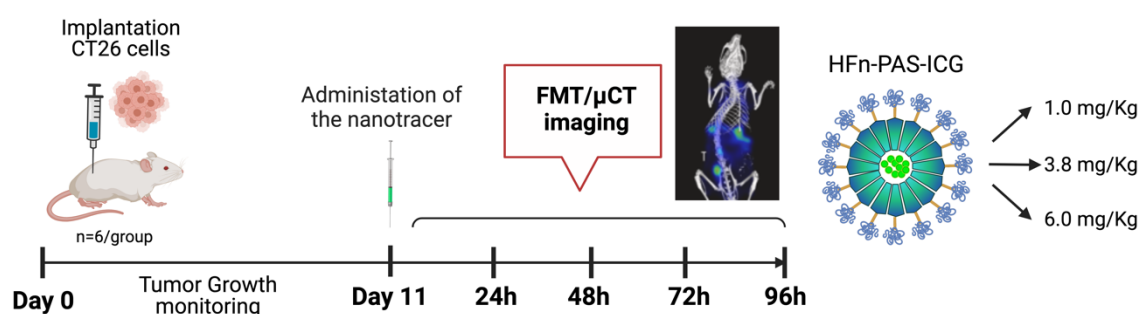


Figure 3.8 Scheme of the experimental design. CT26-tumor bearing mice were intravenously injected with HFn-PAS-ICG at the concentrations of 1.0 mg/Kg, 3.8 mg/Kg and 6 mg/Kg. The accumulation at the tumor mass was observed by FMT.

### Statistical analysis

Statistical analyses were conducted using either two-way Anova and Student's t-test using the GraphPad Prism version 8.00 for Windows (Graph-Pad Software, USA). All tests assumed normal distribution and the statistical significance threshold was set at  $p < 0.05$  and all data were expressed as the mean  $\pm$  SD.

### 3.4 Results

#### 3.4.1 Production and purification of HF<sub>n</sub> and HF<sub>n</sub>-PAS

The first phase of the study involved the recombinant production of the nanocages in *E. coli*. HF<sub>n</sub> has been efficiently produced with a yield of 26.00 mg  $\pm$  5 mg of pure protein per 1 L of bacteria culture. The 6 collected fractions obtained from the purification step and subsequently dialyzed, were analyzed by SDS-PAGE. They display a protein band that migrates in correspondence to the 20 kDa molecular weight marker, which is the expected size of HF<sub>n</sub>. The SDS-PAGE reported a good amount of protein in all fractions except for fraction 6. In addition, an excellent degree of purity was observed in all the fractions, given that no nonspecific bands appeared (Figure 3.9).

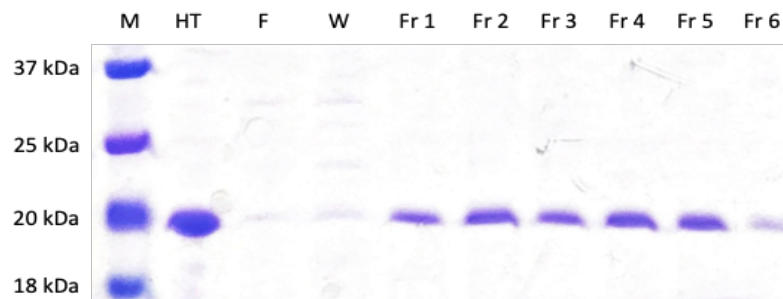


Figure 3.9 SDS-PAGE of HF<sub>n</sub> fractions. 12  $\mu$ g of heat-treated sample (HT), flow-through fraction (F) and wash (W) were loaded on 12% SDS-PAGE, while 4  $\mu$ g of protein fractions obtained by ion-exchange chromatography followed by dialysis were loaded in samples marked as fraction 1 (Fr 1), fraction 2 (Fr 2), fraction 3 (Fr 3), fraction 4 (Fr 4), fraction 5 (Fr 5), fraction 6 (Fr 6). M= molecular weight marker. SDS-PAGE were stained with Coomassie Blue.

HF<sub>n</sub>-PAS was purified as soluble fractions after IEC with a yield equivalent of 24.55 mg  $\pm$  10.2 mg of proteins per 1 L of bacteria culture. A good amount of HF<sub>n</sub>-PAS was detected in the flow-through fraction and in fractions 1, 2, 3 and 4, whereas a limited amount was detected in the remaining fractions. The obtained fractions were analyzed by SDS-PAGE and displayed a band profile at the expected molecular weight of 27 kDa (Figure 3.10). This first purification method allowed us to obtain a good amount of protein, even if lower compared to that of HF<sub>n</sub>. However, the purity of the collected samples was unsatisfactory since multiple nonspecific bands were visible (Figure 3.10 A). For this reason, we have developed an optimized purification strategy.

The second chromatographic method applied to the purification of HF<sub>n</sub>-PAS was a SEC of the heat-treated sample. Notably, the SEC absorbance profile of HF<sub>n</sub>-PAS collected in fractions F10 and F11, corresponding to the tenth and eleventh mL of the elution was found to be highly pure and concentrated obtaining a yield of 12.5 mg  $\pm$

10.2 mg of proteins per 1 L of bacteria culture (Figure 3.10 B-C). On the contrary, the following fractions (F12) were found to be associated with nonspecific protein content at molecular weights different from HF<sub>n</sub>-PAS and therefore discarded (Figure 3.10 B). Thus, the SEC method run with FPLC was chosen as the ideal method for carrying out the optimized production of HF<sub>n</sub>-PAS.

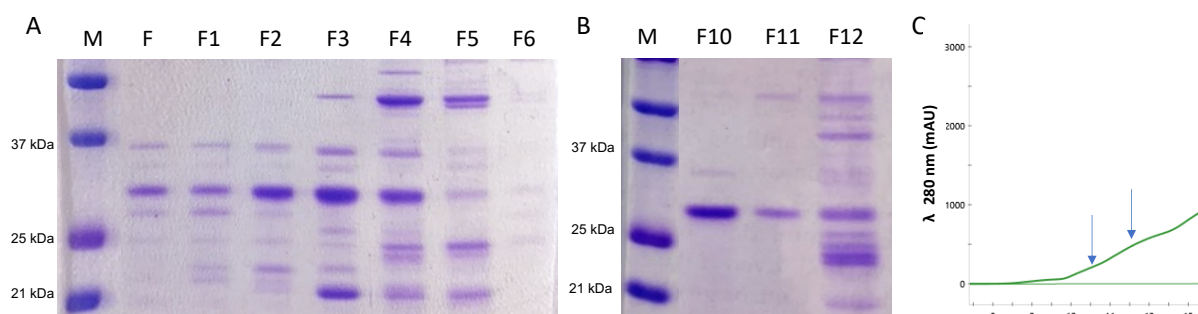


Figure 3.10 A) HF<sub>n</sub>-PAS characterization after IEC. HF<sub>n</sub>-PAS flow-through (F), fraction 1 (F1), fraction 2 (F2), fraction 3 (F3) fraction 4 (F4), fraction 5 (F5) and fraction 6 (F6). B) HF<sub>n</sub>-PAS characterization after SEC. Fraction 10 (F10), fraction 11 (F11), fraction 12 (F12). Samples were loaded (20 µg of protein) in a 12% (v/v) polyacrylamide SDS-PAGE stained with comassie blue. M: protein marker C) Chromatogram of the SEC run analysed in B) reporting the absorbance protein profile at 280 nm for each mL (F10= 10mL, F11=11 mL, F12 =12 mL) of eluted sample. Blue arrows indicate fractions in which pure HF<sub>n</sub>-PAS was found.

### 3.4.2 Purification of HF<sub>n</sub> and HF<sub>n</sub>-PAS from endotoxin contamination

To confirm whether the purity level achieved was compatible with an *in vivo* study, a LAL assay was performed after the application of the ETX removal protocol, already established in my laboratory<sup>125</sup>. The LAL assay is an FDA-approved method for the detection of ETX is the most common assay used. It is based on the ability of a particular molecule found in the amoebocytes of the *Limulus* species to react with ETX. Considering that ETX concentration is generally extremely low if compared to the concentration of the target protein, the overall amount of ETX is normally expressed in EU (ETX unit), where 1 EU approximately corresponds to 0.1/0.2 ng.

For what concerns HF<sub>n</sub>, the LAL test performed on fractions before and after the execution of the ETX removal protocol, revealed a 30000-fold reduction of ETX, as reported in Figure 3.11, ETX content in two representative purified samples (#A, #B) were 0.02 and 0.08 EU/mg. The protein concentration in the two samples was 7.4 and 6.8 mg/mL, corresponding to 0.14 and 0.61 EU/mL, respectively (Figure 3.11). These values are well below the accepted limit of 1 EU/mL, making this formulation appropriate for *in vivo* preclinical applications.



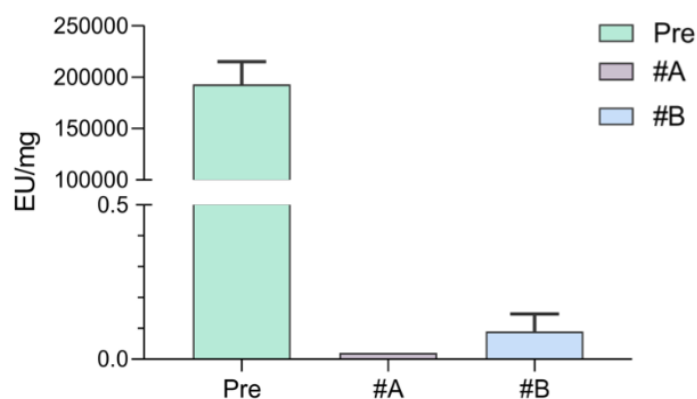


Figure 3.11 ETX levels (EU/mg) obtained by LAL test of HFn samples before the purification with 1% Triton X-114 (Pre) and after ETX protocol of sample A (#A) and B (#b). Results are reported as the average  $\pm$ SD of three experiments.

The ETX removal procedure was successfully performed also for HFn-PAS. Indeed, after performing a LAL test on fractions subjected to the ETX protocol repeated for 4 cycles, we achieved an ETX content in terms of EU/mL of 0.8 EU/mL, which is adequate for *in vivo* parenteral injection.

### 3.4.3 *In vitro* characterization of HFn and HFn-PAS nanocages

After confirming the removal of ETX contamination for both nanocages, a robust characterization of HFn and HFn-PAS became crucial to proceed with the next steps towards *in vivo* studies. The biophysical characterization of the HFn and HFn-PAS was performed using different biophysical techniques which comprise TEM, DLS and CD.

TEM evaluation was conducted on HFn and HFn-PAS samples to investigate their size and morphology. The structural integrity of HFn-PAS nanocages was confirmed by TEM images which clearly evidenced that HFn-PAS retains the native HFn ability to adopt a spherical cage-like structure and a well-visible internal cavity (Figure 3.12).

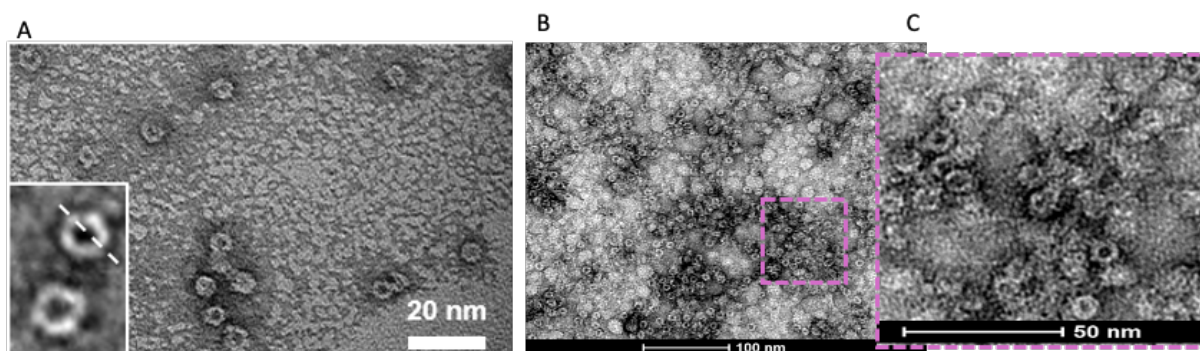


Figure 3.12 A) TEM image of HFn; B) TEM images of HFn-PAS; C) magnification of panel B.

Subsequently, the DLS analysis performed allowed us to confidently measure the size distribution profiles of nanocages. Indeed, DLS measures the hydrodynamic



diameter of nanoparticles in solution and provides information on the aggregation state of NPs in solution. The obtained measurements evidenced the slight difference in size in comparison to HFn in terms of diameter, given the PAS shell steric hindrance (Figure 3.13 A). Moreover, the homogeneity of the solution was proved by the presence of a single peak for each sample, confirming the absence of aggregated species (Figure 3.13 A).

To acquire information about the secondary structure and the conformational state of HFn and HFn-PAS we took advantage of CD. This imaging technique is a rapid and effective tool to determine whether an expressed, purified protein is folded, or if a mutation affects its conformation or stability. In this regard, the CD spectrum of HFn-PAS samples highlighted a conformational difference when compared to HFn<sup>60</sup>. Even if the analyzes to correctly estimate CD spectra with a dedicated software are still ongoing, the visual inspection of the CD spectrum suggested an increase in random coil content in HFn-PAS samples (Figure 3.13 B). Indeed, while the spectrum for HFn is characterized by a strong presence of alpha helix structure, the contribution of unstructured sequences such as PAS sequences, drives a variation in the CD spectrum towards a random coil conformation around 210-220 nm (Figure 3.13 B). This insight enriched our knowledge about the protein secondary structure of HFn-PAS and provided further certainty on its correct conformation.

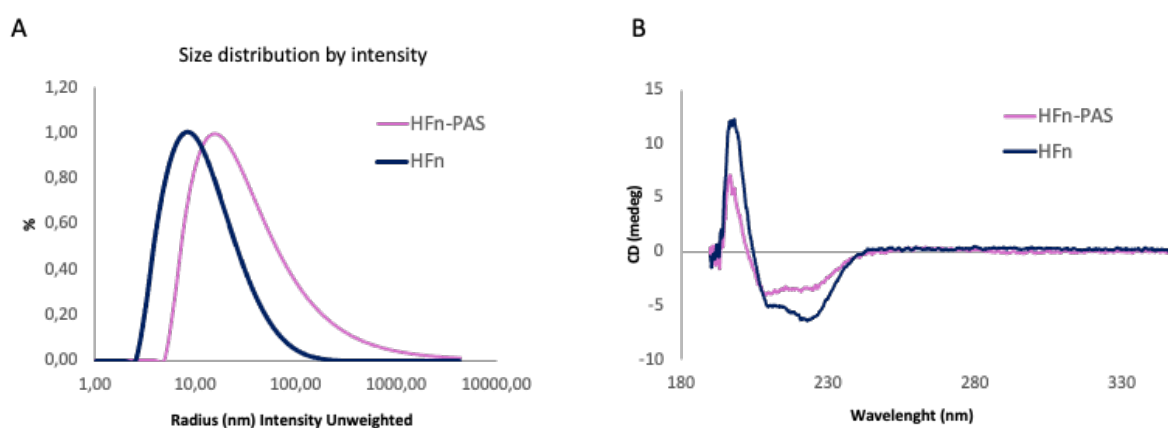


Figure 3.13 A) DLS profiles of HFn-PAS in comparison with HFn wild type; B) CD spectra of HFn-PAS in comparison with HFn

The enzyme-responsive strategy adopted for the novel nanocage HFn-PAS is based on the recognition of a cleavable linker responsive to MMP from which derives the removal of PAS sequences. To confirm the responsiveness to proteolytic cleavage we mimicked the conditions occurring at the TME in the presence of MMP. The removal of PAS sequences from HFn-PAS nanocages has been assessed by incubating

separately HFn-PAS with collagenase A, collagenase I and collagenase III (containing different percentages of MMP-2 and 9) at 37 °C (Figure 3.14). Then, samples collected at different timepoints were analyzed by SDS-PAGE. In each of the three samples we have observed the release of 20 kDa HFn core as a result of MMP-mediated cleavage. Indeed, after 1 h of digestion HFn-PAS migration in SDS-PAGE was essentially the same as HFn. The efficacy of PAS removal was therefore demonstrated for each one of the collagenases tested and underlined that the MMP cleavable sites weren't in any way masked or not accessible owing to the presence of PAS sequences.

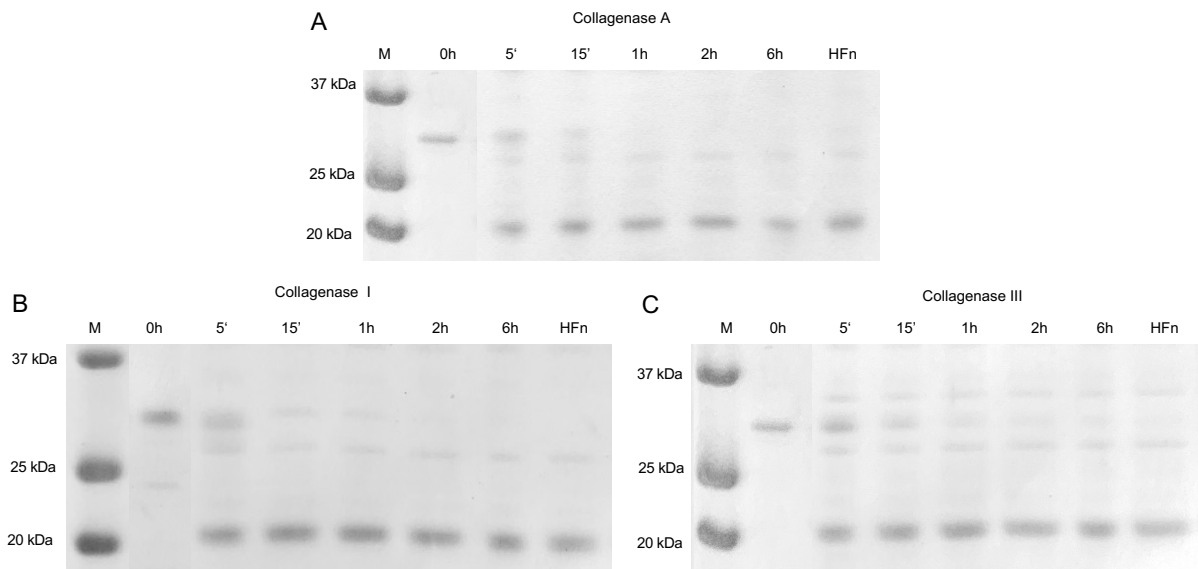


Figure 3.14 Cleavage of PAS domain from HFn-PAS with MMP2/9 proteinases. SDS-PAGE of HFn-PAS before incubation with collagenases (0h) and after *in vitro* digestion at 37°C for 5 minutes, 15 minutes, 1h, 2h and 6h with Collagenase A A), Collagenase I B) and Collagenase III C) with a ratio 4:1 (ferritin:collagenase). Lane 1: protein marker (M), Lane 6: positive control HFn.

Moreover, HFn-PAS demonstrated to remain stable up to 6 months after storage at -20°C (Figure 3.15 A). We confirmed the stability of HFn-PAS after storage up to 6 months as visible from the SDS-PAGE, where the specific band for HFn-PAS was maintained at every timepoint, without giving evidence of the loss of the PAS sequence. In addition, after thawing HFn-PAS samples stored at -20 °C for 4 months we assessed its responsivity to proteolytic cleavage. SDS-PAGE confirmed the completed cleavage of HFn-PAS after 1h in incubation con collagenase I, thus reinforcing evidence about the stability of the whole nanocage (Figure 3.15 B).

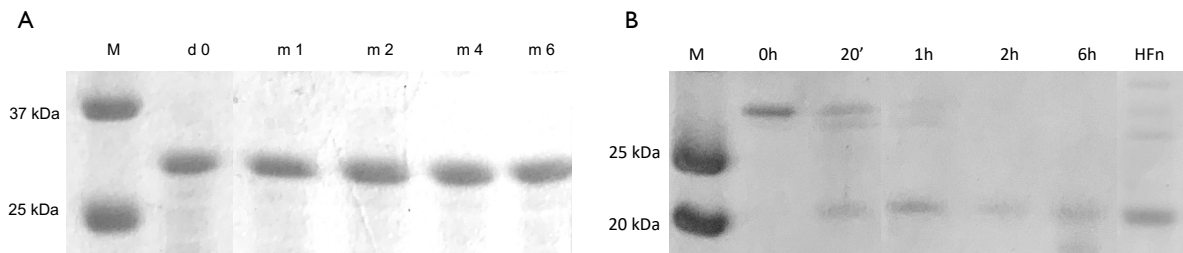


Figure 3.15 A) HFn-PAS fractions 1 tested at day 0 (d 0) after 1 (m1), 2 (m2), 4 (m4) and 6 months (m6) after being stored at  $-20^{\circ}\text{C}$ . B) HFn-PAS fraction thawed after 4 months and incubated with Collagenase I with a ratio 4:1 (ferritin:collagenase), at  $37^{\circ}\text{C}$  for 5 minutes, 15 minutes, 1 h, 2 h and 6 h. Lane 1: protein marker (M), Lane 6: positive control HFn.

### 3.4.4 *In vitro* binding assay

At this point, to proceed with the subsequent studies, it was necessary to carry out an *in vitro* study to evaluate the interaction of the nanocage HFn-PAS with cancer cells. The ability of HFn-PAS to bind 4T1 murine BC cells was assessed with a binding assay performed by flow cytometry. As shown in Figure 3.16, 4T1 cells showed lower interaction with FITC-labeled HFn-PAS (HFn-PAS-F) at both concentrations tested (respectively 1.5% and 9%). On the contrary, a 4-fold enhancement in percentage of positive cells were detected in presence of HFn after PAS cleavage. Here, percentages of positive cells close to 18% for the lower concentration, and 40% for the higher concentration were observed. Thus, we could point out a dose-dependent recognition, as demonstrated by the increase in binding percentages when incubating cells with  $100\ \mu\text{g}/\text{mL}$  of HFn-PAS or HFn after PAS cleavage. These results evidenced that the PAS shell inhibits TfR1 mediated interaction with 4T1 cells, while after PAS removal this interaction is restored allowing the specific binding.

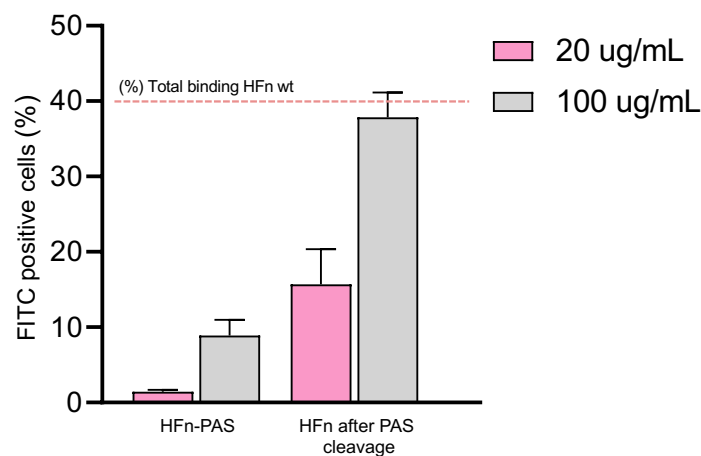


Figure 3.16. Flow cytometric analysis of HFn-PAS. 4T1 cells were incubated 2 h at  $4^{\circ}\text{C}$  in PBS buffer and 0.3% BSA with different amounts of HFn-PAS-F (20 and  $100\ \mu\text{g}/\text{mL}$ ) and HFn-PAS-F after PAS cleavage (20 and  $100\ \mu\text{g}/\text{mL}$ ). Cells were processed for FC using untreated cells to set the positive region and the singlet gate. Data are reported as average  $\pm$  S.D. of three independent experiments and expressed as percentage of cells in the positive region to HFn-F fluorescence; The dotted line represents the total binding of HFn wt.

### 3.4.5 Development of HFn-ICG and HFn-PAS-ICG

So far, the empty HFn and HFn-PAS nanocages have demonstrated sufficient adequacy to proceed with the nanoformulation phase. Thus, we performed the encapsulation of ICG within them to obtain the final nanotracer for further studies. HFn and HFn-PAS nanocages loaded with ICG were obtained with an easy and reproducible procedure (Figure 3.17) already reported for HFn<sup>122</sup>. For what concerns HFn-PAS-ICG, a good loading efficiency was achieved, obtaining an ICG encapsulated concentration of  $1.4 \pm 0.075$  mg/mL, which was 1.4 times higher than the one obtained with HFn-ICG.

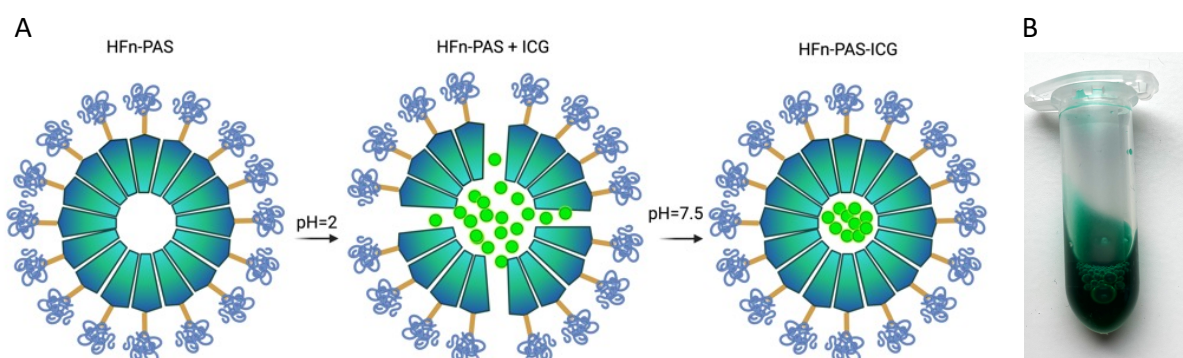


Figure 3.17 A) Schematic representation of the pH-dependent disassembly/ reassembly method used for HFn-PAS loading with ICG. ICG is represented light green and HFn-PAS is represented in dark green; B) Final product HFn-PAS-ICG.

At this point, we considered it reasonable to proceed with the *in vivo* assessment of HFn-ICG and HFn-PAS-ICG to explore their behavior as tumor-targeted nanotracers.

### 3.4.6 *In vivo* evaluation of HFn-ICG biodistribution and tumor targeting

Once obtained a HFn-ICG batch suitable for *in vivo* parenteral injection, we assessed its performances as tumor-targeted nanotracer in comparison to free ICG, using an orthotopic and syngeneic model of murine BC. 4T1-Luc tumor-bearing mice were intravenously injected with 3.8 mg/Kg ICG or HFn-ICG and sacrificed 2 h, 6 h, and 24 h after injection. After the sacrifice, mice were imaged with Karl Storz endoscope, which is one of the most used equipment for FGS. It is equipped with a full HD camera to detect the fluorescent signal associated with ICG. We performed the *ex vivo* comparison between the biodistribution of our nanotracer (i.e. HFn-ICG) and free ICG only at 6 and 24 h because 2 h after injection the signal suffers from strong diffusion, preventing us from discriminating the anatomical structures. Results obtained with Karl Storz/ICG endoscopic system demonstrate that HFn can deliver the ICG to the tumor more efficiently than the free dye<sup>26</sup>. As visible in Figure 3.18, ICG related

fluorescent signal in blue was localized in the tumor mass of mice treated with HFn-ICG at 6 h and it was still detectable after 24 h. Concerning mice injected with ICG, the fluorescence signal is poor at 6 h, while it is almost absent at 24 h (Figure 3.18 A). In order to quantify the fluorescence signal detected by Karl Storz endoscope, we have analyzed the same tumors using IVIS Lumina II system, which confirmed what was observed in Figure 3.18 B. Moreover, image quantification performed with Living image software revealed a significant difference in the levels of fluorescence between HFn-ICG and free ICG at 6 h as well as with ICG at 24 h (Figure 3.18 C).

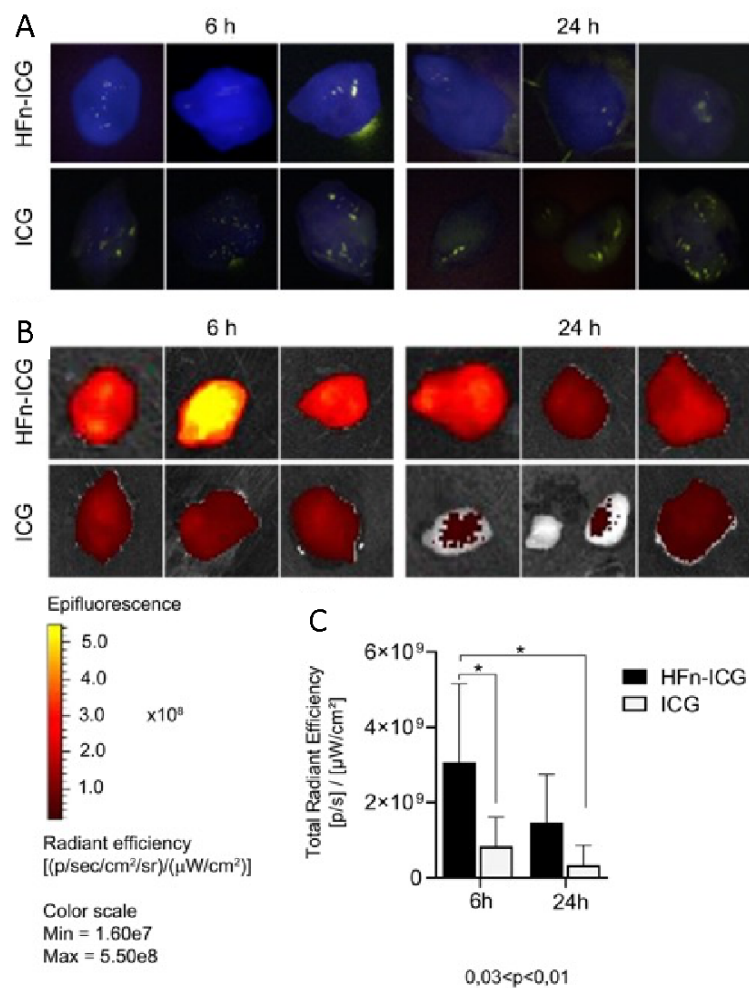


Figure 3.18 A) Tumor accumulation of HFn-ICG and ICG free. Fluorescence signal in the tumor was evaluated in the 4T1 murine model of BC 6h and 24h after intravenous administration. In this figure are reported the images obtained by Karl Storz NIR/ICG endoscopic system, where the ICG signal is represented in blue. B) Tumor accumulation of HFn-ICG and ICG free. Fluorescence signal in the tumor was evaluated in the 4T1 murine model of BC 6 and 24h after intravenous administration. In this figure are reported the images obtained by IVIS Lumina II. ICG signal is represented by a yellow hot scale expressed as total radiant efficiency ( $\times 10^8$ ),  $n = 6$ . C) Quantification of IVIS Lumina II detected in tumors. Bar chart of the comparison between the fluorescent signals quantified in tumor samples from mice treated with HFn-ICG or free ICG. Statistical significance \* $p$ -value = 0.0345; # $p$ -value=0.0112.



Then, we collected and analyzed off-target organs by IVIS Lumina II in order to study biodistribution of ICG upon nanoformulation. We have quantified the signal associated with ICG as described above. Results reported in Figure 3.19A suggested that HFn encapsulation modifies the kinetics of ICG biodistribution in the off-target organs. Indeed, in mice treated with HFn-ICG the amount of fluorescence signal was superior in all organs and at each time point in comparison to that detected in mice treated with ICG free (Figure 3.19B) Thus, HFn encapsulation seems to modify kinetics of ICG biodistribution at the off-target organs and significantly preserve ICG fluorescence by protecting it from rapid metabolism and degradation, therefore allowing it to remain in circulation longer to be able to accumulate at the tumor.

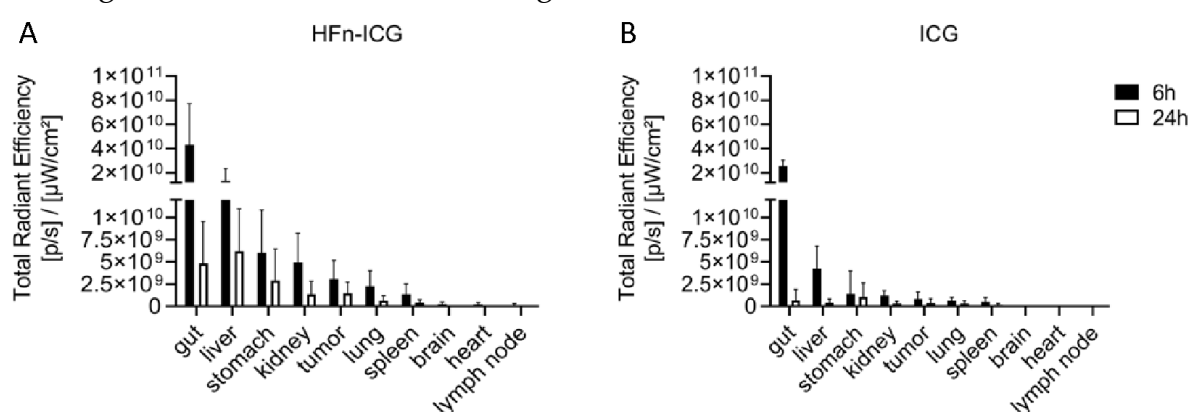


Figure 3.19 ICG biodistribution profile of off-target organs from mice treated with HFn-ICG A) and ICG B). Histogram shows the mean fluorescence value measured in each organ respectively 6 h and 24 h after injection.

The detailed comparison performed in terms of tumor accumulation, off-target biodistribution and kinetics of clearance prodromic to *in vivo* assess tracking capability of HFn-ICG was published as “**Tumor Accumulation and Off-Target Biodistribution of an Indocyanine-Green Fluorescent Nanotracer: An Ex Vivo Study on an Orthotopic Murine Model of Breast Cancer**” Int. J. Mol. Sci. 2021, 22, 1601. and reported as Appendix 4.

### 3.4.7 Mass spectrometry analysis on organs homogenates

Overall, the first *in vivo* experiment confirmed the relevance of the encapsulation in HFn in determining an improved tumor-targeted delivery of ICG which resulted in an increased visualization of the tumor mass. Therefore, it becomes necessary to uncover if the nanoformulation could have a major role in driving a specific targeting of the dye to the tumor, or rather a protective action on ICG’s fluorescence.

Organs obtained from the biodistribution study were homogenized and used to extract ICG for its quantification by UHPLC-MS/MS with the aim of investigating the relevance of the encapsulation in HFn in determining an improved ICG signal at the tumor. As shown above, the administration of HFn-ICG resulted in an increased fluorescence signal of ICG, thus it was important to uncover if the nanoformulation could have a major role in driving a specific targeting of the dye to the tumor, or rather a protective action on ICG's fluorescence.

Results obtained by UHPLC-MS/MS quantification on tumor homogenates were matched and compared with data collected from the *ex vivo* measurement of fluorescence detected by IVIS Lumina II.

After 20 minutes from i.v., we observed a higher ICG amount measured by UHPLC-MS/MS in most of the organs collected from mice injected with ICG free in comparison to those treated with the same amount of nanoformulated ICG (Figure 3.20 A-G). This quantification of the dye reflects what is observed in fluorescence analysis by optical imaging and strongly highlights the non-specific and widespread behavior of ICG. Indeed, 20 minutes after i.v. ICG spreads faster and permeates the tissues in a non-specific way. Conversely, ICG nanoformulated in HFn seems to require more time to permeate tissues as a result of a targeted internalization process. The sole exceptions involved the liver, in which we observed a higher fluorescent signal associated with the nanoformulation, and the stomach, where an increased ICG amount was detected by mass spectrometry. However, to compare more accurately the signals reported by UHPLC-MS/MS quantifications and *ex vivo* fluorescence, it was necessary to refer to a specific accumulation of the dye performing the analyses at longer timepoints. As it can be observed in Figure 3.20 H, showing the abdominal region of a mouse 20 minutes after i.v. of HFn-ICG and analyzed by KARL STORZ NIR/ICG endoscopic system, the fluorescence signal distinguishable in blue is abundantly spread in all districts.

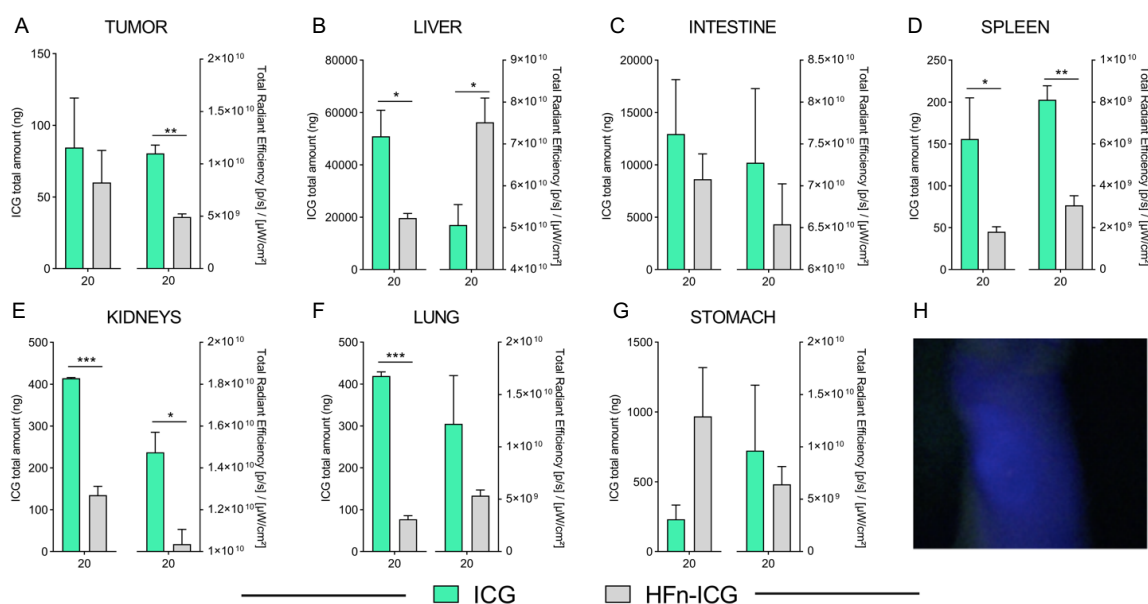


Figure 3.20 Comparison between ICG concentration measured by UHPLC-MS/MS as ICG total amount and fluorescence detected as Total Radiant Efficiency in tumor (A), liver (B), intestine (C), kidneys (D), spleen (E), lungs (F), and stomach (G) homogenates obtained from mice organs 20 minutes after injection with ICG or HFn-ICG. Student t-test \*  $0.01 < p < 0.02$ , \*\*  $0.001 < p < 0.003$ , \*\*\*  $0.00005 < p < 0.0009$ . H) Representative image of mouse injected with HFn-ICG and analyzed after 20 minutes by KARL STORZ NIR/ICG endoscopic system.

Afterwards, we focused on the accumulation of ICG at the tumor over time. As shown in Figure 3.21 A, UHPLC-MS/MS quantification on tumor homogenates of mice injected with HFn-ICG, displayed a higher ICG concentration at each tested timepoint. A similar trend can be observed in relation to the higher amount of fluorescence signal detected in the same samples, where a significant difference between the two groups was determined at 1, 2 and 6h (Figure 3.21 B), confirming the positive contribution of formulation in increased tumor accumulation. Indeed, the higher visualization of the tumor in terms of fluorescent signal is not only due to a protective and stabilizing effect on the fluorescence given by the nanoformulation, but it is mainly attributable to a specific tumor targeted delivery. The good correlation ( $r=0.6$ ) between the ICG total amount detected by UHPLC-MS/MS quantification and the corresponding fluorescence signal for HFn-ICG and ICG (Figure 3.21 C) confirmed this hypothesis. By contrast, a weaker correlation ( $r=4$ ) was determined in samples from mice injected with ICG, evidencing that also a weak ICG stabilizing contribution of HFn nanoformulation may occur. However, the superior tumor accumulation in mice treated with HFn-ICG confirmed its major role in driving ICG tumor homing rather than in the preservation of its fluorescence properties.



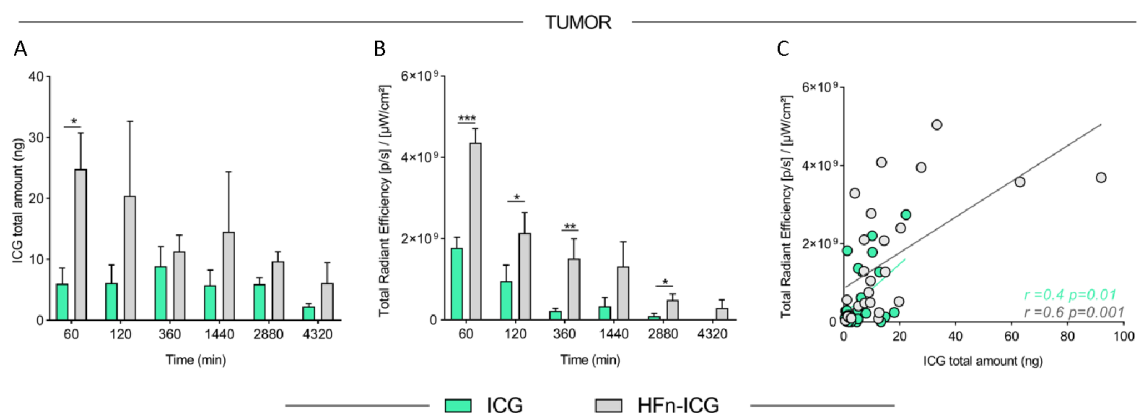


Figure 3.21 Comparison between ICG concentration measured in tumor homogenates by UHPLC-MS/MS and fluorescence detected at the tumor of mice injected with ICG or HFn-ICG during the biodistribution study. A) Bar chart showing the total amount of ICG (ng) measured in tumor homogenates; B) Total fluorescence values detected in tumors. Student t-test \*  $0.02 < p < 0.04$ , \*\*  $p = 0.004$ ; \*\*\*  $p = 0.001$ ; C) Scatter plots of the correlation coefficient between the total amount of ICG and total fluorescence detected at the tumor for ICG ( $r = 0.4$ ,  $p = 0.01$ ) and for HFn-ICG ( $r = 0.6$ ,  $p = 0.001$ ).

In addition, our results confirmed that HFn-ICG does not alter the biodistribution of ICG in the organs responsible for its metabolism (i.e., liver and intestine) or in off-target organs (i.e., spleen, kidneys, lungs, stomach) (manuscript under revision). In conclusion, this approach offers a method of particular interest for studying the tissue distribution of ICG and further validates the advantage of the nanoformulation in guiding a specific delivery of ICG at the tumor.

The results obtained so far corroborate the ability of HFn-ICG to accumulate at the tumor site and mark cancer cells more efficiently than the free dye. However, in order to exploit it as a reliable tool for FGS applications, it is necessary to improve aspects such as stability and plasma half-life. Indeed, the achievement of a proper time window that could provide improved signal at the tumor concurrently with a reduction of the aspecific signal represented by the off-target tissues, would be extremely advantageous for any FGS application.

Thus, our endeavors have been focused on the *in vivo* investigation of HFn-PAS-ICG which is expected to be provided with enhanced circulation time and therefore capability to localize at a tumor for longer.

### 3.4.8 Evaluation of HF<sub>n</sub>-PAS-ICG tumor accumulation in a breast cancer murine model

After the extensive characterization of HF<sub>n</sub>-PAS, we decided to proceed with testing the optimized HF<sub>n</sub>-PAS-ICG *in vivo* to investigate its suitability as a nanotracer for the detection of cancer cells in comparison with ICG free and the previously studied nanocage HF<sub>n</sub>-ICG (Figure 3.22).

The *in vivo* study in a BC model of fluorescence signal at the tumor revealed a significantly higher accumulation of the HF<sub>n</sub>-PAS-ICG compared to ICG and HF<sub>n</sub>-ICG and a superior retention until one week (Figure 3.22 A). Indeed, as visible both at 24 h and at the last timepoint after 1 week from injection, the fluorescence signal at the tumor mass is strongly noticeable in mice injected with HF<sub>n</sub>-PAS-ICG, while for the other groups almost no longer detectable (Figure 3.22 A). Indeed, the *ex vivo* measurement at the tumor proved a 3-fold higher signal for the nanocage constituted by HF<sub>n</sub>-PAS-ICG (Figure 3.22 B-C). In addition, by analyzing the signal to background ratio, we observed a prominent advantage of HF<sub>n</sub>-PAS-ICG after 24 h, thus improving the lesion signal identification and reducing the background noise which is a fundamental aspect to discriminate tumor cells from healthy tissues and improve bioimaging in FGS applications (Figure 3.22 D).

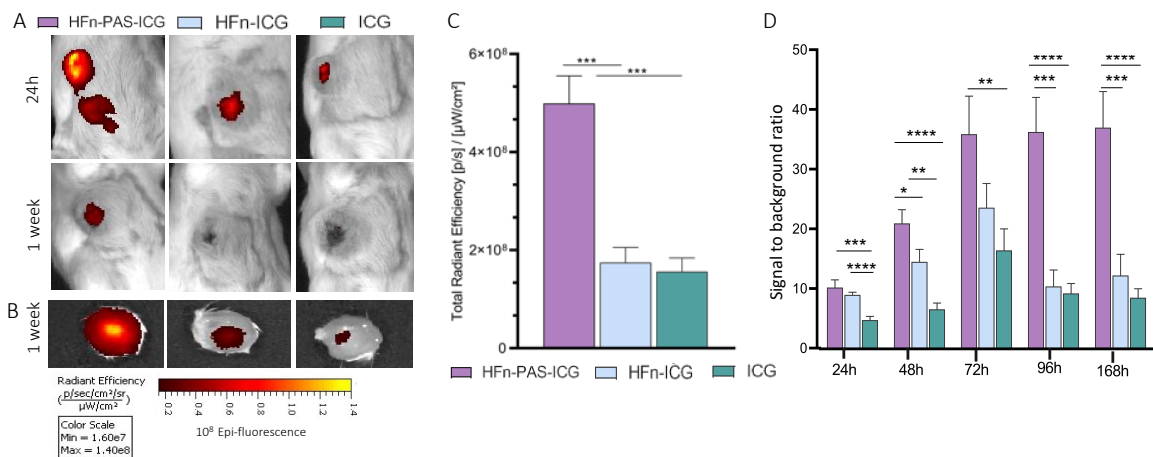


Figure 3.22 A) *In vivo* accumulation of the fluorescence signal at the tumor for HF<sub>n</sub>-PAS-ICG, HF<sub>n</sub>-ICG or ICG at 24h and 1 week. B) Fluorescence signal in excised tumors after 1 week. C) Quantification of the fluorescence signal detected in excised tumors \*\*\* $p < 0.0001$  D) Signal to background ratio from 24h to 1 week \* $p = 0.01$ ; \*\* $0.001 < p < 0.007$ ; \*\*\* $0.0005 < p < 0.0001$ . The bars are the mean value  $\pm$  SD,  $n = 6$ .

Moreover, as shown in Table 3.1, the accumulation of the dye at the tumor measured overtime *in vivo*, is progressively reduced in all groups by one order of magnitude from  $10^9$  to  $10^8$ . In fact, based on our observations, right after injection the ICG signal is spread in a non-specific way in all districts, while starting from 6 h is it possible to

highlight a specific signal at the tumor. Thus, in comparison to HF<sub>n</sub>-ICG and ICG, HF<sub>n</sub>-PAS-ICG stands out for maintaining the signal which is always superior and prolonged in time.

Group	2h	4h	6h	24h	48h	72h	96h	168h
<b>HF<sub>n</sub>-PAS-ICG</b>	6.85E+09 ±	4.53E+09 ±	2.50E+09 ±	1.13E+09 ±	9.01E+08 ±	7.28E+08 ±	6.71E+08 ±	6.34E+08 ±
	2.12E+09 (**,###)	1.62E+09 (**,###)	1.03E+09 (**,###)	3.57E+08 (**,####)	2.43E+08 (**,####)	3.16E+08 (**,###)	2.62E+08 (**,###)	2.55E+08 (**,####)
<b>HF<sub>n</sub>-ICG</b>	4.87E+09 ±	3.22E+09 ±	1.59E+09 ±	8.31E+08 ±	5.07E+08 ±	3.97E+08 ±	2.74E+08 ±	1.94E+08 ±
	1.51E+09	3.89E+08 (\$\$)	3.79E+08 (\$)	1.03E+08 (\$\$\$)	1.81E+08	1.68E+08 (\$\$)	1.78E+08	1.16E+08
<b>ICG</b>	3.76E+09 ±	2.48E+09 ±	1.30E+09 ±	4.43E+08 ±	2.88E+08 ±	2.25E+08 ±	2.43E+08 ±	1.56E+08 ±
	6.03E+08	4.37E+08	5.25E+08	1.41E+08	1.12E+08	1.21E+08	1.08E+08	6.69E+07

Table 3.1 Quantification of fluorescent signal at the tumor detected by IVIS Lumina II reported as Total Radiant Efficiency. Data are reported as mean value ± SD, n = 6. Student t-test HF<sub>n</sub>-PAS-ICG vs HF<sub>n</sub>-ICG (\*) \*\* 0.046 < p < 0.024, \*\*\* 0.007 < p < 0.0009. HF<sub>n</sub>-PAS-ICG vs ICG (#) ### 0.007 < p < 0.0009, ### p < 0.0009. HF<sub>n</sub>-ICG vs ICG (\$) \$ p = 0.05, \$\$ 0.046 < p < 0.024, \$\$\$ 0.007 < p < 0.0009, \$\$\$\$ p < 0.0009.

The promising results obtained so far in this pilot study corroborated the refinement provided by the introduction of the novel nanotracer HF<sub>n</sub>-PAS-ICG and strongly support its study also in other kinds of tumors.

### 3.9.9 Evaluation of HF<sub>n</sub>-PAS-ICG tumor accumulation in a CRC murine model

Finally, the feasibility of the nanotracer HF<sub>n</sub>-PAS-ICG was also studied in a subcutaneous murine model of CRC, thanks to a collaboration with the Institute for Experimental and Molecular Imaging (ExMI). By taking advantage of the advanced imaging devices present in the German institute, we further investigate the behavior of the nanotracer by comparing 3 different concentrations of the nanocage to select the best time window in order to obtain the highest accumulation at the tumor and a complete wash-out from off-target organs. In particular, the combination of FMT with  $\mu$ CT analysis has been identified as an outstanding approach for the longitudinal and quantitative *in vivo* determination of the fluorescence distribution in depths of several centimeters. Thanks to the complete 3D reconstruction, which is currently ongoing, we devise obtaining a precise quantification of the biodistribution of HF<sub>n</sub>-PAS-ICG and, later, a powerful approach to study the tumor tracking capability in a metastatic model.

Overall, the preliminary results collected supported the efficacy of HF<sub>n</sub>-PAS-ICG also in this model. Indeed, the FMT images (Figure 3.23 A) revealed a visible accumulation of the nanotracer in correspondence to the tumor masses until 96 h and the signal

observed in the excised tumor appeared higher in comparison to that at the liver, suggesting an improved signal to background ratio (Figure 3.23 B). Furthermore, the 3D quantification will allow us to depict the best timepoint for an optimized accumulation at the tumor to plan following studies on metastatic models.

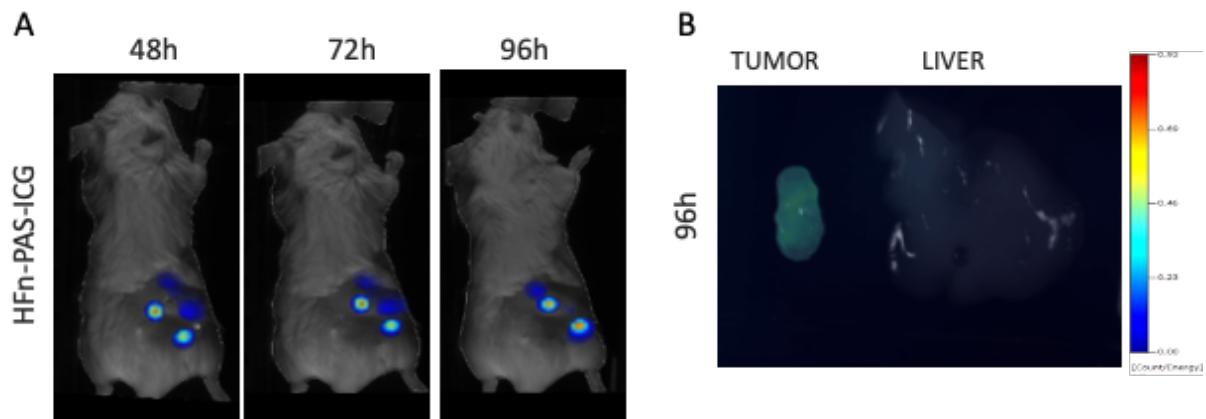


Figure 3.23 A) *In vivo* accumulation of the fluorescence signal at the tumor for HFn-PAS-ICG at the concentration of 6 mg/kg at 48h, 72h and 96h obtained with FMT imaging. B) *Ex vivo* accumulation of fluorescence signal at the tumor and at the liver at 96h obtained with FMT imaging.

### 3.5 Discussion and conclusion

With the idea of developing a nanotracer for oncological FGS, we reasoned that encapsulating ICG into a tumor targeted nanodelivery system could be a valuable approach to achieve a tailored surgery. Thus, we decided to integrate the features of ICG with those offered by HF<sub>n</sub>, whose implementation is particularly interesting for its relevant translational impact.

In this study we started from the development of the HF<sub>n</sub> nanocage loaded with ICG to accomplish the evaluation of its *in vivo* potential as fluorescent nanotracer.

*In vivo*<sup>122</sup> and *ex vivo*<sup>126</sup> assessments of ICG tumor targeting performed with endoscope Karl Storz/ICG, revealed that the HF<sub>n</sub> can deliver ICG to the tumor with higher specificity and efficiency than the free dye, defining anatomic structure. Indeed, HF<sub>n</sub>-ICG displayed improved ICG accumulation in tumor in comparison to free dye, thanks to HF<sub>n</sub>-ICG tumor homing with respect to mice treated with free ICG. Moreover HF<sub>n</sub>-ICG signal was still visible at 24 h. The quantification performed on IVIS Lumina II acquisitions, supports the same topic revealing significant differences between the mice treated with HF<sub>n</sub>-ICG and ICG. To date, fluorescence evaluations at early time points (i.e., 2 h after injection) were not effective since the blue fluorescent signal in the tumor mass was highly diffused avoiding the discrimination of the anatomical structures. These results in the whole not only support the suitability of HF<sub>n</sub>-ICG for tumor tracking, but also suggest that it is necessary to wait some time to achieve the proper accumulation of fluorescence signals.

Moreover, we have analyzed the accumulation in off-target organs to study the ICG and HF<sub>n</sub>-ICG biodistribution, evidencing that the nanoformulation slows down the tracer's kinetic. To decipher the role of HF<sub>n</sub> nanoformulation in influencing ICG's fate, we proceeded with UHPLC-MS/MS quantification on organ homogenates. By investigating the accumulation of ICG using mass spectrometry, we confirmed the superior delivery of ICG thanks to the nanoformulation which drives a real accumulation at the tumor instead of only having a role in the preservation of its fluorescence (manuscript under review).

Nevertheless, these results also evidenced that the performance of this nanotracer should be improved to exploit it as a suitable imaging tool for the detection of tumors with unknown localization and micrometastasis and to accelerate its wash-out from non-target organs to obtain more specific signals in cancer. In fact, we noticed that the signal associated with HF<sub>n</sub>-ICG and the tumor signal to background ratio reported *in*

*in vivo* was still suboptimal due to short circulation time <sup>126</sup>. Indeed, despite incredible advantages conferred to ICG, HFn has a reduced plasma half-life after systemic injection, which limits its full potential as a delivery system.

For this reason, we studied a new strategy to raise the circulation time of HFn. The new improved nanocage HFn-PAS is aimed at achieving increased stability and improved half-life while maintaining the already efficient tumor accumulation. We optimized the procedure for HFn-PAS purification, which required different steps and a massive optimization work. Indeed, despite the apparent slight differences, HFn-PAS has completely different features than those of HFn. We encountered a reduced purification yield of HFn-PAS in comparison to HFn probably due to the size of the protein, which is almost twice the molecular weight of HFn, or to the presence of sequences lacking secondary structure (i.e., PAS sequences). In any case, the production of the novel nanocage was successfully achieved and it was possible to perform a rigorous *in vitro* characterization of HFn-PAS by different methods (TEM, DLS and CD). Indeed, collecting precise and valid information on the main characteristics of HFn-PAS using the correct methodologies, is a key step towards a precise understanding and/or prediction of its diagnostic efficacies.

Thanks to these results, we proved that our nanocages display the expected structural morphology and dimensions, in addition to the requirements for injectability in terms of ETX content. Additionally, the results achieved in the tested *in vivo* models strongly support HFn-PAS-ICG reliability as tumor-targeted agents for FGS application.

In the next future, we plan to assess HFn-PAS-ICG as an FGS metastasis tracer within the project “Targeted NIR nanotracer for Image-Guided surgery: tailored resection and intraoperative solid cancers' stadiation \_TIGER” (ID 27107- P.I. Mazzucchelli) funded by AIRC.

To conclude, several studies are required to better investigate the properties of HFn-based nanoformulations and to understand how to improve their features to attain a reliable nanodiagnostic tool for FGS. However, the present research study provides important insights on its potential as a cancer specific nanotracer effective for several cancer subtypes where FGS is considered a valuable therapeutic option.

## 4. Study 2: Ferritin nanocages loaded with doxorubicin: a strategy to preserve antitumor immunity from doxorubicin toxicity

Manuscript in preparation.

### 4.1 Introduction

The anthracycline doxorubicin (DOX) is the first-line therapy for the treatment of different cancer types, including leukemia, lung cancer, and is considered as a mainstay for BC treatment due to its excellent cytotoxic activity. This chemotherapeutic has a direct cytotoxic effect against cancer cells by interfering with DNA replication<sup>127</sup>. However, DOX is active also against other rapidly dividing cells, resulting in severe off-target toxicities.

Besides its direct killing of rapidly proliferating tumor cells, DOX is reported to induce the immunogenic cancer cell death (ICCD) and promote tumor immunogenicity as a consequence of the stimulation of dendritic cell (DC) antigen-presenting function<sup>128-131</sup>. Thus, DOX-based chemotherapy facilitates the upregulation of death receptors and several cancer neoantigens become immediately available to DCs leading to the induction of anti-tumor immune responses<sup>132</sup>. DCs stimulate rare naïve cancer-specific T-cells maturation and clonal expansion, resulting in an induced adaptive-antitumor immune response, which is crucial to develop a complete remission and to generate a successful immunological memory able to surveil for relapses and/or metastasis development<sup>133</sup>.

However, concurrently, this antitumor response is restricted by DOX itself. Indeed, neutropenia is considered one of the most significant hematological toxicities associated to DOX chemotherapy, and despite it is mostly a transient effect, they cause long-lived alterations to immunity.<sup>134</sup> Therefore, T-cells clonal expansion which is one of the most proliferative events observed in biological systems it is expected to be strongly reduced or even suppressed by DOX treatment<sup>135 136,137</sup>.

So far, the investigation about the effect of an anthracycline's regimen on dividing T-cells to improve DOX immune-mediated antitumor activity is fragmentary and the subject of unsolved questions<sup>138</sup>. Simultaneously, there is growing interest in

developing refined DOX formulations to mitigate detrimental effects such as severe cardiotoxicity resulting from unfavorable pharmacokinetics and inadequate targeting of tumors.

Among novel nanoformulations, those based on NPs showed the ability to enhance the physicochemical properties of a wide variety of drugs used in oncology to limit off-site side effects and improve their therapeutic efficacy, increasing drug accumulation in target tissue<sup>52,139,140</sup>. The use of ferritin nanocages as carriers for encapsulating DOX presents a promising avenue in drug delivery. Indeed, ferritin nanocaged DOX capitalize on the unique structural properties of ferritin which is a naturally occurring protein capable of self-assembling into nanoscale cages, offering a controlled and efficient platform for encapsulating DOX. Here we identify FerOX, a DOX formulation in ferritin nanocages, as an alternative nanodrug capable to preserve the proliferative potential of T cells<sup>141</sup>.

## 4.2 Aim of the study two

According to previous studies conducted by our group<sup>91</sup>, the development of HF<sub>n</sub> nanocages loaded with DOX (FerOX) has the potential to offer enhanced therapeutic efficacy and reduced cardiotoxicity in comparison to free DOX.

In this study I aim to characterize DOX uptake and effect on human lymphocytes, firstly derived from healthy donors, then from BC patients that underwent neoadjuvant chemotherapy (NAC). Indeed, the paradox regarding the dual effect of DOX on tumors warrants further examination. First, DOX by directly killing tumor cells acts as an immunogenic drug and triggers an effective immune stimulus to fight tumors. However, at the same time, this antitumor response is restricted by DOX itself which massively prevents lymphocyte's proliferation.

As a result of that, the second purpose of this study regards the investigation of the impact on primary human T cell obtained from Peripheral Blood Mononuclear Cells (PBMC) in terms of uptake and proliferative potential of FerOX, a HF<sub>n</sub>-based DOX nanoformulation conceived as a strategy to preserve the proliferative potential of the T-cell compartment during a DOX treatment.

## 4.3 Materials and Methods



**Patient recruitment**

Thirty patients affected by BC at any stage and candidate to neoadjuvant chemotherapy with anthracyclines at ICS Maugeri IRCCS between April 2018 and October 2021 were enrolled in Armageddon protocol (number 2201CE). A written informed consent to participate in the present protocol was obtained from each patient. Blood samples from healthy donors and from BC patients before and after (about 3 h) the first cycle of DOX chemotherapy were collected and used in this study.

**Peripheral Blood Mononuclear Cells collection**

Blood samples collected in EDTA-coated tubes were treated by Ficoll gradient to isolate PBMC. Briefly, up to 4.5 mL of blood were gently added to a 15 mL tube containing 5 mL of RT Ficoll (Histopaque®-1077, Sigma) and centrifuged at RT at 400-g for 30 minutes in a swinging- bucket rotor without brake. Then, the upper layer of plasma fraction was carefully removed, the mononuclear cell layer containing PBMC was transferred to a 50 mL conical tube and rinsed with 35 mL of phosphate buffer (PBS, Euroclone). PBMC were washed by centrifugation at RT at 400-g for 10 minutes. In case of red blood cell contamination, a 5 minute treatment in ACK lysis buffer was performed. PBMC were frozen in Foetal Bovine Serum (FBS, Euroclone) supplemented with 10% DMSO (Sigma) and stored at  $-80^{\circ}\text{C}$  until usage.

***In vitro* Doxorubicin uptake**

$2 \cdot 10^5$  PBMC were seeded in 96 multiwell plates in 200  $\mu\text{L}$  of RPMI medium supplemented with 10% FBS, 1% Penicillin/Streptomycin (Euroclone) and 1% Glutamine (Euroclone) and treated with different concentrations of Doxorubicin free (DOX; 0.01, 0.1, 1 and 10  $\mu\text{M}$ ) or with the nanoformulation FerOX and the liposomal DOX formulation already introduced in clinical practice Myocet (1  $\mu\text{M}$  of DOX equivalent). After 1, 3 and 24 h (h), cells were collected and analyzed by FC (Cytoflex, Beckman Coulter) to quantify DOX mean fluorescence intensity after staining with Live/Dead (L34976; Thermo Scientific). Acquisition was performed on 20000 events, within the selected region of live singlets. Untreated PBMC were used to select the region of positivity.

To analyze what populations are mainly involved in DOX uptake,  $2 \cdot 10^5$  PBMC were seeded as reported above and treated DOX free (1 and 5  $\mu\text{M}$ ) or with the nanoformulations FerOX and Myocet (5  $\mu\text{M}$  of DOX equivalent) for 24 h. Then, cells were collected and stained for Live/Dead, CD3-PECy7, CD4-EF506, CD8a-FITC,

CD45RA-AF700 and CD197-APC. DOX internalization was quantified by FC. CD4<sup>+</sup> T-cells were identified as CD3<sup>+</sup>/CD4<sup>+</sup>, while CD8<sup>+</sup> collected CD3<sup>+</sup>/CD8<sup>+</sup> cells. T cells subpopulation were identified as follow: Central Memory (CM, CD197<sup>+</sup> CD45RA<sup>-</sup>), Naïve (CD197<sup>+</sup> CD45RA<sup>+</sup>), Effector Memory (EM, CD197<sup>-</sup> CD45RA<sup>-</sup>), Terminally Differentiated Effector (TDE, CD197<sup>-</sup> CD45RA<sup>+</sup>). Acquisition was performed on 20000 events, within the selected region of live singlets. Untreated PBMCs were used to select the region of DOX positivity. Biological replicates n=3-6.

### **Doxorubicin quantification in PBMCs from BC patients**

PBMC collected from BC patients following the guidelines of Armageddon protocol were analyzed by FACS to quantify DOX mean fluorescence intensity after staining with Live/Dead (L34976; Thermo Scientific). To identify subpopulations involved in DOX uptake, cells were stained with CD3-PECy7 (clone OKT3, Thermo Scientific), CD4-EF506 (clone RPA-T4, Thermo Scientific), CD8a-FITC (clone OKT-8, Thermo Scientific), CD45RA-AF700 (clone HI100, Thermo Scientific) and CD197-APC (clone 3D12, Thermo Scientific). T cells subpopulations were identified as follow: Central Memory (CM, CD197<sup>+</sup> CD45RA<sup>-</sup>), Naïve (CD197<sup>+</sup> CD45RA<sup>+</sup>), Effector Memory (EM, CD197<sup>-</sup> CD45RA<sup>-</sup>), Terminally Differentiated Effector (TDE, CD197<sup>-</sup> CD45RA<sup>+</sup>). Acquisition was performed on 20000 events, within the selected region of live singlets. Untreated PBMC were used to select the region of positivity.

### **FerOX production**

HF<sub>n</sub> nanocages were produced in BL21(DE3) ClearColi® strain and purified by bacterial endotoxins as previously described<sup>125</sup>. FerOX was obtained loading DOX inside HF<sub>n</sub> using the pH disassembly-reassembly method already described by our group<sup>92</sup>. HF<sub>n</sub> dissolved at 0.5 mg/mL in 150 mM NaCl were disassembled lowering the pH to 2 and incubating HF<sub>n</sub> under shaking (180 rpm, RT) for 15 minutes. Then, 200 μM DOX was added, adjusting the pH back to 7.5 and incubating the mixture for 2h under shaking (180 rpm, RT). Then, unloaded DOX was removed by centrifugation (3500g, 15 min) in 100 kDa Amicon membranes (Millipore) and using 7K MWCO Zeba™ Spin Desalting columns (Thermo Fisher). The quantification of FerOX content was determined by spectrofluorimetry (FP-800, Jasco) after DOX extraction in isopropanol chloroform solution<sup>142</sup>.

### **Confocal microscopy**

1·10<sup>5</sup> PBMC were seeded in 96 multiwell plates in 100 µL of RPMI medium supplemented with 10% FBS, 1% Penicillin/Streptomycin and 1% Glutamine and treated with DOX free (0.1, 1 and 10 µM) or with the nanoformulations Myocet and FerOX (1 µM of DOX equivalent). After 24 h, cells were collected, fixed with 4% paraformaldehyde (PFA, Sigma) for 10 min at RT. Then, cells were labelled with DAPI (1:10000) and mounted on coverslips with ProLong™ Gold (Invitrogen, P36935). Confocal microscopy images were acquired at 1024·1024 dpi resolution with the Leica confocal microscope SP8 equipped with 405, 488 and 513 nm lasers.

### CFSE proliferation assay

PBMC from healthy donors or BC patients were marked with CFSE (1µM in PBS; C34554, Invitrogen, Thermo Fisher) for 10 min at RT and washed twice with RPMI medium supplemented with 10% FBS, 1% Pennicilin/Streptomycin and 1% Glutamine. Cells were then seeded in 96 multiwell round bottom plates (2·10<sup>5</sup> cells in 200 µL of RPMI medium supplemented with 10% FBS, 1% Pennicilin/Streptomycin, 1% Glutamine). PBMC from BC patients collected before and after chemotherapy were analyzed by FC 2, 3, 4 and 5 days after stimulation with Concanavalin A (ConA, 5 µg/mL, C0412, Sigma). Biological replicates n=6. PBMC from healthy donors were incubated with 5µM of DOX equivalent (free DOX, Myocet and FerOX) for 3 h and analyzed by FC at 2, 3, 4 and 5 days after ConA stimulation. Biological replicates n=3. Some PBMC from BC patients collected before chemotherapy were used to simulate an *ex vivo* treatment and incubated with 5µM of DOX equivalent (free DOX, Myocet and FerOX) for 3 h and then stimulated with ConA. Three days after ConA treatment, they were labelled with Live/Dead (L34976, Thermo Scientific), CD3-PECy7 (clone OKT3, Thermo Scientific), CD4-EF506 (clone RPA-T4, Thermo Scientific), CD19-SB346 (clone HIB19, Thermo Scientific) and analyzed by FC. Biological replicates n=3. The proliferation index was calculated using the software FlowJo (version 10).

### Drug screening on Patient-Derived Organoids

Twelve BC Patient Derived Organoids (PDOs) stored in the in the “Bruno Boerci Oncological Biobank” at ICS Maugeri IRCCS according to a protocol approved the ethical committee of ICS Maugeri IRCCS in July 2009 and classified as Luminal A (n=4), Luminal B (n=4), HER2+ BC (n=2) and Triple-Negative BC (TNBC; n= 2) were used to assess FerOX biological activity. PDOs cultured as previously described<sup>152</sup>, have been sheared 2-3 days before the seeding to obtain smaller and uniform in size PDOs. Briefly, PDOs were isolated from Cultrex® Ultimatix Reduced Growth Factor

Basement Membrane Matrix (BME, Bio-techne, BME0010), by incubation with Dispase 1  $\mu\text{g}/\text{mL}$  (Gibco, 17105-041) at 37°C for 1-2 h. Once the BME was dissolved, PDOs were collected in 15 mL tube and they were washed twice with Ad-DF +++ medium (Hyclone DMEM-F/12 1:1 supplemented with 10 mM HEPES, 1% Penicillin/Streptomycin and 1% L-glutamine). The PDOs were counted, diluted in culture medium, supplemented with 10% BME and seeded 10.000 cells/well in a 96-wells spheroid microplate (Corning, 4520) at the concentration of 200 cells/ $\mu\text{L}$ . After 24 h, 8 different concentrations of DOX, Myocet and FerOX (0.05, 0.1, 0.5, 1, 10, 20, 50, 100  $\mu\text{M}$ ) were added in 10 replicates. Untreated cells were used as negative control. After 3 days of incubation at 37°C and 5% CO<sub>2</sub>, the Cell Titer Glo 3D Kit (Promega, G9682) was used, according to manufacturer's instructions, to measure the ATP content as an indicator of cell viability. Emitted luminescence was read in microplate reader (PerkinElmer, Victor Nivo Multimode) and data were analyzed using GraphPad Prism 8.

### **TfR1 expression on Patient Derived Organoids**

$3 \times 10^6$  organoids have been isolated from BME by Dispase 1  $\mu\text{g}/\text{mL}$  treatment. Once collected, PDOs have been reduced into single cells through the shearing procedure using TrypLe™ Select (1X; Gibco, 12563-029). After three washes with HBSS (HyClone Hank's Balanced Salt Solution), SH30268.02), the cells were fixed with PFA 4% for 5-10 minutes in ice. Fixed cells have been washed thrice with HBSS supplemented with FBS 2% and stained. Staining has been with anti-TfR1 antibody (1  $\mu\text{g}/\text{tube}$ ; clone ICO-92; Thermo Fischer Scientific) in PBS, 2% Bovine Serum Albumin (BSA; Sigma) and 2% goat serum (Euroclone) for 30 min at RT. Then, cells were washed thrice with PBS and immunodecorated with Alexa Fluor 488 goat anti-mouse secondary antibody (1  $\mu\text{L}/\text{tube}$ ; A-11001; Invitrogen; Thermo Fischer Scientific) in PBS, 2% BSA and 2% goat serum for 30 min at RT. After three washes with PBS cells were analyzed by CytoFLEX flow cytometer (Beckman Coulter). 20000 events were acquired for each analysis, after gating on viable cells and on singlets. The region of positivity has been set using cells immunodecorated only with secondary antibodies.

### Statistical analysis

Statistics was evaluated using GraphPad Prism 8.0a version (GraphPad Software Inc.). Data are reported as mean  $\pm$  Standard Error Mean (SEM). The level of statistical significance was set at  $p < 0.05$ . Proliferation index and DOX uptake have been analyzed by paired t-test, while One-way ANOVA has been used to assess DOX uptake in different T-cells populations. Two-way ANOVA has been used to study IC<sub>50</sub> results on PDO considering both the effect of drug and organoid type.

## 4.4 Results and Discussion

### 4.4.1 Human Peripheral Blood Mononuclear Cells internalized DOX in a dose and time-dependent manner

It is important to investigate the effect of DOX on dividing T-cells to determine whether DOX's immunogenicity can be better exploited by developing a nanoformulation that selectively kills tumor cells, and at the same time preserving antitumor immune response. Hence, we have investigated the effect of DOX on lymphocytes from healthy donors. Of note, we observed that patient-derived PBMC, incubated up to 24 h with DOX concentrations starting from 0.01 to 10  $\mu$ M, displayed a dose and time dependent internalization profile, as evidenced by mean fluorescence intensity (MFI) values of DOX positive PBMC population analyzed by FC (Figure 4.1 A). Upon internalization, DOX accumulates in the nucleus (Figure 4.1 B), where it exerts its cytotoxic action by intercalating into the double-helix and disrupting topoisomerase-II-mediated DNA repair<sup>143</sup>.

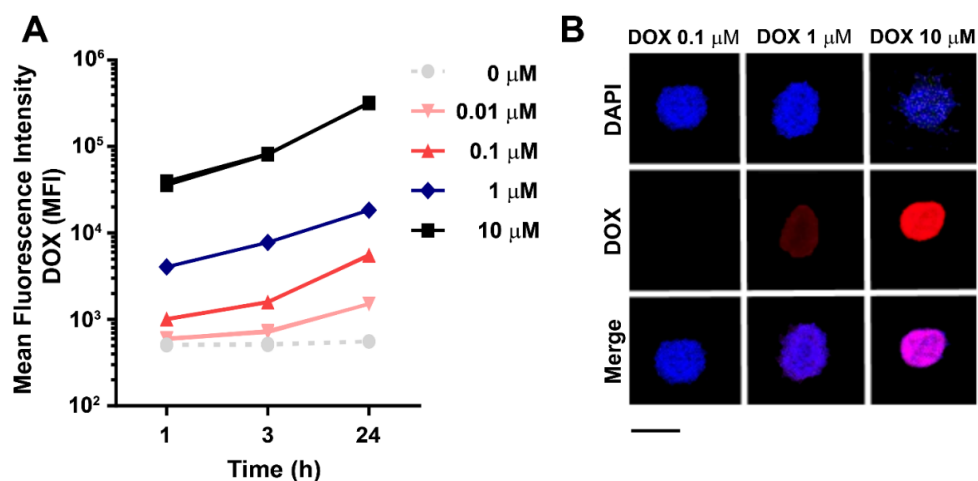


Figure 4.1 DOX internalization in peripheral blood lymphocytes. A) PBMC collected from healthy donors and treated with different concentrations of DOX (0.01, 0.1, 1 and 10  $\mu\text{M}$ ) for 1, 3 and 24 h to assess drug uptake. DOX uptake has been monitored during time by FC measuring DOX mean fluorescence intensity in DOX<sup>+</sup> cells. Untreated PBMC were used to select the region of positivity. B) PBMC treated with DOX at 0.1, 1 and 10  $\mu\text{M}$  for 24 h and acquired by confocal microscopy. Nuclei were stained with DAPI (blue), while the DOX fluorescence signal was reported in red. Scale bar = 10  $\mu\text{m}$ .

#### 4.4.2 DOX internalization affects the proliferative potential of human Peripheral Blood Mononuclear Cells

To assess whether the accumulation of DOX at the nucleus visible in Figure 4.1 B induces a reduction in proliferation and could thus affect the generation of a successful antitumor immune response, CFSE-labeled PBMCs from healthy donors were exposed to DOX before being treated with the Concanavalin A (ConA) mitogen. In absence of DOX, ConA drove PBMC proliferation in a ConA dose-dependent manner (i.e., 5 and 0.5  $\mu\text{g}/\text{mL}$ ), as evidenced by the presence of the proliferating PBMC populations with lower CFSE fluorescence (Figure 4.2 A). On the other hand, in PBMC previously incubated with DOX, the capability to respond to ConA was strongly reduced (Figure 4.2 B). Indeed, DOX-treated, ConA-stimulated samples showed almost a four-fold reduction (i.e., 3.84) in the PBMC population with lower CFSE fluorescence in comparison to that observed in untreated, ConA-stimulated sample (16.6% vs 63.7%; Figure 4.2A and B). These results confirm that DOX uptake is strictly coupled with an impairment of proliferative capability in human PBMCs. After incubating PBMC with 5  $\mu\text{M}$  DOX for 24 h, there was a significant decrease in the proliferation index observed in the overall lymphocyte population (Figure 4.2 C), as well as in CD4<sup>+</sup> and CD8<sup>+</sup> T cells (Figure 4.2 D and 4.2 E) showing a global impairment of T-cells mediated immune response after DOX treatment. As PBMC are promptly exposed to DOX during parenteral infusion of DOX-based chemotherapy, we have then evaluated the DOX uptake and the proliferative potential in match-paired PMBC isolated from BC

patients before and immediately after (approximately 3 h after the start of infusion) the first cycle of DOX based NAC.

FC analysis reported in figure 4.2 F and 4.2 G revealed a DOX<sup>+</sup> cell population internalizing DOX after chemotherapy and exhibiting a four-fold elevation in DOX MFI. Consistent with results obtained from healthy donors PBMC exposed *in vitro* to DOX, also patient's *in vivo* DOX uptake resulted in a significant proliferative impairment in response to mitogenic stimulations, lasting for at least five days (Figure 4.2 H and 4.2 I). These results confirmed that DOX chemotherapy, while releasing immunogenic tumor antigens upon tumor cells killing, can also affect adaptive antitumor immune response, limiting the benefits of ICCD, as already evidenced<sup>134</sup>. It is also crucial to underline that the negative impact of DOX chemotherapy on PBMC population is quick and already detectable after the end of the first cycle of drug infusion. Indeed, performing the count of collected viable cells before and after NAC, it is immediately evident that a marked decrease in cell number occurs upon DOX infusion, as reported in Table 4.1. After infusion, less than half of the circulating immune cells remain alive, but these surviving cells are not able to proliferate (see Figure 4.2 F-I), hence can't exert an effective response anymore. These results together describe the well-known toxic action of DOX chemotherapy against blood circulating lymphocytes and further indicate that preserving the immune competence is an urgent still unmet clinical need<sup>144,145</sup>.

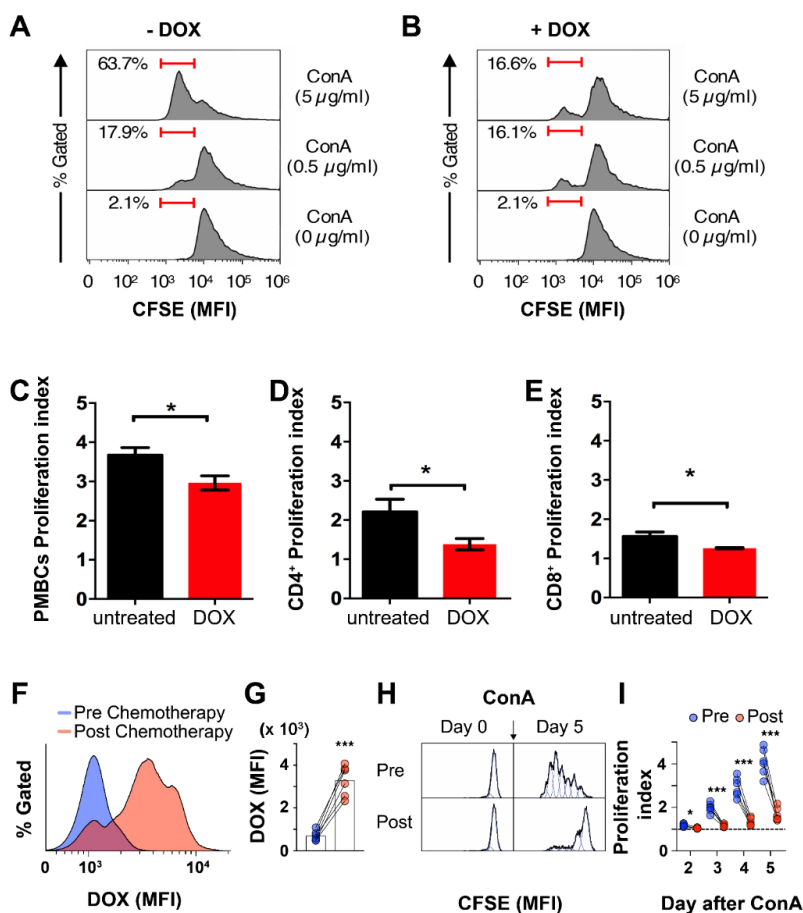


Figure 4.2 DOX uptake affects peripheral blood lymphocytes proliferation *in vitro* and *ex vivo*. A) Representative proliferation profile of PBMC collected from healthy donors, labelled with CFSE 1 $\mu$ M and stimulated with Concanavalin A (ConA, 0.5-5  $\mu$ g/mL). Cell proliferation resulted in reduced CFSE mean fluorescence intensity (MFI). B) Representative proliferation profile of PBMC collected from healthy donors, labelled with CFSE 1 $\mu$ M, treated with DOX 5  $\mu$ M for 24 h and stimulated with ConA (0.5-5  $\mu$ g/mL). C) Proliferation index of PBMC after 24h *in vitro* treatment with DOX 5  $\mu$ M calculated using the software FlowJo (version 10). Statistical significance: \*  $p < 0.05$  (paired t-test). D) Proliferation index of CD4<sup>+</sup> T-cells after 24h *in vitro* treatment with DOX 5  $\mu$ M. Statistical significance: \*  $p < 0.05$  (paired t-test). E) Proliferation index of CD8<sup>+</sup> T-cells after 24h *in vitro* treatment with DOX 5  $\mu$ M. Statistical significance: \*  $p < 0.05$  (paired t-test). F) Representative profile of DOX MFI in PBMC collected from BC patients before and after the first cycle of DOX neoadjuvant chemotherapy. G) DOX fluorescence signals detected by FC in matched PBMC from BC patients collected before and after the first cycle of DOX chemotherapy (n= 6). Statistical significance: \*\*\*  $p < 0.005$  (paired t-test). H) Representative profiles of CFSE MFI signal detected by FC before and 5 days after ConA stimulation in PBMC population collected from BC patients before and immediately after the first cycle of DOX neoadjuvant chemotherapy. I) Proliferation index calculated at day 2, 3, 4 and 5 after ConA stimulation in matched PBMC collected before and immediately after the first cycle of DOX neoadjuvant chemotherapy (n=6). Statistical significance: \*  $p < 0.05$ , \*\*\*  $p < 0.005$  (paired t-test).

	PBMC /mL of blood	Ratio post/ pre
	Mean $\pm$ St.dev	
PBMC pre-DOX neoadjuvant chemotherapy	1.24 $\cdot$ 10 <sup>6</sup> $\pm$ 6.70 $\cdot$ 10 <sup>5</sup>	-
PBMC post-DOX neoadjuvant chemotherapy	5.26 $\cdot$ 10 <sup>5</sup> $\pm$ 1.48 $\cdot$ 10 <sup>5</sup>	0.48 $\pm$ 0.15

Table 4.1. Count of mean values of viable PBMC collected from 8 BC patients before and after NAC recruited in Armageddon protocol.



#### 4.4.3 DOX treatment predominantly targets CD8<sup>+</sup> T cells

To investigate if DOX has a preferential effect on a specific T-cell population during chemotherapy, we analyzed DOX uptake in subsets of CD4<sup>+</sup> and CD8<sup>+</sup> cells. Despite the CD3<sup>+</sup>/CD4<sup>+</sup> population being the most represented in PBMC collected from BC patients (Figure 4.3A), CD3<sup>+</sup>/CD4<sup>+</sup> and CD3<sup>+</sup>/CD8<sup>+</sup> are almost equally represented in the DOX<sup>+</sup> population (Figure 4.3 B). In the meantime, the higher DOX uptake is observed in CD8<sup>+</sup> population (Figure 4.3 C), that displayed almost a two-fold DOX MFI, in comparison to CD4<sup>+</sup> cells, evidencing that CD8<sup>+</sup> is more prone to DOX internalization than CD4<sup>+</sup>. Among DOX<sup>+</sup>CD4<sup>+</sup> cells, we observed high frequency of naïve cells (CD45RA<sup>+</sup>CD197<sup>+</sup>), followed by Central Memory (CM) and Effector Memory (EM) cells, while only a little fraction of them are Terminal Differentiated Effector (TDE), as reported in Figure 4.3 D and 4.3 E. Although the high percentage of CD4<sup>+</sup> Naïve cells observed in DOX<sup>+</sup> population, they displayed the lowest DOX MFI, suggesting a lower drug uptake (Figure 4.3F). On the contrary, CD4<sup>+</sup> CM, EM and TDE populations showed two-fold higher DOX MFI, evidencing that a higher amount of DOX has been internalized in these cells. DOX<sup>+</sup> cells in CD8<sup>+</sup> population are mainly subclustered as TDE, followed by Naïve and EM cells, while only a little fraction of them are CM, as reported in Figure 4.3 G-4.3 H. Also in this case, despite the relatively high percentage of CD8<sup>+</sup> Naïve cells observed in DOX<sup>+</sup> population, they displayed the lowest DOX MFI, suggesting a lower drug uptake (Figure 4.3 I). Similarly, those observed in CD4<sup>+</sup> population, CD8<sup>+</sup> CM, EM and TDE populations, showed two-fold higher DOX MFI, evidencing once again that a higher amount of DOX has been internalized in these cells <sup>146,147</sup>.

These results are consistent with that already observed in the literature, where DOX chemotherapy seems to have a higher negative impact on CD8<sup>+</sup> T cells <sup>146</sup>.

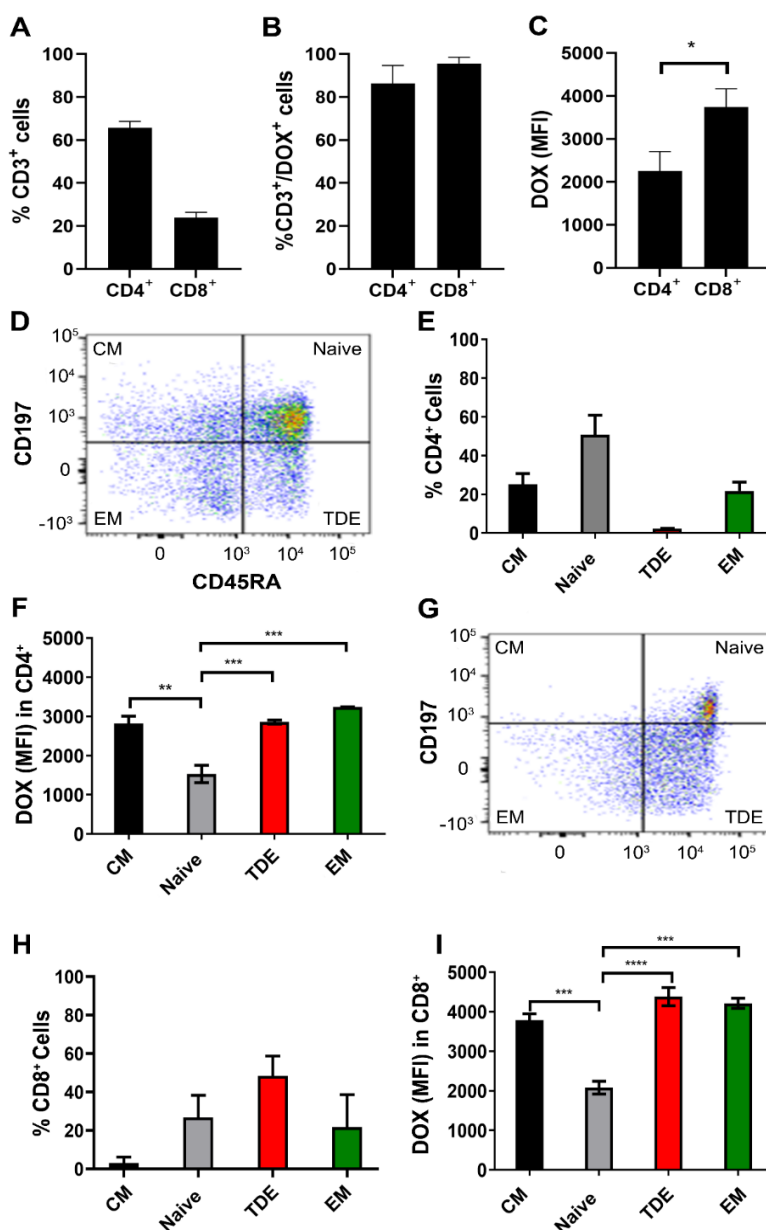


Figure 4.3 DOX uptake in peripheral blood lymphocytes subpopulations collected from BC patients immediately after the first cycle of chemotherapy. A) CD8<sup>+</sup> and CD4<sup>+</sup> distribution in BC patients' PBMC collected immediately after the first cycle of chemotherapy. B) CD8<sup>+</sup> and CD4<sup>+</sup> distribution in DOX<sup>+</sup> population of BC patients' PBMC collected immediately after the first cycle of chemotherapy. C) Mean DOX fluorescence intensity in DOX<sup>+</sup> T cells populations from BC patients' PBMC collected immediately after the first cycle of chemotherapy. Statistical significance: \*  $p < 0.05$  (One-way ANOVA). D) Representative dot-plot of distribution of CD4<sup>+</sup> T cells subpopulations from BC patients' PBMC collected immediately after the first cycle of chemotherapy. E) CD4<sup>+</sup> T cells distribution in BC patients' PBMC collected immediately after the first cycle of chemotherapy. F) Mean DOX fluorescence intensity in DOX<sup>+</sup>/CD4<sup>+</sup> T cells subpopulations from BC patients' PBMC collected immediately after the first cycle of chemotherapy. Statistical significance: \*\*  $p < 0.01$ , \*\*\*  $p < 0.005$  (One-way ANOVA). G) Representative dot-plot of distribution of CD8<sup>+</sup> T cells subpopulations from BC patients' PBMC collected immediately after the first cycle of chemotherapy. H) CD8<sup>+</sup> T cells distribution in BC patients' PBMC collected immediately after the first cycle of chemotherapy. I) Mean DOX fluorescence intensity in DOX<sup>+</sup>/CD8<sup>+</sup> T cells subpopulations from BC patients' PBMC collected immediately after the first cycle of chemotherapy. Statistical significance: \*\*\*  $p < 0.005$ , \*\*\*\*  $p < 0.001$  (One-way ANOVA). All assessments have been performed at least on PBMCs collected from at least 3 patients.

#### 4.4.4 DOX formulation in ferritin nanocages (FerOX) preserve DOX activity in a panel of Patient-derived organoids

The results obtained provided evidence that DOX uptake varies in CD8<sup>+</sup> and CD4<sup>+</sup> subsets in patients, and that this differential uptake impacts the proliferative potential of T cells. Since the preservation of proliferative competence is critical for T cell-mediated adaptive antitumor immune response, we decided to evaluate the effect of alternative DOX formulations on these cells. Therefore, we chose to compare Myocet which is already introduced in clinical practice and DOX nanoformulation (i.e., FerOX)<sup>91,92,142,148–150</sup> that has been extensively studied by nanotechnologists in the past two decades but has not yet been introduced into clinical practice<sup>79,141</sup>. FerOX is a protein-based nanoformulation of DOX, which exploits the human protein H-ferritin (HF<sub>n</sub>). Here, DOX is enclosed in a 12 nm diameter cage sphere structure constituted by 24 H-ferritin subunits<sup>92</sup>. The specific binding of the Transferrin receptor 1 (TfR1), which is highly expressed in cancer tissues and mediates the internalization of nanoparticles, facilitated the tumor-targeted recognition of this nanoformulation<sup>151</sup>. Thanks to its unique biotechnological properties, HF<sub>n</sub> quaternary structure could be disassembled lowering the pH until 2.0, and then refolded bringing back the pH to the neutrality<sup>92,141</sup>. When DOX is added to the solution during this process, the HF<sub>n</sub> shell is capable of encapsulating it, leading to the production of FerOX (Figure 4.4 A). FerOX antitumor activity has been assessed on a panel of 12 BC PDOs to demonstrate its suitability to treat human cancers in comparison to free DOX and Myocet<sup>152,153</sup>. FerOX showed equivalent anticancer activity to free DOX, as demonstrated in Figure 4B, in a viability assay conducted to determine the IC<sub>50</sub> of all DOX formulations. On the other side, both FerOX and free DOX exhibited greater efficacy than Myocet in inhibiting the proliferation of BC-PDO, as shown by the nearly 15- to 20-fold increase in Myocet IC<sub>50</sub> (Figure 4.4 B). Moreover, FerOX IC<sub>50</sub> values displayed an inverse correlation with TfR1 expression, confirming the capability of FerOX to mediate a specific tumor-targeted delivery of DOX, as previously described in literature (Figure 4.4 C)<sup>91,92,141,142,151</sup>.

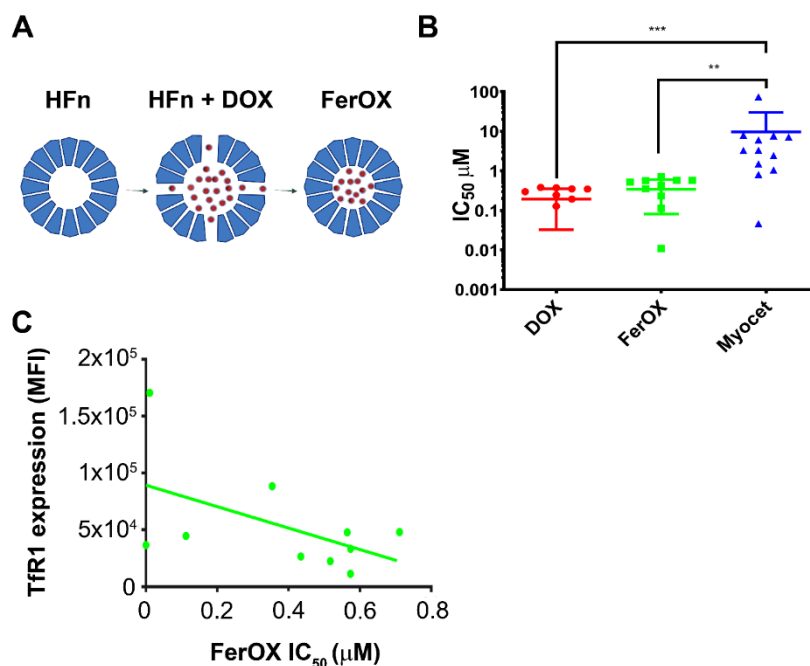


Figure 4.4 FerOX production and antitumor activity compared to DOX and Myocet. A) Schematic representation of FerOX production. HFfn nanocages have been loaded with DOX following the pH-dependent disassembly/reassembly procedure. B) IC<sub>50</sub> of PDOs treated with FerOX, DOX and Myocet. PDO's viability data used to calculate IC<sub>50</sub> have been obtained by Cell titer Glo assay. Statistical significance: \*\*  $p < 0.01$ , \*\*\*  $p < 0.005$  (Two-way ANOVA). C) Correlation between FerOX IC<sub>50</sub> and TFR1 expression of each PDOs ( $r = -0.6083$ ;  $p = 0.0310$ ). TFR1 expression has been determined as MFI evaluated by flow cytometry.

#### 4.4.5 FerOX reduces DOX internalization in Peripheral Blood Mononuclear Cells

Subsequently, we evaluated the impact of various nanoformulations on DOX uptake in PBMCs obtained from healthy donors to determine their potential effects on preserving T cell immune competence. PBMCs incubated up to 24 h with 1 µM of free DOX, FerOX or Myocet (DOX equivalents) displayed a time dependent internalization profile, as shown by MFI values of treated cells analyzed by flow-cytometry (Figure 4.5A). DOX-treated PBMC displayed the higher DOX uptake in comparison to those treated with the same amount of DOX nanoformulated in FerOX (0.8-fold less) or in Myocet (0.6-fold less) (Figure 4.5 A). In addition, upon internalization, DOX fluorescence was visible in the nucleus of Myocet and FerOX-treated PBMC only at the highest drug concentration of 10 µM, while in those cells treated with free DOX it is detectable even at the lowest concentration of DOX (i.e., 1 µM; Figure 4.5 B and 4.5 C). These data evidence that free DOX has potential higher toxicity for immune cells compared with DOX nanoformulations, suggesting that nanoformulation changed mechanisms and kinetics of DOX uptake. To date, comparing DOX uptake confocal microscopy images here obtained with PBMC treated with free DOX (Figure 4.5 B) with those already published in literature with HeLa and MDA-MB 468 BC cells, is clear that drug uptake in the same and this is consistent with an aspecific uptake

mechanism<sup>92</sup>. Indeed, when DOX is nanoformulated, drug uptake is reduced in cells with low TfR1 expression (i.e., PBMC), as expected in case of TfR1-mediated internalization. To date, it is well reported in literature an up-regulation of TfR1 expression upon CD4<sup>+</sup> and CD8<sup>+</sup> T-cells activation consequent to mitogen treatment<sup>154,155</sup>. Since the assessment of DOX-mediated proliferative impairment in PBMCs requires ConA mitogen stimulation, it would be crucial to characterize FerOX impact in proliferating PBMCs.

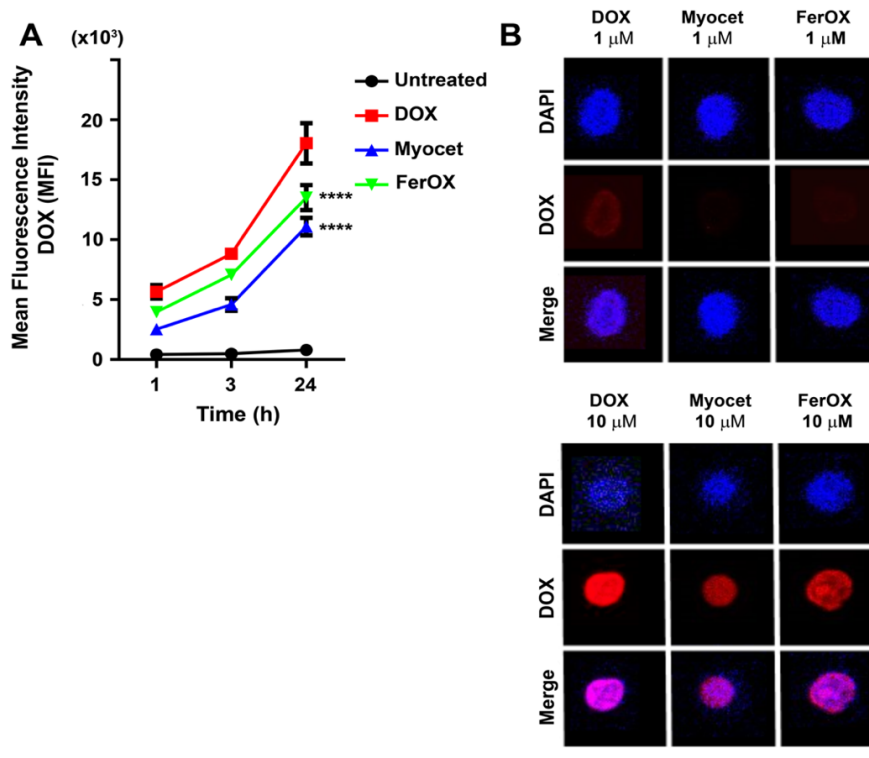


Figure 4.5 FerOX internalization in peripheral blood lymphocytes. A) PBMC collected from healthy donors and treated with DOX, FerOX and Myocet (1 μM) for 1, 3 and 24 h to assess drug uptake. Drug uptake has been monitored during time by FC measuring DOX mean fluorescence intensity in DOX<sup>+</sup> cells. Statistical significance vs DOX \*\*\*\* $p < 0.001$  (Two-way ANOVA). B) PBMC treated with DOX, FerOX and Myocet at 1 and 10 μM for 24 h and acquired by confocal microscopy. Nuclei were stained with DAPI (blue), while the DOX fluorescence signal was reported in red. Scale bar = 10 μm.

#### 4.4.6 FerOX displays a reduced uptake in T cells, sparing central memory, effector memory and naive subpopulations

To investigate whether a specific cell subtype exhibits a preferential uptake, the internalization of DOX was evaluated in various human T cell subpopulations following *in vitro* incubation with free-DOX, Myocet, or FerOX nanoformulations. We found that a population characterized by higher DOX uptake (DOX<sup>+</sup>) could be detected in total CD4<sup>+</sup> (Figure 4.6A) and in CD8<sup>+</sup> T cells (Figure 4.6B) when exposed to free-DOX for 24 h *in vitro*. In contrast, when human CD4<sup>+</sup> T cells were exposed to

Myocet or FerOX under the same conditions, we observed a significant 95% and 85% reduction in DOX<sup>+</sup> cells, respectively (Figure 4.6A). Similarly, CD8<sup>+</sup> T cells exhibited a reduction of 77% and 60% in DOX<sup>+</sup> cells when exposed to Myocet or FerOX, respectively (Figure 4.6B). Importantly, when looking at the differential DOX uptake across different T cells subpopulations, we found that both nanoformulations significantly limited DOX uptake in CD4<sup>+</sup> and CD8<sup>+</sup> CM, EM, TDE and Naïve subpopulations (Figure 4.6C-D). Overall, these findings may hold promise for preserving the competence of T cells to effectively mount an antitumor response.

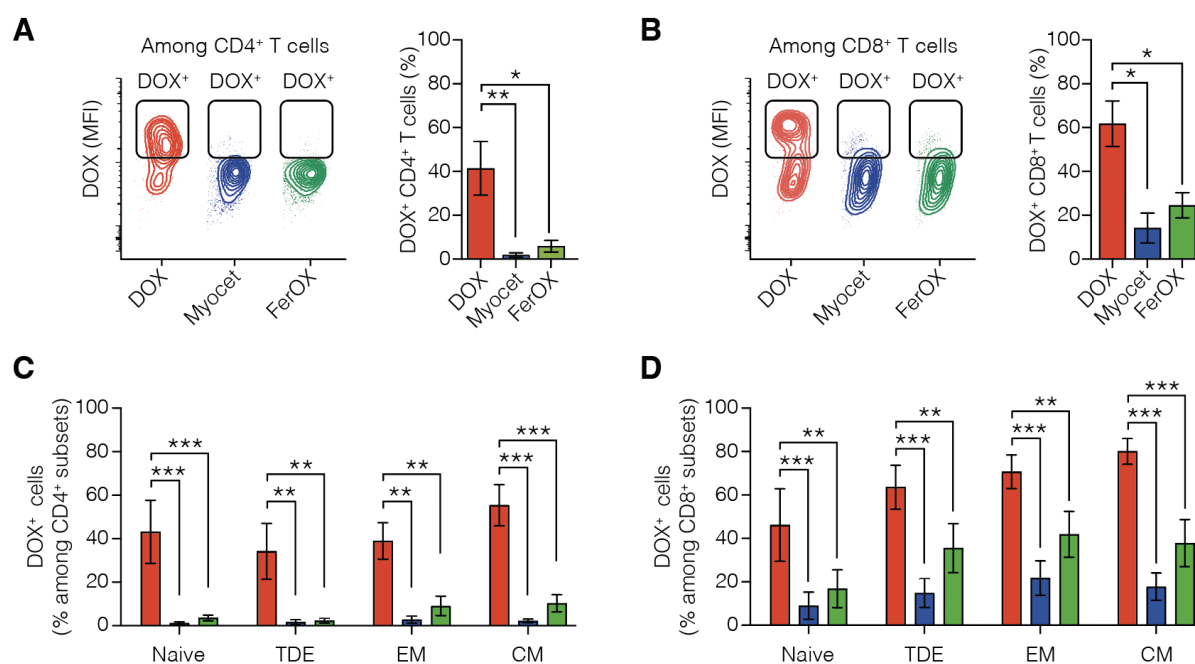


Figure 4.6 Comparison of DOX, Myocet and FerOX *in vitro* uptake of human peripheral T cells populations. A) Representative plots (left panel) and frequencies (right panel) of DOX<sup>+</sup> CD4<sup>+</sup> T cells analyzed in human PBMCs after 24 h incubation with 5  $\mu$ M of DOX, Myocet and FerOX. B) Representative plots (left panel) and frequencies (right panel) of DOX<sup>+</sup> CD8<sup>+</sup> T cells analyzed in human PBMCs after 24 h incubation with 5  $\mu$ M of DOX, Myocet and FerOX. Statistical significance vs DOX: \* $p$ <0.05; \*\* $p$ <0.01; \*\*\* $p$ <0.001 (One-way ANOVA). C) Frequencies of DOX<sup>+</sup> cells among Central Memory (CM), Naïve (CD197<sup>+</sup> CD45RA<sup>+</sup>), Terminally Differentiated Effector (TDE, CD197<sup>-</sup> CD45RA<sup>+</sup>) and Effector Memory (EM, CD197<sup>-</sup> CD45RA<sup>-</sup>) CD4<sup>+</sup> T cells. D) Frequencies of DOX<sup>+</sup> cells among CM, Naïve, TDE and EM CD8<sup>+</sup> T cells. Statistical significance vs DOX: \*\*  $p$ <0.01; \*\*\*  $p$ <0.001 (Two-way ANOVA).  $n = 4$  / group, data are represented as mean  $\pm$  SEM.

#### 4.4.7 FerOX suitability in cancer patients by preserving PBMC proliferative potential

To determine whether the reduced uptake of nanoformulated DOX in PBMCs can positively influence T cell mediated immune response, we conducted *in vitro* experiments where PBMCs from healthy donors were incubated with DOX, Myocet, or FerOX. These experimental conditions were designed to simulate neoadjuvant chemotherapy, with a DOX concentration of 5  $\mu$ M and a contact time of approximately 3 h. In contrast to untreated cells, PBMCs treated with DOX showed a significant

reduction in proliferation index (Figure 4.7 A). However, there was no statistically significant decrease in proliferation index observed in PBMCs treated with FerOX and Myocet, indicating that the lower drug uptake resulting from nanoformulated and targeted drug delivery can preserve immune competence and lead to a better antitumor immune response. Analyzing the proliferation of T cell populations upon treatment with free or nanoformulated DOX, we confirmed the toxic activity of free DOX against both CD4<sup>+</sup> and CD8<sup>+</sup> cells (Figure 4.7 B and 4.7 C). We observed that Myocet-treated cells also exhibited a decrease in proliferative potential in CD4<sup>+</sup> T cells, whereas the proliferation capability of CD4<sup>+</sup> T cells was unaffected in those treated with FerOX (Figure 4.7 B). In contrast, when considering only the CD8<sup>+</sup> population, the response of Myocet and FerOX-treated cells was consistent with that observed in the entire PBMC population (as shown in Figure 4.7 C). Both FerOX and Myocet formulations were found to be safe, with a statistically significant difference in the proliferation index observed between DOX and FerOX-treated cells (Figure 4.7 C).

Although these results suggest that DOX nanoformulations, particularly FerOX, are superior in preserving T cell immune competence and facilitating a better antitumor immune response, it is important to observe that these findings were obtained from healthy donors and may not accurately reflect the behavior of PBMCs in cancer patients. Therefore, we repeated similar experiments with PBMC collected from BC patients under DOX NAC to compare them with the *ex vivo* treatment with FerOX. We then compared the proliferation index of PBMCs obtained from BC patients immediately after the completion of the first cycle of DOX chemotherapy with those obtained from patients before the start of the first cycle of DOX chemotherapy. We also examined the effect of *ex vivo* treatment with DOX, Myocet, or FerOX on the proliferation index of PBMCs collected from the same patients. As expected, PBMCs collected from BC patients immediately after the end of the first cycle of DOX chemotherapy displayed an impairment of proliferative potential similar to that observed in PBMCs collected from BC patients before the start of the first cycle of DOX chemotherapy and treated *ex vivo* with DOX (Figure 4.7 D). The same behavior could be observed if we analyze only CD4<sup>+</sup> and CD8<sup>+</sup> populations (Figure 4.7 E and 4.7 F). Furthermore, PBMCs treated *ex vivo* with Myocet and FerOX demonstrated similar proliferation activity to untreated PBMCs obtained from BC patients. These results support the safety of these nanoformulations and their minimal negative effect on the adaptive antitumor immune response (Figure 4.7 D, 4.7 E, and 4.7 F).



These findings, coupled with the FerOX anticancer activity observed in BC-PDO, strongly highlights the promising potential of this nanoformulation and supports the need of conducting additional research to establish the suitability of FerOX for clinical applications.

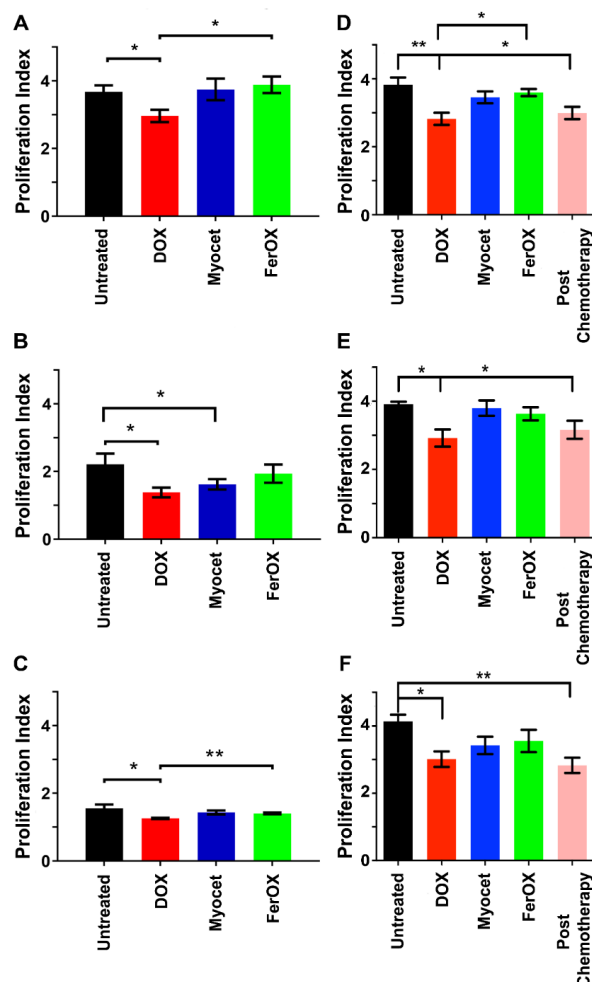


Figure 4.7 FerOX uptake preserves PBMC proliferation *in vitro* and *ex vivo*. A) Proliferation index of PBMC collected from healthy donors, labelled with CFSE 1µM and stimulated with ConA (5 µg/mL) after 3 h *in vitro* treatment with DOX, Myocet or FerOX 5 µM to simulate what occurs during the infusion time of DOX neoadjuvant chemotherapy NAC. Proliferation index was calculated with the software FlowJo (version 10). Statistical significance: \*  $p < 0.05$  (paired t-test). B) Proliferation index of CD4<sup>+</sup> T-cells collected from healthy donors, labelled with CFSE 1µM and stimulated with ConA (5 µg/mL) after 3 h *in vitro* treatment with DOX, Myocet or FerOX 5 µM. Statistical significance: \*  $p < 0.05$  (paired t-test). C) Proliferation index of CD8<sup>+</sup> T-cells collected from healthy donors, labelled with CFSE 1µM and stimulated with ConA (5 µg/mL) after 3 h *in vitro* treatment with DOX, Myocet or FerOX 5 µM. Statistical significance: \*  $p < 0.05$ ; \*\*  $p < 0.01$  (paired t-test). D) Proliferation index of PBMC collected from BC patients before and after DOX NAC, labelled with CFSE 1µM and stimulated with ConA (5 µg/mL). PBMC collected from BC patients before DOX NAC have been treated *in vitro* for 3 h with DOX, Myocet or FerOX 5 µM, to simulate chemotherapy. Statistical significance: \*  $p < 0.05$ ; \*\*  $p < 0.01$  (paired t-test). E) Proliferation index of CD4<sup>+</sup> T-cells collected from BC patients before and after DOX NAC, labelled with CFSE 1µM and stimulated with ConA (5 µg/mL). PBMC collected from BC patients before DOX NAC have been treated *in vitro* for 3 h with DOX, Myocet or FerOX 5 µM, in order to simulate chemotherapy. Statistical significance: \*  $p < 0.05$  (paired t-test). F) Proliferation index of CD8<sup>+</sup> T-cells collected from BC patients before and after DOX NAC, labelled with CFSE 1µM and stimulated with ConA (5 µg/mL). PBMC collected from BC patients before DOX NAC have been treated *in vitro* for 3 h with DOX, Myocet or FerOX 5 µM, in order to simulate chemotherapy. Statistical significance: \*  $p < 0.05$ ; \*\*  $p < 0.01$  (paired t-test).



## 4.5 Conclusions

Further to its direct cytotoxicity against highly proliferating cancers like BC, DOX has been recently demonstrated to also exert an immunostimulatory effect in several ways. However, the underlying mechanism of DOX on the sensitization of BC and the effect on the adaptative immune response has not yet been elucidated and deserves to be scrupulously investigated to decipher molecular determinants for complete immune-mediated tumor eradication.

This work, aimed at characterizing the interaction of DOX on primary human T cells in terms of uptake and proliferative potential, demonstrated a global proliferative impairment in PBMCs both from healthy donors and DOX treated BC patients. Of note, results confirmed that the higher negative impact of DOX is observed in the subset of CD8<sup>+</sup> cells, in line with what described in literature <sup>146,147</sup>.

Since the preservation of proliferative potential is crucial for the generation of an adaptive antitumor response in patients with BC, we evaluated the capability of alternative DOX based formulations. Thus, we assessed the potential effects on preserving T-cell immune competence of the DOX nanoformulation FerOX and Myocet. After confirming the capability of FerOX to mediate a specific tumor-targeted delivery of DOX in a panel of BC PDOs, we provided evidence about the reduced undesired uptake of DOX in PBMCs, meanwhile preserving their proliferative potential. In conclusion, FerOX was found to be particularly competitive in preserving T cells facilitating the development of a potential adaptative immune response in comparison with the free drug. In addition, these results complement the superiority in terms of tumor targeting of FerOX observed by our group in previous studies. Overall, this study offers novel understanding on the interaction between HFn-based nanotherapeutic and the immune system and supports the development of new nanoformulations for the immunomodulation of the tumor immune infiltrate and their significance for clinical translation in BC and other solid tumors treatments.

## 5. Study 3: Ferritin-Trastuzumab nanoconjugates: a strategy to vehicle Trastuzumab to the brain and tackle HER2-positive breast cancer brain metastasis

The results have been published as:

Marta Sevieri,<sup>1</sup> Serena Mazzucchelli,<sup>1</sup> Linda Barbieri,<sup>2</sup> Stefania Garbujo,<sup>2</sup> Stephana Carelli,<sup>3,4</sup> Arianna Bonizzi,<sup>5</sup> Federica Rey,<sup>3,4</sup> Camilla Recordati,<sup>6,7</sup> Matteo Recchia,<sup>6,7</sup> Raffaele Allevi,<sup>1</sup> Leopoldo Sitia,<sup>1</sup> Carlo Morasso,<sup>5</sup> Pietro Zerbi,<sup>8</sup> Davide Prospero,<sup>2</sup> Fabio Corsi<sup>1,5\*</sup>, Marta Truffi<sup>5\*</sup>

**Ferritin nanoconjugates guide trastuzumab brain delivery to promote an antitumor response in murine HER2+ breast cancer brain metastasis** <sup>156</sup>.

### 5.1 Aim of the study three

Starting from the idea that HFn can mediate drug delivery across the BBB both for encapsulated and surface conjugated drugs, this study aims to investigate the potential of HFn-based nanoconjugates to deliver the therapeutic antibody TZ to the brain and to exert an antitumor response. Indeed, one of the main unsolved clinical challenges in the treatment of HER2+ BC is represented by the onset of brain metastasis (BM). Even if the patient is able to achieve pCR after NAC with TZ, the risk of subsequent development of BM still remains high. This is mainly due to an inconsistent penetrance of TZ across the BBB, that prevents the prophylactic treatment of the brain during both NAC and adjuvant treatment with TZ. Therefore, the achievements of an effective prophylactic treatment towards HER2 positive BC BM onset is an unsolved clinical challenge. Despite efforts in the development of more permeable drugs, nowadays there are no recommended first-line treatments with demonstrated capability to prevent brain disease, and TZ remains the main therapeutic option in HER2 positive BC. Therefore, it is of utmost importance to develop novel strategies to prevent brain involvement in HER2 positive BC, especially using appropriate models to ensure the achievement of reliable preclinical data for a straightforward clinical translation.

In 2021, we conceived and produced a nanoconjugate based on the covalent conjugation of TZ to HFn (H-TZ)<sup>157</sup>. We demonstrated that H-TZ enhanced the trans-BBB delivery of TZ *in vitro*, preserving target specificity toward HER2+ BC cells<sup>154</sup>. In the present study, we aimed to test the as-designed nanoconjugate *in vivo*, by parenterally injecting H-TZ and evaluating its accumulation and functional activity in HER2 positive BC BM-bearing mice.

The novelty of the study is represented not only by the extremely promising results in terms of BM targeting and antitumor response, but also by the preclinical model used. To date, we established a mouse model of BC-derived BM, which combined specific molecular features of engineered BC cells, overexpressing human HER2 and the luciferase transgene, with a controlled intracranial implantation, to generate an *in vivo*-trackable BM sensitive to TZ. This model has the advantage to (i) overexpress the human HER2 protein thus displaying the specific ligand for TZ activity; (ii) be easily visualized *in vivo* by bio-luminescence imaging thanks to the stable expression of luciferase; (iii) more closely mimic the biological interactions occurring during metastatization between the BC cells derived from a primary tumor and the brain microenvironment.

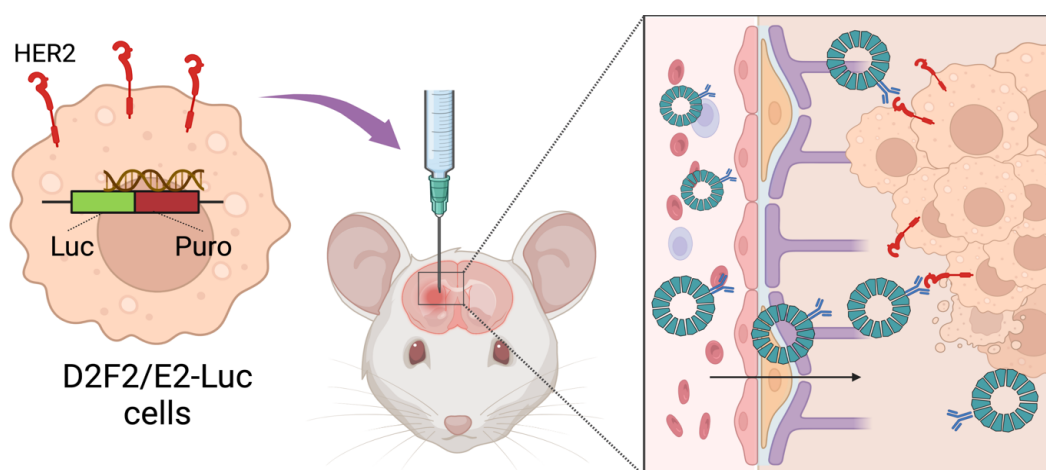


Figure 5.1 The graphical abstract represents the ability of HFn-based TZ nanoconjugates to vehicle TZ to the brain and tackle breast cancer brain metastasis in a murine model<sup>156</sup>.



Contents lists available at [ScienceDirect](https://www.sciencedirect.com)

Pharmacological Research

journal homepage: [www.elsevier.com/locate/yphrs](http://www.elsevier.com/locate/yphrs)



## Ferritin nanoconjugates guide trastuzumab brain delivery to promote an antitumor response in murine HER2 + breast cancer brain metastasis

Marta Sevieri <sup>a</sup>, Serena Mazzucchelli <sup>a</sup>, Linda Barbieri <sup>b</sup>, Stefania Garbujo <sup>b</sup>, Stephana Carelli <sup>c,d</sup>, Arianna Bonizzi <sup>e</sup>, Federica Rey <sup>c,d</sup>, Camilla Recordati <sup>f,g</sup>, Matteo Recchia <sup>f,g</sup>, Raffaele Allevi <sup>a</sup>, Leopoldo Sitia <sup>a</sup>, Carlo Morasso <sup>e</sup>, Pietro Zerbi <sup>h</sup>, Davide Prosperi <sup>b</sup>, Fabio Corsi <sup>a,e,\*</sup>, Marta Truffi <sup>e,\*\*,1</sup>

<sup>a</sup> Department of Biomedical and Clinical Sciences, Università degli Studi di Milano, via G.B. Grassi 74, 20157 Milan, Italy <sup>b</sup>

Department of Biotechnology and Biosciences, University of Milano-Bicocca, P.zza della Scienza 2, 20126 Milano, Italy

<sup>c</sup> Pediatric Clinical Research Center "Romeo ed Enrica Invernizzi", Department of Biomedical and Clinical Science, University of Milan, 20157 Milan, Italy <sup>d</sup> Center of Functional Genomics and Rare Diseases, Department of Pediatrics, Buzzi Children's Hospital, Milano, Italy <sup>e</sup> Istituti Clinici Scientifici Maugeri IRCCS, via Maugeri 4, 27100 Pavia, Italy

<sup>f</sup> Mouse and Animal Pathology Laboratory, Fondazione Unimi, viale Ortles 22/4, 20139 Milano, Italy

<sup>g</sup> Dipartimento di Medicina Veterinaria e Scienze Animali, Università di Milano, via dell'Anatomia Patologica, ASST Santi Paolo e Carlo, via Pio II, 3, Milano, Italy <sup>h</sup> Università 6, 26900 Lodi, Italy <sup>1</sup>

### ARTICLE INFO

#### Keywords:

Ferritin nanoparticle  
Trastuzumab  
Brain metastasis  
HER2 + breast cancer  
Drug delivery

### ABSTRACT

Brain metastasis (BM) represents a clinical challenge for patients with advanced HER2 + breast cancer (BC). The monoclonal anti-HER2 antibody trastuzumab (TZ) improves survival of BC patients, but it has low central nervous system penetration, being ineffective in treating BM. Previous studies showed that ferritin nanoparticles (HF<sub>n</sub>) may cross the blood brain barrier (BBB) through binding to the transferrin receptor 1 (TfR1). However, whether this has efficacy in promoting the trans-BBB delivery of TZ and combating BC BM was not studied yet. Here, we investigated the potential of HF<sub>n</sub> to drive TZ brain delivery and promote a targeted antitumor response in a murine model of BC BM established by stereotaxic injection of engineered BC cells overexpressing human HER2. HF<sub>n</sub> were covalently conjugated with TZ to obtain a nanoconjugate endowed with HER2 and TfR1 targeting specificity (H-TZ). H-TZ efficiently achieved TZ brain delivery upon intraperitoneal injection and triggered stable targeting of cancer cells. Treatment with H-TZ plus docetaxel significantly reduced tumor growth and shaped a protective brain microenvironment by engaging macrophage activation toward cancer cells. H-TZ-based treatment also avoided TZ-associated cardiotoxicity by preventing drug accumulation in the heart and did not induce any other major side effects when combined with docetaxel. These results provided in vivo demonstration of the pharmacological potential of H-TZ, able to tackle BC BM in combination with docetaxel. Indeed, upon systemic administration, the nanoconjugate guides TZ brain accumulation, reduces BM growth and limits side effects in off-target organs, thus showing promise for the management of HER2 + BC metastatic to the brain.

**Abbreviations:** ALT, alanine transaminase; AST, aspartate transaminase; BBB, blood-brain barrier; BC, breast cancer; BLI, bioluminescence imaging; BM, brain metastasis; BSA, bovine serum albumin; Dtx, docetaxel; EDTA, ethylenediaminetetraacetic acid; FFPE, formalin-fixed paraffin-embedded; GFAP, glial fibrillary acidic protein; HER2, human epidermal growth factor receptor 2; HF<sub>n</sub>, human ferritin; H-TZ, ferritin-trastuzumab nanoconjugate; Iba1, ionized calcium-binding adapter molecule 1; IL, interleukin; IP, intraperitoneal; Luc, luciferase; MFI, mean fluorescence intensity; OCT, optimal cutting temperature; PEG, polyethylene glycol; PBS, phosphate-buffered saline; PFA, paraformaldehyde; RT, room temperature; TEM, transmission electron microscopy; TfR1, transferrin receptor 1; TNF $\alpha$ , tumor necrosis factor alpha; TZ, trastuzumab.

\* Corresponding author at: Dipartimento di Scienze Biomediche e Cliniche, Università di Milano, via G.B. Grassi 74, 20157 Milano, Italy. <sup>1</sup> \*\*

Corresponding author.

E-mail addresses: [fabio.corsi@unimi.it](mailto:fabio.corsi@unimi.it), [fabio.corsi@icsmaugeri.it](mailto:fabio.corsi@icsmaugeri.it) (F. Corsi), [marta.truffi@icsmaugeri.it](mailto:marta.truffi@icsmaugeri.it) (M. Truffi). <sup>1</sup>

ORCID ID: 0000-0002-1095-4188 <https://doi.org/10.1016/j.phrs.2023.106934>

Received 23 May 2023; Received in revised form 31 August 2023; Accepted 18 September 2023

Available online 19 September 2023

1043-6618/© 2023 The Authors. Published by Elsevier Ltd. This is an open access article under the CC BY license (<http://creativecommons.org/licenses/by/4.0/>).

## 1. Introduction

Breast cancer (BC) overexpressing the human epidermal growth factor receptor 2 (HER2) represents 15–20% of breast malignancies and it is particularly prone to form distant metastases [1,2]. The advent of HER2-targeting agents has prolonged survival in patients with advanced disease, but the prevention and management of brain metastases (BM) still poses unique clinical challenges [3,4]. BM represents a catastrophic event that portends a poor prognosis and, once established, lack an effective cure. This is mainly due to an inconsistent penetrance of anti-HER2 therapies across the blood–brain barrier (BBB), a highly-selective filter that surveys the entry of substances to the brain and hinders drug efficacy in case of BM [5–7]. Despite efforts in the development of more permeable drugs, nowadays do not yet exist recommended first-line treatments with demonstrated capability to prevent brain recurrence, and trastuzumab (TZ) remains the first therapeutic option in HER2 + disease [8–10]. New generation of antibody-drug conjugates, which combine HER2-specific antibody backbone with a potent cytotoxic payload, has shown a reduction of metastases in advanced HER2 + BC. However, there was no decrease in the risk of BM as the first site of relapse [11,12]. Moreover, these potent drugs are associated with non-negligible toxicity and adverse events that raise questions on their use [13].

Based on these observations, it is of utmost importance to develop more effective and less toxic strategies to control, and ultimately prevent, brain involvement in HER2 + BC, especially using appropriate models to ensure the achievement of reliable preclinical data for a straightforward clinical translation.

Human Ferritin (HF<sub>n</sub>) is a versatile and biocompatible nanoparticle holding several advantages for cancer application [14–17]. Among many properties, HF<sub>n</sub> is able to cross the BBB exploiting the Transferrin Receptor 1 (TfR1), overexpressed in the BBB endothelium [18–20]. The trans-BBB permeability of HF<sub>n</sub> was successfully demonstrated both by our and other group research work by using a fluorescent tracer payload as a proof of principle or drugs loaded inside HF<sub>n</sub> cavity [21–23]. More recently, we demonstrated that HF<sub>n</sub> can bind brain endothelial cells in a dose-dependent manner and favour the trans-BBB crossing of curcuminoids through a BBB cellular model [24]. We also demonstrated the feasibility of HF<sub>n</sub> use as a vector for the trans-BBB delivery of high molecular weight compounds, such as therapeutic monoclonal antibodies [25]. Ferritin nanoconjugates based on the covalent conjugation of TZ on HF<sub>n</sub> surface (H-TZ) were designed to preserve both HER2-targeting specificity and the capability of HF<sub>n</sub> subunits to bind TfR1. As reported in a previous paper, as-designed H-TZ were able to translocate across a transwell BBB system *in vitro*, preserving their target specificity and antitumor activity toward HER2 + BC cells *in vitro* [25].

Aim of this study was to investigate the potential of H-TZ to enhance the trans-BBB permeation *in vivo*, and to promote targeted antitumor response for an effective brain protection. To this aim, we established a mouse experimental model of BC-derived BM, which combined specific molecular features of engineered BC cells, overexpressing the human HER2 and the luciferase transgene, with a controlled intracranial implantation, for the generation of *in vivo*-trackable BM sensitive to TZ. After model characterization, we assessed the capability of H-TZ to reach the brain tumor upon a systemic administration, and investigated the impact on tumor growth of

H-TZ combined with the cytotoxic drug docetaxel. As standard of care, a group of mice was administered with free TZ, equally dosed, combined with docetaxel. The effect of treatment on microglia was also analyzed as the brain microenvironment is an important mediator of effective antitumor response. Finally, we investigated side effects generally associated to chemotherapy based on anti-HER2 *plus* taxanes, to gain insights into potential toxicity triggered by H-TZ treatment.

## 2. Methods

### 2.1. Cell line

The murine breast tumor cell line D2F2/E2, stably expressing the human HER2 receptor, was originally obtained from prof. Wei Zen-Wei (Wayne University). Cells were transduced with RediFect Red-FLuc- Puro Lentiviral Particles (Perkin Elmer, Boston, MA, USA) following the manufacturer's instructions. The lentiviral particles carry the luciferase reporter transgene (Luc) fused with a selectable marker that confers resistance to the antibiotic puromycin. Transduced cells were selected by applying a selective medium containing puromycin (1 µg/mL). Then, selected puromycin resistant clones were expanded in culture to assay for expression of luciferase. D2F2/E2-Luc cells were maintained at 37 °C in a humidified atmosphere containing 5% CO<sub>2</sub> in high glucose Dulbecco's modified Eagle's medium (DMEM) supplemented with 2 mM L-glutamine, 10% fetal bovine serum (FBS), 1% non-essential amino acids, 1% penicillin/streptomycin, G418 (0.8 mg/mL) and puromycin (250 ng/mL). Cells were passaged at sub-confluence using trypsin/EDTA and amplified for 2 weeks before implant in mice. All cell culture reagents were purchased by Euroclone (Italy).

### 2.2. Murine model of breast cancer brain metastasis

Nude BALB/c female mice (6–8 weeks old) were purchased by Charles River Laboratories (Calco, Italy), group housed in IVC cages with free access to sterile food and water and allowed to acclimate for one week before tumor implant. Animals were handled in accordance with an experimental study approved by the Italian Ministry of Health (aut. N. 6/2017-PR). Mice were anesthetized using isoflurane and positioned in a stereotactic apparatus (2Biological Instruments). A linear skin incision was made over the bregma. Then, D2F2/E2-Luc cells (1 × 10<sup>5</sup>) were suspended in cold serum-free DMEM medium and injected into the mouse brain (4 µL total volume, speed rate 2 µL min<sup>-1</sup>) with a 10 µL Hamilton syringe under constant isoflurane anesthesia (1.5%). Stereotactic coordinates were 1 mm right from the bregma, 3 mm depth from the skull. After injection, the skin was closed with absorbable stitches, and tramadol (30 mg kg<sup>-1</sup>) was administered by intraperitoneal (IP) injection to relieve post-operative pain. Mice wellness was monitored daily, and tumor growth was followed by bio-luminescence imaging (BLI) at the specified time-points before euthanasia. BLI signals were acquired with the IVIS Lumina II imaging system (Perkin Elmer) 5 min after IP injection of D-luciferin (150 µg kg<sup>-1</sup>, Perkin Elmer) with an exposure time of 10 s. Images were quantified using regions of interest analysis of individual mice and the signal was expressed as total BLI Counts.

### 2.3. Preparation of H-TZ nanoconjugate



HF<sub>n</sub> nanoparticles were produced and purified as previously reported [26]. HF<sub>n</sub> were conjugated to the anti-HER2 mAb trastuzumab (TZ, Ogivri, Mylan) according to a protocol already described by our group to obtain a 1:1 HF<sub>n</sub>/TZ ratio per nanoparticle [25]. Briefly, A PEG-based heterobifunctional crosslinker (MW PEG ≈ 5000 Da), bearing one N-hydroxysuccinimidyl ester (NHS) and one maleimide (Mal) group, was used to anchor TZ on HF<sub>n</sub> in a two steps reaction. Next, reaction products were isolated by size exclusion chromatography (SEC-FPLC), which identifies distinct peaks for the protein complex and each unreacted species. The reaction product (H-TZ) was characterized by SDS-PAGE, western blot and dynamic light scattering analysis.

#### 2.4. *In vitro* cell-binding assays

D2F2/E2-Luc cells ( $5 \times 10^5$  cells/tube) were collected and incubated for 2 h at 4 °C with H-TZ (0.01, 0.1, 1, 10, 100 µg/mL) or with corresponding concentrations of free TZ diluted in PBS with 0.3% BSA. After incubation, cells were washed thrice with PBS and incubated for 15 min at RT with anti-human Alexa Fluor 488 secondary antibody (1 µg/tube, Invitrogen) diluted in PBS with 2% BSA, 2% goat serum. Labelled cells were washed thrice with PBS and analyzed in triplicates using CytoFLEX flow cytometer (Beckman Coulter). Acquisition was performed on 20,000 events, after gating on singlets viable cells. Untreated cells immunodecorated with the secondary antibody only were used to set the region of positivity.

For the kinetics assay, cells ( $5 \times 10^4$ ) were seeded in 12-well plates and incubated for 1 h at 37 °C with 100 µg/mL of H-TZ or corresponding concentration of TZ diluted in the culture medium. Cells were then washed thrice with PBS and provided with fresh culture medium. After 1, 4, 24, 48, 72 h cells were detached with Trypsin/EDTA, labelled with anti-human Alexa Fluor 488 secondary antibody and acquired with CytoFLEX as described above.

#### 2.5. Intracranial injection of TZ

To check efficacy of TZ in murine HER2 + BC BM, 1 µL of TZ (0.08 and 0.8 mg Kg<sup>-1</sup>, corresponding to 1% and 10% of the standard parenteral dose, respectively) was mixed with 3 µL of cell suspension ( $1 \times 10^5$  cells) and immediately injected intracranially using the stereotactic apparatus as described above. As control, 1 µL of saline was used instead of TZ in a group of mice. The BLI analysis was used to evaluate the therapeutic efficiency from 4 to 14 days after tumor cells were implanted. Mice were sacrificed at day 7 (n = 6/group) and day 14 (n = 6/group) post tumor implant, and brains were then dissected on ice and processed for analysis.

#### 2.6. Systemic therapy studies

For the systemic therapy study, mice were randomly assigned into four groups (n = 15 mice per group). The first group of mice was treated with a combination of TZ (Ogivri, Mylan) and docetaxel (Dtx, Accord) as a standard of care treatment scheduled for HER2 + metastatic BC. The second group received H-TZ (equivalent TZ dose) and Dtx. The third group received Dtx alone. A fourth group received saline solution as placebo treatment and was considered the untreated

control. Free TZ or nanoformulated H-TZ were administered IP at 8 mg kg<sup>-1</sup> every 3 days for 2 weeks, with the first injection performed 30 min before tumor implant and then repeated after 4, 7 and 11 days. Dtx (15 mg kg<sup>-1</sup>) was intravenously injected via the tail vein at 4 days post-tumor implant. The BLI analysis was used to evaluate the therapeutic efficiency of different treatments from 4 to 14 days after tumor cells were implanted. Nine mice per group were sacrificed at day 7 post-tumor implant, brains were dissected on ice and either fixed in paraformaldehyde (PFA, 4%) to assess TZ accumulation into the tumor (n = 3/group), or snap frozen to extract RNA (n = 3/group), or fixed in formalin to perform histological evaluations (n = 3/group). The remaining mice (n = 6 per group) were sacrificed at day 14 post-tumor implant to gain insights into the potential long term toxicity effects of H-TZ treatment.

#### 2.7. Tumor histology assessment

For histological examination, mice brains were fixed in 10% neutral buffered formalin for a minimum of 24 h. Three coronal sections (obtained by using Adult Mouse Brain Slicer Matrix BSMAS005-1, Zivic Instruments, USA) were routinely processed for paraffin embedding, sectioned at 4 µm thickness, stained with hematoxylin-eosin (H&E, Mayer's haematoxylin, cat. No. C0302; Eosin G, cat. No. C0362, Diapath, Martinengo, Bergamo, Italy), and evaluated under a light microscope.

At day 7 p.i. a semi-quantitative grading system considering distribution (1 = focal; 2 = multifocal) and size (0 = absent; 1 = diameter < 500 µm; 2 = 500 µm < diameter < 2000 µm; 3 = diameter > 2000 µm) of the tumors in different brain regions (parenchyma, sub-ventricular zone, ventricles, leptomeninges) was applied. A histology score (HS) was obtained multiplying the distribution by the size in each region in the three coronal sections. Then, for each animal, a total HS was calculated summing all the HS. Histopathological evaluation was performed in a blind fashion (i.e., without information about the treatment groups).

#### 2.8. Immunofluorescence and confocal microscopy

After PFA fixation, brain tissues were embedded in optimal cutting temperature (OCT) compound (VWR International) and frozen at -80 °C. Then, 10 µm-thick cryosections were cut, washed with PBS, permeabilized with 0.1% Triton X-100 for 5 min and incubated with blocking solution (2% goat serum, 2% BSA in PBS) for 2 h at RT. TZ was visualized in sections using anti-human Alexa Fluor 546 secondary antibody (Invitrogen) diluted 1:300 in blocking buffer and incubated overnight at 4 °C. HER2 was stained on adjacent slices with anti-HER2/ ErbB2 (29D8, Cell Signaling Technology, Inc.) diluted 1:200 in blocking buffer and incubated overnight at 4 °C as a primary detection antibody, and goat anti-rabbit Alexa Fluor 546 as secondary antibody (Invitrogen, 1:300) for 2 h at RT. Nuclei were stained with DAPI (0.1 µg/mL for 15 min) and slides were mounted in ProLong Gold antifade reagent (Invitrogen).

For astrocytes analysis, 4 µm-thick FFPE brain tissue slides were deparaffinized with Xylene (AppliChem), rehydrated with graded ethanol, equilibrated in PBS, blocked with 2% goat serum, 2% BSA, 0.01% Triton X-100 for 1 h at RT, incubated with anti-GFAP antibody (PRB-571 C, Covance) diluted 1:1000 in 1% goat serum, 1% BSA, 0.01% Triton X-100 for 3 h at RT and then stained with goat anti-rabbit Alexa Fluor 546 secondary antibody (Invitrogen, 1:300) overnight at 4 °C.

Nuclei were stained with DAPI (0.1  $\mu\text{g}/\text{mL}$  for 15 min) and slides were mounted in ProLong Gold antifade reagent (Invitrogen) for microscopic acquisition.

Images of the tumor were acquired at 20  $\times$  magnification with SP8 confocal microscope (Leica) using the Tile Scan function of the Leica LAS X Navigator. Quantification of the fluorescence signal was performed on single scans by measuring the integrated density in single-channel calibrated images and calculating the mean from multiple images. All analyzed images had the same area and resolution was of 512  $\times$  512 pixels. Analysis of captured images was performed using Fiji software.

graded alcohol series and coverslipped with resinous mounting medium.

Immunostained sections were digitalized using the NanoZoomer S60 Digital slide scanner (Hamamatsu, C13210-01) at the Unitech Nolimits (UNIMI, Milano) and images were captured by using the NDP.view2 Viewing software (Hamamatsu, U12388-01). The % of Iba1-positive immunostained area and the number of Iba1-positive cells were evaluated using the ImageJ analysis program (<https://imagej.nih.gov/ij/>) in 3 20x microscopic fields randomly selected within the tumor (intra-tumoral), and surrounding the tumor (peri-tumoral). A mean value of the microscopic fields was then calculated for each sample.

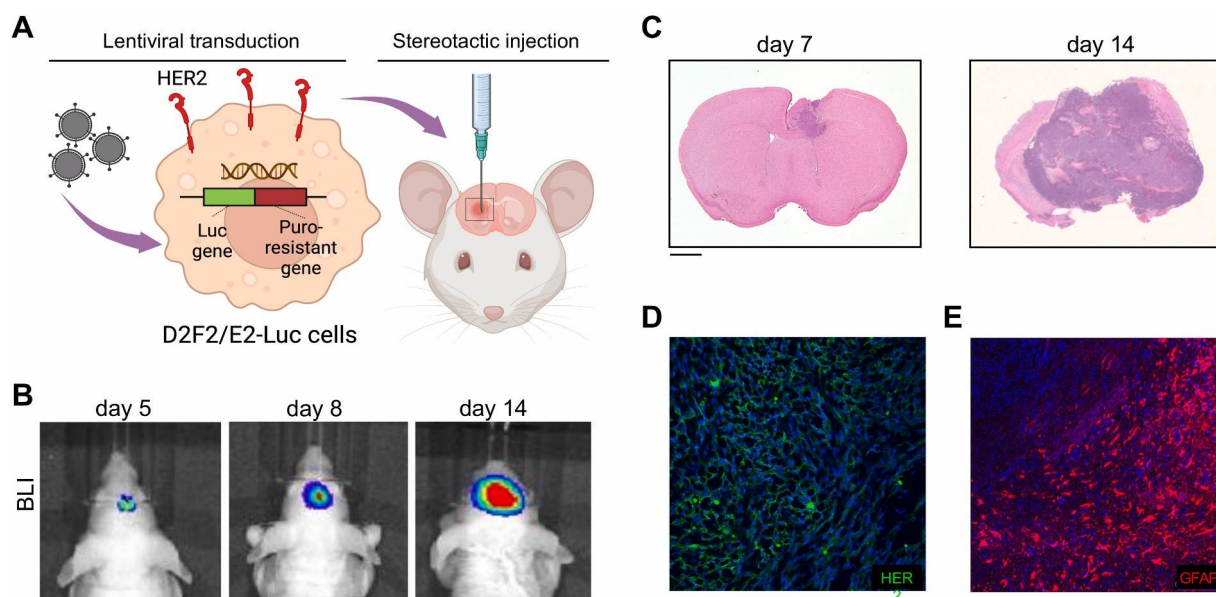


**Fig. 1.** Murine model of BC-derived HER2 + BM. A) D2F2/E2 BC cells expressing human HER2 were engineered by lentiviral transduction to express luciferase reporter and puromycin-resistant gene, and injected in the brain of mice by stereotactic injection. B) BLI was assessed in vivo at different time-points up to 14 days post-tumor implant. C) Hematoxylin and eosin staining was performed on FFPE sections from the frontotemporal part of brain dissected from mice at 7 and 14 days post-tumor implant. Scale bar = 1 mm. Expression of HER2 on tumor cells (D, green) and GFAP on reactive astrocytes (E, red) was assessed by immunofluorescence on brain tumor sections at 14 days post-implant. Nuclei were stained with DAPI (blue). Scale bar = 100  $\mu\text{m}$ .

## 2.9. Immunohistochemistry

For immunohistochemistry (IHC), brain sections underwent deparaffinization and heat induced epitope retrieval (HIER) in a water bath for 30 min at 100  $^{\circ}\text{C}$  (Dewax and HIER Buffer H, Thermo Scientific Lab Vision, cat. No. TA-999-DHBH). The slides were rinsed in PBS and placed in an autostainer (Lab Vision<sup>®</sup> Autostainer 480S-2D Thermo fischer scientific) after application of PapPen (Liquid Daido Sangyo Co., Ltd.). Endogenous peroxidase activity was blocked by incubating sections with 3%  $\text{H}_2\text{O}_2$  for 10 min. Slides were rinsed, incubated with PBS containing 10% normal goat serum for 30 min at room temperature to prevent nonspecific background staining and then incubated for 1 h at room temperature with the primary antibody rabbit polyclonal anti-Iba1 (marker of microglia, ab178846, Clone:EPR16588, Abcam). Sections were subsequently rinsed in PBS and incubated with a biotinylated secondary antibody (goat anti-rabbit, Vector Laboratories, USA, cat. No. BA-1000) and labelled by the avidin-biotin-peroxidase procedure (VECTASTAIN<sup>®</sup> Elite ABC-Peroxidase Kit Standard, Vector Laboratories, USA, cat. No. PK-6100). The immunoreaction was visualized with 3,3'-diaminobenzidine substrate (DAB, Peroxidase DAB Substrate Kit, Vector Laboratories, USA, cat. No. SK-4105). Sections were counterstained with Mayer's haematoxylin (Diapath, Martinengo (BG), Italy, cat. No. C0302), dehydrated in a

## 2.10. Cytokines analysis by qRT-PCR

Mice brains (n = 3/group) were dissected on ice and cut with a scalpel to obtain the frontotemporal part of the right hemisphere, corresponding to the brain fragment containing the tumor (1/4 of the total brain). Brain fragments were snap frozen in liquid nitrogen immediately after dissection and preserved at  $-80^{\circ}\text{C}$ . Total RNA was extracted using TRIZOL<sup>®</sup> reagent (Thermo Fisher Scientific) following the manufacturer's instructions, and then quantified with the Multiskan GO spectrophotometer (Thermo Fisher Scientific). RNA was retro-transcribed using the iScript<sup>™</sup> Reverse Transcription Supermix for RT-qPCR (Bio-Rad) kit following manufacturer's instructions. Real-Time PCR was performed with the CFX Connect Real-Time PCR System (Bio-Rad) using Optimum qPCR Master Mix with SYBR<sup>®</sup> Green (Genespin). The NCBI's Primer-BLAST tool was used to design primers. Gene expression was calculated using the  $2^{-\text{ddCt}}$  method. GAPDH was used as endogenous control. The list of primers used in this study is reported in [Supporting Table S1](#).

## 2.11. Heart lysate and western blot

## 2.13. Assessment of liver and kidneys functionality

Before euthanasia, blood was collected from the retro-orbital plexus of anesthetized mice and collected in EDTA-coated tubes (Becton Dickinson). Plasma was isolated by centrifugation at 2000g for 10 min at RT, followed by a second centrifugation at 2500g for 10 min at 4 °C to remove platelets. Liver and kidneys functionality were assessed after 2 weeks of treatment by measuring the plasma levels of AST and ALT (for liver), urea and creatinine (for kidneys). The following kits were used according to the manufacturer's protocols: QuantiChrom™ Urea Assay Kit, QuantiChrom™ Creatinine Assay Kit, EnzyChrom™ Aspartate Transaminase Assay Kit and EnzyChrom™ Alanine Transaminase Assay Kit (BioAssay Systems).

## 2.14. Statistical analysis

Statistical analysis was done using GraphPad Prism 6 (San Diego, CA, USA). The Student t-test or the non-parametric Mann Whitney test were used when comparing two groups in case of normal and non-normal distribution of the data, respectively. The Kruskal-Wallis test followed by Dunnett's multiple comparison's tests was applied when comparing more than two groups. Statistical significance was set at p-value < 0.05.

Hearts were dissected from treated mice (n = 3/group) at day 14 post tumor implant, snap frozen in liquid nitrogen and stored at - 80 °C until usage. Frozen tissues were homogenized in water (10% w/v), lysed for 30 min at 4 °C in 20 mM Tris HCl pH 7.6, 150 mM NaCl, 1 mM EDTA, 1% Triton X-100, 1% glycerol, 1 mM Na<sub>3</sub>VO<sub>4</sub>, 10 mM NaF, Protease Inhibitor Cocktail, 1 mM PMSF, and centrifuged to discard cell debris. Protein content was determined by Bradford assay. A total of 35 µg of lysate was loaded on SDS-PAGE (12% acrylamide) and transferred onto PVDF membrane (Sigma-Aldrich). Membranes were blocked in TBS supplemented with 5% nonfat dry milk and 0.1% Tween 20 (Sigma- Aldrich) for 1 h and then incubated overnight at 4 °C with goat anti- human antibody conjugated with horseradish peroxidase (#GTX26759, Tebu-bio) diluted 1:2000 in TBS with 0.1% Tween 20. Vinculin was used as loading control protein. Chemiluminescence reaction was developed with Clarity Western ECL Substrate (Biorad) and images were acquired with the Chemidoc System (Biorad).

## 2.12. Transmission electron microscopy (TEM)

From 3 mice/group, heart tissue was excised after the sacrifice and fixed in 2.5% glutaraldehyde in 0.1 M phosphate buffer, pH 7.2 at 4 °C. After rinsing with PBS, specimens were post-fixed in 1.5% osmium tetroxide for 2 h, dehydrated by 50%, 70%, 90%, and 100% EtOH and embedded in epoxy resin (PolyBed 812 Polysciences Inc.). Ultrathin sections were cut with an ultramicrotome (Ultracut E (Reichert-Jung)), stained with uranyl acetate and lead citrate and examined by TEM (Tecnai Spirit, FEI). Mitochondria quantification and mitochondria morphometric measurements were performed using ImageJ software as previously described [27].

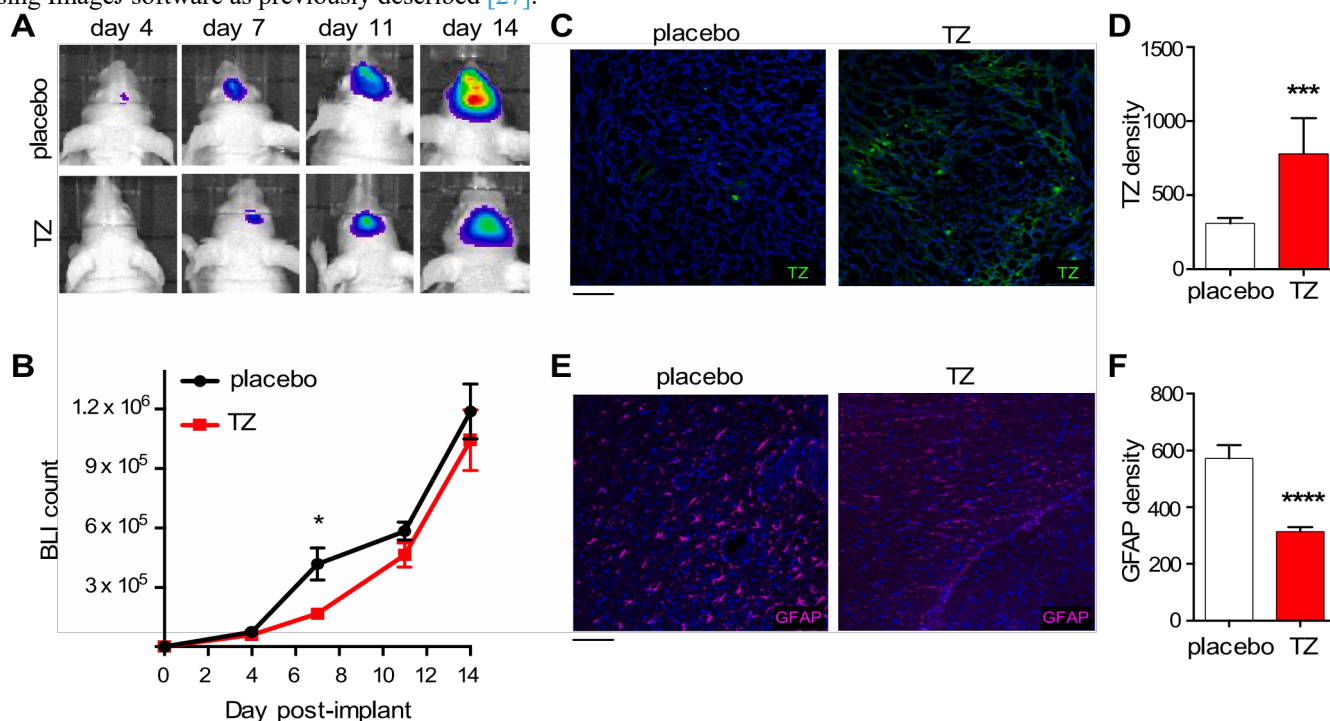


**Fig. 2.** Antitumor effect of TZ injected intracranially. A) In vivo bio-luminescence of tumors treated with placebo or with intracranial TZ at different time-points post- tumor implant. B) Mean tumor growth curves were drafted based on the BLI counts of TZ-treated (red) and untreated (black) mice, measured at 4, 7, 11 and 14 days post-tumor implant. Data are means ± SEM (n = 6/group). \*p = 0.011 unpaired t-test. Brains were dissected at day 7 post-tumor implant and tissue sections were stained with anti-human secondary antibody to visualize TZ (C) or with anti-GFAP antibody to analyze reactive astrocytes (E). Nuclei were stained with DAPI (blue). Scale bar = 100 µm. D) Mean TZ signal intensity was quantified on single-channel images taken within the tumor of 3 mice per group; at least 3 fields of view, all with the same area, were analyzed per each tumor. Data are means ± SEM. \*\*\*p = 0.0003 Mann Whitney test. F) Mean GFAP signal intensity was quantified on single- channel images taken in the peri-tumoral region of 2 mice per group; at least 10 fields of view, all with the same area, were analyzed per each tumor. Data are means ± SEM. \*\*\*\*p < 0.0001 Mann Whitney test.



### 3. Results and Discussion

#### 3.1. Experimental model of BC-derived BM

In order to study the potential of H-TZ nanoconjugates to promote TZ brain delivery *in vivo*, we first set up a suitable experimental model of BC-derived BM. We took advantage of the murine BC cell line D2F2/E2, which overexpressed human HER2 and has been previously used by us for therapeutic studies involving TZ [27]. Before implant in mice, the cells were engineered by transduction with RediFect lentiviral particles to make them express the luciferase transgene (Luc) fused to the puromycin resistance gene as a selection marker. Stable clones were selected for resistance to puromycin and stability of bioluminescent signal, and then intracranially injected via stereotactic technique to generate an orthotopic model of brain tumor derived from HER2 + BC (Fig. 1A). This model has the advantages to (i) overexpress the human HER2 protein thus displaying the specific ligand for TZ anchoring; (ii) be easily visualized *in vivo* by bio-luminescence imaging (BLI) thanks to the stable Luc expression; (iii) more closely mimic the biological interactions between the tumor and the brain

microenvironment since the tumor cells originate from the same species of the host.

After tumor implant, the BLI analysis revealed engraftment of the cells and rapid tumor growth in the brain of mice between 4 and 14 days post-injection (Fig. 1B). Tumor histology, assessed at 7 and 14 days post-injection, showed that the tumor expanded around the injection site and localized in the frontotemporal part of the right hemisphere invading the brain parenchyma (Fig. 1C). HER2 expression was clearly detected by immunofluorescence on the membrane of tumor cells grown for 2 weeks in the mouse brain (Fig. 1D). Images with higher magnification displaying in detail the localization of HER2 have been included in the Supporting Information (Fig. S1). The tumor also induced alteration in the brain microenvironment, triggering the formation of a glial reaction around the boundaries of tumor mass. Staining for GFAP identified a multitude of reactive astrocytes in the brain parenchyma surrounding the tumor (Fig. 1E). Images with higher magnification displaying in detail the localization of GFAP are reported in the Supporting Information (Fig. S2). GFAP overexpression is typical of the profound remodeling and shaping of astrocytes in certain pathological conditions in which homeostasis has been compromised [28,29]. Reactive

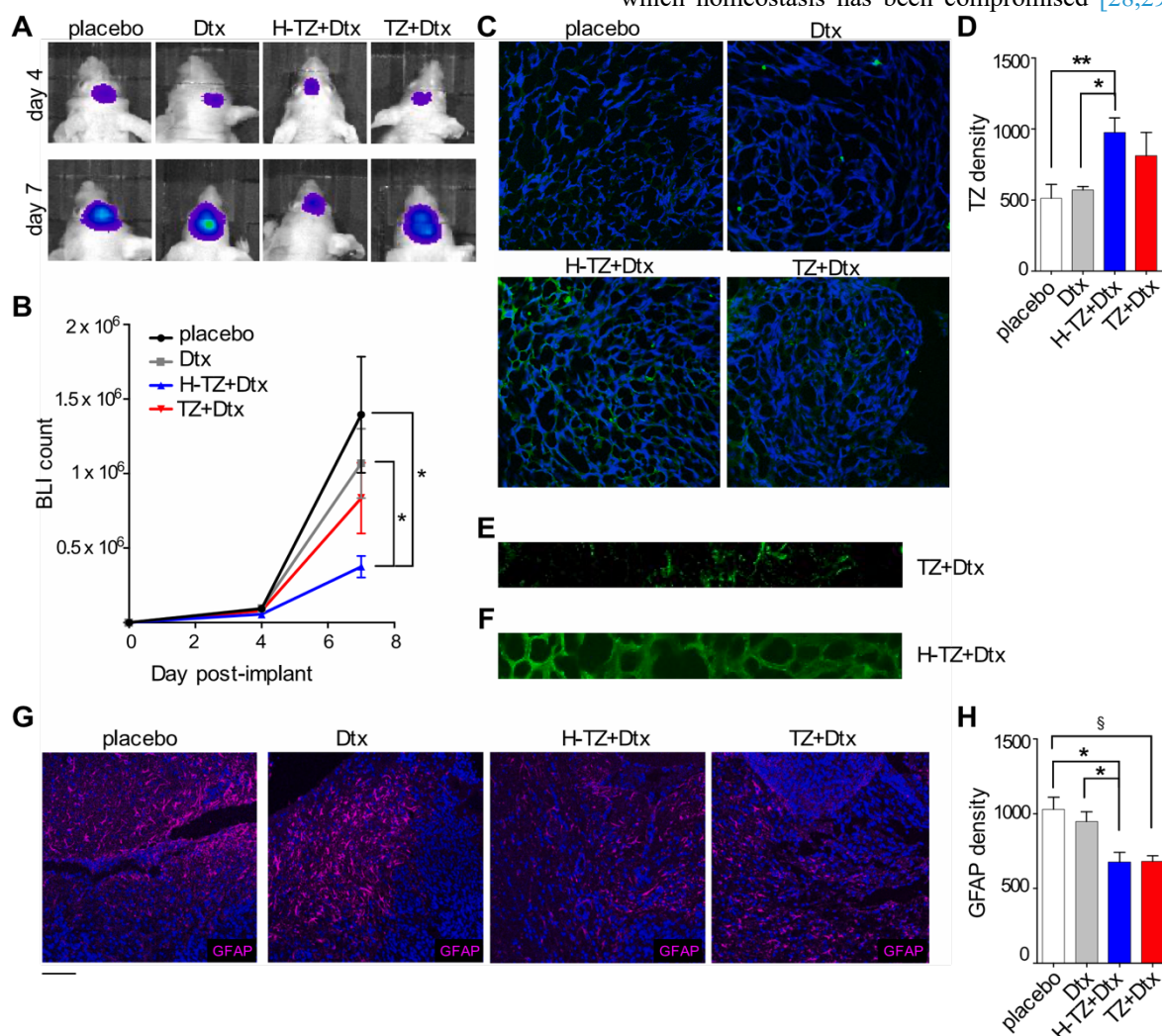


**Fig. 3.** Systemic treatment with free TZ or H-TZ in combination with Dtx. A) *In vivo* bio-luminescence of tumors treated with placebo, Dtx, H-TZ+Dtx or TZ+Dtx at 4 and 7 days post-tumor implant. B) Mean tumor growth curves were drafted based on the BLI counts of untreated mice (black) or mice treated with Dtx (grey), H-TZ+Dtx (blue), TZ+Dtx (red). Data are means  $\pm$  SEM ( $n = 15$ /group). \* $p = 0.01$  unpaired t-test. C) Brains were dissected at day 7 and stained with anti-human secondary antibody to visualize TZ (green). Nuclei were stained with DAPI (blue). D) Mean TZ signal intensity was quantified on single-channel images taken within the tumor of 2 mice per group; at least 3 fields of view, all with the same area, were analyzed per each tumor. Data are means  $\pm$  SEM. \* $p = 0.016$ ; \*\* $p = 0.006$  Kruskal Wallis test. E-F) High magnification of single channel images from representative tumors treated with H-TZ+Dtx (E) or TZ+Dtx (F). G) Immunofluorescence analysis of GFAP (magenta) on brain tissue slices at day 7. Nuclei were stained with DAPI (blue). Scale bar = 100  $\mu$ m. H) Mean GFAP signal intensity was quantified on single-channel images taken in the peri-tumoral region of 2 mice per group; at least 7 fields of view, all with the same area, were analyzed per each tumor. Data are means  $\pm$  SEM. \* $p = 0.008$ ; § $p = 0.006$  Kruskal Wallis test.

astrocytes have been extensively described also in the context of BC BM [30, 31]. They are activated by the tumor and in turn play a prominent role in promoting the growth of cancer cells by paracrine cytokine signaling [32–34]. Being important players in BM formation, reactive astrocytes represented a key step of characterization of our experimental model, further supporting how it recapitulates the physiopathological interplay between the tumor and the brain microenvironment.

### 3.2. Sensitivity to TZ

To prove whether the experimental model of BC-derived BM was sensitive to TZ, we performed a pilot study by injecting a small dose of TZ intracranially, simultaneously to the inoculation of tumor cells. In this setup TZ was locally administered, so no issue was imposed regarding BBB permeability, and the direct sensitivity of the tumor to TZ could be analyzed. To choose an appropriate dosage, we reasoned that only a very small amount of a drug normally administered via parenteral

injection can reach the brain [35]; therefore, we tested two doses of TZ corresponding to 10% and 1% of the dose that is recommended for therapeutic purpose in mice, i.e. 0.8 and 0.08 mg Kg<sup>-1</sup>, respectively. Results from a pilot study demonstrated that both dosages significantly slowed down tumor growth to a similar extent (see [Supporting Fig. S3](#)), hence we chose the lowest effective dose for the further phase of the study. TZ administration was performed through a stereotactic injection together with the tumor cells, to ensure that the drug came into contact with its target. After 4, 7, 11 and 14 days post-injection, the proliferation of viable tumor cells was monitored in vivo through BLI, thanks to stable expression of Luc ([Fig. 2A](#)). Tumors treated with 0.08 mg Kg<sup>-1</sup> of TZ showed a significant reduction of growth at 7 days post-treatment as compared to untreated tumors ( $p = 0.011$ , [Fig. 2B](#)).

To investigate the effects of TZ at a cellular level, mouse brains were dissected at day 7 and analyzed by immunofluorescence. The analysis allowed to detect the presence of TZ bound to tumor cells in the group of TZ-treated mice ([Fig. 2C-D](#)). TZ treatment also triggered a reduced astrocytic reaction in the brain parenchyma, as a consequence of the reduced tumor growth ([Fig. 2E](#)). Images with higher magnification are included in the [Supporting Information](#) (Figs. S4–S5). While GFAP overexpression was observed on astrocytes in the placebo group, a lower intensity of GFAP was measured in TZ-treated brains, as shown by quantitative image analysis on brain sections ([Fig. 2F](#)). These data proved sensitivity of the model to TZ, and indicated a 7-day time window to detect drug efficacy on tumor progression. At 11 days post-treatment, the aggressiveness of the tumor overcame the pharmacological effect of the drug and the tumor started growing again, requiring the ethical sacrifice of the animals at day 14 in both placebo and TZ groups ([Fig. 2B](#)). This observation confirmed the aggressiveness of BM and underlined the need to intervene early in order to achieve pharmacological efficacy.

### 3.3. H-TZ brain delivery and antitumor activity

Considering that local intracranial administration of drugs is extremely invasive and often not easily translatable to the clinic, especially in the case of many brain injuries localized in different areas of the brain, we conceived a bio-nanoconjugate suitable for the active delivery of TZ across the BBB via a

systemic administration, thus avoiding intracranial injection. The nanoconjugate was designed to achieve covalent conjugation of TZ antibody on the surface of HFN nanoparticles through a heterobifunctional PEG linker. The nanoconjugate's features, including particle size and morphology, were previously published [25] and reported in [Supporting Information](#) ([Fig. S6](#)). Upon conjugation, the antibody was readily accessible for HER2 targeting. At the same time, HFN maintained its natural capability to bind TfR1, a receptor overexpressed on many solid tumors and on the BBB endothelium. The capability of H-TZ to successfully cross the BBB preserving its targeted specificity and antitumor activity toward HER2 + BC cells was proved in vitro and reported in a previously published paper [25]. Here, we decided to challenge it in vivo, assessing the brain distribution of nanoformulated TZ vs. free TZ upon systemic IP administration in a murine model of BM.

This experimental design reproduced a first-line treatment used in clinics for HER2 + metastatic BC, based on anti-HER2 *plus* a taxane [36, 37]. Since in clinical practice TZ is never used as a single agent but always administered in combination with cytotoxic drugs, we decided to combine it with docetaxel (Dtx), administered 4 days post-tumor implant. Moreover, it allowed to simultaneously study brain distribution and therapeutic performance of the nanodrug. Given that the described therapeutic scheduling never involves the administration of TZ alone, by respecting the principle of reduction for animal welfare, we did not consider it necessary to include a group treated with H-TZ only. Animals were sacrificed 7 days post-implant to explore drug efficacy in a relevant therapeutic window.

Results obtained by in vivo BLI revealed that H-TZ+Dtx treatment induced a significant reduction of the tumor growth 7 days post-tumor implant as compared to both placebo ( $p = 0.01$ ) and mice treated with Dtx alone ( $p = 0.01$ , [Fig. 3A-B](#)). By contrast, mice treated with free TZ+Dtx did not achieve a statistically significant effect on the tumor growth ( $p = 0.21$  vs. placebo;  $p = 0.49$  vs. Dtx), confirming inefficacy of traditional chemotherapy toward BM. Immunofluorescence on brain tumor sections demonstrated a clear and bright signal corresponding to TZ in the brain of mice treated with H-TZ+Dtx ([Fig. 3C](#)). Images with higher magnification are included in the [Supporting Information](#) ([Fig. S7](#)). Quantification of the signal intensity further confirmed that H-TZ reached the brain and successfully accumulated in the tumor ( $p = 0.006$  vs. placebo;  $p = 0.016$  vs. Dtx) to a greater extent than free TZ did ( $p = 0.27$  vs. placebo;  $p = 0.20$  vs. Dtx) ([Fig. 3D](#)). Some TZ was retrieved also in the brain of mice treated with the free standard formulation TZ+Dtx. However, free TZ was detected as a weak pinpoint signal on very few cells only, as observed in the high magnification image ([Fig. 3E](#)). In case of H-TZ+Dtx, instead, the signal appeared uniformly distributed on the membrane of cancer cells ([Fig. 3F](#)), suggesting a more stable targeting of HER2 + tumor cells by the nanoformulation vs. free TZ.

Immunofluorescence analysis also revealed that treatment with H-TZ+Dtx triggered a reduced astrocytic reaction in the brain parenchyma, as indicated by analysis of GFAP marker ([Fig. 3G](#)). For magnified images, refer to the [Supporting Information](#) ([Fig. S8](#)).

Signal quantification confirmed that tumors treated with H-TZ+Dtx were associated to reduced GFAP expression as compared to placebo and Dtx ( $p = 0.008$ ). Also, in TZ+Dtx

group a reduced density of GFAP staining was observed on astrocytes with respect to placebo ( $p = 0.006$ ), but not with respect to Dtx alone (Fig. 3H), further demonstrating a limited contribution of free TZ in shaping an antitumor response.

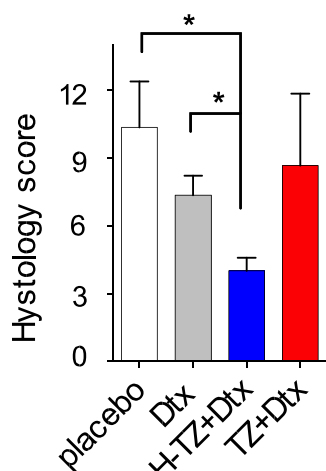


**Fig. 4.** Histological assessment in H&E-stained brain sections at 7 days post-implant. A total histology score was obtained by semi-quantitative grading system in different treatment groups. Data are means  $\pm$  SEM ( $n = 3$ /group). \* $p = 0.04$  one-tail Mann Whitney test.

Then, we assessed the histopathological features of the brain tumor by performing H&E staining on multiple sequential brain

sections. A pathologist, blinded to the treatment conditions of each animal, analyzed the brain slides to evaluate tumor histology. The results showed that the lesions recovered in the brain of mice treated with H- TZ+Dtx were reduced as compared to placebo and Dtx groups ( $p = 0.04$ , Fig. 4). Instead, the total histology score in TZ+Dtx group was not significantly different ( $p = 0.35$  vs. placebo and Dtx), confirming inefficacy of standard free drug administered systemically in the context of BM.

Overall, these data indicated a relevant contribution of H-TZ in driving TZ brain accumulation and targeting of cancer cells. Moreover, they showed that treatment with H-TZ+Dtx shaped a less aggressive and slower tumor progression, when administered systemically in the early phase of BM formation.

#### 3.4. Microglia recruitment and effect on neuroinflammation

Highly malignant brain tumors are characterized by large numbers of microglia/macrophages that influence cancer progression, being able to suppress or support the malignancy depending on their activation and polarization state [38,39]. In this study we investigated whether H-TZ+Dtx treatment had an impact on the density and distribution of Iba1, a marker of microglia/macrophages. Iba1-positive area was found increased in the peri-tumoral regions of mice treated with H-TZ+Dtx (Fig. 5A), while the number of Iba1-positive cells remained similar. Quantitative analysis of Iba1 immunostaining is shown in Supporting Table S2. By correlation analysis between Iba1 positivity and the total histology score in matched

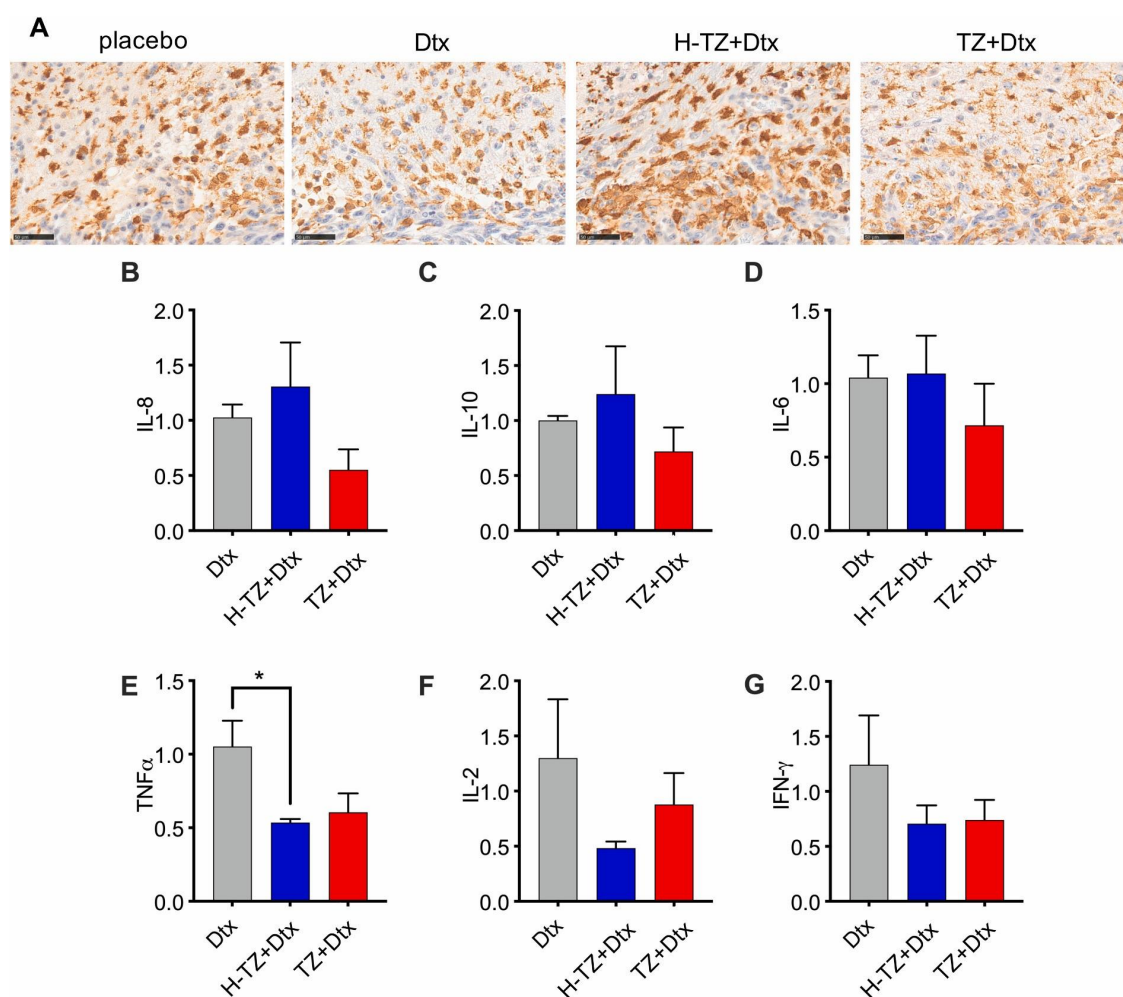


**Fig. 5.** Investigation of pro- and anti-inflammatory biomarker in mouse brains. A) Immunohistochemistry of Iba1 (brown signal) in the peri-tumoral region. Scale bar = 50  $\mu$ m. B-E) Real Time qPCR was performed on brain tumor specimens to measure expression of IL-8 (B), IL-10 (C), IL-6 (D), TNF $\alpha$  (E), IL-2 (F) and IFN- $\gamma$  (G) in the treatment groups. Results are expressed as RNA fold change. Dtx group was used for normalization. Data are means  $\pm$  SEM, each animal was analyzed in duplicate ( $n = 6$ /group).



animals, we observed that reduced development tumor was associated with an increase in the Iba1-positive area ( $r = -0.85$ ,  $p = 0.004$ ). Therefore, enhanced efficacy of the H-TZ+Dtx treatment was strongly associated with increased activation of macrophages around the tumor. This is likely due to a mechanism mediated by the interaction between macrophage receptors and antibodies bound to the cells. Once engaged by the antibody, activated macrophages trigger an antibody-dependent cancer cell killing, contributing to the antitumor response [40,41]. We thus hypothesized that, by guiding TZ brain accumulation, H-TZ not only allowed direct interaction with HER2 signaling, but also triggered a sustained activation of macrophages toward the cancer cells to shape a protective microenvironment against the tumor.

To further explore the impact of the treatment on the brain microenvironment, we measured the expression of cytokines, important mediators of neuroinflammation. Brains treated with H-TZ+Dtx were compared with those treated with Dtx alone or with the combination TZ+Dtx. Protective cytokines, like IL-8 and IL-10, were analyzed because it has been shown that they can be released by macrophages actively engaged in antibody-dependent cancer cell killing [42,43]. Their expression in brain tissues showed a trend toward increase in H-TZ+Dtx group as compared to TZ+Dtx group (Fig. 5B-C). Despite this was only

the expression of some proinflammatory cytokines, hence these results may correspond to the increase of IL-10 found in H-TZ+Dtx group. TNF $\alpha$  decrease is particularly interesting considering that this cytokine can be a double edge sword in cancer pathology, and its decrease was shown to enhance therapeutic efficacy [44,45]. Moreover, IFN- $\gamma$  was recently found to promote metastatic lesions in the brain, suggesting that its decrease could indicate an efficacy of therapy.

### 3.5. H-TZ anchoring to target tumor cells

Given the higher antitumor response achieved by H-TZ+Dtx treatment as compared to free TZ+Dtx, we hypothesized that the nanoconjugate, endowed with a double specificity for HER2 and Tfr1, could promote a more stable anchoring to the target tumor cells, therefore conditioning the tumor more extensively. To test this hypothesis, we analyzed the performance of H-TZ in a binding assay with D2F2/E2-Luc cells in vitro. Equal concentrations of nanoformulated or free TZ were incubated for 2 h at 4 °C with the cells and then analyzed by flow cytometry to visualize TZ bound on the cells. Both H-TZ and TZ were able to efficiently bind the cells in a dose-dependent manner, with more than 99% of the cells found positive at a drug concentration as low as 1  $\mu\text{g}/\text{mL}$  (Fig. 6A). By increasing the

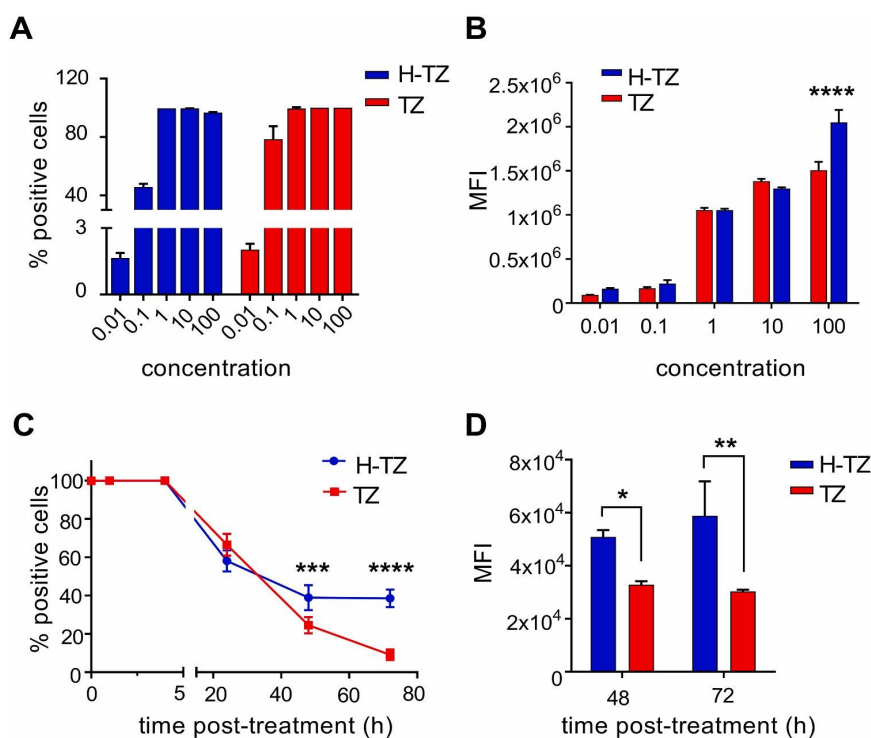


**Fig. 6.** In vitro cell binding assay. A) Binding of H-TZ and TZ incubated at 0.01, 0.1, 1, 10, 100  $\mu\text{g}/\text{mL}$  with tumor cells. B) Mean fluorescence intensity (MFI) of H-TZ or TZ bound to the cells. \* \* \* \*  $p = 0.005$  unpaired t-test. C) Persistence of H-TZ and TZ on the cells after 1, 4, 24, 48, 72 h post-treatment. Statistics by 2-way ANOVA. D) MFI of H-TZ or TZ bound to the cells after 48 and 72 h post-treatment. Statistics by 2-way ANOVA. All data are means  $\pm$  SD ( $n = 3$ ).

a trend with no statistical significance, the increased expression of IL-8 and IL-10 could be associated to the enhanced Iba1 positivity observed by immunohistochemistry, and further supported the antitumor activity of H-TZ in the brain. The expression of the IL-6 proinflammatory cytokine remained unchanged (Fig. 5D). We decided to investigate the expression of other proinflammatory cytokines (TNF $\alpha$ , IL-2 and IFN- $\gamma$ ) highlighting relevant differences. We observed a significant decrease in TNF $\alpha$  expression in H-TZ+Dtx group (Fig. 5E), along with the decrease in IL-2 (Fig. 5F) and IFN- $\gamma$  (Fig. 5G) in the same condition. Indeed, IL-10 was found to downregulate

dose, the mean fluorescence intensity (MFI) of the positive events increased, meaning that more H-TZ or TZ molecules attached to the same cell (Fig. 6B). At 100  $\mu\text{g}/\text{mL}$ , a higher MFI was observed for H-TZ as compared to free TZ ( $p = 0.005$ ). This result likely suggests advantage of the nanoconjugate, which can overcome the saturation of single HER2 target by engaging Tfr1 in the binding, thus increasing the upper limit of molecules per cell. Instead, the MFI for free TZ did not increase further between 10 and 100  $\mu\text{g}/\text{mL}$ , indicating that even increasing the drug dosage no more receptors could be engaged in binding.

Then we performed a kinetic assay by incubating the cells with an equal concentration of H-TZ or free TZ and measuring for how long they persist on the cell surface (Fig. 6C). The percentage of TZ-positive cells was maintained high after 1 and 4 h, then decreased down to 24.6% and 9.1% at 48 and 72 h, respectively. In the case of H-TZ, the percentage of positive cells also decreased over time, but a significantly higher percentage of cells, i.e. 38.9% and 38.5%, was still positive after 48 h and 72 h, respectively. To further document the longer on-cell persistence of H-TZ over free TZ, we analyzed the MFI of the events collected at 48 and 72 h. We found that MFI related to H-TZ was significantly higher than that of TZ (Fig. 6D), suggesting that at the indicated time-points there were on average more H-TZ particles exposed on the cells as compared to TZ.

These data demonstrated that H-TZ may trigger a more stable and lasting anchoring to the cancer cells as compared to free TZ, thus extending the residence time and the drug load at the target site. This *in vitro* observation further supported what was found *in vivo*, i.e. a stronger signal of H-TZ stably and uniformly distributed on cancer cells than free TZ (Fig. 3D). Moreover, it suggested that the advantage of H-TZ nanoconjugate may not only rely on active HF<sub>n</sub>-mediated trans-BBB delivery of TZ, but also on the persistence of TZ anchored to the tumor cells, further prolonging its pharmacological efficacy.

### 3.6. H-TZ do not induce cardiotoxicity and relevant off-target effects

Once analyzed the therapeutic effect, we explored whether H-TZ could be associated with long-term systemic toxic effects. To this aim we scheduled a complete therapeutic cycle, by repeating the IP injection of H-TZ twice weekly for 2 weeks, and combining it with a single intravenous injection of Dtx. As control, free TZ was administered instead of H-TZ in a group of mice, and combined with Dtx to mimic standard of care treatment.

We monitored tumor growth by BLI for the entire duration of the treatment. The tumor growth curve showed that mice treated with H-TZ+Dtx had a significant reduction of the tumor growth at day 7 ( $p = 0.043$  vs. placebo and Dtx;  $p = 0.037$  vs. TZ+Dtx) and day 11 ( $p = 0.039$  vs. placebo and Dtx), further supporting the pharmacological potential of the nanoconjugate. At day 14 post-implant, the benefit of the nanotherapy was not statistically significant anymore, but an evident trend towards reduced tumor growth was still observed in the H-TZ+Dtx as compared to the other groups. By contrast, treatments with TZ+Dtx or Dtx alone did not achieve effective reduction of the tumor growth at any of the examined time-point (Fig. 7A), being ineffective against BM.

At day 14 post-tumor implant, animals were sacrificed and we investigated the effect of the treatments on major known drawback associated to TZ-based chemotherapy, i.e. cardiotoxicity [46]. Heart tissues were analyzed by transmission electron microscopy to explore the ultrastructural features of cardiomyocytes at the end of the treatment. The images showed severe ultrastructural changes in the TZ+Dtx group, with swollen mitochondria and severe cristae disruption (Fig. 7B). This phenotype indirectly indicated impaired functionality of

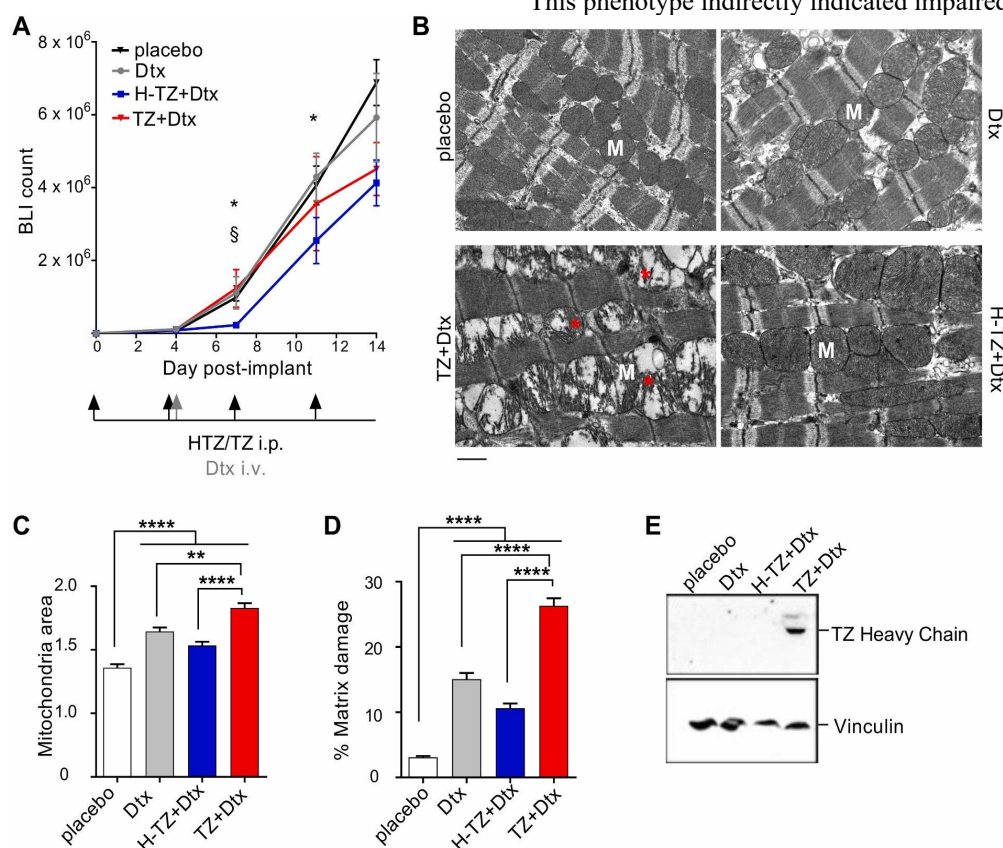


**Fig. 7.** Toxicity analysis. A) Tumor growth curve of untreated mice (black) or mice treated with Dtx (grey), H-TZ+Dtx (blue), TZ+Dtx (red). Data are means  $\pm$  SEM ( $n = 6$ /group). Day 7: \* $p = 0.043$  H-TZ+Dtx vs. placebo/Dtx;  $\$p = 0.037$  H-TZ+Dtx vs. TZ+Dtx. Day 11: \* $p = 0.039$  H-TZ+Dtx vs. placebo/Dtx, unpaired t-test. B) Representative TEM images of heart tissues excised at day 14 post-treatment ( $n = 3$ /group). It is evident a significant difference in terms of both mitochondrial area (M) and matrix damage (\*) in the TZ+Dtx group in comparison with the other groups. Scale bar = 1  $\mu$ m. C) Analysis of mean mitochondria area expressed in  $\mu$ m<sup>2</sup>. D) Analysis of the percentage of damaged matrix mitochondrial area. Data are means  $\pm$  SEM. Quantification of mitochondria area and area occupied by the matrix

were performed on at least 10 images/group, measuring at least 100 mitochondria/sample. \* \*p < 0.01; \* \* \* \*p < 0.0001 Kruskal-Wallis test. E) Western blot analysis of heart excised at the end of treatment and lysed to quantify TZ. Vinculin was used as loading control protein.

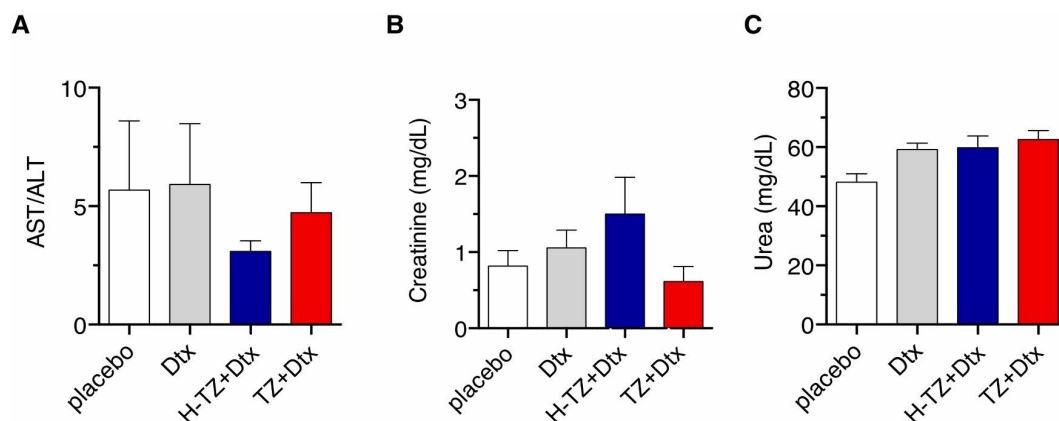


**Fig. 8.** Assessment of liver and kidney functionality. Aspartate to alanine aminotransferase ratio (AST/ALT) (A), Creatinine (B) and Urea (C) levels measured in the plasma collected from placebo and treated mice were used as biomarkers of liver and kidney dysfunction, respectively (n = 8 /group). Statistical analysis confirmed no significant differences among the groups.

the mitochondria in oxidative phosphorylation and consequent heart failure in meeting adequate energy demand. Alterations in mitochondria area observed in the TZ+Dtx group were significantly marked in comparison to the other treatments (Fig. 7C), and this is likely due to a compensative mechanism for deficiency in mitochondrial cristae, which were replaced by matrix (Fig. 7D). Mitochondrial ultrastructure was severely compromised by the addition of TZ in the TZ+Dtx group as compared to Dtx alone. By contrast, H-TZ+Dtx treatment did not induce further detrimental effects on either the mitochondria area or the percentage of matrix, as compared to Dtx alone, indicating a great potential advantage of the H-TZ nanoconjugate in protecting toward TZ-induced cardiotoxicity (Fig. 7C-D). The absence of additive alterations in cardiac mitochondria was explained by the fact that no TZ accumulation was found in heart tissue lysates upon treatment with H-TZ+Dtx (Fig. 7E). By contrast, a TZ-specific band was detected by western blot in the heart of mice treated with TZ+Dtx, suggesting accumulation of the free drug, but not the nanoformulated drug, in this organ. Based on these observations, we reasoned that the nanoconjugate guided the biodistribution of the drug differently, by achieving enhanced TZ brain delivery and reducing accumulation in the heart. In another paper from our group, HF<sub>n</sub> nanoformulation was found to reduce heart accumulation and protect against cardiotoxicity associated to the chemotherapy doxorubicin [47], further supporting our observation and confirming the advantage of HF<sub>n</sub>-based nanodrugs in terms of heart protection.

We further assessed the systemic toxicity profile of H-TZ-based treatment by looking at liver and kidney functionalities. In fact, previous data on HF<sub>n</sub> demonstrated that a prevalent fraction of nanoparticles that were not captured by the tumor distributed in the liver and were rapidly sequestered by the kidneys for urinary excretion [47]. Plasma levels of aspartate transaminase (AST) and alanine transaminase (ALT), and urea and creatinine were analyzed as markers of liver and kidney function, respectively. Our results showed that AST/ALT ratios in all the treatment groups were comparable to the placebo and in the range of reference (Fig. 8A) [48–50]. Urea (Fig. 8B) and creatinine (Fig. 8C) dosage did not show significant alterations upon

treatment with H-TZ+Dtx as compared to placebo and Dtx alone, confirming the overall safety of H-TZ nanoconjugate.

Finally, we looked at blood count results to explore any potential side effect of H-TZ-based cancer treatment detectable in peripheral blood. No remarkable alterations were observed in the levels of white blood cells (WBC), red blood cells (RBC), and platelets (PLT). Hemoglobin concentration (HGB) was also measured, and did not highlight a clinical picture of anemia in any of the treated animals (Supporting Table S3).

No lesions were observed by histopathology in other off target organs (Supplementary Fig. S9).

#### 4. Conclusions

Achieving a curative treatment of HER2 + BC BM is an unsolved clinical challenge [51]. The anti-HER2 antibody TZ improves survival of BC patients and controls the systemic disease, but it has low BBB permeability, being ineffective at treating BM [4,52]. Our prior findings obtained in vitro support H-TZ as a promising approach for the treatment of brain tumors by virtue of their ability to cross the BBB and achieve cytotoxic effect against tumor cells [21,25]. The present study, aimed at investigating the potential of H-TZ to enhance the trans-BBB permeation in vivo, demonstrated that HF<sub>n</sub> is able to actively guide TZ delivery to the brain upon systemic administration in a murine model of HER2 + BM. H-TZ bound cancer cells efficiently and stably, reducing tumor growth in vivo and shaping an antitumor response in combination with Dtx. H-TZ-based therapy also triggered activation of microglia toward cancer cells and induced alterations in the neuroinflammation, further supporting enhanced activity as compared to free TZ. These results have translational relevance, as they demonstrate that active delivery of TZ to the brain by HF<sub>n</sub> nanoparticles may exert pharmacological activity in the context of HER2 + BC BM, which is a great promise in the field. HF<sub>n</sub> drives TZ distribution to the brain and reduces major harmful accumulation in off-target organs, like the heart, thus reducing side effects and undesired toxicity generally associated with treatments currently used in clinics.



In conclusion, we first described the *in vivo* potential of HFn-based TZ nanoconjugates able to vehicle effective TZ to the brain and tackle BC-derived BM without major toxic effects. As perspective, H-TZ nanoconjugates deserve attention as they could be exploited for a prophylactic treatment of HER2 + advanced BC aimed to condition the tumor and timely shape a protective brain microenvironment.

### Ethics statement

Animals were handled in accordance with an experimental study approved by the Italian Ministry of Health (aut. N. 6/2017-PR). The procedures followed were in accordance with the ethical standards of the WMA Statement on Animal Use in Biomedical Research.

### CRedit authorship contribution statement

**MS:** Conducted experiments *in vivo* and contributed to data analysis and data curation; **SM, AB:** contributed to *in vivo/ex vivo* analyses and data curation. **SC, FR:** performed RNA analysis; **CR, MR, PZ:** contributed to histology and immunohistochemistry; **LB, SG, DP:** produced the nanoconjugate; **RA:** performed TEM analysis; **LS, CM:** Contributed to data analysis and interpretation. **FC, MT:** contributed to the conception and design of the work and supervised the study. All authors contributed to drafting the work or revising it critically for important intellectual content. All authors read and approved the final manuscript.

### Declaration of Competing Interest

The authors declare that they have no known competing financial interests or personal relationships that could have appeared to influence the work reported in this paper.

### Data Availability

Data will be made available on request. Raw data are available at [https://doi.org/10.13130/RD\\_UNIMI/IG8LEA](https://doi.org/10.13130/RD_UNIMI/IG8LEA).

### Acknowledgements

This work was partially funded by the Ricerca Corrente funding scheme of the Italian Ministry of Health and by AIRC under IG 2017 - ID. 20172 – P.I. Corsi Fabio. We acknowledge the Pediatric Clinical Research Center “Romeo ed Enrica Invernizzi” (Universita di Milano) for `imaging facility and the Laboratorio Analisi Murine (IRCCS San Raffaele Hospital) for hematologic analysis. We also thank Francesco Mainini, Matteo Monieri, Beatrice Marchini for experimental help.

### Appendix A. Supporting information

Supplementary data associated with this article can be found in the online version at [doi:10.1016/j.phrs.2023.106934](https://doi.org/10.1016/j.phrs.2023.106934).

### References

- [1] H. Hosseini, M.M.S. Obradović, M. Hoffmann, et al., Early dissemination seeds metastasis in breast cancer, *Nature* 540 (2016) 552–558.
- [2] S. Loibl, L. Gianni, HER2-positive breast cancer, *Lancet* 389 (2017) 2415–2429.
- [3] S. Dawood, K. Broglio, A.U. Buzdar, G.N. Hortobagyi, S.H. Giordano, Prognosis of women with metastatic breast cancer by HER2 status and trastuzumab treatment: an institutional-based review, *J. Clin. Oncol. J. Am. Soc. Clin. Oncol.* 28 (2010) 92–98.
- [4] A.S. Zimmer, A.E.D. Van Swearingen, C.K. Anders, HER2-positive breast cancer brain metastasis: A new and exciting landscape, *Cancer Rep.* 5 (2022), e1274.
- [5] M. Kim, S.H. Kizilbash, J.K. Laramy, et al., Barriers to effective drug treatment for brain metastases: a multifactorial problem in the delivery of precision medicine, *Pharm. Res.* 35 (2018) 177.
- [6] S. Rathi, J.I. Griffith, W. Zhang, et al., The influence of the blood-brain barrier in the treatment of brain tumours, *J. Intern Med* 292 (2022) 3–30.
- [7] N.J. Abbott, Blood-brain barrier structure and function and the challenges for CNS drug delivery, *J. Inher. Metab. Dis.* 36 (2013) 437–449.
- [8] K.A. Gelmon, F.M. Boyle, B. Kaufman, et al., Lapatinib or trastuzumab plus taxane therapy for human epidermal growth factor receptor 2-positive advanced breast cancer: final results of NCIC CTG MA.31, *J. Clin. Oncol. J. Am. Soc. Clin. Oncol.* 33 (2015) 1574–1583.
- [9] S.M. Swain, J. Baselga, D. Miles, et al., Incidence of central nervous system metastases in patients with HER2-positive metastatic breast cancer treated with pertuzumab, trastuzumab, and docetaxel: results from the randomized phase III study CLEOPATRA, *Ann. Oncol. J. Eur. Soc. Med Oncol.* 25 (2014) 1116–1121.
- [10] I.E. Krop, N.U. Lin, K. Blackwell, et al., Trastuzumab emtansine (T-DM1) versus lapatinib plus capecitabine in patients with HER2-positive metastatic breast cancer and central nervous system metastases: a retrospective, exploratory analysis in EMILIA, *Ann. Oncol. J. Eur. Soc. Med Oncol.* 26 (2015) 113–119.
- [11] G. von Minckwitz, C.-S. Huang, M.S. Mano, et al., Trastuzumab emtansine for residual invasive HER2-positive breast cancer, *New Engl. J. Med.* 380 (2019) 617–628.
- [12] E. Ferraro, J.Z. Drago, S. Modi, Implementing antibody-drug conjugates (ADCs) in HER2-positive breast cancer: state of the art and future directions, *Breast Cancer Res.* 23 (2021), 84.
- [13] S. Modi, C. Saura, T. Yamashita, et al., Trastuzumab deruxtecan in previously treated HER2-positive breast cancer, *New Engl. J. Med.* 382 (2020) 610–621.
- [14] F. Mainini, A. Bonizzi, M. Sevieri, et al., Protein-based nanoparticles for the imaging and treatment of solid tumors: the case of ferritin nanocages, a narrative review, *Pharmaceutics* 13 (2021) 2000.
- [15] M. Truffi, L. Fiandra, L. Sorrentino, M. Monieri, F. Corsi, S. Mazzucchelli, Ferritin nanocages: A biological platform for drug delivery, imaging and therapeutics in cancer, *Pharm. Res* 107 (2016) 57–65.
- [16] M. Liang, K. Fan, M. Zhou, et al., H-ferritin-nanocaged doxorubicin nanoparticles specifically target and kill tumors with a single-dose injection, *Proc. Natl. Acad. Sci. USA* 111 (2014) 14900–14905.
- [17] J. He, K. Fan, X. Yan, Ferritin drug carrier (FDC) for tumor targeting therapy, *J. Control. Release Soc.* 311–312 (2019) 288–300.
- [18] C. Lv, S. Yin, X. Zhang, J. Hu, T. Zhang, G. Zhao, 16-Mer ferritin-like protein templated gold nanoclusters for bioimaging detection of methylmercury in the brain of living mice, *Anal. Chim. Acta* 1127 (2020) 149–155.
- [19] L. Li, C.J. Fang, J.C. Ryan, et al., Binding and uptake of H-ferritin are mediated by human transferrin receptor-1, *Proc. Natl. Acad. Sci. USA* 107 (2010) 3505–3510.
- [20] C. Cao, X. Wang, Y. Cai, et al., Targeted *in vivo* imaging of microscopic tumors with ferritin-based nanoprobe across biological barriers, *Adv. Mater.* 26 (2014) 2566–2571.
- [21] L. Fiandra, S. Mazzucchelli, M. Truffi, M. Bellini, L. Sorrentino, F. Corsi, *In vitro* permeation of FITC-loaded ferritins across a rat blood-brain barrier: a model to study the delivery of nanoformulated molecules, *JoVE* (2016).
- [22] K. Fan, X. Jia, M. Zhou, et al., Ferritin nanocarrier traverses the blood brain barrier and kills glioma, *ACS Nano* 12 (2018) 4105–4115.
- [23] W. Liu, Q. Lin, Y. Fu, et al., Target delivering paclitaxel by ferritin heavy chain nanocages for glioma treatment, *J. Control Release Soc.* 323 (2020) 191–202.
- [24] S. Gagliardi, M. Truffi, V. Tinelli, et al., Bisdemethoxycoumarin (BDC)-loaded H-ferritin-nanocages mediate the regulation of inflammation in Alzheimer’s disease patients, *Int. J. Mol. Sci.* 23 (2022) 9237.
- [25] M.A. Rizzuto, R. Dal Magro, L. Barbieri, et al., H-Ferritin nanoparticle-mediated delivery of antibodies across a BBB *in vitro* model for treatment of brain malignancies, *Biomater. Sci.* 9 (2021) 2032–2042.
- [26] F. Silva, L. Sitia, R. Allevi, et al., Combined method to remove endotoxins from protein nanocages for drug delivery applications: the case of human ferritin, *Pharmaceutics* 13 (2021) 229.
- [27] F. Andreatta, A. Bonizzi, M. Sevieri, et al., Co-administration of H-ferritin- doxorubicin and Trastuzumab in neoadjuvant setting improves efficacy and prevents cardiotoxicity in HER2 + murine breast cancer model, *Sci. Rep.* 10 (2020), 11425.
- [28] H. Gomi, T. Yokoyama, S. Itoharu, Role of GFAP in morphological retention and distribution of reactive astrocytes induced by scrapie encephalopathy in mice, *Brain Res.* 1312 (2010) 156–167.
- [29] L. Li, A. Lundkvist, D. Andersson, et al., Protective role of reactive astrocytes in brain ischemia, *J. Cereb. Blood Flow. Metab. J. Int. Soc. Cereb. Blood Flow Metab.* 28 (2008) 468–481.
- [30] M. Lorger, B. Felding-Habermann, Capturing changes in the brain microenvironment during initial steps of breast cancer brain metastasis, *Am. J. Pathol.* 176 (2010) 2958–2971.
- [31] D.P. Fitzgerald, D. Palmieri, E. Hua, et al., Reactive glia are recruited by highly proliferative brain metastases of breast cancer and promote tumor cell colonization, *Clin. Exp. Metastasis* 25 (2008) 799–810.
- [32] S.-J. Kim, J.-S. Kim, E.S. Park, et al., Astrocytes upregulate survival genes in tumor cells and induce protection from chemotherapy, *Neoplasia* 13 (2011) 286–298.
- [33] F. Xing, Y. Liu, S. Sharma, et al., Activation of the c-Met pathway mobilizes an inflammatory network in the brain microenvironment to promote brain metastasis of breast cancer, *Cancer Res.* 76 (2016) 4970–4980.
- [34] C. Choy, K.I. Ansari, J. Neman, et al., Cooperation of neurotrophin receptor TrkB and Her2 in breast cancer cells facilitates brain metastases, *Breast Cancer Res.* 19 (2017), 51.
- [35] T.B. Terrell-Hall, M.I. Nounou, F. El-Amrawy, J.I.G. Griffith, P.R. Lockman, Trastuzumab distribution in an *in-vivo* and *in-vitro* model of brain metastases of breast cancer, *Oncotarget* 8 (2017) 83734–83744.
- [36] M. De Laurentis, G. Canello, L. Zinno, et al., Targeting HER2 as a therapeutic strategy for breast cancer: a paradigmatic shift of drug development in oncology, *Ann. Oncol. J. Eur. Soc. Med. Oncol.* 16 (4) (2005) iv7–iv13.
- [37] O. Martinez-Saez, A. Prat, Current and future management of HER2-positive metastatic breast cancer, *JCO Oncol. Pract.* 17 (2021) 594–604.
- [38] D.H. Gutmann, H. Kettenmann, Microglia/Brain macrophages as central drivers of brain tumor pathobiology, *Neuron* 104 (2019) 442–449.
- [39] S.-Y. Wu, K. Watabe, The roles of microglia/macrophages in tumor progression of brain cancer and metastatic disease, *Front. Biosci* 22 (2017) 1805–1829.

- [40] Y. Shi, X. Fan, H. Deng, et al., Trastuzumab triggers phagocytic killing of high HER2 cancer cells in vitro and in vivo by interaction with Fcγ receptors on macrophages, *J. Immunol.* 194 (2015) 4379–4386.
- [41] J.O. Richards, S. Karki, G.A. Lazar, H. Chen, W. Dang, J.R. Desjarlais, Optimization of antibody binding to FcγRIIIa enhances macrophage phagocytosis of tumor cells, *Mol. Cancer Ther.* 7 (2008) 2517–2527.
- [42] F.S. Sutterwala, G.J. Noel, P. Salgame, D.M. Mosser, Reversal of proinflammatory responses by ligating the macrophage Fcγ receptor type I, *J. Exp. Med.* 188 (1998) 217–222.
- [43] J. Pander, M. Heusinkveld, T. van der Straaten, et al., Activation of tumor-promoting type 2 macrophages by EGFR-targeting antibody cetuximab, *Clin. Cancer Res. J. Am. Assoc. Cancer Res.* 17 (2011) 5668–5673.
- [44] A. Montfort, C. Dufau, C. Colacios, et al., Anti-TNF, a magic bullet in cancer immunotherapy? *J. Immunother. Cancer* 7 (2019), 303.
- [45] A. Montfort, C. Colacios, T. Levade, N. Andrieu-Abadie, N. Meyer, B. Segui, The TNF Paradox in Cancer Progression and Immunotherapy, *Front. Immunol.* 10 (2019), 1818.
- [46] M.S. Ewer, S.M. Lippman, Type II chemotherapy-related cardiac dysfunction: time to recognize a new entity, *J. Clin. Oncol. J. Am. Soc. Clin. Oncol.* 23 (2005) 2900–2902.
- [47] S. Mazzucchelli, M. Bellini, L. Fiandra, et al., Nanometronomic treatment of 4T1 breast cancer with nanocaged doxorubicin prevents drug resistance and circumvents cardiotoxicity, *Oncotarget* 8 (2017) 8383–8396.
- [48] Y. Chen, C. Li, P. Song, et al., Hepatic and renal tissue damage in Balb/c mice exposed to diisodecyl phthalate: The role of oxidative stress pathways, *Food Chem. Toxicol. Int. J. Publ. Br. Ind. Biol. Res Assoc.* 132 (2019), 110600.
- [49] R. Toita, T. Kawano, S. Fujita, M. Murata, J.-H. Kang, Increased hepatic inflammation in a normal-weight mouse after long-term high-fat diet feeding, *J. Toxicol. Pathol.* 31 (2018) 43–47.
- [50] O. Sanchez, A. Arnao, M. Pareja, E. Poch, I. Ramirez, M. Soley, Acute stress-induced tissue injury in mice: differences between emotional and social stress, *Cell Stress Chaperones* 7 (2002) 36–46.
- [51] M.N. Mills, W. King, A. Soyano, et al., Evolving management of HER2+ breast cancer brain metastases and leptomeningeal disease, *J. Neurooncol* 157 (2022) 249–269.
- [52] H.J. Stemmler, S. Kahlert, W. Siekiera, M. Untch, B. Heinrich, V. Heinemann, Characteristics of patients with brain metastases receiving trastuzumab for HER2 overexpressing metastatic breast cancer, *Breast Edinb. Scotl.* 15 (2006) 219–225.



## 6. Conclusions

The present project is intended to propose, from a diagnostic and therapeutic point of view, a nanotechnological solution with beneficial impact in different neoplastic pathologies. The three studies described share in fact the use of HF<sub>n</sub> based nanocages as a versatile nano delivery system.

Moreover, embracing the scientific translational research approach promoted by the PhD course in Translational Medicine, the present work directly aims at dealing with hot topics in the field of precision oncology and surgery.

As described in study 1, HF<sub>n</sub>-PAS-ICG demonstrated potentiality as a FGS tracer able to identify cancer localization, with groundbreaking prospective for oncologic surgery and cancer management, moving FGS from a visualization tool to a diagnostic/therapeutic technology.

A second important unmet clinical need regards the limitation of off-target toxicities arising from chemotherapy with anthracyclines, such as DOX. The preservation of the immune competence in patients affected with BC could be achieved through the employment of FerOX which, according to results provided in study 2, is reported to circumvent DOX internalization in lymphocytes, allowing a potential adaptative immune response in comparison to the free drug.

Lastly, HF<sub>n</sub> can be successfully exploited to achieve whole-body chemotherapeutic treatment allowing to develop more effective and less toxic strategies to control, and ultimately prevent, BM in BC patients. In study 3 we described HF<sub>n</sub>-based TZ nanoconjugates able to actively guide TZ delivery across the BBB and tackle BM without major toxic effects.

Even if the results achieved so far are still at a preclinical stage, it is necessary to underline how the choice to use the nanoplatform HF<sub>n</sub> is promising from a translational point of view. In fact, compared to other nanomaterials which are unlikely to be suitable for use in patients, HF<sub>n</sub> has the advantage of being biocompatible and naturally capable of tumor targeting, ranking one step ahead towards clinical translation. Overall, the results emerged from this thesis provide intriguing perspectives which endorse formal evaluation of HF<sub>n</sub> for clinical practice translation suitability.

## 7. References

- (1) Siegel, R. L.; Miller, K. D.; Fuchs, H. E.; Jemal, A. Cancer Statistics, 2022. *CA. Cancer J. Clin.* **2022**, *72* (1), 7–33. <https://doi.org/10.3322/caac.21708>.
- (2) Breast Cancer Facts & Figures 2022-2024. <https://www.cancer.org/content/dam/cancer-org/research/cancer-facts-and-statistics/breast-cancer-facts-and-figures/2022-2024-breast-cancer-fact-figures-acf.pdf>.
- (3) Onkar, S. S.; Carleton, N. M.; Lucas, P. C.; Bruno, T. C.; Lee, A. V.; Vignali, D. A. A.; Oesterreich, S. The Great Immune Escape: Understanding the Divergent Immune Response in Breast Cancer Subtypes. *Cancer Discov.* **2023**, *13* (1), 23–40. <https://doi.org/10.1158/2159-8290.CD-22-0475>.
- (4) Giaquinto, A. N.; Sung, H.; Miller, K. D.; Kramer, J. L.; Newman, L. A.; Minihan, A.; Jemal, A.; Siegel, R. L. Breast Cancer Statistics, 2022. *CA. Cancer J. Clin.* **2022**, *72* (6), 524–541. <https://doi.org/10.3322/caac.21754>.
- (5) Harbeck, N.; Penault-Llorca, F.; Cortes, J.; Gnant, M.; Houssami, N.; Poortmans, P.; Ruddy, K.; Tsang, J.; Cardoso, F. Breast Cancer. *Nat. Rev. Dis. Primer* **2019**, *5* (1), 66. <https://doi.org/10.1038/s41572-019-0111-2>.
- (6) Russnes, H. G.; Lingjærde, O. C.; Børresen-Dale, A.-L.; Caldas, C. Breast Cancer Molecular Stratification. *Am. J. Pathol.* **2017**, *187* (10), 2152–2162. <https://doi.org/10.1016/j.ajpath.2017.04.022>.
- (7) Perou, C. M.; Sørlie, T.; Eisen, M. B.; Van De Rijn, M.; Jeffrey, S. S.; Rees, C. A.; Pollack, J. R.; Ross, D. T.; Johnsen, H.; Akslen, L. A.; Fluge, Ø.; Pergamenschikov, A.; Williams, C.; Zhu, S. X.; Lønning, P. E.; Børresen-Dale, A.-L.; Brown, P. O.; Botstein, D. Molecular Portraits of Human Breast Tumours. *Nature* **2000**, *406* (6797), 747–752. <https://doi.org/10.1038/35021093>.
- (8) Balma, M.; Liberini, V.; Racca, M.; Laudicella, R.; Bauckneht, M.; Buschiazzo, A.; Nicolotti, D. G.; Peano, S.; Bianchi, A.; Albano, G.; Quartuccio, N.; Abgral, R.; Morbelli, S. D.; D’Alessandria, C.; Terreno, E.; Huellner, M. W.; Papaleo, A.; Deandreis, D. Non-Conventional and Investigational PET Radiotracers for Breast Cancer: A Systematic Review. *Front. Med.* **2022**, *9*, 881551. <https://doi.org/10.3389/fmed.2022.881551>.
- (9) Nolan, E.; Lindeman, G. J.; Visvader, J. E. Deciphering Breast Cancer: From Biology to the Clinic. *Cell* **2023**, *186* (8), 1708–1728. <https://doi.org/10.1016/j.cell.2023.01.040>.
- (10) Loibl, S.; Gianni, L. HER2-Positive Breast Cancer. *The Lancet* **2017**, *389* (10087), 2415–2429. [https://doi.org/10.1016/S0140-6736\(16\)32417-5](https://doi.org/10.1016/S0140-6736(16)32417-5).
- (11) Arvold, N. D.; Oh, K. S.; Niemierko, A.; Taghian, A. G.; Lin, N. U.; Abi-Raad, R. F.; Sreedhara, M.; Harris, J. R.; Alexander, B. M. Brain Metastases after Breast-Conserving Therapy and Systemic Therapy: Incidence and Characteristics by Biologic Subtype. *Breast Cancer Res. Treat.* **2012**, *136* (1), 153–160. <https://doi.org/10.1007/s10549-012-2243-x>.
- (12) Mittendorf, E. A.; Wu, Y.; Scaltriti, M.; Meric-Bernstam, F.; Hunt, K. K.; Dawood, S.; Esteva, F. J.; Buzdar, A. U.; Chen, H.; Eksambi, S.; Hortobagyi, G. N.; Baselga, J.; Gonzalez-Angulo, A. M. Loss of *HER2* Amplification Following Trastuzumab-Based Neoadjuvant Systemic Therapy and Survival Outcomes. *Clin. Cancer Res.* **2009**, *15* (23), 7381–7388. <https://doi.org/10.1158/1078-0432.CCR-09-1735>.
- (13) Waks, A. G.; Winer, E. P. Breast Cancer Treatment: A Review. *JAMA* **2019**, *321* (3), 288. <https://doi.org/10.1001/jama.2018.19323>.
- (14) Cardoso, F.; Kyriakides, S.; Ohno, S.; Penault-Llorca, F.; Poortmans, P.; Rubio, I. T.; Zackrisson, S.; Senkus, E. Early Breast Cancer: ESMO Clinical Practice Guidelines for

- Diagnosis, Treatment and Follow-Up. *Ann. Oncol.* **2019**, *30* (8), 1194–1220. <https://doi.org/10.1093/annonc/mdz173>.
- (15) Hong, R.; Xu, B. Breast Cancer: An Up-to-date Review and Future Perspectives. *Cancer Commun.* **2022**, *42* (10), 913–936. <https://doi.org/10.1002/cac2.12358>.
- (16) Li, Y.; Zhang, H.; Merkher, Y.; Chen, L.; Liu, N.; Leonov, S.; Chen, Y. Recent Advances in Therapeutic Strategies for Triple-Negative Breast Cancer. *J. Hematol. Oncol. J Hematol Oncol* **2022**, *15* (1), 121. <https://doi.org/10.1186/s13045-022-01341-0>.
- (17) Jerusalem, G.; Collignon, J.; Schroeder, H.; Lousberg, L. Triple-Negative Breast Cancer: Treatment Challenges and Solutions. *Breast Cancer Targets Ther.* **2016**, 93. <https://doi.org/10.2147/BCTT.S69488>.
- (18) Han, H. S.; Vikas, P.; Costa, R. L. B.; Jahan, N.; Taye, A.; Stringer-Reasor, E. M. Early-Stage Triple-Negative Breast Cancer Journey: Beginning, End, and Everything in Between. *Am. Soc. Clin. Oncol. Educ. Book* **2023**, No. 43, e390464. [https://doi.org/10.1200/EDBK\\_390464](https://doi.org/10.1200/EDBK_390464).
- (19) Won, K.; Spruck, C. Triple-negative Breast Cancer Therapy: Current and Future Perspectives (Review). *Int. J. Oncol.* **2020**, *57* (6), 1245–1261. <https://doi.org/10.3892/ijo.2020.5135>.
- (20) Meng, Y.; Zheng, L.; Yang, Y.; Wang, H.; Dong, J.; Wang, C.; Zhang, Y.; Yu, X.; Wang, L.; Xia, T.; Zhang, D.; Guo, Y.; Li, B. A Monoclonal Antibody Targeting ErbB2 Domain III Inhibits ErbB2 Signaling and Suppresses the Growth of ErbB2-Overexpressing Breast Tumors. *Oncogenesis* **2016**, *5* (3), e211–e211. <https://doi.org/10.1038/oncsis.2016.25>.
- (21) Zhu, H.; Zhang, G.; Wang, Y.; Xu, N.; He, S.; Zhang, W.; Chen, M.; Liu, M.; Quan, L.; Bai, J.; Xu, N. Inhibition of ErbB2 by Herceptin Reduces Survivin Expression via the ErbB2- $\beta$ -Catenin/TCF4-Survivin Pathway in ErbB2-Overexpressed Breast Cancer Cells. *Cancer Sci.* **2010**, *101* (5), 1156–1162. <https://doi.org/10.1111/j.1349-7006.2010.01528.x>.
- (22) Slamon, D. J.; Leyland-Jones, B.; Shak, S.; Fuchs, H.; Paton, V.; Bajamonde, A.; Fleming, T.; Eiermann, W.; Wolter, J.; Pegram, M.; Baselga, J.; Norton, L. Use of Chemotherapy plus a Monoclonal Antibody against HER2 for Metastatic Breast Cancer That Overexpresses HER2. *N. Engl. J. Med.* **2001**, *344* (11), 783–792. <https://doi.org/10.1056/NEJM200103153441101>.
- (23) Sitia, L.; Sevieri, M.; Signati, L.; Bonizzi, A.; Chesi, A.; Mainini, F.; Corsi, F.; Mazzucchelli, S. HER-2-Targeted Nanoparticles for Breast Cancer Diagnosis and Treatment. *Cancers* **2022**, *14* (10), 2424. <https://doi.org/10.3390/cancers14102424>.
- (24) Nahta, R. Molecular Mechanisms of Trastuzumab-Based Treatment in HER2-Overexpressing Breast Cancer. *ISRN Oncol.* **2012**, *2012*, 1–16. <https://doi.org/10.5402/2012/428062>.
- (25) Delgado, J.; Vleminckx, C.; Sarac, S.; Sosa, A.; Bergh, J.; Giuliani, R.; Enzmann, H.; Pignatti, F. The EMA Review of Trastuzumab Emtansine (T-DM1) for the Adjuvant Treatment of Adult Patients with HER2-Positive Early Breast Cancer. *ESMO Open* **2021**, *6* (2), 100074. <https://doi.org/10.1016/j.esmoop.2021.100074>.
- (26) Rinnerthaler, G.; Gampenrieder, S.; Greil, R. HER2 Directed Antibody-Drug-Conjugates beyond T-DM1 in Breast Cancer. *Int. J. Mol. Sci.* **2019**, *20* (5), 1115. <https://doi.org/10.3390/ijms20051115>.
- (27) Hosseini, H.; Obradović, M. M. S.; Hoffmann, M.; Harper, K. L.; Sosa, M. S.; Werner-Klein, M.; Nanduri, L. K.; Werno, C.; Ehrl, C.; Maneck, M.; Patwary, N.; Haunschild, G.; Gužvić, M.; Reimelt, C.; Grauvogl, M.; Eichner, N.; Weber, F.; Hartkopf, A. D.; Taran, F.-A.; Brucker, S. Y.; Fehm, T.; Rack, B.; Buchholz, S.; Spang, R.; Meister, G.;

- Aguirre-Ghiso, J. A.; Klein, C. A. Early Dissemination Seeds Metastasis in Breast Cancer. *Nature* **2016**, *540* (7634), 552–558. <https://doi.org/10.1038/nature20785>.
- (28) Dawood, S.; Broglio, K.; Buzdar, A. U.; Hortobagyi, G. N.; Giordano, S. H. Prognosis of Women With Metastatic Breast Cancer by *HER2* Status and Trastuzumab Treatment: An Institutional-Based Review. *J. Clin. Oncol.* **2010**, *28* (1), 92–98. <https://doi.org/10.1200/JCO.2008.19.9844>.
- (29) Zimmer, A. S. “Triple-Negative Breast Cancer Central Nervous System Metastases From the Laboratory to the Clinic.” *Cancer J.* **2021**, *27* (1), 76–82. <https://doi.org/10.1097/PPO.0000000000000503>.
- (30) Porter, A. L.; Youtie, J.; Shapira, P.; Schoeneck, D. J. Refining Search Terms for Nanotechnology. *J. Nanoparticle Res.* **2008**, *10* (5), 715–728. <https://doi.org/10.1007/s11051-007-9266-y>.
- (31) “Plenty of Room” Revisited. *Nat. Nanotechnol.* **2009**, *4* (12), 781–781. <https://doi.org/10.1038/nnano.2009.356>.
- (32) Bayda, S.; Adeel, M.; Tuccinardi, T.; Cordani, M.; Rizzolio, F. The History of Nanoscience and Nanotechnology: From Chemical-Physical Applications to Nanomedicine. *Mol. Basel Switz.* **2019**, *25* (1), 112. <https://doi.org/10.3390/molecules25010112>.
- (33) Nanoscience and Nanotechnologies: Opportunities and Uncertainties. (2004).
- (34) Auffan, M.; Rose, J.; Bottero, J.-Y.; Lowry, G. V.; Jolivet, J.-P.; Wiesner, M. R. Towards a Definition of Inorganic Nanoparticles from an Environmental, Health and Safety Perspective. *Nat. Nanotechnol.* **2009**, *4* (10), 634–641. <https://doi.org/10.1038/nnano.2009.242>.
- (35) Tinkle, S.; McNeil, S. E.; Mühlebach, S.; Bawa, R.; Borchard, G.; Barenholz, Y. C.; Tamarkin, L.; Desai, N. Nanomedicines: Addressing the Scientific and Regulatory Gap: Nanomedicines. *Ann. N. Y. Acad. Sci.* **2014**, *1313* (1), 35–56. <https://doi.org/10.1111/nyas.12403>.
- (36) Farokhzad, O.; Langer, R. Nanomedicine: Developing Smarter Therapeutic and Diagnostic Modalities☆. *Adv. Drug Deliv. Rev.* **2006**, *58* (14), 1456–1459. <https://doi.org/10.1016/j.addr.2006.09.011>.
- (37) Garbayo, E.; Pascual-Gil, S.; Rodríguez-Nogales, C.; Saludas, L.; Estella-Hermoso De Mendoza, A.; Blanco-Prieto, M. J. Nanomedicine and Drug Delivery Systems in Cancer and Regenerative Medicine. *WIREs Nanomedicine Nanobiotechnology* **2020**, *12* (5), e1637. <https://doi.org/10.1002/wnan.1637>.
- (38) Domingues, C.; Santos, A.; Alvarez-Lorenzo, C.; Concheiro, A.; Jarak, I.; Veiga, F.; Barbosa, I.; Dourado, M.; Figueiras, A. Where Is Nano Today and Where Is It Headed? A Review of Nanomedicine and the Dilemma of Nanotoxicology. *ACS Nano* **2022**, *16* (7), 9994–10041. <https://doi.org/10.1021/acsnano.2c00128>.
- (39) Wagner, V.; Dullaart, A.; Bock, A.-K.; Zweck, A. The Emerging Nanomedicine Landscape. *Nat. Biotechnol.* **2006**, *24* (10), 1211–1217. <https://doi.org/10.1038/nbt1006-1211>.
- (40) Anselmo, A. C.; Mitragotri, S. Nanoparticles in the Clinic: An Update Post COVID -19 Vaccines. *Bioeng. Transl. Med.* **2021**, *6* (3), e10246. <https://doi.org/10.1002/btm2.10246>.
- (41) Shukla, A.; Maiti, P. Nanomedicine and Versatile Therapies for Cancer Treatment. *MedComm* **2022**, *3* (3), e163. <https://doi.org/10.1002/mco2.163>.
- (42) Shi, J.; Kantoff, P. W.; Wooster, R.; Farokhzad, O. C. Cancer Nanomedicine: Progress, Challenges and Opportunities. *Nat. Rev. Cancer* **2017**, *17* (1), 20–37. <https://doi.org/10.1038/nrc.2016.108>.

- (43) Kotelevets, L.; Chastre, E.; Desmaële, D.; Couvreur, P. Nanotechnologies for the Treatment of Colon Cancer: From Old Drugs to New Hope. *Int. J. Pharm.* **2016**, *514* (1), 24–40. <https://doi.org/10.1016/j.ijpharm.2016.06.005>.
- (44) Van Der Meel, R.; Sulheim, E.; Shi, Y.; Kiessling, F.; Mulder, W. J. M.; Lammers, T. Smart Cancer Nanomedicine. *Nat. Nanotechnol.* **2019**, *14* (11), 1007–1017. <https://doi.org/10.1038/s41565-019-0567-y>.
- (45) Allen, C. The Question of Toxicity of Nanomaterials and Nanoparticles. *J. Controlled Release* **2019**, *304*, 288. <https://doi.org/10.1016/j.jconrel.2019.06.008>.
- (46) Egbuna, C.; Parmar, V. K.; Jeevanandam, J.; Ezzat, S. M.; Patrick-Iwuanyanwu, K. C.; Adetunji, C. O.; Khan, J.; Onyeike, E. N.; Uche, C. Z.; Akram, M.; Ibrahim, M. S.; El Mahdy, N. M.; Awuchi, C. G.; Saravanan, K.; Tijjani, H.; Odoh, U. E.; Messaoudi, M.; Ifemeje, J. C.; Olisah, M. C.; Ezeofor, N. J.; Chikwendu, C. J.; Ibeabuchi, C. G. Toxicity of Nanoparticles in Biomedical Application: Nanotoxicology. *J. Toxicol.* **2021**, *2021*, 1–21. <https://doi.org/10.1155/2021/9954443>.
- (47) Wicki, A.; Witzigmann, D.; Balasubramanian, V.; Huwyler, J. Nanomedicine in Cancer Therapy: Challenges, Opportunities, and Clinical Applications. *J. Controlled Release* **2015**, *200*, 138–157. <https://doi.org/10.1016/j.jconrel.2014.12.030>.
- (48) Parmanik, A.; Bose, A.; Ghosh, B. Research Advancement on Magnetic Iron Oxide Nanoparticles and Their Potential Biomedical Applications. *Minerva Biotechnol. Biomol. Res.* **2022**, *34* (2). <https://doi.org/10.23736/S2724-542X.21.02830-3>.
- (49) Stanley, S. Biological Nanoparticles and Their Influence on Organisms. *Curr. Opin. Biotechnol.* **2014**, *28*, 69–74. <https://doi.org/10.1016/j.copbio.2013.11.014>.
- (50) Ferreira Soares, D. C.; Domingues, S. C.; Viana, D. B.; Tebaldi, M. L. Polymer-Hybrid Nanoparticles: Current Advances in Biomedical Applications. *Biomed. Pharmacother.* **2020**, *131*, 110695. <https://doi.org/10.1016/j.biopha.2020.110695>.
- (51) Pelaz, B.; Alexiou, C.; Alvarez-Puebla, R. A.; Alves, F.; Andrews, A. M.; Ashraf, S.; Balogh, L. P.; Ballerini, L.; Bestetti, A.; Brendel, C.; Bosi, S.; Carril, M.; Chan, W. C. W.; Chen, C.; Chen, X.; Chen, X.; Cheng, Z.; Cui, D.; Du, J.; Dullin, C.; Escudero, A.; Feliu, N.; Gao, M.; George, M.; Gogotsi, Y.; Grünweller, A.; Gu, Z.; Halas, N. J.; Hampp, N.; Hartmann, R. K.; Hersam, M. C.; Hunziker, P.; Jian, J.; Jiang, X.; Jungebluth, P.; Kadhiresan, P.; Kataoka, K.; Khademhosseini, A.; Kopeček, J.; Kotov, N. A.; Krug, H. F.; Lee, D. S.; Lehr, C.-M.; Leong, K. W.; Liang, X.-J.; Ling Lim, M.; Liz-Marzán, L. M.; Ma, X.; Macchiaroni, P.; Meng, H.; Möhwald, H.; Mulvaney, P.; Nel, A. E.; Nie, S.; Nordlander, P.; Okano, T.; Oliveira, J.; Park, T. H.; Penner, R. M.; Prato, M.; Puntès, V.; Rotello, V. M.; Samarakoon, A.; Schaak, R. E.; Shen, Y.; Sjöqvist, S.; Skirtach, A. G.; Soliman, M. G.; Stevens, M. M.; Sung, H.-W.; Tang, B. Z.; Tietze, R.; Udugama, B. N.; VanEpps, J. S.; Weil, T.; Weiss, P. S.; Willner, I.; Wu, Y.; Yang, L.; Yue, Z.; Zhang, Q.; Zhang, Q.; Zhang, X.-E.; Zhao, Y.; Zhou, X.; Parak, W. J. Diverse Applications of Nanomedicine. *ACS Nano* **2017**, *11* (3), 2313–2381. <https://doi.org/10.1021/acsnano.6b06040>.
- (52) Mitchell, M. J.; Billingsley, M. M.; Haley, R. M.; Wechsler, M. E.; Peppas, N. A.; Langer, R. Engineering Precision Nanoparticles for Drug Delivery. *Nat. Rev. Drug Discov.* **2021**, *20* (2), 101–124. <https://doi.org/10.1038/s41573-020-0090-8>.
- (53) Capriotti, G.; Varani, M.; Lauri, C.; Franchi, G.; Pizzichini, P.; Signore, A. Copper-64 Labeled Nanoparticles for Positron Emission Tomography Imaging: A Review of the Recent Literature. *Q. J. Nucl. Med. Mol. Imaging* **2020**, *64* (4). <https://doi.org/10.23736/S1824-4785.20.03315-4>.
- (54) Kim, J.; Lee, N.; Hyeon, T. Recent Development of Nanoparticles for Molecular Imaging. *Philos. Trans. R. Soc. Math. Phys. Eng. Sci.* **2017**, *375* (2107), 20170022. <https://doi.org/10.1098/rsta.2017.0022>.

- (55) Liu, Y.; Miyoshi, H.; Nakamura, M. Nanomedicine for Drug Delivery and Imaging: A Promising Avenue for Cancer Therapy and Diagnosis Using Targeted Functional Nanoparticles. *Int. J. Cancer* **2007**, *120* (12), 2527–2537. <https://doi.org/10.1002/ijc.22709>.
- (56) Mohanraj, V. J.; Chen, Y. Nanoparticles - A Review. *Trop. J. Pharm. Res.* **2007**, *5* (1), 561–573. <https://doi.org/10.4314/tjpr.v5i1.14634>.
- (57) Grobmyer, S. R.; Iwakuma, N.; Sharma, P.; Moudgil, B. M. What Is Cancer Nanotechnology? In *Cancer Nanotechnology*; Grobmyer, S. R., Moudgil, B. M., Eds.; Methods in Molecular Biology; Humana Press: Totowa, NJ, 2010; Vol. 624, pp 1–9. [https://doi.org/10.1007/978-1-60761-609-2\\_1](https://doi.org/10.1007/978-1-60761-609-2_1).
- (58) Attia, M. F.; Anton, N.; Wallyn, J.; Omran, Z.; Vandamme, T. F. An Overview of Active and Passive Targeting Strategies to Improve the Nanocarriers Efficiency to Tumour Sites. *J. Pharm. Pharmacol.* **2019**, *71* (8), 1185–1198. <https://doi.org/10.1111/jphp.13098>.
- (59) Du, J.; Lane, L. A.; Nie, S. Stimuli-Responsive Nanoparticles for Targeting the Tumor Microenvironment. *J. Controlled Release* **2015**, *219*, 205–214. <https://doi.org/10.1016/j.jconrel.2015.08.050>.
- (60) Rosenblum, D.; Joshi, N.; Tao, W.; Karp, J. M.; Peer, D. Progress and Challenges towards Targeted Delivery of Cancer Therapeutics. *Nat. Commun.* **2018**, *9* (1), 1410. <https://doi.org/10.1038/s41467-018-03705-y>.
- (61) Kheirollahpour, M.; Mehrabi, M.; Dounighi, N. M.; Mohammadi, M.; Masoudi, A. Nanoparticles and Vaccine Development. *Pharm. Nanotechnol.* **2020**, *8* (1), 6–21. <https://doi.org/10.2174/2211738507666191024162042>.
- (62) Reutovich, A. A.; Srivastava, A. K.; Arosio, P.; Bou-Abdallah, F. Ferritin Nanocages as Efficient Nanocarriers and Promising Platforms for COVID-19 and Other Vaccines Development. *Biochim. Biophys. Acta BBA - Gen. Subj.* **2023**, *1867* (3), 130288. <https://doi.org/10.1016/j.bbagen.2022.130288>.
- (63) Nguyen, B.; Tolia, N. H. Protein-Based Antigen Presentation Platforms for Nanoparticle Vaccines. *Npj Vaccines* **2021**, *6* (1), 70. <https://doi.org/10.1038/s41541-021-00330-7>.
- (64) Vu, M. N.; Pilkington, E. H.; Lee, W. S.; Tan, H.; Davis, T. P.; Truong, N. P.; Kent, S. J.; Wheatley, A. K. Engineered Ferritin Nanoparticle Vaccines Enable Rapid Screening of Antibody Functionalization to Boost Immune Responses. *Adv. Healthc. Mater.* **2023**, *12* (17), 2202595. <https://doi.org/10.1002/adhm.202202595>.
- (65) Ayan, S.; Aranci-Ciftci, K.; Ciftci, F.; Ustundag, C. B. Nanotechnology and COVID-19: Prevention, Diagnosis, Vaccine, and Treatment Strategies. *Front. Mater.* **2023**, *9*, 1059184. <https://doi.org/10.3389/fmats.2022.1059184>.
- (66) Vu, M. N.; Kelly, H. G.; Kent, S. J.; Wheatley, A. K. Current and Future Nanoparticle Vaccines for COVID-19. *eBioMedicine* **2021**, *74*, 103699. <https://doi.org/10.1016/j.ebiom.2021.103699>.
- (67) Chen, J.; Guo, Z.; Tian, H.; Chen, X. Production and Clinical Development of Nanoparticles for Gene Delivery. *Mol. Ther. - Methods Clin. Dev.* **2016**, *3*, 16023. <https://doi.org/10.1038/mtm.2016.23>.
- (68) Mendes, B. B.; Connot, J.; Avital, A.; Yao, D.; Jiang, X.; Zhou, X.; Sharf-Pauker, N.; Xiao, Y.; Adir, O.; Liang, H.; Shi, J.; Schroeder, A.; Conde, J. Nanodelivery of Nucleic Acids. *Nat. Rev. Methods Primer* **2022**, *2* (1), 24. <https://doi.org/10.1038/s43586-022-00104-y>.
- (69) Duan, L.; Ouyang, K.; Xu, X.; Xu, L.; Wen, C.; Zhou, X.; Qin, Z.; Xu, Z.; Sun, W.; Liang, Y. Nanoparticle Delivery of CRISPR/Cas9 for Genome Editing. *Front. Genet.* **2021**, *12*, 673286. <https://doi.org/10.3389/fgene.2021.673286>.

- (70) Pearce, A. K.; O'Reilly, R. K. Insights into Active Targeting of Nanoparticles in Drug Delivery: Advances in Clinical Studies and Design Considerations for Cancer Nanomedicine. *Bioconjug. Chem.* **2019**, *30* (9), 2300–2311. <https://doi.org/10.1021/acs.bioconjchem.9b00456>.
- (71) Bazak, R.; Hourri, M.; El Achy, S.; Kamel, S.; Refaat, T. Cancer Active Targeting by Nanoparticles: A Comprehensive Review of Literature. *J. Cancer Res. Clin. Oncol.* **2015**, *141* (5), 769–784. <https://doi.org/10.1007/s00432-014-1767-3>.
- (72) Chen, F.; Ehlerding, E. B.; Cai, W. Theranostic Nanoparticles. *J. Nucl. Med.* **2014**, *55* (12), 1919–1922. <https://doi.org/10.2967/jnumed.114.146019>.
- (73) Greish, K.; Mathur, A.; Bakhiet, M.; Taurin, S. Nanomedicine: Is It Lost in Translation? *Ther. Deliv.* **2018**, *9* (4), 269–285. <https://doi.org/10.4155/tde-2017-0118>.
- (74) Nirmala, M. J.; Kizhuveetil, U.; Johnson, A.; G, B.; Nagarajan, R.; Muthuvijayan, V. Cancer Nanomedicine: A Review of Nano-Therapeutics and Challenges Ahead. *RSC Adv.* **2023**, *13* (13), 8606–8629. <https://doi.org/10.1039/D2RA07863E>.
- (75) Fan, D.; Cao, Y.; Cao, M.; Wang, Y.; Cao, Y.; Gong, T. Nanomedicine in Cancer Therapy. *Signal Transduct. Target. Ther.* **2023**, *8* (1), 293. <https://doi.org/10.1038/s41392-023-01536-y>.
- (76) Li, Y.; Lin, T.; Luo, Y.; Liu, Q.; Xiao, W.; Guo, W.; Lac, D.; Zhang, H.; Feng, C.; Wachsmann-Hogiu, S.; Walton, J. H.; Cherry, S. R.; Rowland, D. J.; Kukis, D.; Pan, C.; Lam, K. S. A Smart and Versatile Theranostic Nanomedicine Platform Based on Nanoporphyrin. *Nat. Commun.* **2014**, *5* (1), 4712. <https://doi.org/10.1038/ncomms5712>.
- (77) Mohanty, A.; Parida, A.; Raut, R. K.; Behera, R. K. Ferritin: A Promising Nanoreactor and Nanocarrier for Bionanotechnology. *ACS Bio Med Chem Au* **2022**, *2* (3), 258–281. <https://doi.org/10.1021/acsbiochemau.2c00003>.
- (78) Truffi, M.; Fiandra, L.; Sorrentino, L.; Monieri, M.; Corsi, F.; Mazzucchelli, S. Ferritin Nanocages: A Biological Platform for Drug Delivery, Imaging and Theranostics in Cancer. *Pharmacol. Res.* **2016**, *107*, 57–65. <https://doi.org/10.1016/j.phrs.2016.03.002>.
- (79) Lee, N. K.; Cho, S.; Kim, I.-S. Ferritin – a Multifaceted Protein Scaffold for Biotherapeutics. *Exp. Mol. Med.* **2022**, *54* (10), 1652–1657. <https://doi.org/10.1038/s12276-022-00859-0>.
- (80) Zhu, Y.; Zhu, Y.; Cao, T.; Liu, X.; Liu, X.; Yan, Y.; Shi, Y.; Wang, J.-C. Ferritin-Based Nanomedicine for Disease Treatment. *Med. Rev.* **2023**, *3* (1), 49–74. <https://doi.org/10.1515/mr-2023-0001>.
- (81) Mainini, F.; Bonizzi, A.; Sevieri, M.; Sitia, L.; Truffi, M.; Corsi, F.; Mazzucchelli, S. Protein-Based Nanoparticles for the Imaging and Treatment of Solid Tumors: The Case of Ferritin Nanocages, a Narrative Review. *Pharmaceutics* **2021**, *13* (12), 2000. <https://doi.org/10.3390/pharmaceutics13122000>.
- (82) Plays, M.; Müller, S.; Rodriguez, R. Chemistry and Biology of Ferritin. *Met. Integr. Biometal Sci.* **2021**, *13* (5), mfab021. <https://doi.org/10.1093/mtomcs/mfab021>.
- (83) Boyd, D.; Vecoli, C.; Belcher, D. M.; Jain, S. K.; Drysdale, J. W. Structural and Functional Relationships of Human Ferritin H and L Chains Deduced from cDNA Clones. *J. Biol. Chem.* **1985**, *260* (21), 11755–11761.
- (84) Arosio, P.; Ingrassia, R.; Cavadini, P. Ferritins: A Family of Molecules for Iron Storage, Antioxidation and More. *Biochim. Biophys. Acta* **2009**, *1790* (7), 589–599. <https://doi.org/10.1016/j.bbagen.2008.09.004>.
- (85) Hempstead, P. D.; Yewdall, S. J.; Fernie, A. R.; Lawson, D. M.; Artymiuk, P. J.; Rice, D. W.; Ford, G. C.; Harrison, P. M. Comparison of the Three-Dimensional Structures of Recombinant Human H and Horse L Ferritins at High Resolution 1.1 Edited by R. Huber. *J. Mol. Biol.* **1997**, *268* (2), 424–448. <https://doi.org/10.1006/jmbi.1997.0970>.

- (86) Mesquita, G.; Silva, T.; Gomes, A. C.; Oliveira, P. F.; Alves, M. G.; Fernandes, R.; Almeida, A. A.; Moreira, A. C.; Gomes, M. S. H-Ferritin Is Essential for Macrophages' Capacity to Store or Detoxify Exogenously Added Iron. *Sci. Rep.* **2020**, *10* (1), 3061. <https://doi.org/10.1038/s41598-020-59898-0>.
- (87) Santambrogio, P.; Levi, S.; Cozzi, A.; Corsi, B.; Arosio, P. Evidence That the Specificity of Iron Incorporation into Homopolymers of Human Ferritin L- and H-Chains Is Conferred by the Nucleation and Ferroxidase Centres. *Biochem. J.* **1996**, *314* (1), 139–144. <https://doi.org/10.1042/bj3140139>.
- (88) Fan, K.; Gao, L.; Yan, X. Human Ferritin for Tumor Detection and Therapy. *WIREs Nanomedicine Nanobiotechnology* **2013**, *5* (4), 287–298. <https://doi.org/10.1002/wnan.1221>.
- (89) Song, X.; Zheng, Y.; Zhu, L.; Zhang, L.; Meng, H.; Yu, R.; Zhang, C. Development of Robust and Facile Purification Process for Production of Recombinant Human Ferritin Heavy Chain Nanoparticle from Escherichia Coli. *Process Biochem.* **2021**, *104*, 1–9. <https://doi.org/10.1016/j.procbio.2021.02.014>.
- (90) He, J.; Fan, K.; Yan, X. Ferritin Drug Carrier (FDC) for Tumor Targeting Therapy. *J. Controlled Release* **2019**, *311–312*, 288–300. <https://doi.org/10.1016/j.jconrel.2019.09.002>.
- (91) Andreatta, F.; Bonizzi, A.; Sevieri, M.; Truffi, M.; Monieri, M.; Sitia, L.; Silva, F.; Sorrentino, L.; Allevi, R.; Zerbi, P.; Marchini, B.; Longhi, E.; Ottria, R.; Casati, S.; Vanna, R.; Morasso, C.; Bellini, M.; Prosperi, D.; Corsi, F.; Mazzucchelli, S. Co-Administration of H-Ferritin-Doxorubicin and Trastuzumab in Neoadjuvant Setting Improves Efficacy and Prevents Cardiotoxicity in HER2 + Murine Breast Cancer Model. *Sci. Rep.* **2020**, *10* (1), 11425. <https://doi.org/10.1038/s41598-020-68205-w>.
- (92) Bellini, M.; Mazzucchelli, S.; Galbiati, E.; Sommaruga, S.; Fiandra, L.; Truffi, M.; Rizzuto, M. A.; Colombo, M.; Tortora, P.; Corsi, F.; Prosperi, D. Protein Nanocages for Self-Triggered Nuclear Delivery of DNA-Targeted Chemotherapeutics in Cancer Cells. *J. Controlled Release* **2014**, *196*, 184–196. <https://doi.org/10.1016/j.jconrel.2014.10.002>.
- (93) Colombo, M.; Rizzuto, M. A.; Pacini, C.; Pandolfi, L.; Bonizzi, A.; Truffi, M.; Monieri, M.; Catrambone, F.; Giustra, M.; Garbujo, S.; Fiandra, L.; Corsi, F.; Prosperi, D.; Mazzucchelli, S. Half-Chain Cetuximab Nanoconjugates Allow Multitarget Therapy of Triple Negative Breast Cancer. *Bioconjug. Chem.* **2018**, *29* (11), 3817–3832. <https://doi.org/10.1021/acs.bioconjchem.8b00667>.
- (94) Huang, P.; Rong, P.; Jin, A.; Yan, X.; Zhang, M. G.; Lin, J.; Hu, H.; Wang, Z.; Yue, X.; Li, W.; Niu, G.; Zeng, W.; Wang, W.; Zhou, K.; Chen, X. Dye-Loaded Ferritin Nanocages for Multimodal Imaging and Photothermal Therapy. *Adv. Mater.* **2014**, *26* (37), 6401–6408. <https://doi.org/10.1002/adma.201400914>.
- (95) Sevieri, M.; Pinori, M.; Chesi, A.; Bonizzi, A.; Sitia, L.; Truffi, M.; Morasso, C.; Corsi, F.; Mazzucchelli, S. Novel Bioengineering Strategies to Improve Bioavailability and *In Vivo* Circulation of H-Ferritin Nanocages by Surface Functionalization. *ACS Omega* **2023**, *8* (8), 7244–7251. <https://doi.org/10.1021/acsomega.2c07794>.
- (96) Wender, R. C.; Brawley, O. W.; Fedewa, S. A.; Gansler, T.; Smith, R. A. A Blueprint for Cancer Screening and Early Detection: Advancing Screening's Contribution to Cancer Control. *CA. Cancer J. Clin.* **2019**, *69* (1), 50–79. <https://doi.org/10.3322/caac.21550>.
- (97) Niell, B. L.; Freer, P. E.; Weinfurter, R. J.; Arleo, E. K.; Drukteinis, J. S. Screening for Breast Cancer. *Radiol. Clin. North Am.* **2017**, *55* (6), 1145–1162. <https://doi.org/10.1016/j.rcl.2017.06.004>.



- (98) Whelehan, P.; Evans, A.; Vinnicombe, S.; Brown, D.; McLean, D. Gamma Probe and Ultrasound-Guided Percutaneous Localisation of the Sentinel Lymph Node in Breast Cancer Patients. *Breast Cancer Res.* **2012**, *14* (1), O6. <https://doi.org/10.1186/bcr3255>.
- (99) Hernot, S.; van Manen, L.; Debie, P.; Mieog, J. S. D.; Vahrmeijer, A. L. Latest Developments in Molecular Tracers for Fluorescence Image-Guided Cancer Surgery. *Lancet Oncol.* **2019**, *20* (7), e354–e367. [https://doi.org/10.1016/S1470-2045\(19\)30317-1](https://doi.org/10.1016/S1470-2045(19)30317-1).
- (100) Tringale, K. R.; Pang, J.; Nguyen, Q. T. Image-guided Surgery in Cancer: A Strategy to Reduce Incidence of Positive Surgical Margins. *WIREs Syst. Biol. Med.* **2018**, *10* (3). <https://doi.org/10.1002/wsbm.1412>.
- (101) Egloff-Juras, C.; Bezdetnaya, L.; Dolivet, G.; Lassalle, H.-P. NIR Fluorescence-Guided Tumor Surgery: New Strategies for the Use of Indocyanine Green. *Int. J. Nanomedicine* **2019**, *14*, 7823–7838. <https://doi.org/10.2147/IJN.S207486>.
- (102) He, J.; Yang, L.; Yi, W.; Fan, W.; Wen, Y.; Miao, X.; Xiong, L. Combination of Fluorescence-Guided Surgery With Photodynamic Therapy for the Treatment of Cancer. *Mol. Imaging* **2017**, *16*, 153601211772291. <https://doi.org/10.1177/1536012117722911>.
- (103) Galema, H. A.; Meijer, R. P. J.; Lauwerends, L. J.; Verhoef, C.; Burggraaf, J.; Vahrmeijer, A. L.; Hutteman, M.; Keereweer, S.; Hilling, D. E. Fluorescence-Guided Surgery in Colorectal Cancer; A Review on Clinical Results and Future Perspectives. *Eur. J. Surg. Oncol.* **2022**, *48* (4), 810–821. <https://doi.org/10.1016/j.ejso.2021.10.005>.
- (104) Cassinotti, E.; Boni, L.; Baldari, L. Application of Indocyanine Green (ICG)-Guided Surgery in Clinical Practice: Lesson to Learn from Other Organs—an Overview on Clinical Applications and Future Perspectives. *Updat. Surg.* **2023**, *75* (2), 357–365. <https://doi.org/10.1007/s13304-022-01361-y>.
- (105) Van Keulen, S.; Hom, M.; White, H.; Rosenthal, E. L.; Baik, F. M. The Evolution of Fluorescence-Guided Surgery. *Mol. Imaging Biol.* **2023**, *25* (1), 36–45. <https://doi.org/10.1007/s11307-022-01772-8>.
- (106) Sutton, P. A.; Van Dam, M. A.; Cahill, R. A.; Mieog, S.; Polom, K.; Vahrmeijer, A. L.; Van Der Vorst, J. Fluorescence-Guided Surgery: Comprehensive Review. *BJS Open* **2023**, *7* (3), zrad049. <https://doi.org/10.1093/bjsopen/zrad049>.
- (107) Boogerd, L. S. F.; Hoogstins, C. E. S.; Schaap, D. P.; Kusters, M.; Handgraaf, H. J. M.; Van Der Valk, M. J. M.; Hilling, D. E.; Holman, F. A.; Peeters, K. C. M. J.; Mieog, J. S. D.; Van De Velde, C. J. H.; Farina-Sarasqueta, A.; Van Lijnschoten, I.; Framery, B.; Pèlegri, A.; Gutowski, M.; Nienhuijs, S. W.; De Hingh, I. H. J. T.; Nieuwenhuijzen, G. A. P.; Rutten, H. J. T.; Cailler, F.; Burggraaf, J.; Vahrmeijer, A. L. Safety and Effectiveness of SGM-101, a Fluorescent Antibody Targeting Carcinoembryonic Antigen, for Intraoperative Detection of Colorectal Cancer: A Dose-Escalation Pilot Study. *Lancet Gastroenterol. Hepatol.* **2018**, *3* (3), 181–191. [https://doi.org/10.1016/S2468-1253\(17\)30395-3](https://doi.org/10.1016/S2468-1253(17)30395-3).
- (108) Lu, C.-H.; Hsiao, J.-K. Indocyanine Green: An Old Drug with Novel Applications. *Tzu Chi Med. J.* **2021**, *33* (4), 317. [https://doi.org/10.4103/tcmj.tcmj\\_216\\_20](https://doi.org/10.4103/tcmj.tcmj_216_20).
- (109) Leiloglou, M.; Kedrzycki, M. S.; Chalau, V.; Chiarini, N.; Thiruchelvam, P. T. R.; Hadjiminias, D. J.; Hogben, K. R.; Rashid, F.; Ramakrishnan, R.; Darzi, A. W.; Leff, D. R.; Elson, D. S. Indocyanine Green Fluorescence Image Processing Techniques for Breast Cancer Macroscopic Demarcation. *Sci. Rep.* **2022**, *12* (1), 8607. <https://doi.org/10.1038/s41598-022-12504-x>.
- (110) Alam, I. S.; Steinberg, I.; Vermesh, O.; Van Den Berg, N. S.; Rosenthal, E. L.; Van Dam, G. M.; Ntziachristos, V.; Gambhir, S. S.; Hernot, S.; Rogalla, S. Emerging Intraoperative Imaging Modalities to Improve Surgical Precision. *Mol. Imaging Biol.* **2018**, *20* (5), 705–715. <https://doi.org/10.1007/s11307-018-1227-6>.

- (111) Sheng, Z.; Hu, D.; Xue, M.; He, M.; Gong, P.; Cai, L. Indocyanine Green Nanoparticles for Theranostic Applications. *Nano-Micro Lett.* **2013**, *5* (3), 145–150. <https://doi.org/10.1007/BF03353743>.
- (112) Pathak, R. A.; Hemal, A. K. Intraoperative ICG-Fluorescence Imaging for Robotic-Assisted Urologic Surgery: Current Status and Review of Literature. *Int. Urol. Nephrol.* **2019**, *51* (5), 765–771. <https://doi.org/10.1007/s11255-019-02126-0>.
- (113) Wan, J.; Wang, S.; Yan, B.; Tang, Y.; Zheng, J.; Ji, H.; Hu, Y.; Zhuang, B.; Deng, H.; Yan, J. Indocyanine Green for Radical Lymph Node Dissection in Patients with Sigmoid and Rectal Cancer: Randomized Clinical Trial. *BJS Open* **2022**, *6* (6), zrac151. <https://doi.org/10.1093/bjsopen/zrac151>.
- (114) Reinhart, M. B.; Huntington, C. R.; Blair, L. J.; Heniford, B. T.; Augenstein, V. A. Indocyanine Green: Historical Context, Current Applications, and Future Considerations. *Surg. Innov.* **2016**, *23* (2), 166–175. <https://doi.org/10.1177/1553350615604053>.
- (115) Bargon, C. A.; Huibers, A.; Young-Afat, D. A.; Jansen, B. A. M.; Borel-Rinkes, I. H. M.; Lavalaye, J.; Van Slooten, H.-J.; Verkooijen, H. M.; Van Swol, C. F. P.; Doeksen, A. Sentinel Lymph Node Mapping in Breast Cancer Patients Through Fluorescent Imaging Using Indocyanine Green: The INFLUENCE Trial. *Ann. Surg.* **2022**, *276* (5), 913–920. <https://doi.org/10.1097/SLA.0000000000005633>.
- (116) Sevieri, M.; Silva, F.; Bonizzi, A.; Sitia, L.; Truffi, M.; Mazzucchelli, S.; Corsi, F. Indocyanine Green Nanoparticles: Are They Compelling for Cancer Treatment? *Front. Chem.* **2020**, *8*, 535. <https://doi.org/10.3389/fchem.2020.00535>.
- (117) Wang, H.; Li, X.; Tse, B. W.-C.; Yang, H.; Thorling, C. A.; Liu, Y.; Touraud, M.; Chouane, J. B.; Liu, X.; Roberts, M. S.; Liang, X. Indocyanine Green-Incorporating Nanoparticles for Cancer Theranostics. *Theranostics* **2018**, *8* (5), 1227–1242. <https://doi.org/10.7150/thno.22872>.
- (118) Ting, C.-W.; Chou, Y.-H.; Huang, S.-Y.; Chiang, W.-H. Indocyanine Green-Carrying Polymeric Nanoparticles with Acid-Triggered Detachable PEG Coating and Drug Release for Boosting Cancer Photothermal Therapy. *Colloids Surf. B Biointerfaces* **2021**, *208*, 112048. <https://doi.org/10.1016/j.colsurfb.2021.112048>.
- (119) Gowsalya, K.; Yasothamani, V.; Vivek, R. Emerging Indocyanine Green-Integrated Nanocarriers for Multimodal Cancer Therapy: A Review. *Nanoscale Adv.* **2021**, *3* (12), 3332–3352. <https://doi.org/10.1039/D1NA00059D>.
- (120) Mieog, J. S. D.; Achterberg, F. B.; Zlitni, A.; Hutteman, M.; Burggraaf, J.; Swijnenburg, R.-J.; Gioux, S.; Vahrmeijer, A. L. Fundamentals and Developments in Fluorescence-Guided Cancer Surgery. *Nat. Rev. Clin. Oncol.* **2022**, *19* (1), 9–22. <https://doi.org/10.1038/s41571-021-00548-3>.
- (121) Vreeburg, M. T. A.; Azargoshasb, S.; Van Willigen, D.; Molenaar, T.; Van Oosterom, M. N.; Buckle, T.; Slof, L. J.; Klop, M.; Karakullukcu, B.; Donswijk, M.; Van Der Poel, H. G.; Van Leeuwen, F. W. B.; Brouwer, O. R.; Rietbergen, D. D. D. Comparison of Two Hybrid Sentinel Node Tracers: Indocyanine Green (ICG)-99mTc-Nanocolloid vs. ICG-99mTc-Nanoscan from a Nuclear Medicine and Surgical Perspective. *Eur. J. Nucl. Med. Mol. Imaging* **2023**, *50* (8), 2282–2291. <https://doi.org/10.1007/s00259-023-06157-9>.
- (122) Sitia, L.; Sevieri, M.; Bonizzi, A.; Allevi, R.; Morasso, C.; Foschi, D.; Corsi, F.; Mazzucchelli, S. Development of Tumor-Targeted Indocyanine Green-Loaded Ferritin Nanoparticles for Intraoperative Detection of Cancers. *ACS Omega* **2020**, *5* (21), 12035–12045. <https://doi.org/10.1021/acsomega.0c00244>.
- (123) Fracasso, G.; Falvo, E.; Colotti, G.; Fazi, F.; Ingegnere, T.; Amalfitano, A.; Doglietto, G. B.; Alfieri, S.; Boffi, A.; Morea, V.; Conti, G.; Tremante, E.; Giacomini, P.; Arcovito,

- A.; Ceci, P. Selective Delivery of Doxorubicin by Novel Stimuli-Sensitive Nano-Ferritins Overcomes Tumor Refractoriness. *J. Controlled Release* **2016**, *239*, 10–18. <https://doi.org/10.1016/j.jconrel.2016.08.010>.
- (124) Falvo, E.; Tremante, E.; Arcovito, A.; Papi, M.; Elad, N.; Boffi, A.; Morea, V.; Conti, G.; Toffoli, G.; Fracasso, G.; Giacomini, P.; Ceci, P. Improved Doxorubicin Encapsulation and Pharmacokinetics of Ferritin–Fusion Protein Nanocarriers Bearing Proline, Serine, and Alanine Elements. *Biomacromolecules* **2016**, *17* (2), 514–522. <https://doi.org/10.1021/acs.biomac.5b01446>.
- (125) Silva, F.; Sitia, L.; Allevi, R.; Bonizzi, A.; Sevieri, M.; Morasso, C.; Truffi, M.; Corsi, F.; Mazzucchelli, S. Combined Method to Remove Endotoxins from Protein Nanocages for Drug Delivery Applications: The Case of Human Ferritin. *Pharmaceutics* **2021**, *13* (2), 229. <https://doi.org/10.3390/pharmaceutics13020229>.
- (126) Sevieri, M.; Sitia, L.; Bonizzi, A.; Truffi, M.; Mazzucchelli, S.; Corsi, F. Tumor Accumulation and Off-Target Biodistribution of an Indocyanine-Green Fluorescent Nanotracer: An Ex Vivo Study on an Orthotopic Murine Model of Breast Cancer. *Int. J. Mol. Sci.* **2021**, *22* (4), 1601. <https://doi.org/10.3390/ijms22041601>.
- (127) Thorn, C. F.; Oshiro, C.; Marsh, S.; Hernandez-Boussard, T.; McLeod, H.; Klein, T. E.; Altman, R. B. Doxorubicin Pathways: Pharmacodynamics and Adverse Effects. *Pharmacogenet. Genomics* **2011**, *21* (7), 440–446. <https://doi.org/10.1097/FPC.0b013e32833ffb56>.
- (128) Sawasdee, N.; Wattanapanitch, M.; Thongsin, N.; Phanthaphol, N.; Chiawpanit, C.; Thuwajit, C.; Yenchitsomanus, P.-T.; Panya, A. Doxorubicin Sensitizes Breast Cancer Cells to Natural Killer Cells in Connection with Increased Fas Receptors. *Int. J. Mol. Med.* **2022**, *49* (3), 40. <https://doi.org/10.3892/ijmm.2022.5095>.
- (129) Mattarollo, S. R.; Loi, S.; Duret, H.; Ma, Y.; Zitvogel, L.; Smyth, M. J. Pivotal Role of Innate and Adaptive Immunity in Anthracycline Chemotherapy of Established Tumors. *Cancer Res.* **2011**, *71* (14), 4809–4820. <https://doi.org/10.1158/0008-5472.CAN-11-0753>.
- (130) Panis, C.; Lemos, L. G. T.; Victorino, V. J.; Herrera, A. C. S. A.; Campos, F. C.; Colado Simão, A. N.; Pinge-Filho, P.; Cecchini, A. L.; Cecchini, R. Immunological Effects of Taxol and Adryamicin in Breast Cancer Patients. *Cancer Immunol. Immunother.* **2012**, *61* (4), 481–488. <https://doi.org/10.1007/s00262-011-1117-0>.
- (131) Casares, N.; Pequignot, M. O.; Tesniere, A.; Ghiringhelli, F.; Roux, S.; Chaput, N.; Schmitt, E.; Hamai, A.; Hervas-Stubbs, S.; Obeid, M.; Coutant, F.; Métivier, D.; Pichard, E.; Aucouturier, P.; Pierron, G.; Garrido, C.; Zitvogel, L.; Kroemer, G. Caspase-Dependent Immunogenicity of Doxorubicin-Induced Tumor Cell Death. *J. Exp. Med.* **2005**, *202* (12), 1691–1701. <https://doi.org/10.1084/jem.20050915>.
- (132) Wennerberg, E.; Sarhan, D.; Carlsten, M.; Kaminsky, V. O.; D’Arcy, P.; Zhivotovsky, B.; Childs, R.; Lundqvist, A. Doxorubicin Sensitizes Human Tumor Cells to NK Cell- and T-Cell-Mediated Killing by Augmented TRAIL Receptor Signaling: Novel Use of Doxorubicin in Adoptive Cell Therapy. *Int. J. Cancer* **2013**, *133* (7), 1643–1652. <https://doi.org/10.1002/ijc.28163>.
- (133) Crotty, S.; Ahmed, R. Immunological Memory in Humans. *Semin. Immunol.* **2004**, *16* (3), 197–203. <https://doi.org/10.1016/j.smim.2004.02.008>.
- (134) Verma, R.; Foster, R. E.; Horgan, K.; Mounsey, K.; Nixon, H.; Smalle, N.; Hughes, T. A.; Carter, C. Rd. Lymphocyte Depletion and Repopulation after Chemotherapy for Primary Breast Cancer. *Breast Cancer Res.* **2016**, *18* (1), 10. <https://doi.org/10.1186/s13058-015-0669-x>.
- (135) Blattman, J. N.; Antia, R.; Sourdive, D. J. D.; Wang, X.; Kaech, S. M.; Murali-Krishna, K.; Altman, J. D.; Ahmed, R. Estimating the Precursor Frequency of Naive

- Antigen-Specific CD8 T Cells. *J. Exp. Med.* **2002**, *195* (5), 657–664. <https://doi.org/10.1084/jem.20001021>.
- (136) Tacar, O.; Sriamornsak, P.; Dass, C. R. Doxorubicin: An Update on Anticancer Molecular Action, Toxicity and Novel Drug Delivery Systems. *J. Pharm. Pharmacol.* **2012**, *65* (2), 157–170. <https://doi.org/10.1111/j.2042-7158.2012.01567.x>.
- (137) Gu, F.; Hu, C.; Cao, W.; Li, C.; Xia, Q.; Gao, Y.; Liu, Y.; Gao, S. Tumor Microenvironment Multiple Responsive Nanoparticles for Targeted Delivery of Doxorubicin and CpG Against Triple-Negative Breast Cancer. *Int. J. Nanomedicine* **2022**, *Volume 17*, 4401–4417. <https://doi.org/10.2147/IJN.S377702>.
- (138) Lee, J.; Um, W.; Moon, H.; Joo, H.; Song, Y.; Park, M.; Yoon, B.; Kim, H.-R.; Park, J. H. Evading Doxorubicin-Induced Systemic Immunosuppression Using Ultrasound-Responsive Liposomes Combined with Focused Ultrasound. *Pharmaceutics* **2022**, *14* (12), 2603. <https://doi.org/10.3390/pharmaceutics14122603>.
- (139) Yao, Y.; Zhou, Y.; Liu, L.; Xu, Y.; Chen, Q.; Wang, Y.; Wu, S.; Deng, Y.; Zhang, J.; Shao, A. Nanoparticle-Based Drug Delivery in Cancer Therapy and Its Role in Overcoming Drug Resistance. *Front. Mol. Biosci.* **2020**, *7*, 193. <https://doi.org/10.3389/fmolb.2020.00193>.
- (140) Patra, J. K.; Das, G.; Fraceto, L. F.; Campos, E. V. R.; Rodriguez-Torres, M. D. P.; Acosta-Torres, L. S.; Diaz-Torres, L. A.; Grillo, R.; Swamy, M. K.; Sharma, S.; Habtemariam, S.; Shin, H.-S. Nano Based Drug Delivery Systems: Recent Developments and Future Prospects. *J. Nanobiotechnology* **2018**, *16* (1), 71. <https://doi.org/10.1186/s12951-018-0392-8>.
- (141) Mainini, F.; Bonizzi, A.; Sevieri, M.; Sitia, L.; Truffi, M.; Corsi, F.; Mazzucchelli, S. Protein-Based Nanoparticles for the Imaging and Treatment of Solid Tumors: The Case of Ferritin Nanocages, a Narrative Review. *Pharmaceutics* **2021**, *13* (12), 2000. <https://doi.org/10.3390/pharmaceutics13122000>.
- (142) Mazzucchelli, S.; Bellini, M.; Fiandra, L.; Truffi, M.; Rizzuto, M. A.; Sorrentino, L.; Longhi, E.; Nebuloni, M.; Prosperi, D.; Corsi, F. Nanometronomic Treatment of 4T1 Breast Cancer with Nanocaged Doxorubicin Prevents Drug Resistance and Circumvents Cardiotoxicity. *Oncotarget* **2017**, *8* (5), 8383–8396. <https://doi.org/10.18632/oncotarget.14204>.
- (143) Kciuk, M.; Gielecińska, A.; Mujwar, S.; Kołat, D.; Kałuzińska-Kołat, Ż.; Celik, I.; Kontek, R. Doxorubicin—An Agent with Multiple Mechanisms of Anticancer Activity. *Cells* **2023**, *12* (4), 659. <https://doi.org/10.3390/cells12040659>.
- (144) Alizadeh, D.; Trad, M.; Hanke, N. T.; Larmonier, C. B.; Janikashvili, N.; Bonnotte, B.; Katsanis, E.; Larmonier, N. Doxorubicin Eliminates Myeloid-Derived Suppressor Cells and Enhances the Efficacy of Adoptive T-Cell Transfer in Breast Cancer. *Cancer Res.* **2014**, *74* (1), 104–118. <https://doi.org/10.1158/0008-5472.CAN-13-1545>.
- (145) Yang, S.; Shim, M. K.; Kim, W. J.; Choi, J.; Nam, G.-H.; Kim, J.; Kim, J.; Moon, Y.; Kim, H. Y.; Park, J.; Park, Y.; Kim, I.-S.; Ryu, J. H.; Kim, K. Cancer-Activated Doxorubicin Prodrug Nanoparticles Induce Preferential Immune Response with Minimal Doxorubicin-Related Toxicity. *Biomaterials* **2021**, *272*, 120791. <https://doi.org/10.1016/j.biomaterials.2021.120791>.
- (146) Park, J. Y.; Jang, M. J.; Chung, Y. H.; Kim, K. Y.; Kim, S. S.; Lee, W. B.; You, S.; Choi, Y. S.; Hur, D. Y.; Kim, D. Doxorubicin Enhances CD4+ T-Cell Immune Responses by Inducing Expression of CD40 Ligand and 4-1BB. *Int. Immunopharmacol.* **2009**, *9* (13–14), 1530–1539. <https://doi.org/10.1016/j.intimp.2009.09.008>.
- (147) Das, R. K.; O'Connor, R. S.; Grupp, S. A.; Barrett, D. M. Lingering Effects of Chemotherapy on Mature T Cells Impair Proliferation. *Blood Adv.* **2020**, *4* (19), 4653–4664. <https://doi.org/10.1182/bloodadvances.2020001797>.

- (148) D'Angelo, N. A.; Noronha, M. A.; Câmara, M. C. C.; Kurnik, I. S.; Feng, C.; Araujo, V. H. S.; Santos, J. H. P. M.; Feitosa, V.; Molino, J. V. D.; Rangel-Yagui, C. O.; Chorilli, M.; Ho, E. A.; Lopes, A. M. Doxorubicin Nanoformulations on Therapy against Cancer: An Overview from the Last 10 Years. *Biomater. Adv.* **2022**, *133*, 112623. <https://doi.org/10.1016/j.msec.2021.112623>.
- (149) Chen, Y.; Zeng, L.; Zhu, H.; Wu, Q.; Liu, R.; Liang, Q.; Chen, B.; Dai, H.; Tang, K.; Liao, C.; Huang, Y.; Yan, X.; Fan, K.; Du, J.; Lin, R.; Wang, J. Ferritin Nanocaged Doxorubicin Potentiates Chemo-Immunotherapy against Hepatocellular Carcinoma via Immunogenic Cell Death. *Small Methods* **2023**, *7* (5), 2201086. <https://doi.org/10.1002/smt.202201086>.
- (150) Liang, M.; Fan, K.; Zhou, M.; Duan, D.; Zheng, J.; Yang, D.; Feng, J.; Yan, X. H-Ferritin–Nanocaged Doxorubicin Nanoparticles Specifically Target and Kill Tumors with a Single-Dose Injection. *Proc. Natl. Acad. Sci.* **2014**, *111* (41), 14900–14905. <https://doi.org/10.1073/pnas.1407808111>.
- (151) Fan, K.; Cao, C.; Pan, Y.; Lu, D.; Yang, D.; Feng, J.; Song, L.; Liang, M.; Yan, X. Magnetoferritin Nanoparticles for Targeting and Visualizing Tumour Tissues. *Nat. Nanotechnol.* **2012**, *7* (7), 459–464. <https://doi.org/10.1038/nnano.2012.90>.
- (152) Signati, L.; Allevi, R.; Piccotti, F.; Albasini, S.; Villani, L.; Sevieri, M.; Bonizzi, A.; Corsi, F.; Mazzucchelli, S. Ultrastructural Analysis of Breast Cancer Patient-Derived Organoids. *Cancer Cell Int.* **2021**, *21* (1), 423. <https://doi.org/10.1186/s12935-021-02135-z>.
- (153) Mazzucchelli, S.; Piccotti, F.; Allevi, R.; Truffi, M.; Sorrentino, L.; Russo, L.; Agozzino, M.; Signati, L.; Bonizzi, A.; Villani, L.; Corsi, F. Establishment and Morphological Characterization of Patient-Derived Organoids from Breast Cancer. *Biol. Proced. Online* **2019**, *21* (1), 12. <https://doi.org/10.1186/s12575-019-0099-8>.
- (154) Moura, I. C. A Neutralizing Monoclonal Antibody (mAb A24) Directed against the Transferrin Receptor Induces Apoptosis of Tumor T Lymphocytes from ATL Patients. *Blood* **2004**, *103* (5), 1838–1845. <https://doi.org/10.1182/blood-2003-07-2440>.
- (155) Li, L.; Fang, C. J.; Ryan, J. C.; Niemi, E. C.; Lebrón, J. A.; Björkman, P. J.; Arase, H.; Torti, F. M.; Torti, S. V.; Nakamura, M. C.; Seaman, W. E. Binding and Uptake of H-Ferritin Are Mediated by Human Transferrin Receptor-1. *Proc. Natl. Acad. Sci.* **2010**, *107* (8), 3505–3510. <https://doi.org/10.1073/pnas.0913192107>.
- (156) Sevieri, M.; Mazzucchelli, S.; Barbieri, L.; Garbujo, S.; Carelli, S.; Bonizzi, A.; Rey, F.; Recordati, C.; Recchia, M.; Allevi, R.; Sitia, L.; Morasso, C.; Zerbi, P.; Prospero, D.; Corsi, F.; Truffi, M. Ferritin Nanoconjugates Guide Trastuzumab Brain Delivery to Promote an Antitumor Response in Murine HER2 + Breast Cancer Brain Metastasis. *Pharmacol. Res.* **2023**, *196*, 106934. <https://doi.org/10.1016/j.phrs.2023.106934>.
- (157) Rizzuto, M. A.; Dal Magro, R.; Barbieri, L.; Pandolfi, L.; Sguazzini-Viscontini, A.; Truffi, M.; Salvioni, L.; Corsi, F.; Colombo, M.; Re, F.; Prospero, D. H-Ferritin Nanoparticle-Mediated Delivery of Antibodies across a BBB *in Vitro* Model for Treatment of Brain Malignancies. *Biomater. Sci.* **2021**, *9* (6), 2032–2042. <https://doi.org/10.1039/D0BM01726D>.

## Appendix 1:



Review

# HER-2-Targeted Nanoparticles for Breast Cancer Diagnosis and Treatment

Leopoldo Sitia <sup>1</sup>, Marta Sevieri <sup>1</sup>, Lorena Signati <sup>1</sup>, Arianna Bonizzi <sup>1</sup>, Arianna Chesi <sup>1</sup>, Francesco Mainini <sup>1</sup>, Fabio Corsi <sup>1,2</sup> and Serena Mazzucchelli <sup>1,\*</sup>



**Citation:** Sitia, L.; Sevieri, M.; Signati, L.; Bonizzi, A.; Chesi, A.; Mainini, F.; Corsi, F.; Mazzucchelli, S. HER-2-Targeted Nanoparticles for Breast Cancer Diagnosis and Treatment. *Cancers* **2022**, *14*, 2424. <https://doi.org/10.3390/cancers14102424> Academic Editor: Javier Cortes

Received: 13 April 2022

Accepted: 10 May 2022

Published: 13 May 2022

**Publisher's Note:** MDPI stays neutral with regard to jurisdictional claims in published maps and institutional affiliations.



**Copyright:** © 2022 by the authors. Licensee MDPI, Basel, Switzerland. This article is an open access article distributed under the terms and conditions of the Creative Commons Attribution (CC BY) license (<https://creativecommons.org/licenses/by/4.0/>).

<sup>1</sup> Dipartimento di Scienze Biomediche e Cliniche, Università di Milano, 20157 Milano, Italy; leopoldo.sitia@unimi.it (L.S.); marta.sevieri@unimi.it (M.S.); lorena.signati@unimi.it (L.S.); arianna.bonizzi@unimi.it (A.B.); arianna.chesi@unimi.it (A.C.); francesco.mainini@unimi.it (F.M.); fabio.corsi@unimi.it (F.C.)

<sup>2</sup> IRCCS Istituti Clinici Scientifici Salvatore Maugeri, 27100 Pavia, Italy

\* Correspondence: serena.mazzucchelli@unimi.it

**Simple Summary:** Despite tremendous efforts in finding new therapeutic strategies and promoting screening programs to increase early diagnosis, breast cancer is still a major cause of death in the female worldwide population. Preclinical and

clinical evidence have shown that nanotechnologies can significantly contribute to improving both therapeutic and diagnostic aspects. This is particularly true for human epidermal growth factor receptor-2 (HER-2) overexpressing (HER-2<sup>+</sup>) breast cancer, where recurrence rates and drug resistance still make it one of the most aggressive breast cancer subtypes, despite the development of promising targeted therapies. The aim of this review is to provide an update on the most promising nanoparticle-based approaches developed in the last decade in the context of HER-2-positive breast cancer therapy and diagnosis.

**Abstract:** Human epidermal growth factor receptor-2 (HER-2) overexpressing breast cancer is a breast cancer subtype characterized by high aggressiveness, high frequency of brain metastases and poor prognosis. HER-2, a glycoprotein belonging to the ErbB receptor family, is overexpressed on the outer membrane of cancer cells and has been an important therapeutic target for the development of targeted drugs, such as the monoclonal antibodies trastuzumab and pertuzumab. These therapies have been available in clinics for more than twenty years. However, despite the initial enthusiasm, a major issue emerged limiting HER-2 targeted therapy efficacy, i.e., the evolution of drug resistance, which could be tackled by nanotechnology. The aim of this review is to provide a first critical update on the different types of HER-2-targeted nanoparticles that have been proposed in the literature in the last decade for therapeutic purposes. We focus on the different targeting strategies that have been explored, their relative outcomes and current limitations that still need to be improved. Then, we review the nanotools developed as diagnostic kits, focusing on the most recent techniques, which allow accurate quantification of HER-2 levels in tissues, with the aim of promoting more personalized medicinal approaches in patients.

## 1. Introduction

Breast cancer (BC) is the most commonly diagnosed cancer and one of the main causes of death in women, despite advances in early diagnosis and novel therapies [1]. According to GLOBOCAN 2020, BC caused 684,996 deaths (one in six of all cancer deaths) and its incidence was 2.3 million new cases worldwide in 2020 [2]. These numbers highlight that BC still represents a public health problem; therefore it is of paramount importance to identify the most effective therapeutic strategy for the patient. Based on the gene expression profile of biological markers, BC has been classified into four molecular subtypes: Luminal A, Luminal B, HER-2 enriched, and Basal-like[3]. Among them, the human epidermal growth factor receptor 2-positive (HER-2+) and HER-2 enriched BC account for 20–30% of BC. These are highly proliferative and aggressive BC subtypes often related to drug resistance [4–7] and associated with a higher incidence of brain metastasis and worse clinical outcomes [9,10]. From the molecular point of view, they are characterized by the overexpression of HER-2, a glycoprotein with a tyrosine kinase activity, which belongs to the ErbB receptors family. HER-2 is an orphan receptor, which exists as constitutively active form suitable for dimerization with other ErbB members. HER-2-mediated activation of ErbB receptor signaling promotes cell proliferation, motility, differentiation and survival [10]. Hence, HER-2 amplification or over-expression leads to the constitutive activation of the PI3K/Akt and Ras/Raf/MAPK pathways, which results in the development of many epithelial cancers [11–14]. HER-2 status analysis is performed by immunohistochemistry (IHC) or fluorescence in situ hybridization (FISH), and it has been established that an IHC score of 3+ or 2+, and concomitant amplification, is considered HER-2+ BC [15].

Despite a huge effort in research, after the introduction of the first targeted therapies there has been a lack of new agents contributing significantly to HER-2+ BC treatment, which is still an unmet clinical need. In our opinion, two factors would greatly contribute to an improvement in HER-2+ BC management: the development of new targeted therapeutic strategies and the introduction of new agents allowing a rapid and personalized diagnosis. The aim of this review is to critically highlight the main reasons of this lack of success and to provide an overview of the most promising nanotechnological approaches introduced in the last 10 years on the therapeutic and diagnostic side.

## 2. HER-2+ BC Current Therapies and Main Drawbacks

The first-line treatment for HER-2+ BC patients generally includes three steps: first, neoadjuvant chemotherapy is aimed at reducing the tumor size before surgical resection, which consists of a combination of taxanes and dual HER-2 blockade with monoclonal antibodies (mAb) [16,17]. Surgery is then performed to remove the tumor, followed by adjuvant therapy which includes chemotherapy, radiation therapy and targeted therapy to eliminate any remaining tumor cells and to reduce the risk of recurrence [18,19].

The clinical outcomes of the early and metastatic HER-2+ patients were extensively improved after the advent of the HER-2 targeted therapies, such as mAb, antibody-drug conjugates, specific pathway inhibitors and immunotherapy.

### 2.1. Monoclonal Antibodies and Antibody-Drug Conjugates

The first and most relevant example of HER-2<sup>+</sup>-targeted therapy is the FDA approved humanized mAb Trastuzumab (Herceptin™; TZ). TZ has been demonstrated to increase disease-free survival (DFS) and overall survival (OS) in HER-2<sup>+</sup> BC patients [20–22]. Its mechanism of action consists in binding the HER-2 receptor to alter downstream signaling, inhibiting cell cycle progression and consequently arresting tumor growth [23,24]. Despite the wide use of TZ and its success, a great number of patients experience disease progression and relapse due to the onset of several TZ resistance mechanisms such as: (i) heterodimerization with other ErbB members or IGF-1R; (ii) the inactivation of Antibody-Dependent Cellular Cytotoxicity (ADCC); (iii) the expression of the p95-ErbB2 truncated form of the receptor that maintains its intracellular kinase domain; (iv) the decreased levels of expression of the tumor suppressor PTEN, and (v) the hyperactivation of PI3K/AKT pathway [25–30]. To limit TZ resistance, a new antibody called Pertuzumab has been developed [19,20,31,32]. Pertuzumab and TZ target two different domains of the ErbB2 receptor (domain II and IV, respectively), and this has proven to prevent heterodimerization with other ErbB receptors, thus limiting a possible cause of resistance. More recently, Margetuximab (Margetuximab) has been approved by the FDA based on data from a SOPHIA trial that demonstrated the major advantage of Margetuximab compared with TZ in combination with chemotherapy in pre-treated HER-2<sup>+</sup> metastatic BC patients [33]. Margetuximab has been associated with a significantly longer PFS and better OS with respect to TZ. As has been shown for other HER-2 inhibitors, one of the side effects that could occur from Margetuximab administration is the left ventricular dysfunction.

An interesting evolution of targeted therapy is the possibility of directly conjugating TZ with anticancer drugs (antibody-drug conjugates, ADCs), thus conferring an intrinsic HER2 targeting ability to the drug and reducing the toxicity of chemotherapy alone [34]. This approach was exploited to develop Trastuzumab emtansine (T-DM1, Kadcyla®, Genentech, San Francisco, CA, USA), one of the commercially available ADCs developed, starting from TZ. The efficacy of T-DM1 in metastatic HER-2<sup>+</sup> BC was first demonstrated in the EMILIA trial, where improved OS and PFS were observed in patients treated with TDM1 in comparison to those treated with Capecitabine plus Lapatinib [35]. More recently, the KRISTINE study has demonstrated better efficacy of T-DM1 in the adjuvant setting instead of its use as neoadjuvant therapy [16,19].

In addition to the mechanisms of action of TZ [30,36–38], T-DM1 exerts its anticancer activity through internalization in HER-2<sup>+</sup> cancer cells, where the conjugated drug DM1 prevents the assembly of the mitotic spindle, leading to cell cycle arrest. However, T-DM1 efficacy is still limited by the onset of resistance mechanisms adopted by tumor cells to evade DM1 activity, such as overexpression of drug efflux transporters that excrete DM1 outside BC cell [39,40]. Among the ADC categories, Trastuzumab Deruxtecan (T-Dxd, DS-8201, Enhertu®, Daiichi Sankyo, Tokyo, Japan) has recently received accelerated approval by the FDA on the basis of its adequate efficacy and safety demonstrated in the DESTINY-Breast01 study. T-Dxd is recommended for the treatment of patients with unresectable or metastatic HER-2<sup>+</sup> BC who have already received at least two or more prior anti-HER-2<sup>+</sup> treatments [41]. The conjugated cytotoxic drug Dxd is a topoisomerase I inhibitor attached to TZ with a tetrapeptide-based linker. It is stable in the plasma but easily cleavable near tumor cells because of the presence of cathepsins highly expressed on their surface. Indeed, the drug has selective permeability of the cell membrane of tumor cells in HER-2<sup>+</sup> low-expressing cells [42]. Despite the great potential of the response in T-DM1-resistant HER-2<sup>+</sup> BC, T-Dxd can lead to interstitial lung disease. In fact, adverse reactions caused by its administration are currently under investigation in ongoing clinical trials.

### 1.3 HER-2 Pathway Inhibitors and Immunotherapy

In addition to mAb and ADCs, another HER-2 targeted therapeutic strategy is blockade of the main cellular pathways leading to the characteristic aggressiveness of HER-2<sup>+</sup> BC, such as PI3K/AKT/mTOR and MAPK pathways, by using specific inhibitors. The aberrant activation of PI3K/mTOR/AKT pathway in BC is mediated by the mutation of the PI3KCA gene (more frequent in ER<sup>+</sup> and HER-2<sup>+</sup>) [25], which results in its hyperactivation with consequent dysfunction in the PTEN gene, resulting in AKT overactivation. These mutations lead to uncontrolled cell growth, migration and deregulated apoptosis [43,44]. Several examples of PI3K/AKT/mTOR pathway inhibitors have been developed, all interfering with one or more of the pathway's components. Among these, the most promising ones are: Everolimus, Alpelisib, Taselisib and Buparlisib [45]. Everolimus in combination with Paclitaxel or Vinorelbine and TZ has displayed increased efficacy in metastatic BC patients, although it did not affect PFS [45]. Typically, these inhibitors are used in relapsed BC as a second-line treatment to induce cell death and inhibit cancer cell proliferation.

Another HER-2-targeted therapy is based on small tyrosine kinase inhibitors (TKIs), such as Neratinib, Lapatinib, Tucatinib and Afatinib [46,47]. These inhibitors are used in advanced or relapsed HER-2<sup>+</sup> BC as a second-line treatment and are able to inhibit HER-2 receptor kinase activity. Neratinib, which has been validated in combination with Capecitabine in advanced or metastatic HER-2<sup>+</sup> BC [46,48–50], has resulted in a higher rate of pathological complete response (pCR) in comparison to TZ plus chemotherapy [48]. Moreover, Lapatinib in combination with Capecitabine has improved the OS in patients previously treated with TZ and standard chemotherapy [51], although mechanisms of resistance often arise.

Since increased levels of tumor-infiltrating lymphocytes (TILs) in HER-2<sup>+</sup> BC have been associated with a higher rate of pCR, good prognosis and improved survival after neoadjuvant chemotherapy [52], an immunotherapeutic approach has also been proposed in the last few decades. Indeed, the expression of PD-L1 in HER-2<sup>+</sup> BC is associated with increased OS [53] and monoclonal antibodies such as, Atezolizumab, Pembrolizumab, Nivolumab, directed against PD-1 receptor and its ligand PD-L1, are able to restore antitumoral immunity [54–56].

## 3. Nanotechnological Strategies to Target HER-2 Receptor

Despite the available HER-2 targeted therapies described above, a significant fraction of patients relapse or progress due to the escape mechanisms adopted by HER-2<sup>+</sup> cancer cells in response to inhibitory therapies. Nanotechnology promises to overcome some of these clinical challenges by the development of novel HER-2-guided nanosystems suitable as powerful tools in cancer imaging, targeting and therapy [57]. During the past 10 years, there has been an increase in the number of scientific publications based on nanotechnological strategies addressing HER-2<sup>+</sup> BC specifically [58]. Hence, our intention is to propose a comprehensive review concerning the main approaches for therapy and diagnosis to fight HER-2<sup>+</sup> BC developed in the last decade.

Most engineered NPs developed for HER-2<sup>+</sup> BC therapy take advantage of HER-2 receptor targeting strategies. Active targeting techniques have been employed by applying ligands to NP surfaces, such as antibodies, peptides and aptamers, that selectively recognize overexpressed receptors on cancer cells. This is aimed at accumulating the nanosystem in the cancer-affected areas, as well as favoring controlled and specific internalization in tumor cells, resulting in enhanced therapeutic efficacy [57]. Achieving specific targeting is so crucial that researchers constantly propose new strategies to drive the HER-2 targeting process. As said, the plethora of proposed solutions is so wide that finding the most robust ones to guide further translational research is an extremely hard task.

Here, we describe the most recent and successful strategies used to functionalize NPs with specific HER-2 targeting agents (Figure 1I–IV). As this is strictly related to improving the interactions of these agents with their target cells, this section is mainly focused on approaches involving *in vitro* research and, when available, we provide a short description of their *in vivo* application.



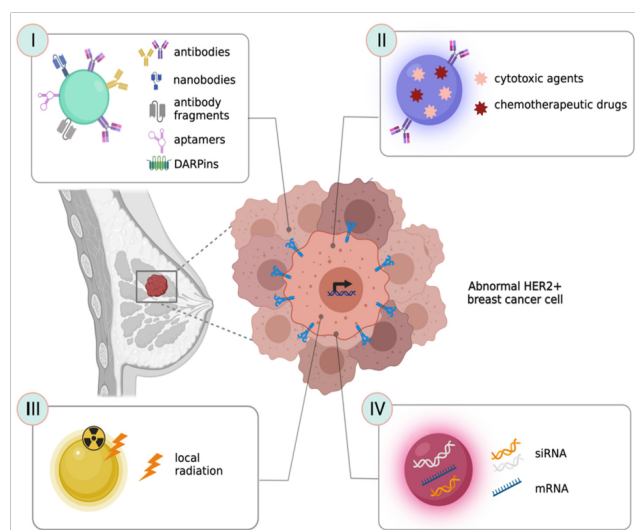


**Figure 1.** Strategies for HER-2<sup>+</sup> BC therapy (I) NPs functionalized with HER-2 targeting ligands ensure a specific targeting into HER-2<sup>+</sup> cancer cells; (II) NPs can vehicle chemotherapeutic drugs or cytotoxic agents into HER-2<sup>+</sup> cancer cells; (III) NPs functionalized with photothermal agents can promote local radiation to obtain tumor ablation; (IV) NPs can deliver nucleic acids or gene silencing molecules to enable gene expression regulation and overcome the insurgence of resistance to conventional therapies.

### 3.1. Antibodies as Ligands to Target HER-2<sup>+</sup> Cancer Cells

Therapeutic antibodies are widely employed in the surface functionalization of targeted nanosystems that can vehicle chemotherapeutic drugs, gene silencing agents or diagnostic molecules for the diagnosis and treatment of HER-2<sup>+</sup> cancer cells [59]. These antibodies can be anchored to different types of NPs through two main approaches: adsorption or covalent conjugation [57,60]. Functionalization through adsorption methods is simpler, compared to covalent binding strategies, but is less stable. On the other hand, it can facilitate the release of the mAb in the tumor site, enforcing its anti-cancer activity [61]. However, adsorption methods require greater amounts of mAb resulting in a more expensive procedure. Otherwise, covalent binding provides excellent reproducibility and is less subject to spontaneous disassembly. Moreover, covalent binding can be used to obtain orderly antibody orientation when compared with adsorption, since it takes advantage of different conjugation strategies such as carbodiimide chemistry, maleimide chemistry and click chemistry [57,60,62].

TZ is the most widely explored mAb to obtain HER-2 targeted nanosystems for BC therapy [57,61]. In the next paragraph, we focus on the plethora of NPs exploiting TZ conjugation proposed in the last decade.

Several gold-based NPs, such as nanospheres [63–65] and nanorods [66] covalently conjugated with TZ have been proposed to specifically target the HER-2 receptor. In addition, different kinds of polymeric NPs take advantage of the targeting mediated by TZ. Zhang et al. proposed an example of lipid-polymer hybrid NPs electrostatically conjugated with TZ [67], while a similar approach was applied to a novel NP delivery system obtained from polyethylenimine (PEI) and poly (D,L-lactide-co-glycolide) (PLGA) by Yu et al. [68]. Other examples of polymeric NPs exploited a covalent conjugation with TZ to specifically interact with the HER-2 receptor in HER-2<sup>+</sup> BC [69–71], while Dominguez Ríos et al. proposed a solution based on an HER-2-targeted PLGA nanoplatform covalently biofunctionalized with TZ for HER-2<sup>+</sup> ovarian cancer [72]. Moreover, magnetic [73,74], carbon-based [75,76] and protein-based [77] NPs conjugated with TZ have been studied.

One of the main advantages of functionalizing NPs with TZ is that the mAb is commercially available, it has been widely used at a clinical level, and its activity is widely demonstrated. On the other hand, one of the main disadvantages of such an approach is the high molecular weight of TZ (approximately 148 kDa) and its relatively large size (around 12 nm) that might significantly modify the physicochemical characteristics of the smallest NPs, and hence their biodistribution. TZ could be used with more success to functionalize bigger NPs, such as polymeric ones that are ten times bigger than the mAb. Another limitation is rapid blood clearance due to increased reticuloendothelial system kidnapping of full antibody-targeted NPs mediated by the Fc recognition site expressed by antigen-presenting cells [78]. Finally, due to their high affinity, anti-HER-2 mAbs can bind HER-2 receptors not only on cancer cells, but also on healthy cells. This specific yet non-selective binding to HER-2 receptors on healthy cells can lead to a reduction in drug concentration at the tumor site coupled with undesired toxic effects in off-target cells/organs [79].

### 3.2. Nanobodies and Antibody-Fragments as Ligands to Target HER-2<sup>+</sup> Cancer Cells

As an alternative to the use of whole mAbs such as TZ, nanobodies and antibody fragments can be used to address HER-2<sup>+</sup> BC [80,81]. Indeed, these molecules, smaller in size, succeeded in improving targeting and anticancer activity, since they interfere to a limited extent with the physical and chemical features of the NP [59]. In contrast to what is observed with

full antibody-targeted NPs, smaller antibody fragments seem to provide enhanced pharmacokinetic profiles and increased tumor tissue penetration [78,80,82].

Among small targeting moieties exploitable to address the HER-2 receptor, singledomain antibodies (sdAb), also known as nanobodies, were recently proposed for their interesting properties [81,83]. Nanobodies are small antigen-binding fragments (~15 kDa) derived from heavy-chain only antibodies present in camelids [84]. It has been reported that these types of molecules display low immunogenicity due to their similarity to human immunoglobulin heavy-chain (VH) sequences, and improved penetration into solid tumors due to their smaller size. Moreover, they have increased solubility and stability compared to full-size human/humanized monoclonal antibodies. Nanobodies targeting a wide range of receptors, including HER-2, have been developed. The HER-2-targeted nanobody 11A4 was used to achieve improved and selective uptake of polymeric NPs in HER-2<sup>+</sup> BC cells SKBR3 as compared to HER-2 MDA.MB.231 cells [84], while the sdAb C7b conjugated to silica NPs has been used to delivery drugs, imaging and theranostic agents [81]. Indeed, in vitro studies in SKBR-3 demonstrated a significantly higher uptake of the silica-based-C7b NPs compared to HER-2 larynx carcinoma Hep2 cells, and an improved performance in photodynamic treatment in an SKBR-3 xenograft murine model [81].

As an alternative to nanobodies, the use of antibody fragments (Fab) has been evaluated as an HER-2 targeting tool. Similar to nanobodies, Fab are reported to be less immunogenic and, due to their reduced size, should be less prone to alter the physicochemical properties of NPs. Fab obtained by papain cleavage of TZ (TmAb) and panitumumab (PmAb) was employed by Houdaih et al. to obtain targeted polymeric NPs [80]. In another study, silica NPs were conjugated with the anti-HER-2 Fab-6His, finely tuning ligand density and orientation. In these NPs, the modulation of ligand density and orientation were demonstrated to reduce protein corona formation and to affect specific targeting towards SKBR-3 HER-2<sup>+</sup> BC in vitro, improving NPs targeting efficacy upon increasing the Fab density [85]. The superiority of Fabs compared to full mAbs as NP targeting molecules was clearly demonstrated by Duan et al. in vitro and in vivo. They compared targeting and accumulation of PLGA-PEG NPs loaded with curcumin and functionalized with full TZ or a particular TZ Fab in BT-474 HER-2<sup>+</sup> against MDA-MB-231 HER-2<sup>-</sup> BC cells. The authors reported a five-fold increase in NP accumulation into the tumor mass of heterotopic BT-474 tumor-bearing BALB/c mice when functionalized with the Fab as compared to the full antibody [78].

Single-chain variable fragments (scFv) derived from TZ have also been studied as targeting entities. Recently, Shi et al. reported the development of cell-derived exosome NPs genetically engineered to display two different mAb on the surface. Due to the presence of both anti-human CD3 and anti-human HER-2 derived scFv, this nanostrategy is capable of simultaneously targeting T-cell surface CD3 and cancer cell-associated HER-2 receptors, exhibiting enhanced and specific anti-tumor activity, both in vitro and in vivo, compared to SKBR-3, HCC 1954 HER-2<sup>+</sup> and MDA-MB-468 HER-2<sup>-</sup> BC cells using an HCC 1954 xenograft tumor model [86].

### 3.3. Peptides, Aptamers and Ankyrins as Ligands to Target HER-2<sup>+</sup> Cancer Cells

Among targeting molecules, small peptides derived from TZ have been considered another alternative NP functionalization strategy [79]. The anti-HER-2 peptide AHNP is a small exocyclic peptide derived from TZ. It is able to bind to the HER-2 receptor with high affinity (Kd = 150 nM), inhibiting effectively the receptor's kinase activity [87–89]. This peptide was recently exploited as a targeting moiety for different kinds of NPs: a polymeric nanoconstruct bearing HER-2 specific antisense oligonucleotides [88], liposomal NPs [79] and iron oxide NPs [89]. An innovative approach was proposed by Zhang et al. that uses non-toxic transformable peptides able to self-assemble into micelles under aqueous conditions, following interaction with HER-2 on HER-2<sup>+</sup> BC cells [90]. Another strategy exploited to target HER-2 is represented by the use of aptamers. These consist of single-stranded DNA or RNA with unique tertiary structures that allow them to specifically bind to target molecules [91]. Smaller size, low immunogenicity, good tissue penetration and easy manipulation are prominent features for their use. Moreover, the implementation of aptamers to functionalize NPs holds great promise for targeted drug delivery and cancer therapy [92]. Recently, several aptamer-decorated NPs have been designed to address HER2<sup>+</sup> BC. Gold nanoconstructs conjugated with anti-HER-2 aptamers have demonstrated the ability to recognize HER-2 on SKBR-3 cells and then to be internalized via HER-2-mediated endocytosis. Accumulation of these complexes in lysosomes resulted in accelerated degradation of HER-2 and the suppression of cancer cell growth [93]. In addition, pH-responsive mesoporous silica NPs functionalized with anti-HER-2 aptamers [94], and albumin NPs decorated with a new DNA aptamer named HB5, obtained by exponential enrichment technology, have also been proposed [92]. Moreover, DNA-based nanorobots functionalized with anti-HER-a aptamers have been developed. Ma and coworkers designed and explored in vitro the potential of SKBR-3 cells with a tetrahedral framework of nucleic acids decorated with an anti-HER-2 aptamer, and showed that the construct is able to specifically target HER-2<sup>+</sup> BC in SKBR-3 cells and induce lysosomal degradation of HER-2 [95].

An interesting targeting strategy as an alternative to antibodies, is the use of designed ankyrin repeat proteins (DARPs). Ankyrins are naturally occurring proteins that act as a link between a variety of cell membrane proteins and the spectrin-actin cytoskeleton in a non-immunoglobulin-based approach [96]. DARPs are recombinant engineered binding proteins with a binding affinity comparable to antibodies, but with smaller size, higher stability, and cheaper production methods [97,98]. A DARPs-based drug (Abicipar pegol) is now under clinical evaluation for age-related macular degeneration [99]. In the context of HER-2<sup>+</sup> BC, several DARPs have been shown to bind to different extracellular HER-2 domains with low nanomolar affinity and extremely high specificity. This was confirmed in both highly overexpressing

SKBR-3 cells and mildly overexpressing MCF7 cells [100]. Moreover, DARPins were used to evaluate HER-2 expression in paraffin embedded tissues from cancer patients, showing again high specificity and equivalence with traditional anti HER-2 immunohistochemistry [101]. In vivo experiments with CD1-FOXn1/nu SK-OV3 bearing mice showed that by PEGylating DAPRins, their biodistribution and a high tumor-blood ratio but were affected by a rapid clearance, while PEGylated DAPRins had much slower clearance that, on one hand, further increased tumor accumulation, but on the other hand decreased the tumor-blood ratio [102]. In this context, DARPins have been used to functionalize different types of NPs, including magnetic and paramagnetic NPs, gold nanorods, and polymeric NPs as novel diagnostic, therapeutic and theranostic agents [103–105]

Finally, an interesting approach exploits NPs obtained from molecularly imprinted polymers that obstruct the HER-2 signaling by blocking the dimerization site of HER-2 receptors and thereby suppressing the growth of SKBR-3 HER-2<sup>+</sup> BC as compared to MCF-7 HER-2<sup>-</sup> basal cells. These imprinted NPs target HER-2 via binding to its glycans differently from the other biochemicals and chemicals, which target HER-2 by binding to one of its domains or sub-domains [106].

In summary, among all the different classes of HER-2<sup>+</sup> BC targeting nanoagents, it is still impossible to identify the winning strategy. The choice should depend on the final intended application and NP of election. It has already been discussed that small NPs could not be functionalized with whole antibodies without the risk of altering their pharmacokinetics and stability profiles. In parallel, if NPs are developed with a therapeutic goal, the targeting agent should retain the same anticancer activity observed for TZ. Having said that, all reported results seem very interesting and promising and a new class of nanoagents able to specifically target HER-2<sup>+</sup> BC to deliver cytotoxic or contrast agents would allow us to solve two major unmet clinical needs: (i) the insurgence of resistance mechanisms to available TZ-based targeted therapies and (ii) the difficulties encountered in the process of diagnosis. In this context, the difficulties that physicians have in precisely quantifying HER-2 levels in patients still limit the prescription of proper treatments and the prediction of their efficacy [107]. Both these aspects are evaluated in detail in the following paragraphs.

## 4. Nanotechnological Strategies for the Treatment of HER-2<sup>+</sup> BC

### 4.1. Strategies to Deliver Chemotherapeutic Drugs and Other Cytotoxic Agents

In recent years, NPs functionalized with the above-mentioned HER-2 targeting ligands have been exploited to deliver different kinds of therapeutic agents in HER-2<sup>+</sup> BC. The vast majority of them have been investigated by in vitro assays at the preclinical level.

Among these, we can find several interesting and convincing works, as summarized in Table 1 and Table 2. TZ-coated polymer-based NPs loaded with docetaxel showed increased target selectivity, cellular uptake, and cytotoxicity in HER-2<sup>+</sup> BT474 cells but not in HER-2<sup>-</sup> control cells [67]. Cisplatin-loaded lipid, and/or polymer-based NPs, displayed higher in vitro efficacy in comparison to non-targeted NPs and free drug only in HER-2<sup>+</sup> SKOV-3 but not in HER-2<sup>-</sup> HCC70 cells [71]. Doxorubicin (DOX), widely exploited for therapeutic purposes in HER-2<sup>+</sup> BC, has been loaded into polymeric NPs functionalized with an antiHER-2 antibody and displayed higher cytotoxicity toward HER-2<sup>+</sup> MCF7 cancer cells than both non-targeted DOX-NPs and free DOX, without significantly damaging healthy cells [69]. Moreover, novel pH-sensitive, aptamer-conjugated mesoporous silica NPs loaded with DOX were described by Shen et al. These NPs released the drug in a pH-dependent manner, along with effective uptake and enhanced cytotoxic effects in HER-2<sup>+</sup> BC SKBR3 cells [94]. Several HER-2-targeted polymeric NPs have been studied in vitro for the delivery of paclitaxel (PTX), either alone [68] or in combination with everolimus [74]. PTX has also been delivered to HER-2<sup>+</sup> BC SKBR-3 cells using iron oxide NPs conjugated with an anti-HER-2/neu peptide, or using worm-like nanocrystal micelles functionalized with TZ [70].

Other works describe the in vivo efficacy of HER-2-targeted NPs loaded with chemotherapeutics. Pegylated carbon-based NPs conjugated with TZ and loaded with DOX have been proposed as well. These NPs are stable under physiological pH conditions but, in presence of the lower tumor environment pH and following endocytosis, DOX is released in a controlled manner resulting in high uptake and activity in vitro and in vivo in HER-2<sup>+</sup> BC (SKBR-3 models) [75]. Finally, pegylated DOX liposomes conjugated with an anti-HER-2 peptide [108] or with an anti-HER-2 affibody [109] demonstrated good potential in the treatment of a TUBO HER-2<sup>+</sup> BC model in vivo.

HER-2-targeted NPs have been exploited for intratumor delivery of the ribosome-inactivating protein saporin [84]. PLGA NPs decorated with HER-2 nanobody and loaded with saporin selectively induced cell death of SKBR-3 cells in combination with Photochemical Internalization (PCI). This technique uses a photosensitizer and local light exposure to trigger endosomal escape of entrapped nanocarriers [84].

Another drug encapsulated in TZ-functionalized polymeric NPs is the anti-SRC kinase inhibitor Dasatinib. In this case, the nanoformulation improves its in vitro cytotoxicity against BT474 HER-2<sup>+</sup> BC cell lines [110]. Curcumin has also been nanoformulated and exploited for BC treatment using SKBR-3 human serum albumin NPs decorated with an anti HER-2 aptamer [92].

An albumin nanoformulation for the delivery of Lapatinib has been suggested, too. The ability of being internalized and inducing apoptosis was confirmed in SKBR-3 cells and stronger anti-tumor efficacy compared to lapatinib alone was determined in tumor-bearing mice with no sub-chronic toxicity [111].

#### 4.2. Strategies to Vehicle Nucleic Acids or Gene Silencing Molecules

Short interfering RNA (siRNA) molecules are a class of double-stranded non-coding RNA molecules. In recent years, they have been extensively studied in BC as an emerging class of drug, since they are able to regulate gene expression. With the use of siRNAs, it is possible to inhibit specific genes and perform cancer treatment of undruggable targets. However, siRNAs cannot not be employed *in vivo* as such, since they are affected by inherent instability [112]. In the attempt to overcome issues of resistance to conventional therapies, Gu et al. developed mesoporous silica NPs conjugated with HER-2-targeting antibodies to deliver HER-2 siRNA, demonstrating *in vitro* that HER-2<sup>+</sup> BC cells usually do not develop resistance to HER-2 siRNA compared to TZ or lapatinib. Moreover, this siRNA can silence HER-2 at the mRNA level, preventing adaptational changes and survival mechanisms in BT474, SKBR-3 and HCC1954 cells. The authors conclude that ablation of HER-2 receptor using HER-2 siRNA [113] could overcome the reactivation of signaling in a BT474 *in vivo* model, typical of cells resistant to different chemotherapies (e.g., lapatinib) [114,115].

Cristofolini et al. studied a magnetic hybrid nanostructure of iron oxide stabilized by caffeic acid coating for magnetic responsive delivery of negatively charged siRNA entrapped in a middle layer of calcium phosphate. This structure, externally coated with PEG to improve colloidal stability and evading immune system recognition, is able to enhance the delivery of HER-2 siRNAs to a human HCC1954 BC cell line *in vitro* [116]. In another work, siRNA delivery was improved by assembling RNA-based NPs designed to resist nucleases. This novel nanostructure has highly efficient gene silencing ability, tumor targeting specificity, and chemical and thermal stability. In addition, a 2'-F-modified 3WJHER-2aptasiXBPI siRNA has been incorporated in the NPs, becoming more metabolically and structurally stable and displaying a higher renal filtration clearance [117].

Another advantage of using NPs is the possibility of co-loading them with more than one agent to perform a dual therapy. Indeed, the combination of a newly developed HER-3 siRNA and TZ has been used for the treatment of HER-2<sup>+</sup> BC using polyethyleneiminefunctionalized carbon dots. Overexpression of HER-3, a member of ErbB receptor family, is associated with TZ resistance. In recent studies, it has been demonstrated that siRNAs that targets HER-3 can increase antitumoral efficacy of TZ in HER-2<sup>+</sup> cancer cells. Therefore, a combination therapy of TZ and an HER-3 specific siRNA is effective in blocking HER-2/HER-3 signals, since increased tumor penetration downregulates HER-3 overexpression and is able to inhibit proliferation of BT474 cells without inducing resistance to the therapy [76].

Another study reported the use of a polymalic acid-based mini nanodrug attached to HER-2-specific antisense oligonucleotides and peptides able to target HER-2 receptors on BT474 cells [88]. Here, the authors claim that the shape and size of their mini nanodrugs are important in enhancing penetration of multiple bio-barriers by the nanoconstructs to enhance their therapeutic efficacy.

Finally, NPs have been used to deliver the mRNA of TZ *in vivo* to overcome many of the gaps in antibody production and therapeutic application. The mRNA encoding for TZ was protected from degradation by encapsulation into lipid-based NPs designed to allow liver-targeted production of TZ. In this way, prolonged expression of full-size TZ was achieved in the liver, providing an effective cancer treatment and offering a valuable alternative to protein administration [118].

#### 4.3. Nanostrategies to Improve Radiation Efficacy in HER-2<sup>+</sup> Tumors

Radiation therapy is widely used both in the treatment of early and advanced stage BC and as palliative treatment to mitigate pain in patients with metastatic BC. This procedure takes advantage of high energy beams to kill cancer cells and shrink tumor masses.

Gold pegylated NPs linked to TZ and complexed with Auger electron-emitter <sup>111</sup>In, showed inhibition of tumor growth *in vitro* and *in vivo* (SKBR-3 models) without toxicity to normal tissues. In addition, the author showed the critical role of functionalization in increasing the internalization capacity of NPs in HER-2<sup>+</sup> cells [64]. In another report, TZmodified AuNPs labeled with <sup>177</sup>Lu were developed to target the HER-2 receptor on SKBR-3 and BT474 BC cells, and were more effective in inhibiting tumor growth *in vivo* compared with non-targeted AuNP-<sup>177</sup>Lu [119]. Magnetite NPs can be exploited in antitumor local radiation. Modifying the magnetite core using  $\alpha$  emitter <sup>225</sup>Ac, it is possible to obtain a combination of ionizing radiation and magnetic hyperthermia in a single drug, while the TZ conjugation confers tumor targeting specificity in SKOV-3 cells [73].

A completely new radiation therapy, named  $\alpha$ -nanobrachytherapy, has been proposed for solid unresectable tumors. This approach has been utilized for selective therapy of HER-2<sup>+</sup> BC and involves the injection of 5 nm diameter gold NPs labeled with an <sup>211</sup>At emitter, and the  $\alpha$  irradiation of bismuth target. NPs used in this approach are stabilized with PEG and conjugated with TZ to achieve target selectivity. <sup>211</sup>At-AuNPs-PEG-TZ can be effectively used as a local therapy for HER-2<sup>+</sup> cancers, as suggested by *in vitro* studies with ovarian SKOV-3 cancer cells [65].

Radioactive upconversion NPs (UPNPs) coupled with the beta-emitting radionuclide yttrium-90 (<sup>90</sup>Y) and functionalized with specific DARPins binding HER-2 (DARPin 9-29) were shown to improve therapeutic efficacy in SK-BR-3 HER-2<sup>+</sup> cells compared to HER-2<sup>-</sup> CHO cells. Moreover, these NPs confirmed their therapeutic activity in HER-2 xenograft tumors *in vivo*, where they delayed and reduced tumor growth after intratumor injection [120]. Even if promising, this approach should be further improved by carefully evaluating off-target toxicity after systemic administration.

Another emerging field of local radiation is represented by photothermal therapy (PTT). PTT is a minimally-invasive therapeutic approach based on the toxic effect produced when specific photothermal agents that accumulate into the tumor

are locally irradiated with an external source to convert this energy into heat that shrinks the tumor mass. NPs with the ability of specific tumor accumulation and high photothermal conversion rate have been proposed to improve PTT efficacy. Among these, gold nanorods display interesting properties. Indeed, by tailoring the size and shape of nanorods it is possible to tune the near infrared wavelength of absorption, transforming them into extremely good photothermal agents [66]. However, bare gold nanorods cannot effectively target the tumor, thus limiting their efficacy. Therefore, Kang et al. designed gold nanorods (GNRs) functionalized with TZ and porphyrin, obtaining improved targeting specificity and significantly higher inhibition of tumor growth in a BT474 xenograft in vivo model [66]. This study showed how GNRs represent a promising tool for the treatment of HER-2+ BC. DARPins have also been used as targeting moieties to improve SKBR-3 HER-2+ cell accumulation of UCNPs to be used as PTT agents. This approach was confirmed in vivo in a Lewis lung cancer (LLC) mouse model, in which the administration of functionalized UPNCs reduced tumor growth after a single laser irradiation [121].

**Table 1.** Summary of all significant examples of organic NPs developed for HER-2+ BC therapy.

	Mechanism of Action and Targeting Molecule	Achievements	NP Type		Reference
Antibodies	Targeted delivery of anticancer drug. TZ ( <i>LuyePharma, Yantai, China/Genentech, South San Francisco, CA, USA</i> )	- Increment of anticancer activity, decrease of toxicity towards healthy cells - Lower chemotherapeutic dose required for treatment	Polymeric/lipid	in vitro	[67–71]
	Delivery of in vitro-transcribed mRNA coding for TZ	- Improved PK profile - Suppression of tumor growth - Reduction of off-target effects	Lipid	in vitro—in vivo	[118]
	Targeted delivery of anticancer drug. TZ ( <i>Roche, Basel, Switzerland</i> )	- Prevention of chemoresistance - Higher cytotoxicity on cancer cells	Polymeric	in vitro	[72]
	Release of anticancer drug in combination with TZ ( <i>Roche, Basel, Switzerland</i> )	- Effective neoadjuvant therapy with reduced toxicity	Albumin-bound Paclitaxel (nab-PTX)	clinical trial	[77]
	Targeted delivery of anticancer drug. TZ ( <i>Roche, Basel, Switzerland</i> )	- Improved NP stability - Induction of apoptosis and cell cycle arrest	Polymeric	in vitro	[110]

Table 1. Cont.

	Mechanism of Action and Targeting Molecule	Achievements	NP Type		Reference
Nanobodies and antibodies fragments (Fab)	Dual-targeted delivery of chemotherapeutics to HER-2 and EGFR. TZ—Panitumumab Fab fragments ( <i>In-house recombinant production</i> )	<ul style="list-style-type: none"> <li>- Enhanced tumor accumulation</li> <li>- Higher cellular internalization and cytotoxicity</li> </ul>	Polymeric	in vitro	[80]
	Targeted delivery of cytotoxic molecule after photochemical internalization. 11A4-nanobody ( <i>In-house recombinant production</i> )	<ul style="list-style-type: none"> <li>- Selective uptake</li> <li>- Strong inhibition of cell proliferation</li> </ul>	Polymeric	in vitro	[84]
	Targeted delivery of cytotoxic agent. TZ fragment ( <i>Genentech, South San Francisco, CA, USA</i> )	<ul style="list-style-type: none"> <li>- Enhanced cellular accumulation and higher cytotoxicity</li> <li>- Higher tumor permeability and in vivo half-life</li> </ul>	Polymeric	in vitro—in vivo	[78]
	Induction of tumor specific immune response. anti-HER2-anti-CD3 dual-scFv	<ul style="list-style-type: none"> <li>- Enhanced stability</li> <li>- Controlled antitumor immunity</li> <li>- Minimal toxicity and immunogenicity</li> </ul>	Cell-derived exosome	in vitro—in vivo	[86]
Peptides	Delivery of antisense oligonucleotide. NH2-PEG200-AHNP	<ul style="list-style-type: none"> <li>- Prevention of HER2 receptor synthesis</li> <li>- Inhibition of cancer cell proliferation</li> <li>- Reduction of tumor growth</li> </ul>	Polymeric	in vitro—in vivo	[88]
	Targeted delivery of cytotoxic agent. HER2 <sub>pep</sub> YCDGFYACY-MDV ( <i>In-house recombinant production</i> )	<ul style="list-style-type: none"> <li>- Higher binding activity to cancer cells and endocytosis of the drug</li> <li>- in vivo anti-tumor efficacy with minimal toxicity</li> </ul>	Liposome	in vitro—in vivo	[79]
	Generation of nanofibers able to disrupt HER2 dimerization. HER2 <sub>pep</sub> BP-FFVLK-YCDGFYACYMDV	<ul style="list-style-type: none"> <li>- Induction of cancer cell apoptosis</li> <li>- Effective in mouse xenograft model</li> </ul>	Peptide-based	in vitro—in vivo	[90]
	Targeted delivery of anticancer drug. AHNP (FCDFYACYADVGGG)	<ul style="list-style-type: none"> <li>- Higher uptake in tumor cells</li> <li>- Increased cytotoxicity and prevention of tumor growth</li> </ul>	Liposome	in vitro—in vivo	[108]
Aptamers	Targeted delivery of anticancer molecule. HB5 DNA aptamer	<ul style="list-style-type: none"> <li>- Good size distribution, solubility and long term stability</li> <li>- Higher cytotoxic effect</li> </ul>	Albumin-based	in vitro	[92]
	XBP1 deletion by therapeutic siRNA delivery. 3WJ-HER2 aptamer ( <i>In-house recombinant production</i> )	<ul style="list-style-type: none"> <li>- Higher tumor cell targeting and lower binding to healthy tissues</li> <li>- Increased gene silencing, suppression of tumor growth and prevention of drug resistance</li> </ul>	RNA-based	in vitro—in vivo	[117]
	Lysosomal degradation of membrane protein HER-2. HApt aptamer ( <i>TaKaRa Ostu, Japan</i> )	<ul style="list-style-type: none"> <li>- Induction of cell apoptosis and inhibition of cell proliferation</li> <li>- Enhanced stability and circulation time</li> </ul>	DNA nanorobot	in vitro—in vivo	[95]

Table 2. Summary of all significant examples of inorganic NPs developed for HER-2<sup>+</sup> BC therapy.

	Mechanism of Action and Targeting Molecule	Achievements	NP Type		Reference
Antibodies	Intratumor retention leading to an immune response activation. TZ (Genentech, South San Francisco, CA, USA)	<ul style="list-style-type: none"> <li>- Antitumor immune response without requiring a therapeutic payload</li> <li>- Reduced tumor growth</li> </ul>	Iron oxide	in vitro—in vivo	[74]
	Targeted photothermal ablation by near-infrared laser. TZ (Roche, Basel, Switzerland)	<ul style="list-style-type: none"> <li>- Enhanced targeting specificity</li> <li>- Inhibition of tumor growth</li> <li>- Limited damaging to surrounding tissues</li> </ul>	Gold nanorods	in vitro—in vivo	[66]
	Selective targeting of HER-2 Increase of pro-apoptotic proteins. TZ (Roche, Basel, Switzerland)	<ul style="list-style-type: none"> <li>- Higher stability and cellular internalization</li> <li>- Higher cytotoxicity related to survival-proliferation pathways decrease</li> </ul>	Gold nanospheres	in vitro	[63]
	HER-2 gene silencing by siRNA delivery. TZ (Roche, Basel, Switzerland)	<ul style="list-style-type: none"> <li>- Reduced proliferation and prevention of tumor initiating cells</li> <li>- More durable inhibition than existing therapeutic monoclonal antibodies and small molecules</li> </ul>	Carbon dots/mesoporous silica	in vitro	[76,114]
	Radio-immunotherapy Magnetic hyperthermia. TZ (Roche, Basel, Switzerland)	<ul style="list-style-type: none"> <li>- Enhanced cytotoxicity due to internal irradiation</li> <li>- Suitable for destroying micrometastatic cancer cells thanks to the reduced size</li> </ul>	Superparamagnetic iron oxide	in vitro—in vivo	[73]
	Antitumor local radiation. TZ (Roche, Basel, Switzerland)	<ul style="list-style-type: none"> <li>- Specific tumor cell binding and internalization and higher cytotoxicity</li> <li>- Inhibition of tumor growth</li> <li>- Suitable for the elimination of single micrometastatic cancer cells</li> </ul>	Gold NPs	in vitro—in vivo	[64,65,119]
	Targeted delivery of anticancer molecule. TZ (Roche, Basel, Switzerland)	<ul style="list-style-type: none"> <li>- Higher cellular uptake and lower toxicity</li> <li>- Efficient inhibition of antitumor activity</li> </ul>	Carbon-based	in vitro—in vivo	[75]



Table 2. Cont.

	Mechanism of Action and Targeting Molecule	Achievements	NP Type		Reference
Nanobodies and antibodies fragments (Fab)	Local irradiation (PDT). <i>sdAb C7b</i> (In-house recombinant production)	- Higher uptake rate - Local hyperaemia, oedema, necrosis after the first irradiation - Modest effect of PDT	Silica	in vitro—in vivo	[81]
	Improved targeting due to the reduced protein corona formation. Anti-HER2 Fab-6His (Hangzhou HealSun Biopharm Co., Ltd., Zhejiang, China)	- Enhanced cytotoxic effect	Silica	in vitro	[85]
Peptides	Targeted delivery of anticancer molecule Inhibition of kinase activity. AHNP (GenScript Inc., Piscataway, NJ, USA)	- Great stability in biological medium thanks to size and uniform shape - Improved targeted delivery of drug in vivo and in vitro	Iron oxide	in vitro—in vivo	[89]
Aptamers	Targeted delivery of anticancer molecule Downregulation of HER-2 Hapt is also an antagonist Synergic mechanism. HApt aptamer (Sangon Biotech Co., Ltd., Shanghai, China)	- Inhibition of cell proliferation by induction of apoptosis	Mesoporous silica nanocarrier	in vitro	[94]
	Downregulation of HER-2. (HApt aptamer IDA Inc., Coralville, IA, USA)	- Efficient lysosomal targeting - Inhibition of cell proliferation - Suitable for PTT applications	Gold nanostars	in vivo	[93]
DARPinS	Targeted delivery of <sup>90</sup> Y radionuclides and toxins. DARPin_9.29 (in-house recombinant production)	- Specific cytotoxicity of DARPin- <sup>90</sup> Y-UPNPs in SKBR-3 cells - Reduced tumor growth after <sup>90</sup> Y-UPNPs intratumoral injection in vivo	Upconversion NPs	in vitro—in vivo	[120]
	Photothermal therapy. DARPin_9.29 (in-house recombinant production)	- Specific cytotoxicity in SKBR-3 cells after laser irradiation - Reduced tumor growth after laser irradiation in vivo	Upconversion NPs	in vitro—in vivo	[121]

## 5. Detection of HER-2<sup>+</sup> BC: State of the Art and Clinical Needs

As already mentioned, HER-2 is an important clinical biomarker, as its overexpression or amplification is associated with greater aggressiveness and influences a patient's management [122,123]. Therefore, a precise quantification of HER-2 levels in patients is of fundamental relevance to guide doctors in elaborating the proper therapeutic strategy and predicting the response to therapy. The standard methods used in clinics to define HER-2 positivity are: (i) IHC, and (ii) FISH and chromogenic in-situ hybridization (CISH). IHC shows the amount of HER-2 protein in the sample, while FISH allows the determination of the number of copies of HER-2 present in tumor cells [124]. CISH is a diagnostic method that combines the chromogenic signal detection method of IHC techniques within situ hybridization [125].

Despite their wide use, these techniques have several limitations. First of all, IHC, FISH and CISH are highly invasive since they require tissue biopsies. Furthermore, their sensitivity and target specificity still need to be improved [125]. It has been reported that about 20% of HER-2 positivity diagnoses made with the available standard methods appear to be inaccurate [126,127]. Moreover, HER-2 expression in primary tumors and metastases is highly discordant, with several reported cases of HER-2<sup>-</sup> primary and HER2<sup>+</sup> metastases. Therefore, several biopsies should be made during the course of treatment, at least in uncertain cases, and not all metastatic foci are available for sampling. In addition, HER-2 gene overexpression may not correlated with protein levels, and FISH results may underestimate HER-2 levels. These aspects may significantly contribute to imprecise quantifications obtained by standard methods [128]. Based on these



considerations, it appears clear that the development of tools able to target HER-2 with high sensitivity, and in a simple and accessible way, would be of great help to enable an early diagnosis of the disease, thus guiding therapeutic choice and increasing the chances of survival [58]. These targeting agents should be able to evaluate HER-2 levels in primary tumors and small metastases, as well as working on circulating tumor cells to enable liquid biopsies [129].

## 6. Nanotechnological Approaches for HER-2<sup>+</sup> BC Diagnosis

Recently, several nano-based approaches have emerged as promising candidates for the detection and screening of HER-2<sup>+</sup> BC, including organic and inorganic NPs, QDs and aptamers (Table 3 and Figure 2) [58].

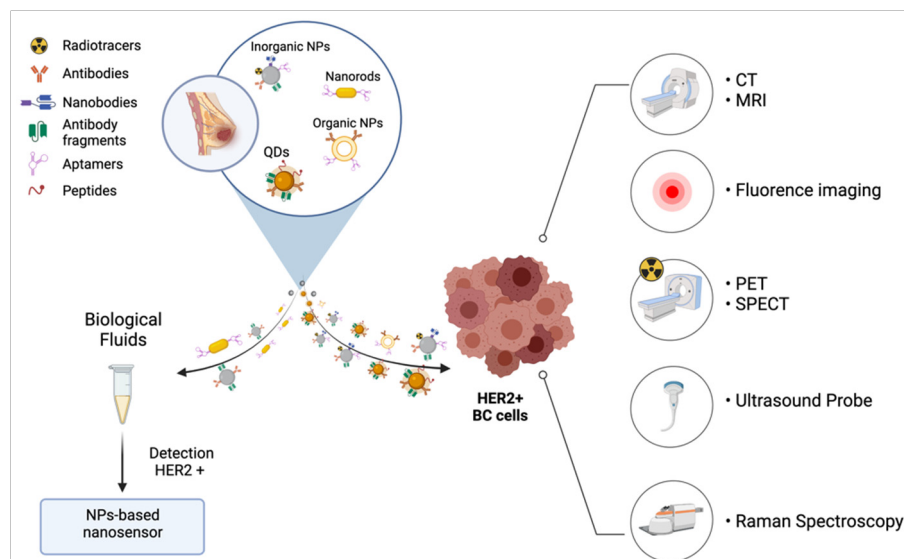


**Figure 2.** Nanotechnology approaches for HER-2<sup>+</sup> BC diagnosis.

### 6.1. Imaging Agents for Early Diagnosis and Tailored Therapy

Using innovative bioimaging techniques, HER-2-targeted NPs can allow oncologists to evaluate HER-2 expression more precisely than with traditional methods and to elaborate the correct therapeutic strategy more rapidly. The imaging techniques that have shown the most promising results are computerized tomography (CT), positron emission tomography (PET), single photon emission computed tomography (SPECT), ultrasounds (US), magnetic resonance imaging (MRI) and optical imaging [58,130,131]. These techniques have their own advantages and disadvantages. PET and SPECT have a much higher sensitivity compared to MRI, but much lower resolution and cannot provide any anatomical information [132].

Most of the targeting agents exploit the anti-HER-2 humanized monoclonal antibodies (Trastuzumab and Pertuzumab), mAbs, Fabs, scFv, etc. Labeling NPs with these targeting moieties has the dual advantage of conferring stability to the targeting agent and loading a single vector with many contrast agents, thus significantly increasing the specificity and intensity of the signal [133]. Moreover, the possibility of modifying the physico-chemical properties of the constructs, allows a much higher control of the biodistribution and clearance kinetics, thus improving tumor retention and allowing prolonged imaging of the tumor tissue [134].

#### 6.1.1. Magnetic Resonance Imaging and Computerized Tomography

MRI is a widely diffused non-invasive imaging tool used in the clinics for diagnosis of tumors. It is characterized by a high degree of soft tissue contrast, and spatial resolution without any limitation due to signal depth. To increase contrast, exogenous contrast agents are administered prior to scanning [132]. Chen et al., explored the possibilities of using superparamagnetic iron oxide NPs modified with dextran and conjugated with Herceptin for detecting HER2 in vitro and in vivo. The authors reported significant magnetic resonance enhancements for the different BC cell lines tested proportional to the HER2/neu expression level (SKBR-3, BT-474, MDA-MB-231, and MCF-7). When TZ-NPs were administered in vivo, the authors observed an accumulation of the contrast agent in the tumor sites, confirming their suitability for detection of HER2/neu-expressing BC [135].

In another work, PEGylated SPIONs were exploited to target HER-2<sup>+</sup> BC. The authors functionalized the particles with a single chain variable fragment directed against HER-2 and labelled them with a Cyanine (Cy) based fluorescent tag to provide dual tracking modality. These NPs demonstrated enhanced uptake into BC cells depending on their HER-2 expression level (BT474, SKBR-3, MDA-MB-231 and MCF-7) [136]. These results, together with their biodegradable nature and biocompatibility profile, represent prominent features for their use in early BC diagnosis.

Another approach is so called “supersensitive magnetic resonance imaging”, that uses contrast agents with a high R2 relaxivity (low T2, as  $R2 = 1/T2$ ) to enhance imaging sensitivity. In this context, Zhang et al., developed recombinant magnetosomes functionalized with an anti-HER-2 affibody that showed high specificity only for the SKBR-3 HER-2<sup>+</sup> BC model up to 24h after IV administration. Interestingly, the immunogenicity of the complex was controlled by chemically removing the lipid bilayer of the extracted magnetosome with a non-pyrogenic stealth lipid mixture. Moreover, the highly negative zeta-potential of the system ( $\approx -20$  mV) significantly reduced the nonspecific binding of magnetosomes to non-target cells. These small details confer to the study an even stronger translation potential toward safe clinical applications [137].

### 6.1.2. In Vivo Fluorescence Imaging

Fluorescence based techniques are widely used at a clinical level for all sorts of diagnostic assays. NIR infrared fluorescence bioimaging is emerging as a powerful technology especially for fluorescence-guided surgery, with many dyes already used at a clinical level, such as indocyanine green. Many tools are being tested preclinically, such as organic natural fluorescent dyes, hybrid fluorescent dyes, protein dyes, polymer dots, and quantum dots.

Quantum dots (QDs) are characterized by a tunable and narrow fluorescence emission spectrum, long lifetime and high optical stability compared to other organic fluorescent dyes [138]. However, their clinical development is limited by toxicity issues, as they are made using heavy metals [139]. Wei et al. developed a method for the identification of HER-2<sup>+</sup> BC using an HER-2 antibody with MnCuInS/ZnS QDs-loaded BSA fluorescence NPs [140]. Interestingly, the authors developed a method to produce heavy metal-free QDs, thus addressing the main concerns related to QD toxicity. In this work, the nanoprobe was tested in HER-2<sup>+</sup> SKBR-3 cells versus HER-2<sup>-</sup> MDA-MB-231 cells. After 4 h of incubation, the authors demonstrated by confocal microscopy that functionalized NPs were able to specifically target HER-2<sup>+</sup> cells with very low cytotoxicity. In another in vitro study, the direct conjugation of the anti-HER-2 antibody to the QD surface for detection of the HER-2 receptor was investigated in HER-2<sup>+</sup>, and HER-2<sup>-</sup> cells. An increase in the uptake of anti-HER-2-QD antibody conjugate was found only in SKBR-3 HER-2<sup>+</sup> cells [141]. Wang and colleagues screened two novel HER-2 targeting peptides, YLFFVFER and KLRLEWNR, and conjugated them to quantum dots to specifically target HER-2<sup>+</sup> in vivo in an SKBR-3 model [142]. Another study reported the possibility of using QDs conjugated with HER-2 targeting single-domain antibodies (sdAb), for detecting micrometastases and disseminated HER-2<sup>+</sup> tumor cells ex vivo [143].

Further, in vivo biodistribution and imaging studies will be important to confirm if these promising results can be translated in clinics, carefully evaluating targeting specificity and sensitivity, to detect single cells ex vivo.

### 6.1.3. Nuclear Medicine

Nuclear imaging techniques such as PET and SPECT represent powerful tools to allow HER-2<sup>+</sup> BC visualization. These have been the first clinically approved molecular imaging modalities and nowadays are widely diffused in clinical practice, with <sup>18</sup>Ffluorodeoxyglucose and <sup>99m</sup>Tc being the most common tracers used for PET and SPECT respectively [130]. However, these agents lack any tumor specificity, and researchers have been developing several engineered tracers with cancer targeting ability. In the case of HER-2<sup>+</sup> cancers, numerous studies have developed radiotracers conjugated with TZ, TZ antibody fragments, affibodies, nanobodies and aptamers to allow specific tumor targeting. Among these, Xavier C. et al. used <sup>18</sup>F labelled with an anti HER-2 nanobody as a PET contrast agent and demonstrated a significantly higher tumor-to-blood ratio, at 1h and 3h after injection, for the targeting tracer compared with non-targeting tracer in a SKOV-3 xenograft model. All agents were quickly cleared through the kidneys [144]. Similarly, Ahlgren et al. used anti HER-2 affibodies labelled with <sup>99m</sup>Tc as specific SPECT cancer imaging agents in two in vivo BC xenograft models with different HER-2 expression. Interestingly, they showed high tumor accumulation of the engineered probes 4h after injection, and this was proportional to the HER-2 expression levels. Moreover, with a modification to the C-terminal cysteine of the construct, they were able to reduce off-target liver uptake [145].

Although interesting, these solutions have limitations, such as low contrast and short half-life, that limit the temporal window to obtain optimal imaging acquisitions. Due to advantages offered by nanotechnology, such as high loading capacity and multiple surface functionalization, it has been possible to develop radiolabeled probes with higher contrast and favorable biodistribution kinetics compared to standard imaging probes [146]. However, most of the studies found in the literature rely on passive tumor targeting, mediated by the so-called Enhanced Permeation and Retention (EPR) effect [147], while only a few works exploit specific surface functionalization to enhance tumor targeting. An example of specific tumor targeting in an HER-2<sup>+</sup> BC attempt was described by Rainone et al. [148]. The authors developed <sup>99m</sup>Tc-radiolabeled silica NPs functionalized with a TZ half-chain and verified the nanoprobe specific affinity with SKBR-3 HER-2<sup>+</sup> BC cells in vitro, and in the relative xenograft animal model ex vivo.

Tumor radioactivity was higher in animals treated with TZ -functionalized probes as compared to non-functionalized ones. However, this difference was not statistically significant since at longer time points the advantage of functionalization was lost [148]. These results suggest that further research needs to be done to optimize NP characteristics and imaging set up to confirm the potential impact of nanotechnology in promoting HER-2 targeting probes for nuclear imaging. Other studies have co-loaded nuclear medicine radiolabels and chemotherapeutic agents inside the same nanocarriers to combine

diagnosis and therapy in the so-called theranostic [149,150]. These are addressed in a dedicated section at the end of this review (Section 7).

#### 6.1.4. Multimodal Hybrid Approaches

As previously said, all imaging techniques have intrinsic advantages and disadvantages. A possible solution would be coupling more than one imaging approach within the same nanoplatform. This is a very powerful approach that could lead to improved diagnosis and should be explored in detail.

An early work using multimodal imaging was reported by Jang et al. [151]. The authors used silica core shell NPs, both fluorescently and magnetically labelled, for fluorescence imaging and MRI (in vitro). The particles were targeted with TZ and provided high contrast in HER-2<sup>+</sup> SKBR-3 cells. Even if very preliminary, these NPs could be interesting agents for further multimodal in vivo imaging applications. Similarly, Li et al. used DARPIn G3-coated fluorescently labelled SPION for HER-2<sup>+</sup> cells and a tumor model in vitro and in vivo, respectively. The authors showed that functionalized SPIONs had a significantly higher binding with SKBR-3 HER-2<sup>+</sup> cells than with MDA-MB-231 HER-2<sup>-</sup> ones. This behaviour was also observed in mouse models, in which, by MRI, much higher contrast in SKBR-3 tumor bearing mice than in MDA-MB-231 bearing mice was observed [104]. Interestingly, the DARPIn G3 has a different binding site compared to TZ, suggesting that DARPIn G3 based HER-2 targeting ability should not be influenced by treatment with TZ.

Ultrasound molecular imaging has undergone significant evolution due to the development of specific ultrasound contrast agents offering high tumor selectivity and high sensitivity [152]. Li et al. used US and MRI in a SKBR-3 in an in vivo model to evaluate the targeting ability and biodistribution of iron oxide-doped silica NPs functionalized with an anti-HER-2 antibody. Even if the synthesized NPs had a short blood half-life (with a peak 60 min after administration) and high liver uptake, mainly due to their large size (diameter of approximately 200 nm), the authors observed specific intratumoral accumulation of NPs both by US and MRI within minutes after administration [153]. Even if the increase in image contrast was not significant between the target and the control group, and the possibility of visualizing metastases was not explored, the idea of coupling these two imaging modalities is extremely interesting.

In another work by Chen et al., MRI was coupled with CT, demonstrating the possibility of specifically imaging an HER-2<sup>+</sup> in vivo model with a generation 5 Polyamidoamine (PAMAM) dendrimer covalently linked to gold NPs and gadolinium, and functionalized with TZ [154]. The authors reported a significant increase in both MRI and CT contrast (30% and 13% respectively) 4 h after IV administration of functionalized dendrimers, as compared to non-functionalized ones. Biodistribution and MRI proved the persistence of functionalized dendrimers in the tumor up to 48h, while the signal in non-target organs started decreasing 4h after administration. The specificity and the possibility of such a wide imaging window are the major strength of this nanotool, that may allow early and non-invasive diagnosis of both HER-2<sup>+</sup> primary tumors and metastases.

Other approaches to address HER-2<sup>+</sup> BC, involve the use of SPIONs-Cy-PEG-scFv as a targeted imaging agent in vivo. The authors reported a significant increase of MR signals in BT474 HER-2<sup>+</sup> tumor-bearing mice 24h after injection, compared to non-functionalized NPs, indicating specificity scFv versus HER-2 overexpressing cells/tumors [136].

In 2018, Chen et al. showed how dual radio (89Zr)-labelled and fluorescently (Cy5.5)labelled ultra-small silica NPs functionalized with anti-HER-2 scFv fragments specifically accumulated in HER-2<sup>+</sup> BT474 tumors [155]. Perfectly aware of the off-target distribution issue, the authors explored NPs with proper size and surface characteristics to avoid offtarget distribution in the liver and limited renal filtration. After 24h, the particles seemed to reach a peak concentration in the tumor that was maintained at an approximately stable level until 72 h after administration. By contrast, the off-target signal slightly decreased. Results showed the highly specific tumor accumulation and clear targeting potential of such NPs.

### 6.2 Nano-Biosensors for the Detection of HER-2 Levels in Biological Fluids and Tissues

Another huge area of research is the development of novel nano-biosensors able to detect and quantify HER-2 in blood or small tissue samples collected from patients. This approach is of extreme interest and would allow an early diagnosis of HER-2<sup>+</sup> BC, the possibility of predicting recurrence, detecting metastases, and improving treatment regimen in the case of low response and acquired resistance to target therapies [156].

#### 6.2.1. Inorganic NPs-Based Nanosensors

A successful nanotechnological non-invasive approach for detecting and quantifying HER-2 levels in serum samples obtained from patients was developed by Emami et al. [157]. The authors developed a label-free immunosensor consisting of pegylated iron oxide NPs conjugated with anti-HER-2 antibodies. This non-invasive strategy was highly sensitive, responding to HER-2 concentrations over the ranges of 0.01–10 ng mL<sup>-1</sup> and 10–100 ng mL<sup>-1</sup>. In addition, the simplicity and accuracy of this method make it comparable to other methods responsive to HER-2.

Apart from the more diffused Iron Oxide Nanoparticles (IONPs), magnetite NPs have been explored as magnetic nano-biosensors. In a preliminary report, Villegas-Serralta et al. developed aminosilane-coated and dextran-coated magnetite nanoparticles (As-M and Dx-M, respectively) conjugated with anti-HER-2 scFvs and evaluated their potential use as biosensors for HER-2 detection using a magnetic based ELISA [158]. The authors showed that As-M NPs were more efficient

in scFv immobilization and had higher biomarker targeting activity. An advantage of such an approach is that As-M were also detectable by Raman-Spectroscopy, which is emerging as a very promising technique for HER-2 detection and quantification. Yang et al., developed a novel surface-enhanced Raman scattering (SERS) probe to distinguish between HER-2<sup>+</sup> SKBR-3 cells and HER-2<sup>-</sup> MCF7 cells [159]. Gold NPs have also been employed as HER-2 nanosensors. Tao et al. developed a nanopatform based on gold nanoclusters encapsulated into liposomes further functionalized with an anti-HER-2 antibody or aptamer [160]. The authors proved that their cost-effective nano-biosensor are highly biocompatible and can precisely quantify HER-2 levels in cell suspensions and identify HER-2<sup>+</sup> cancer cells on tissue slices. As compared to traditional immunoassays, the main advantages of such an approach are related to the intrinsic robustness of gold NPs and to the significantly higher sensitivity due to the high loading capacity of gold NPs inside a single liposome.

Finally, examples of QDs-based HER-2 nanosensors can be found in the work by Tabatabaei-Panah [161]. Herein, they provided the proof of concept of anti HER-2 functionalized QDs as sensors to specifically bind HER-2 over-expressing SKBR-3 cells and tumor tissues *ex vivo*. The authors used a homemade anti HER-2 antibody-biotin conjugate labelled with commercially available QDs (QD525, Invitrogen) in comparison with FITC-labelled antibodies. In both *in vitro* and *ex-vivo* experiments, immunofluorescence analysis showed that labelling with QDs improved the staining index (contrast between specific HER-2 signal and background) by five times compared with FITC. These results are remarkable, and the images in the paper are impressive. However, the authors fail to provide sufficient evidence for the specific labelling of HER-2, since preliminary results were not supported by further histopathological analyses.

### 6.2.2. Aptamers Based Nanosensors

Another approach for the detection of HER-2<sup>+</sup> cancer cells in fluids and tissues is based on the use of aptamer-based organic NPs. Gijs et al. discovered two DNA aptamers (HeA2\_1 and HeA2\_3), by screening a library of ligands obtained by a whole-cell systematic evolution and exponential enrichment (SELEX) method to bind HER-2 protein with high specificity. Their results demonstrated that both aptamers possessed excellent binding affinity to HER-2<sup>+</sup> cell lines (SKOV-3 and SKBR-3) and an HER-2<sup>+</sup> tumor tissue sample in comparison to an MDA-MB-231 cell line (low HER-2 expression level) [162]. Chu et al., developed another HER-2 aptamer (HB5) using the SELEX approach. The HER-2 HB5 aptamer was able to specifically bind to HER-2<sup>+</sup> BC cells (SKBR-3) with minimal binding to HER-2<sup>-</sup> cells (MDA-MB-231). Furthermore, an improved IHC method with an HB5 aptamer was investigated in clinical samples compared to other commercial kits approved by the FDA for the evaluation of the HER-2 expression profile, demonstrating greater efficacy and specificity than commercial kits [163].

Aptamers have also been developed by Kim et al. and used as plasmonic nanosensors for HER-2 in biological fluids. In a preliminary study, the authors coupled anti-HER-2 specific aptamers to dopamine-coated gold nanorods and verified an extremely low limit of detection, thus opening the way to super-sensitive detection methods [164].

## 7. Theranostics

There is great interest in multifunctional NPs that can be used as theranostic agents able to: (i) specifically visualize primary tumors and metastases; (ii) to quantify HER-2 levels allowing more accurate tumor stratification, and (iii) specifically deliver therapeutic agents to HER-2<sup>+</sup> tumors.

In this context, Zheng et al. reported the use of multivalent PLGA NPs loaded with SPIONs and DOX, further labelled with gold NPs and Herceptin. These were used as MRI and photoacoustic dual contrast agents to couple the advantages of both imaging techniques. Furthermore, they promoted both DOX-driven chemotherapy and photothermal therapy due to the presence of gold NPs on the surface of PLGA NPs. These NPs resulted in a unique and complex nanosystem able to modulate immune responses and remodel the tumor microenvironment in a BT474 xenograft model amplifying the antitumor therapeutic effect [165].

Rainone et al. used fluorescent and <sup>99m</sup>Tc-radiolabeled silica NPs functionalized with a TZ half-chain to specifically detect HER-2 overexpressing tumors. Moreover, they loaded the NPs with DOX to simultaneously confer traceability and antitumoral properties in comparison with liposomal DOX (Caelyx) [150]. The developed nanoagents could be utilized as new theranostic agents for HER-2<sup>+</sup> BC lesions. The authors showed high accumulation of NPs in the SKBR-3 tumor mass within the first 4h of treatment, with a fast decay and low tumoral specificity at later time points. This peculiar aspect should be improved to grant longer tumor visualization and to allow the use of these NPs during surgical procedures.

Choi et al. developed pluronic-based NPs functionalized with an anti-HER-2 antibody and labeled with Cy5.5 to enable *in vivo* optical imaging. The authors co-loaded IONPs and DOX to simultaneously couple MRI and chemotherapy. Specific cellular uptake was studied in HER-2 overexpressing SKBR-3 cells. Moreover, in an *in vivo* xenograft tumor, the developed herceptin-functionalized NPs showed higher tumor uptake and antitumor efficacy compared to non-functionalized ones 14 days after treatment [166].

All these examples can be further improved in terms of cancer specificity, off target distribution, and metastases detection to enhance their success in clinical translation. As a general consideration, coupling early detection and therapy could provide an enormous advantage toward future clinical applications to reduce intervention invasiveness and improve treatment schedule.

Table 3. Summary of all significant examples of NPs developed for HER-2<sup>+</sup> BC diagnosis.

Technique	NP Type	Achievements	Reference
Magnetic Resonance Imaging	<i>Herceptin</i> -dextran iron oxide nanoparticles (Roche, Basel, Switzerland)	<ul style="list-style-type: none"> <li>- Low cytotoxicity</li> <li>- Magnetic resonance enhancements proportionally to the HER-2/neu expression level in vitro</li> <li>- Higher level of accumulation of the contrast agent in tumors expressed the HER-2/neu receptor</li> </ul>	in vitro—in vivo [135]
	SPIONs-Cy-PEG-scFv (Recombinant scFv 4D5-Cys)	<ul style="list-style-type: none"> <li>- Higher affinity and specificity in vitro</li> <li>- Selective MRI labelling of HER-2<sup>+</sup> tumors in vivo</li> </ul>	in vitro—in vivo [136]

Table 3. Cont.

Technique	NP Type	Achievements	Reference
Magnetic Resonance Imaging	Magnetosomes functionalized with an anti-HER-2 affibody (Recombinant MamC (GenBank: CDK99608.1) and anti-HER-2 affibody)	<ul style="list-style-type: none"> <li>- Higher specificity for HER-2<sup>+</sup> BC cells</li> <li>- Higher r2 relaxivity, good dispersion and biocompatibility</li> </ul>	in vitro—in vivo [137]
In Vivo Fluorescence Imaging	MnCuInS/ZnS@BSA-Anti-HER-2 bioconjugates (Anti-HER-2 antibody, Sino Biological Inc., Beijing, China)	<ul style="list-style-type: none"> <li>- Good biocompatibility, low cytotoxicity, high colloidal stability</li> <li>- Higher selectivity of HER-2<sup>+</sup> cancer cells</li> </ul>	in vitro [140]
	Anti-HER-2-QD-antibody conjugate (Anti-HER-2 antibody, Invitrogen, Carlsbad, CA, USA)	<ul style="list-style-type: none"> <li>- Localization of HER-2 receptors in both fixed and live cancer cells</li> <li>- Good biocompatibility</li> </ul>	in vitro [141]
	Peptide Nanoprobes	<ul style="list-style-type: none"> <li>- Two novel peptides YLFFVFER (H6) and KLRLWNR (H10) show good specificity toward HER-2</li> <li>- Lower toxicity and good biocompatibility</li> </ul>	in vivo—ex vivo [142]
	sdAb-HER-2-QD	<ul style="list-style-type: none"> <li>- Higher specificity and sensitivity</li> <li>- Detection of micrometastases and disseminated tumor cells</li> </ul>	ex vivo [143]
Nuclear Medicine	[ <sup>18</sup> F]FB-anti-HER-2 nanobody (In-house recombinant anti-HER-2 nb 2Rs15d)	<ul style="list-style-type: none"> <li>- Excellent targeting properties and specificity for HER-2</li> <li>- Higher tumor-to-blood ratio</li> <li>- Non-competitive nature with trastuzumab for binding to the HER-2 receptor</li> </ul>	in vivo [144]
	<sup>99m</sup> Tc-Z <sub>HER2.2385</sub> -Cysc (In-house recombinant production)	<ul style="list-style-type: none"> <li>- High and specific uptake in HER-2<sup>+</sup> cells</li> <li>- Reduced off-target liver uptake</li> </ul>	in vitro—in vivo [145]
	<sup>99m</sup> Tc-radiolabeled nanosilica system, functionalized with a TZ half-chain (Genentech, South San Francisco, CA, USA)	<ul style="list-style-type: none"> <li>- Increased selective accumulation within the HER-2<sup>+</sup> cells</li> <li>- Enhanced (but not significantly) tumor targeting for functionalized NPs 4h post injection</li> <li>- Good safety</li> </ul>	in vitro—ex vivo [148]
Multimodal Hybrid Approaches	TZ-conjugated Lipo[MNP@m-SiO <sub>2</sub> ]-HER-2 <sub>Ab</sub> (Genentech, Inc., South San Francisco, CA, USA)	<ul style="list-style-type: none"> <li>- Biological stability</li> <li>- Higher specificity to HER-2/neu-overexpressing BC cells</li> </ul>	In vitro [151]
	DARPin G3 coated fluorescently labelled SPIONs	<ul style="list-style-type: none"> <li>- Higher binding and improved cytotoxicity in SBKR-3 cells</li> <li>- Higher MRI contrast in vivo after systemic administration of SPIONs</li> </ul>	In vitro—in vivo [104]
	HS-Fe-PEG-HER-2 (Anti-HER-2 antibody, Abcam, Cambridge, UK)	<ul style="list-style-type: none"> <li>- Good physical properties and biosafety, low-cytotoxicity</li> <li>- Dual-mode US-MR-specific imaging agent</li> <li>- Higher specificity to HER-2<sup>+</sup> BC cells</li> </ul>	in vitro—in vivo [153]
	G5-AuNP-Gd-TZ (Genentech, San Francisco, CA, USA)	<ul style="list-style-type: none"> <li>- Higher specificity to HER-2<sup>+</sup> cells</li> <li>- Efficient targeting of HER-2<sup>+</sup> breast tumors</li> <li>- Enhanced MRI signal and CT resolution</li> </ul>	in vitro—in vivo [154]
	SPIONs-Cy-PEG-scFv (Recombinant scFv 4D5-Cys)	<ul style="list-style-type: none"> <li>- Higher affinity and specificity versus HER-2 overexpressing cells/tumors</li> </ul>	In vitro—in vivo [136]
	<sup>89</sup> Zr-DFO-scFv-PEG-Cy5-C' dots (In-house recombinant anti-HER-2 scFv fragments-TZ)	<ul style="list-style-type: none"> <li>- Specific accumulation into HER-2<sup>+</sup> tumors</li> </ul>	in vitro—in vivo [155]
Inorganic NPs	Pegylated iron oxide NPs conjugated with anti-HER-2 antibodies ( <i>Herceptin</i> , F. Hoffmann-La Roche Ltd., Basel, Switzerland)	<ul style="list-style-type: none"> <li>- Simplicity and accuracy of method</li> <li>- The method has a low detection limit with excellent sensitivity</li> </ul>	in vitro [157]
	Dx-M and As-M were conjugated with a monoclonal scFv (In-house recombinant scFvs)	<ul style="list-style-type: none"> <li>- As-M NPs were more efficient in scFv immobilization than Dx-M NPs</li> <li>- chemical modification with aminosilane improved the HER-2 detection.</li> <li>- As-M were also detectable by Raman-Spectroscopy</li> </ul>	in vitro [158]

Table 3. Cont.

Technique	NP Type	Achievements		Reference
Inorganic NPs	Anti-HER-2 antibody-conjugated silver nanoparticles (Anti-HER-2 antibody, Fuzhou Maxim Biotech, Inc., Fuzhou, China)	- High sensitivity for targeting HER-2 - Easy fabrication, high SERS sensitivity and biocompatibility	in vitro	[159]
	BSA-AuNCs-LPs-anti-HER-2 (Anti-HER-2 antibody, R&D Systems, Minneapolis, MN, USA)	- Higher sensitivity and selectivity of the HER-2 <sup>+</sup> BC cell lines/tissue - Simple and economic approach: colorimetric “readout”	in vitro	[160]
	anti HER-2 antibody-biotin conjugate labelled with commercially available QDs (QD525)	- A Sensitive reporter of HER-2 expression in BC cells and tissues - Superiority over conventional fluorophores in terms of resistance to photobleaching - Higher fluorescent intensity, higher staining index and lower minimum detection limit	in vitro	[161]
Aptamers	HeA2_1 and HeA2_3	- Higher specificity to HER-2-overexpressing cells and HER-2 <sup>+</sup> tumor tissue samples - Inhibitory effect on cancer cell growth and viability related to the aptamer’s specificity for HER-2	in vitro—ex vivo	[162]
	HB5	- Specific binding to HER-2 protein and HER-2 <sup>+</sup> BC cells	in vitro	[163]
	APlaS to detect ECD-HER-2 protein	- Higher sensitivity and selectivity	in vitro	[164]
Antibodies	HER2-DOX-SPIOs@PLGA@A (Herceptin)	- High targeting of HER-2 <sup>+</sup> cells - Targeted drug delivery combined with photothermal-responsive drug release - Good biosafety in vivo and good antitumor effect	in vitro—in vivo	[165]
	<sup>99m</sup> Tc-SiNPs-TZ/DOX-SiNPs-TZ	- Good specificity to HER-2 <sup>+</sup> BC lesions - Higher uptake in HER-2 overexpressing cells - DOX-SiNPs-TZ NPs are able to deliver DOX at tumor site: tumor growth inhibition	in vitro—ex vivo—in vivo	[150]
	IONP/DOX-MFNC (Herceptin, Chonnam National University Hwasun Hospital)	- Higher cellular uptake and stronger cytotoxicity - Higher tumor uptake - Enhanced therapeutic effects via HER-2-mediated selectivity: tumor regression	in vitro—in vivo	[166]

## 8. Conclusions

HER-2<sup>+</sup> BC is a pathology much studied by nanotechnologists who have developed many nanosystems aimed at improving the treatment and diagnosis of cancer. Starting from therapeutic antibodies currently used in BC therapy, many targeted NPs have been developed. Therapeutic antibodies and their derivatives have been used to functionalize different kinds of NPs in an attempt to drive tumor recognition, NP accumulation, and internalization, resulting in increased performance as diagnostic devices, and with therapeutic properties.

NPs also allow the delivery of hydrophobic molecules, due to their encapsulation in appropriate nanosystems, improving their bioavailability and hence favoring their use as new therapeutic agents with improved therapeutic and imaging properties. Indeed, by modifying NP characteristics, the pharmacokinetics of injected molecules can be enhanced and their blood half-life extended. The toxicity of parenterally administered drugs can be reduced by enhancing drug accumulation in the target tissue and reducing off-target effects. Moreover, a single NP can be loaded with several drug molecules, allowing testing of different therapeutic combinations to improve BC management and reduce the onset of chemoresistance. In parallel, NPs can be loaded with several contrast agents and used as highly sensitive tools for early cancer diagnosis, as active moieties for radiation therapy and as theranostic tools if co-loaded with active drugs. Moreover, as the cellular uptake mechanisms of encapsulated drugs are completely different from those of free drugs, this has been shown to significantly reduce the evolution of resistance mechanisms.

Among all the nanotechnological solutions proposed so far, a preferred candidate NP, able to be used as a safe and active targeted nanodrug for HER-2<sup>+</sup> BC, has not emerged yet. This is due to several factors that need further investigation, including difficulties in the translation of the results from in vitro to in vivo experiments in murine models of cancer, rapid clearance from the bloodstream and liver sequestration, intrinsic toxicity of the material used to prepare the NPs, and low reproducibility and high production costs.

We believe that in the effort of developing NPs for the management of HER-2<sup>+</sup> BC, the focus on the translational potential of the agents should always be central at the very beginning of nanodrug development.

**Author Contributions:** Writing—original draft preparation, A.B., A.C., M.S., L.S. (Leopoldo Sitia), L.S. (Lorena Signati), F.M. and S.M.; writing—review and editing, L.S. (Leopoldo Sitia), S.M. and F.C. All authors have read and agreed to the published version of the manuscript.

**Funding:** University of Milan for L.S. (Leopoldo Sitia) post-doctoral position and for M.S. and A.B. PhD fellowships, and Fondazione Umberto Veronesi for F.M. postdoctoral position.

**Institutional Review Board Statement:** Not applicable.

**Informed Consent Statement:** Not applicable.

**Acknowledgments:** University of Milan for L.S. (Leopoldo Sitia) post-doctoral position, and for M.S. and A.B. PhD fellowships. Figures were created with BioRender.com.

**Conflicts of Interest:** The authors declare no conflict of interest.

## Abbreviations

BC	Breast cancer
HER-2 <sup>+</sup> BC	Human epidermal growth factor receptor-2 overexpressing breast cancer
NPs	Nanoparticles
EGFR	Epidermal growth factor receptor
AKT	Protein kinase B, PKB
PI3K	Phosphoinositide 3-kinase
MAPK	Mitogen-activated protein kinase
IHC	Immunohistochemistry
FISH	Fluorescence in situ hybridization
mAb	Monoclonal antibodies
TZ	Trastuzumab
DFS	Disease-free survival
OS	Overall survival
ADCC	Antibody-Dependent Cellular Cytotoxicity
T-DM1, Kadcyla <sup>®</sup>	Trastuzumab emtansine
ADCs	Antibody-drug conjugates, anticancer drugs
PFS	Progression-free survival
PTEN	Phosphatase and tensin homolog
TKIs	Tyrosine kinase inhibitors
pCR	Pathological complete response
TILs	Tumor-infiltrating lymphocytes
PEI	Polyethylenimine
PLGA	Poly (D,L-lactide-co-glycolide)
sdAb	Single-domain antibodies
VH	Human immunoglobulin heavy chain
Fab	Antibody fragments
TmAb	Fab obtained by papain cleavage of TZ
PmAb	Fab obtained by papain cleavage of panitumumab
scFv	Single chain variable fragments
DOX	Doxorubicin



PTX	Paclitaxel
PCI	Photochemical Internalization
siRNA	Short interfering RNA
PTT	Photothermal therapy
GNRs	Gold nanorods
AuNPs	Gold nanoparticles
PK	Pharmacokinetic
XBP1	X-box binding protein 1
PDT	Photodynamic therapy
Hapt	Aptamer
IHC	Immunohistochemistry
CISH	Chromogenic in-situ hybridization
CT	Computerized tomography
PET	Positron emission tomography
SPECT	Single photon emission computed tomography
US	Ultrasounds
MRI	Magnetic resonance imaging
SPIONs	Super paramagnetic iron oxide nanoparticles
FGS	Fluorescence guided surgery
QDs	Quantum dots
Cy	Cyanine
BSA	Bovine serum albumin
EPR	Enhanced Permeation and Retention
PAMAM	Polyamidoamine
SERS	Surface-enhanced Raman scattering
SELEX	Systematic evolution of ligands by exponential enrichment

## References

1. Siegel, R.L.; Miller, K.D.; Jemal, A. Cancer Statistics, 2020. *CA Cancer J. Clin.* **2020**, *70*, 7–30. [[CrossRef](#)] [[PubMed](#)]
2. Sung, H.; Ferlay, J.; Siegel, R.L.; Laversanne, M.; Soerjomataram, I.; Jemal, A.; Bray, F. Global Cancer Statistics 2020: GLOBOCAN Estimates of Incidence and Mortality Worldwide for 36 Cancers in 185 Countries. *CA Cancer J. Clin.* **2021**, *71*, 209–249. [[CrossRef](#)] [[PubMed](#)]
3. Howlader, N.; Cronin, K.A.; Kurian, A.W.; Andridge, R. Differences in Breast Cancer Survival by Molecular Subtypes in the United States. *Cancer Epidemiol. Biomark. Prev.* **2018**, *27*, 619–626. [[CrossRef](#)] [[PubMed](#)]
4. Mittendorf, E.A.; Wu, Y.; Scaltriti, M.; Meric-Bernstam, F.; Hunt, K.K.; Dawood, S.; Esteva, F.J.; Buzdar, A.U.; Chen, H.; Eksambi, S.; et al. Loss of HER2 Amplification Following Trastuzumab-Based Neoadjuvant Systemic Therapy and Survival Outcomes. *Clin. Cancer Res.* **2009**, *15*, 7381–7388. [[CrossRef](#)] [[PubMed](#)]
5. Niikura, N.; Liu, J.; Hayashi, N.; Mittendorf, E.A.; Gong, Y.; Palla, S.L.; Tokuda, Y.; Gonzalez-Angulo, A.M.; Hortobagyi, G.N.; Ueno, N.T. Loss of Human Epidermal Growth Factor Receptor 2 (HER2) Expression in Metastatic Sites of HER2-Overexpressing Primary Breast Tumors. *J. Clin. Oncol.* **2012**, *30*, 593–599. [[CrossRef](#)]
6. Mohsin, S.K.; Weiss, H.L.; Gutierrez, M.C.; Chamness, G.C.; Schiff, R.; DiGiovanna, M.P.; Wang, C.-X.; Hilsenbeck, S.G.; Osborne, C.K.; Allred, D.C.; et al. Neoadjuvant Trastuzumab Induces Apoptosis in Primary Breast Cancers. *J. Clin. Oncol.* **2005**, *23*, 2460–2468. [[CrossRef](#)]
7. Gallardo, A.; Lerma, E.; Escuin, D.; Tibau, A.; Muñoz, J.; Ojeda, B.; Barnadas, A.; Adrover, E.; Sánchez-Tejada, L.; Giner, D.; et al. Increased Signalling of EGFR and IGF1R, and Deregulation of PTEN/PI3K/Akt Pathway Are Related with Trastuzumab Resistance in HER2 Breast Carcinomas. *Br. J. Cancer* **2012**, *106*, 1367–1373. [[CrossRef](#)]
8. Arvold, N.D.; Oh, K.S.; Niemierko, A.; Taghian, A.G.; Lin, N.U.; Abi-Raad, R.F.; Sreedhara, M.; Harris, J.R.; Alexander, B.M. Brain Metastases after Breast-Conserving Therapy and Systemic Therapy: Incidence and Characteristics by Biologic Subtype. *Breast Cancer Res Treat.* **2012**, *136*, 153–160. [[CrossRef](#)]
9. Kennecke, H.; Yerushalmi, R.; Woods, R.; Cheang, M.C.U.; Voduc, D.; Speers, C.H.; Nielsen, T.O.; Gelmon, K. Metastatic Behavior of Breast Cancer Subtypes. *J. Clin. Oncol.* **2010**, *28*, 3271–3277. [[CrossRef](#)]
10. Schlessinger, J. Common and Distinct Elements in Cellular Signaling via EGF and FGF Receptors. *Science* **2004**, *306*, 1506–1507. [[CrossRef](#)]
11. Jiang, N.; Dai, Q.; Su, X.; Fu, J.; Feng, X.; Peng, J. Role of PI3K/AKT Pathway in Cancer: The Framework of Malignant Behavior. *Mol. Biol. Rep.* **2020**, *47*, 4587–4629. [[CrossRef](#)] [[PubMed](#)]
12. Ruiz-Saenz, A.; Dreyer, C.; Campbell, M.R.; Steri, V.; Gulizia, N.P.; Moasser, M.M. HER2 Amplification in Tumors Activates PI3K/Akt Signaling Independent of HER3. *Cancer Res.* **2018**, *78*, 3645–3658. [[CrossRef](#)] [[PubMed](#)]
13. Sheen, M.R.; Marotti, J.D.; Allegrezza, M.J.; Rutkowski, M.; Conejo-Garcia, J.R.; Fiering, S. Constitutively Activated PI3K Accelerates Tumor Initiation and Modifies Histopathology of Breast Cancer. *Oncogenesis* **2016**, *5*, e267. [[CrossRef](#)] [[PubMed](#)]



14. Dhillon, A.S.; Hagan, S.; Rath, O.; Kolch, W. MAP Kinase Signalling Pathways in Cancer. *Oncogene* **2007**, *26*, 3279–3290. [[CrossRef](#)]
15. Wolff, A.C.; Hammond, M.E.H.; Allison, K.H.; Harvey, B.E.; Mangu, P.B.; Bartlett, J.M.S.; Bilous, M.; Ellis, I.O.; Fitzgibbons, P.; Hanna, W.; et al. Human Epidermal Growth Factor Receptor 2 Testing in Breast Cancer: American Society of Clinical Oncology/College of American Pathologists Clinical Practice Guideline Focused Update. *Arch. Pathol. Lab. Med.* **2018**, *142*, 1364–1382. [[CrossRef](#)]
16. Cardoso, F.; Senkus, E.; Costa, A.; Papadopoulos, E.; Aapro, M.; André, F.; Harbeck, N.; Aguilar Lopez, B.; Barrios, C.H.; Bergh, J.; et al. 4th ESO–ESMO International Consensus Guidelines for Advanced Breast Cancer (ABC 4). *Ann. Oncol.* **2018**, *29*, 1634–1657. [[CrossRef](#)]
17. Swain, S.M.; Miles, D.; Kim, S.-B.; Im, Y.-H.; Im, S.-A.; Semiglazov, V.; Ciruelos, E.; Schneeweiss, A.; Loi, S.; Monturus, E.; et al. Pertuzumab, Trastuzumab, and Docetaxel for HER2-Positive Metastatic Breast Cancer (CLEOPATRA): End-of-Study Results from a Double-Blind, Randomised, Placebo-Controlled, Phase 3 Study. *Lancet Oncol.* **2020**, *21*, 519–530. [[CrossRef](#)]
18. Cardoso, F.; Kyriakides, S.; Ohno, S.; Penault-Llorca, F.; Poortmans, P.; Rubio, I.T.; Zackrisson, S.; Senkus, E. Early Breast Cancer: ESMO Clinical Practice Guidelines for Diagnosis, Treatment and Follow-Up. *Ann. Oncol.* **2019**, *30*, 1194–1220. [[CrossRef](#)]
19. Slamon, D.J.; Leyland-Jones, B.; Shak, S.; Fuchs, H.; Paton, V.; Bajamonde, A.; Fleming, T.; Eiermann, W.; Wolter, J.; Pegram, M.; et al. Use of Chemotherapy plus a Monoclonal Antibody against HER2 for Metastatic Breast Cancer That Overexpresses HER2. *N. Engl. J. Med.* **2001**, *344*, 783–792. [[CrossRef](#)]
20. Piccart-Gebhart, M.J.; Procter, M.; Leyland-Jones, B.; Goldhirsch, A.; Untch, M.; Smith, I.; Gianni, L.; Baselga, J.; Bell, R.; Jackisch, C.; et al. Trastuzumab after Adjuvant Chemotherapy in HER2-Positive Breast Cancer. *N. Engl. J. Med.* **2005**, *353*, 1659–1672. [[CrossRef](#)]
21. Smith, I.; Procter, M.; Gelber, R.D.; Guillaume, S.; Feyereislova, A.; Dowsett, M.; Goldhirsch, A.; Untch, M.; Mariani, G.; Baselga, J.; et al. 2-Year Follow-up of Trastuzumab after Adjuvant Chemotherapy in HER2-Positive Breast Cancer: A Randomised Controlled Trial. *Lancet* **2007**, *369*, 29–36. [[CrossRef](#)]
22. Vogel, C.L.; Cobleigh, M.A.; Tripathy, D.; Gutheil, J.C.; Harris, L.N.; Fehrenbacher, L.; Slamon, D.J.; Murphy, M.; Novotny, W.F.; Burchmore, M.; et al. Efficacy and Safety of Trastuzumab as a Single Agent in First-Line Treatment of HER2-Overexpressing Metastatic Breast Cancer. *J. Clin. Oncol.* **2002**, *20*, 719–726. [[CrossRef](#)] [[PubMed](#)]
23. Meng, Y.; Zheng, L.; Yang, Y.; Wang, H.; Dong, J.; Wang, C.; Zhang, Y.; Yu, X.; Wang, L.; Xia, T.; et al. A Monoclonal Antibody Targeting ErbB2 Domain III Inhibits ErbB2 Signaling and Suppresses the Growth of ErbB2-Overexpressing Breast Tumors. *Oncogenesis* **2016**, *5*, e211. [[CrossRef](#)] [[PubMed](#)]
24. Zhu, H.; Zhang, G.; Wang, Y.; Xu, N.; He, S.; Zhang, W.; Chen, M.; Liu, M.; Quan, L.; Bai, J.; et al. Inhibition of ErbB2 by Herceptin Reduces Survivin Expression via the ErbB2- $\beta$ -Catenin/TCF4-Survivin Pathway in ErbB2-Overexpressed Breast Cancer Cells. *Cancer Sci.* **2010**, *101*, 1156–1162. [[CrossRef](#)]
25. Davis, N.M.; Sokolosky, M.; Stadelman, K.; Abrams, S.L.; Libra, M.; Candido, S.; Nicoletti, F.; Polesel, J.; Maestro, R.; D’Assoro, A.; et al. Deregulation of the EGFR/PI3K/PTEN/Akt/MTORC1 Pathway in Breast Cancer: Possibilities for Therapeutic Intervention. *Oncotarget* **2014**, *5*, 4603–4650. [[CrossRef](#)]
26. Fiszman, G.L.; Jasnis, M.A. Molecular Mechanisms of Trastuzumab Resistance in HER2 Overexpressing Breast Cancer. *Int. J. Breast Cancer* **2011**, *2011*, 352182. [[CrossRef](#)]
27. Capietto, A.-H.; Martinet, L.; Fournié, J.-J. Stimulated  $\Gamma\delta$  T Cells Increase the In Vivo Efficacy of Trastuzumab in HER-2<sup>+</sup> Breast Cancer. *J. Immunol.* **2011**, *187*, 1031–1038. [[CrossRef](#)]
28. Nagata, Y.; Lan, K.-H.; Zhou, X.; Tan, M.; Esteva, F.J.; Sahin, A.A.; Klos, K.S.; Li, P.; Monia, B.P.; Nguyen, N.T.; et al. PTEN Activation Contributes to Tumor Inhibition by Trastuzumab, and Loss of PTEN Predicts Trastuzumab Resistance in Patients. *Cancer Cell* **2004**, *6*, 117–127. [[CrossRef](#)]
29. Nahta, R.; Esteva, F.J. HER2 Therapy: Molecular Mechanisms of Trastuzumab Resistance. *Breast Cancer Res.* **2006**, *8*, 215. [[CrossRef](#)]
30. Scaltriti, M.; Rojo, F.; Ocana, A.; Anido, J.; Guzman, M.; Cortes, J.; Di Cosimo, S.; Matias-Guiu, X.; Ramon y Cajal, S.; Arribas, J.; et al. Expression of P95HER2, a Truncated Form of the HER2 Receptor, and Response to Anti-HER2 Therapies in Breast Cancer. *JNCI J. Natl. Cancer Inst.* **2007**, *99*, 628–638. [[CrossRef](#)]
31. Hurvitz, S.A.; Martin, M.; Jung, K.H.; Huang, C.-S.; Harbeck, N.; Valero, V.; Stroyakovskiy, D.; Wildiers, H.; Campone, M.; Boileau, J.-F.; et al. Neoadjuvant Trastuzumab Emtansine and Pertuzumab in Human Epidermal Growth Factor Receptor 2-Positive Breast Cancer: Three-Year Outcomes from the Phase III KRISTINE Study. *J. Clin. Oncol.* **2019**, *37*, 2206–2216. [[CrossRef](#)] [[PubMed](#)]
32. Slamon, D.; Eiermann, W.; Robert, N.; Pienkowski, T.; Martin, M.; Press, M.; Mackey, J.; Glaspy, J.; Chan, A.; Pawlicki, M.; et al. Adjuvant Trastuzumab in HER2-Positive Breast Cancer. *N. Engl. J. Med.* **2011**, *365*, 1273–1283. [[CrossRef](#)]
33. Rugo, H.S.; Im, S.-A.; Cardoso, F.; Cortés, J.; Curigliano, G.; Musolino, A.; Pegram, M.D.; Wright, G.S.; Saura, C.; Escrivá-de-Romaní, S.; et al. Efficacy of Margetuximab vs Trastuzumab in Patients with Pretreated ERBB2-Positive Advanced Breast Cancer: A Phase 3 Randomized Clinical Trial. *JAMA Oncol.* **2021**, *7*, 573. [[CrossRef](#)]
34. Lewis Phillips, G.D.; Li, G.; Dugger, D.L.; Crocker, L.M.; Parsons, K.L.; Mai, E.; Blättler, W.A.; Lambert, J.M.; Chari, R.V.J.; Lutz, R.J.; et al. Targeting HER2-Positive Breast Cancer with Trastuzumab-DM1, an Antibody–Cytotoxic Drug Conjugate. *Cancer Res.* **2008**, *68*, 9280–9290. [[CrossRef](#)] [[PubMed](#)]
35. Diéras, V.; Miles, D.; Verma, S.; Pegram, M.; Welslau, M.; Baselga, J.; Krop, I.E.; Blackwell, K.; Hoersch, S.; Xu, J.; et al. Trastuzumab Emtansine versus Capecitabine plus Lapatinib in Patients with Previously Treated HER2-Positive Advanced Breast Cancer (EMILIA): A Descriptive Analysis of Final Overall Survival Results from a Randomised, Open-Label, Phase 3 Trial. *Lancet Oncol.* **2017**, *18*, 732–742. [[CrossRef](#)]
36. Loibl, S.; Majewski, I.; Guarneri, V.; Nekljudova, V.; Holmes, E.; Bria, E.; Denkert, C.; Schem, C.; Sotiriou, C.; Loi, S.; et al. PIK3CA Mutations Are Associated with Reduced Pathological Complete Response Rates in Primary HER2-Positive Breast Cancer: Pooled Analysis of 967 Patients from Five Prospective Trials Investigating Lapatinib and Trastuzumab. *Ann. Oncol.* **2016**, *27*, 1519–1525. [[CrossRef](#)] [[PubMed](#)]

37. Molina, M.A.; Codony-Servat, J.; Albanell, J.; Rojo, F.; Arribas, J.; Baselga, J. Trastuzumab (Herceptin), a Humanized Anti-Her2 Receptor Monoclonal Antibody, Inhibits Basal and Activated Her2 Ectodomain Cleavage in Breast Cancer Cells. *Cancer Res.* **2001**, *61*, 4744–4749.
38. Ghosh, R.; Narasanna, A.; Wang, S.E.; Liu, S.; Chakrabarty, A.; Balko, J.M.; González-Angulo, A.M.; Mills, G.B.; Penuel, E.; Winslow, J.; et al. Trastuzumab Has Preferential Activity against Breast Cancers Driven by HER2 Homodimers. *Cancer Res.* **2011**, *71*, 1871–1882. [[CrossRef](#)]
39. Ríos-Luci, C.; García-Alonso, S.; Díaz-Rodríguez, E.; Nadal-Serrano, M.; Arribas, J.; Ocaña, A.; Pandiella, A. Resistance to the Antibody–Drug Conjugate T-DM1 Is Based in a Reduction in Lysosomal Proteolytic Activity. *Cancer Res.* **2017**, *77*, 4639–4651. [[CrossRef](#)]
40. Sauveur, J.; Matera, E.-L.; Chettab, K.; Valet, P.; Guitton, J.; Savina, A.; Dumontet, C. Esophageal Cancer Cells Resistant to T-DM1 Display Alterations in Cell Adhesion and the Prostaglandin Pathway. *Oncotarget* **2018**, *9*, 21141–21155. [[CrossRef](#)]
41. Columbus, G. Trastuzumab Deruxtecan Receives Accelerated Approval by FDA for HER2+ Breast Cancer. 2019. Available online: <https://www.targetedonc.com/view/trastuzumab-deruxtecan-receives-accelerated-approval-by-fda-for-her2-breastcancer> (accessed on 10 March 2022).
42. Rinnerthaler, G.; Campenrieder, S.; Greil, R. HER2 Directed Antibody-Drug-Conjugates beyond T-DM1 in Breast Cancer. *Int. J. Mol. Sci.* **2019**, *20*, 1115. [[CrossRef](#)] [[PubMed](#)]
43. Martínez-Sáez, O.; Chic, N.; Pascual, T.; Adamo, B.; Vidal, M.; González-Farré, B.; Sanfeliu, E.; Schettini, F.; Conte, B.; BrasóMaristany, F.; et al. Frequency and Spectrum of PIK3CA Somatic Mutations in Breast Cancer. *Breast Cancer Res.* **2020**, *22*, 45. [[CrossRef](#)] [[PubMed](#)]
44. Verret, B.; Cortes, J.; Bachelot, T.; Andre, F.; Arnedos, M. Efficacy of PI3K Inhibitors in Advanced Breast Cancer. *Ann. Oncol.* **2019**, *30*, x12–x20. [[CrossRef](#)] [[PubMed](#)]
45. André, F.; Hurvitz, S.; Fasolo, A.; Tseng, L.-M.; Jerusalem, G.; Wilks, S.; O’Regan, R.; Isaacs, C.; Toi, M.; Burris, H.A.; et al. Molecular Alterations and Everolimus Efficacy in Human Epidermal Growth Factor Receptor 2–Overexpressing Metastatic Breast Cancers: Combined Exploratory Biomarker Analysis From BOLERO-1 and BOLERO-3. *J. Clin. Oncol.* **2016**, *34*, 2115–2124. [[CrossRef](#)]
46. Segovia-Mendoza, M.; González-González, M.E.; Barrera, D.; Díaz, L.; García-Becerra, R. Efficacy and Mechanism of Action of the Tyrosine Kinase Inhibitors Gefitinib, Lapatinib and Neratinib in the Treatment of HER2-Positive Breast Cancer: Preclinical and Clinical Evidence. *Am. J. Cancer Res.* **2015**, *5*, 2531–2561.
47. Esparís-Ogando, A.; Montero, J.; Arribas, J.; Ocaña, A.; Pandiella, A. Targeting the EGF/HER Ligand-Receptor System in Cancer. *Curr. Pharm. Des.* **2016**, *22*, 5887–5898. [[CrossRef](#)]
48. Chan, A.; Delalogue, S.; Holmes, F.A.; Moy, B.; Iwata, H.; Harvey, V.J.; Robert, N.J.; Silovski, T.; Gokmen, E.; Von Minckwitz, G.; et al. Neratinib after Trastuzumab-Based Adjuvant Therapy in Patients with HER2-Positive Breast Cancer (ExteNET): A Multicentre, Randomised, Double-Blind, Placebo-Controlled, Phase 3 Trial. *Lancet Oncol.* **2016**, *17*, 367–377. [[CrossRef](#)]
49. Singh, H.; Walker, A.J.; Amiri-Kordestani, L.; Cheng, J.; Tang, S.; Balcazar, P.; Barnett-Ringgold, K.; Palmby, T.R.; Cao, X.; Zheng, N.; et al. U.S. Food and Drug Administration Approval: Neratinib for the Extended Adjuvant Treatment of Early-Stage HER2-Positive Breast Cancer. *Clin. Cancer Res.* **2018**, *24*, 3486–3491. [[CrossRef](#)]
50. Leo, C.P.; Hentschel, B.; Szucs, T.D.; Leo, C. FDA and EMA Approvals of New Breast Cancer Drugs—A Comparative Regulatory Analysis. *Cancers* **2020**, *12*, 437. [[CrossRef](#)]
51. De Azambuja, E.; Holmes, A.P.; Piccart-Gebhart, M.; Holmes, E.; Di Cosimo, S.; Swaby, R.F.; Untch, M.; Jackisch, C.; Lang, I.; Smith, I.; et al. Lapatinib with Trastuzumab for HER2-Positive Early Breast Cancer (NeoALTTO): Survival Outcomes of a Randomised, Open-Label, Multicentre, Phase 3 Trial and Their Association with Pathological Complete Response. *Lancet Oncol.* **2014**, *15*, 1137–1146. [[CrossRef](#)]
52. Savas, P.; Salgado, R.; Denkert, C.; Sotiriou, C.; Darcy, P.K.; Smyth, M.J.; Loi, S. Clinical Relevance of Host Immunity in Breast Cancer: From TILs to the Clinic. *Nat. Rev. Clin. Oncol.* **2016**, *13*, 228–241. [[CrossRef](#)] [[PubMed](#)]
53. Hou, Y.; Nitta, H.; Wei, L.; Banks, P.M.; Lustberg, M.; Wesolowski, R.; Ramaswamy, B.; Parwani, A.V.; Li, Z. PD-L1 Expression and CD8-Positive T Cells Are Associated with Favorable Survival in HER2-Positive Invasive Breast Cancer. *Breast J.* **2018**, *24*, 911–919. [[CrossRef](#)] [[PubMed](#)]
54. Poole, R.M. Pembrolizumab: First Global Approval. *Drugs* **2014**, *74*, 1973–1981. [[CrossRef](#)] [[PubMed](#)]
55. Markham, A. Atezolizumab: First Global Approval. *Drugs* **2016**, *76*, 1227–1232. [[CrossRef](#)]
56. Guo, L.; Zhang, H.; Chen, B. Nivolumab as Programmed Death-1 (PD-1) Inhibitor for Targeted Immunotherapy in Tumor. *J. Cancer* **2017**, *8*, 410–416. [[CrossRef](#)] [[PubMed](#)]
57. Nieto, C.; Vega, M.A.; Martín del Valle, E.M. Trastuzumab: More than a Guide in HER2-Positive Cancer Nanomedicine. *Nanomaterials* **2020**, *10*, 1674. [[CrossRef](#)] [[PubMed](#)]
58. White, B.E.; White, M.K.; Adhvaryu, H.; Makhoul, I.; Nima, Z.A.; Biris, A.S.; Ali, N. Nanotechnology Approaches to Addressing HER2-Positive Breast Cancer. *Cancer Nano* **2020**, *11*, 12. [[CrossRef](#)]
59. Kumar, M.; Rajnikanth, P.S. A Mini-Review on HER2 Positive Breast Cancer and Its Metastasis: Resistance and Treatment Strategies. *Curr. Nanomed. (Former. Recent Pat. Nanomed.)* **2020**, *10*, 36–47. [[CrossRef](#)]
60. Marques, A.C.; Costa, P.J.; Velho, S.; Amaral, M.H. Functionalizing Nanoparticles with Cancer-Targeting Antibodies: A Comparison of Strategies. *J. Control. Release* **2020**, *320*, 180–200. [[CrossRef](#)]
61. Juan, A.; Cimas, F.J.; Bravo, I.; Pandiella, A.; Ocaña, A.; Alonso-Moreno, C. An Overview of Antibody Conjugated Polymeric Nanoparticles for Breast Cancer Therapy. *Pharmaceutics* **2020**, *12*, 802. [[CrossRef](#)]
62. Lin, X.; O’Reilly Beringhs, A.; Lu, X. Applications of Nanoparticle-Antibody Conjugates in Immunoassays and Tumor Imaging. *AAPS J.* **2021**, *23*, 43. [[CrossRef](#)]
63. Bloise, N.; Massironi, A.; Della Pina, C.; Alongi, J.; Siciliani, S.; Manfredi, A.; Biggiogera, M.; Rossi, M.; Ferruti, P.; Ranucci, E.; et al. Extra-Small Gold Nanospheres Decorated with a Thiol Functionalized Biodegradable and Biocompatible Linear Polyamidoamine as Nanovectors of Anticancer Molecules. *Front. Bioeng. Biotechnol.* **2020**, *8*, 132. [[CrossRef](#)] [[PubMed](#)]
64. Cai, Z.; Chattopadhyay, N.; Yang, K.; Kwon, Y.L.; Yook, S.; Pignol, J.-P.; Reilly, R.M. <sup>111</sup>In-Labeled Trastuzumab-Modified Gold Nanoparticles Are Cytotoxic in Vitro to HER2-Positive Breast Cancer Cells and Arrest Tumor Growth in Vivo in Athymic Mice after Intratumoral Injection. *Nucl. Med. Biol.* **2016**, *43*, 818–826. [[CrossRef](#)] [[PubMed](#)]

65. Dziawer, Ł.; Majkowska-Pilip, A.; Gawęł, D.; Godlewska, M.; Pruszyński, M.; Jastrzebski, J.; Waś, B.; Bilewicz, A. Trastuzumab-Modified Gold Nanoparticles Labeled with 211At as a Prospective Tool for Local Treatment of HER2-Positive Breast Cancer. *Nanomaterials* **2019**, *9*, 632. [[CrossRef](#)] [[PubMed](#)]
66. Kang, X.; Guo, X.; Niu, X.; An, W.; Li, S.; Liu, Z.; Yang, Y.; Wang, N.; Jiang, Q.; Yan, C.; et al. Photothermal Therapeutic Application of Gold Nanorods-Porphyrin-Trastuzumab Complexes in HER2-Positive Breast Cancer. *Sci Rep.* **2017**, *7*, 42069. [[CrossRef](#)] [[PubMed](#)]
67. Zhang, X.; Liu, J.; Li, X.; Li, F.; Lee, R.J.; Sun, F.; Li, Y.; Liu, Z.; Teng, L. Trastuzumab-Coated Nanoparticles Loaded with Docetaxel for Breast Cancer Therapy. *Dose-Response* **2019**, *17*, 1559325819872583. [[CrossRef](#)] [[PubMed](#)]
68. Yu, K.; Zhao, J.; Zhang, Z.; Gao, Y.; Zhou, Y.; Teng, L.; Li, Y. Enhanced Delivery of Paclitaxel Using Electrostatically-Conjugated Herceptin-Bearing PEI/PLGA Nanoparticles against HER-Positive Breast Cancer Cells. *Int. J. Pharm.* **2016**, *497*, 78–87. [[CrossRef](#)] [[PubMed](#)]
69. Naruphontjirakul, P.; Viravaidya-Pasuwat, K. Development of Anti-HER2-Targeted Doxorubicin-Core-Shell Chitosan Nanoparticles for the Treatment of Human Breast Cancer. *Int. J. Nanomed.* **2019**, *14*, 4105–4121. [[CrossRef](#)]
70. Peng, J.; Chen, J.; Xie, F.; Bao, W.; Xu, H.; Wang, H.; Xu, Y.; Du, Z. Herceptin-Conjugated Paclitaxel Loaded PCL-PEG Worm-like Nanocrystal Micelles for the Combinatorial Treatment of HER2-Positive Breast Cancer. *Biomaterials* **2019**, *222*, 119420. [[CrossRef](#)]
71. Varshosaz, J.; Ghassami, E.; Noorbakhsh, A.; Minaiyan, M.; Jahanian-Najafabadi, A. Trastuzumab-conjugated Nanoparticles Composed of Poly(Butylene Adipate-Co-butylene Terephthalate) Prepared by Electro spraying Technique for Targeted Delivery of Docetaxel. *IET Nanobiotechnol.* **2019**, *13*, 829–833. [[CrossRef](#)]
72. Domínguez-Ríos, R.; Sánchez-Ramírez, D.R.; Ruiz-Saray, K.; Ocegüera-Basurto, P.E.; Almada, M.; Juárez, J.; Zepeda-Moreno, A.; del Toro-Arreola, A.; Topete, A.; Daneri-Navarro, A. Cisplatin-Loaded PLGA Nanoparticles for HER2 Targeted Ovarian Cancer Therapy. *Colloids Surf. B Biointerfaces* **2019**, *178*, 199–207. [[CrossRef](#)] [[PubMed](#)]
73. Cedrowska, E.; Pruszyński, M.; Gawęł, W.; Zuk, M.; Krysiński, P.; Bruchertseifer, F.; Morgenstern, A.; Karageorgou, M.-A.; Bouziotis, P.; Bilewicz, A. Trastuzumab Conjugated Superparamagnetic Iron Oxide Nanoparticles Labeled with 225Ac as a Perspective Tool for Combined  $\alpha$ -Radioimmunotherapy and Magnetic Hyperthermia of HER2-Positive Breast Cancer. *Molecules* **2020**, *25*, 1025. [[CrossRef](#)] [[PubMed](#)]
74. Korangath, P.; Barnett, J.D.; Sharma, A.; Henderson, E.T.; Stewart, J.; Yu, S.-H.; Kandala, S.K.; Yang, C.-T.; Caserto, J.S.; Hedayati, M.; et al. Nanoparticle Interactions with Immune Cells Dominate Tumor Retention and Induce T Cell-Mediated Tumor Suppression in Models of Breast Cancer. *Sci. Adv.* **2020**, *6*, eaay1601. [[CrossRef](#)] [[PubMed](#)]
75. Ko, N.R.; Van, S.Y.; Hong, S.H.; Kim, S.-Y.; Kim, M.; Lee, J.S.; Lee, S.J.; Lee, Y.; Kwon, I.K.; Oh, S.J. Dual PH- and GSH-Responsive Degradable PEGylated Graphene Quantum Dot-Based Nanoparticles for Enhanced HER2-Positive Breast Cancer Therapy. *Nanomaterials* **2020**, *10*, 91. [[CrossRef](#)] [[PubMed](#)]
76. Shu, M.; Gao, F.; Yu, C.; Zeng, M.; He, G.; Wu, Y.; Su, Y.; Hu, N.; Zhou, Z.; Yang, Z.; et al. Dual-Targeted Therapy in HER2-Positive Breast Cancer Cells with the Combination of Carbon Dots/HER3 siRNA and Trastuzumab. *Nanotechnology* **2020**, *31*, 335102. [[CrossRef](#)]
77. Tanaka, S.; Matsunami, N.; Morishima, H.; Oda, N.; Takashima, T.; Noda, S.; Kashiwagi, S.; Tauchi, Y.; Asano, Y.; Kimura, K.; et al. De-Escalated Neoadjuvant Therapy with Nanoparticle Albumin-Bound Paclitaxel and Trastuzumab for Low-Risk Pure HER2 Breast Cancer. *Cancer Chemother Pharm.* **2019**, *83*, 1099–1104. [[CrossRef](#)]
78. Duan, D.; Wang, A.; Ni, L.; Zhang, L.; Yan, X.; Jiang, Y.; Mu, H.; Wu, Z.; Sun, K.; Li, Y. Nanoparticle Interactions with Immune Cells Dominate Tumor Retention and Induce T Cell-Mediated Tumor Suppression in Models of Breast Cancer. *Int. J. Nanomed.* **2018**, *13*, 1831–1840. [[CrossRef](#)]
79. Kim, B.; Shin, J.; Wu, J.; Omstead, D.T.; Kiziltepe, T.; Littlepage, L.E.; Bilgicer, B. Engineering Peptide-Targeted Liposomal Nanoparticles Optimized for Improved Selectivity for HER2-Positive Breast Cancer Cells to Achieve Enhanced in Vivo Efficacy. *J. Control. Release* **2020**, *322*, 530–541. [[CrossRef](#)]
80. Houdaïed, L.; Evans, J.C.; Allen, C. Dual-Targeted Delivery of Nanoparticles Encapsulating Paclitaxel and Everolimus: A Novel Strategy to Overcome Breast Cancer Receptor Heterogeneity. *Pharm. Res.* **2020**, *37*, 39. [[CrossRef](#)]
81. Vorotnikov, Y.A.; Novikova, E.D.; Solovieva, A.O.; Shanshin, D.V.; Tsygankova, A.R.; Shcherbakov, D.N.; Efremova, O.A.; Shestopalov, M.A. Single-Domain Antibody C7b for Address Delivery of Nanoparticles to HER2-Positive Cancers. *Nanoscale* **2020**, *12*, 21885–21894. [[CrossRef](#)]
82. Holliger, P.; Hudson, P.J. Engineered Antibody Fragments and the Rise of Single Domains. *Nat. Biotechnol.* **2005**, *23*, 1126–1136. [[CrossRef](#)] [[PubMed](#)]
83. Van Audenhove, I.; Gettemans, J. Nanobodies as Versatile Tools to Understand, Diagnose, Visualize and Treat Cancer. *EBioMedicine* **2016**, *8*, 40–48. [[CrossRef](#)] [[PubMed](#)]
84. Martínez-Jothar, L.; Beztsinna, N.; van Nostrum, C.F.; Hennink, W.E.; Oliveira, S. Selective Cytotoxicity to HER2 Positive Breast Cancer Cells by Saporin-Loaded Nanobody-Targeted Polymeric Nanoparticles in Combination with Photochemical Internalization. *Mol. Pharm.* **2019**, *16*, 1633–1647. [[CrossRef](#)] [[PubMed](#)]
85. Li, M.; Dong, J.; Cheng, F.; Li, C.; Wang, H.; Sun, T.; He, W.; Wang, Q. Controlling Conjugated Antibodies at the Molecular Level for Active Targeting Nanoparticles toward HER2-Positive Cancer Cells. *Mol. Pharm.* **2021**, *18*, 1196–1207. [[CrossRef](#)]
86. Shi, X.; Cheng, Q.; Hou, T.; Han, M.; Smbatyan, G.; Lang, J.E.; Epstein, A.L.; Lenz, H.-J.; Zhang, Y. Genetically Engineered Cell-Derived Nanoparticles for Targeted Breast Cancer Immunotherapy. *Mol. Ther.* **2020**, *28*, 536–547. [[CrossRef](#)]
87. Okarvi, S.M.; AlJammaz, I. Development of the Tumor-Specific Antigen-Derived Synthetic Peptides as Potential Candidates for Targeting Breast and Other Possible Human Carcinomas. *Molecules* **2019**, *24*, 3142. [[CrossRef](#)]
88. Ding, H.; Gangalum, P.R.; Galstyan, A.; Fox, I.; Patil, R.; Hubbard, P.; Murali, R.; Ljubimova, J.Y.; Holler, E. HER2-Positive Breast Cancer Targeting and Treatment by a Peptide-Conjugated Mini Nanodrug. *Nanomed. Nanotechnol. Biol. Med.* **2017**, *13*, 631–639. [[CrossRef](#)]



89. Mu, Q.; Kievit, F.M.; Kant, R.J.; Lin, G.; Jeon, M.; Zhang, M. Anti-HER2/Neu Peptide-Conjugated Iron Oxide Nanoparticles for Targeted Delivery of Paclitaxel to Breast Cancer Cells. *Nanoscale* **2015**, *7*, 18010–18014. [[CrossRef](#)]
90. Zhang, L.; Jing, D.; Jiang, N.; Rojalin, T.; Baehr, C.M.; Zhang, D.; Xiao, W.; Wu, Y.; Cong, Z.; Li, J.J.; et al. Transformable Peptide Nanoparticles Arrest HER2 Signalling and Cause Cancer Cell Death in Vivo. *Nat. Nanotechnol.* **2020**, *15*, 145–153. [[CrossRef](#)]
91. Zhu, G.; Chen, X. Aptamer-Based Targeted Therapy. *Adv. Drug Deliv. Rev.* **2018**, *134*, 65–78. [[CrossRef](#)]
92. Saleh, T.; Soudi, T.; Shojaosadati, S.A. Aptamer Functionalized Curcumin-Loaded Human Serum Albumin (HSA) Nanoparticles for Targeted Delivery to HER-2 Positive Breast Cancer Cells. *Int. J. Biol. Macromol.* **2019**, *130*, 109–116. [[CrossRef](#)] [[PubMed](#)]
93. Lee, H.; Dam, D.H.M.; Ha, J.W.; Yue, J.; Odom, T.W. Enhanced Human Epidermal Growth Factor Receptor 2 Degradation in Breast Cancer Cells by Lysosome-Targeting Gold Nanoconstructs. *ACS Nano* **2015**, *9*, 9859–9867. [[CrossRef](#)] [[PubMed](#)]
94. Shen, Y.; Li, M.; Liu, T.; Liu, J.; Xie, Y.; Zhang, J.; Xu, S.; Liu, H. A Dual-Functional HER2 Aptamer-Conjugated, PH-Activated Mesoporous Silica Nanocarrier-Based Drug Delivery System Provides In Vitro Synergistic Cytotoxicity in HER2-Positive Breast Cancer Cells. *Int. J. Nanomed.* **2019**, *14*, 4029–4044. [[CrossRef](#)]
95. Ma, W.; Zhan, Y.; Zhang, Y.; Shao, X.; Xie, X.; Mao, C.; Cui, W.; Li, Q.; Shi, J.; Li, J.; et al. An Intelligent DNA Nanorobot with in Vitro Enhanced Protein Lysosomal Degradation of HER2. *Nano Lett.* **2019**, *19*, 4505–4517. [[CrossRef](#)] [[PubMed](#)]
96. Bennett, V.; Baines, A.J. Spectrin and Ankyrin-Based Pathways: Metazoan Inventions for Integrating Cells into Tissues. *Physiol. Rev.* **2001**, *81*, 1353–1392. [[CrossRef](#)] [[PubMed](#)]
97. Binz, H.K.; Amstutz, P.; Plückthun, A. Engineering Novel Binding Proteins from Nonimmunoglobulin Domains. *Nat. Biotechnol.* **2005**, *23*, 1257–1268. [[CrossRef](#)]
98. Stumpp, M.T.; Dawson, K.M.; Binz, H.K. Beyond Antibodies: The DARPIn® Drug Platform. *BioDrugs* **2020**, *34*, 423–433. [[CrossRef](#)]
99. Moisseiev, E.; Loewenstein, A. Abicipar Pegol—A Novel Anti-VEGF Therapy with a Long Duration of Action. *Eye* **2020**, *34*, 605–606. [[CrossRef](#)]
100. Zahnd, C.; Pecorari, F.; Straumann, N.; Wyler, E.; Plückthun, A. Selection and Characterization of Her2 Binding-Designed Ankyrin Repeat Proteins. *J. Biol. Chem.* **2006**, *281*, 35167–35175. [[CrossRef](#)]
101. Theurillat, J.-P.; Dreier, B.; Nagy-Davidescu, G.; Seifert, B.; Behnke, S.; Zürcher-Härdi, U.; Ingold, F.; Plückthun, A.; Moch, H. Designed Ankyrin Repeat Proteins: A Novel Tool for Testing Epidermal Growth Factor Receptor 2 Expression in Breast Cancer. *Mod. Pathol.* **2010**, *23*, 1289–1297. [[CrossRef](#)]
102. Zahnd, C.; Kawe, M.; Stumpp, M.T.; de Pasquale, C.; Tamaskovic, R.; Nagy-Davidescu, G.; Dreier, B.; Schibli, R.; Binz, H.K.; Waibel, R.; et al. Efficient Tumor Targeting with High-Affinity Designed Ankyrin Repeat Proteins: Effects of Affinity and Molecular Size. *Cancer Res.* **2010**, *70*, 1595–1605. [[CrossRef](#)]
103. Shipunova, V.O.; Kotelnikova, P.A.; Aghayeva, U.F.; Stremovskiy, O.A.; Novikov, I.A.; Schulga, A.A.; Nikitin, M.P.; Deyev, S.M. Self-Assembling Nanoparticles Biofunctionalized with Magnetite-Binding Protein for the Targeted Delivery to HER2/Neu Overexpressing Cancer Cells. *J. Magn. Magn. Mater.* **2019**, *469*, 450–455. [[CrossRef](#)]
104. Li, D.-L.; Tan, J.-E.; Tian, Y.; Huang, S.; Sun, P.-H.; Wang, M.; Han, Y.-J.; Li, H.-S.; Wu, H.-B.; Zhang, X.-M.; et al. Multifunctional Superparamagnetic Nanoparticles Conjugated with Fluorescein-Labeled Designed Ankyrin Repeat Protein as an Efficient HER2-Targeted Probe in Breast Cancer. *Biomaterials* **2017**, *147*, 86–98. [[CrossRef](#)] [[PubMed](#)]
105. Guryev, E.L.; Shilyagina, N.Y.; Kostyuk, A.B.; Sencha, L.M.; Balalaeva, I.V.; Vodeneev, V.A.; Kutova, O.M.; Lyubeshkin, A.V.; Yakubovskaya, R.I.; Pankratov, A.A.; et al. Preclinical Study of Biofunctional Polymer-Coated Upconversion Nanoparticles. *Toxicol. Sci.* **2019**, *170*, 123–132. [[CrossRef](#)]
106. Dong, Y.; Li, W.; Gu, Z.; Xing, R.; Ma, Y.; Zhang, Q.; Liu, Z. Inhibition of HER2-Positive Breast Cancer Growth by Blocking the HER2 Signaling Pathway with HER2-Glycan-Imprinted Nanoparticles. *Angew. Chem. Int. Ed.* **2019**, *58*, 10621–10625. [[CrossRef](#)]
107. Yezhelyev, M.V.; Gao, X.; Xing, Y.; Al-Hajj, A.; Nie, S.; O'Regan, R.M. Emerging Use of Nanoparticles in Diagnosis and Treatment of Breast Cancer. *Lancet Oncol.* **2006**, *7*, 657–667. [[CrossRef](#)]
108. Zahmatkeshan, M.; Gheybi, F.; Rezayat, S.M.; Jaafari, M.R. Improved Drug Delivery and Therapeutic Efficacy of PEGylated Liposomal Doxorubicin by Targeting Anti-HER2 Peptide in Murine Breast Tumor Model. *Eur. J. Pharm. Sci.* **2016**, *86*, 125–135. [[CrossRef](#)] [[PubMed](#)]
109. Akhtari, J.; Rezayat, S.M.; Teymouri, M.; Alavizadeh, S.H.; Gheybi, F.; Badiie, A.; Jaafari, M.R. Targeting, Bio Distributive and Tumor Growth Inhibiting Characterization of Anti-HER2 Affibody Coupling to Liposomal Doxorubicin Using BALB/c Mice Bearing TUBO Tumors. *Int. J. Pharm.* **2016**, *505*, 89–95. [[CrossRef](#)]
110. Niza, E.; Noblejas-López, M.D.M.; Bravo, I.; Nieto-Jiménez, C.; Castro-Osma, J.A.; Canales-Vázquez, J.; Lara-Sanchez, A.; Galán Moya, E.M.; Burgos, M.; Ocaña, A.; et al. Trastuzumab-Targeted Biodegradable Nanoparticles for Enhanced Delivery of Dasatinib in HER2+ Metastatic Breast Cancer. *Nanomaterials* **2019**, *9*, 1793. [[CrossRef](#)]
111. Wan, X.; Zheng, X.; Pang, X.; Zhang, Z.; Zhang, Q. Incorporation of Lapatinib into Human Serum Albumin Nanoparticles with Enhanced Anti-Tumor Effects in HER2-Positive Breast Cancer. *Colloids Surf. B Biointerfaces* **2015**, *136*, 817–827. [[CrossRef](#)]
112. Dana, H.; Chalbatani, G.M.; Mahmoodzadeh, H.; Karimloo, R.; Rezaiean, O.; Moradzadeh, A.; Mehmandoost, N.; Moazzen, F.; Mazraeh, A.; Marmari, V.; et al. Molecular Mechanisms and Biological Functions of SiRNA. *Int. J. Biomed. Sci* **2017**, *13*, 48–57. [[PubMed](#)]
113. Mainini, F.; Eccles, M.R. Lipid and Polymer-Based Nanoparticle SiRNA Delivery Systems for Cancer Therapy. *Molecules* **2020**, *25*, 2692. [[CrossRef](#)] [[PubMed](#)]
114. Gu, S.; Ngamcherdtrakul, W.; Reda, M.; Hu, Z.; Gray, J.W.; Yantasee, W. Lack of Acquired Resistance in HER2-Positive Breast Cancer Cells after Long-Term HER2 SiRNA Nanoparticle Treatment. *PLoS ONE* **2018**, *13*, e0198141. [[CrossRef](#)] [[PubMed](#)]
115. Gu, S.; Hu, Z.; Ngamcherdtrakul, W.; Castro, D.J.; Morry, J.; Reda, M.M.; Gray, J.W.; Yantasee, W. Therapeutic SiRNA for Drug-Resistant HER2-Positive Breast Cancer. *Oncotarget* **2016**, *7*, 14727–14741. [[CrossRef](#)] [[PubMed](#)]
116. Cristofolini, T.; Dalmina, M.; Sierra, J.A.; Silva, A.H.; Pasa, A.A.; Pittella, F.; Creczynski-Pasa, T.B. Multifunctional Hybrid

- Nanoparticles as Magnetic Delivery Systems for SiRNA Targeting the HER2 Gene in Breast Cancer Cells. *Mater. Sci. Eng. C* **2020**, *109*, 110555. [[CrossRef](#)]
117. Zhang, L.; Mu, C.; Zhang, T.; Wang, Y.; Wang, Y.; Fan, L.; Liu, C.; Chen, H.; Shen, J.; Wei, K.; et al. Systemic Delivery of Aptamer-Conjugated XBP1 SiRNA Nanoparticles for Efficient Suppression of HER2+ Breast Cancer. *ACS Appl. Mater. Interfaces* **2020**, *12*, 32360–32371. [[CrossRef](#)]
  118. Rybakova, Y.; Kowalski, P.S.; Huang, Y.; Gonzalez, J.T.; Heartlein, M.W.; DeRosa, F.; Delcassian, D.; Anderson, D.G. mRNA Delivery for Therapeutic Anti-HER2 Antibody Expression In Vivo. *Mol. Ther.* **2019**, *27*, 1415–1423. [[CrossRef](#)]
  119. Cai, Z.; Yook, S.; Lu, Y.; Bergstrom, D.; Winnik, M.A.; Pignol, J.-P.; Reilly, R.M. Local Radiation Treatment of HER2-Positive Breast Cancer Using Trastuzumab-Modified Gold Nanoparticles Labeled with <sup>177</sup>Lu. *Pharm. Res.* **2017**, *34*, 579–590. [[CrossRef](#)]
  120. Guryev, E.L.; Volodina, N.O.; Shilyagina, N.Y.; Gudkov, S.V.; Balalaeva, I.V.; Volovetskiy, A.B.; Lyubeshkin, A.V.; Sen', A.V.; Ermilov, S.A.; Vodeneev, V.A.; et al. Radioactive (<sup>90</sup>Y) Upconversion Nanoparticles Conjugated with Recombinant Targeted Toxin for Synergistic Nanotheranostics of Cancer. *Proc. Natl. Acad. Sci. USA* **2018**, *115*, 9690–9695. [[CrossRef](#)]
  121. Mironova, K.E.; Khochenkov, D.A.; Generalova, A.N.; Rocheva, V.V.; Sholina, N.V.; Nechaev, A.V.; Semchishen, V.A.; Deyev, S.M.; Zvyagin, A.V.; Khaydukov, E.V. Ultraviolet Phototoxicity of Upconversion Nanoparticles Illuminated with Near-Infrared Light. *Nanoscale* **2017**, *9*, 14921–14928. [[CrossRef](#)]
  122. Aman, N.A.; Doukoure, B.; Koffi, K.D.; Kouli, B.S.; Traore, Z.C.; Kouyate, M.; Effi, A.B. HER2 Overexpression and Correlation with Other Significant Clinicopathologic Parameters in Ivorian Breast Cancer Women. *BMC Clin. Pathol.* **2019**, *19*, 1. [[CrossRef](#)] [[PubMed](#)]
  123. Vi, C.; Mandarano, G.; Shigdar, S. Diagnostics and Therapeutics in Targeting HER2 Breast Cancer: A Novel Approach. *Int. J. Mol. Sci.* **2021**, *22*, 6163. [[CrossRef](#)] [[PubMed](#)]
  124. Gutierrez, C.; Schiff, R. HER2: Biology, Detection, and Clinical Implications. *Arch. Pathol. Lab. Med.* **2011**, *135*, 55–62. [[CrossRef](#)]
  125. Salahandish, R.; Ghaffarinejad, A.; Naghib, S.M.; Majidzadeh-A, K.; Zargartalebi, H.; Sanati-Nezhad, A. Nano-Biosensor for Highly Sensitive Detection of HER2 Positive Breast Cancer. *Biosens. Bioelectron.* **2018**, *117*, 104–111. [[CrossRef](#)] [[PubMed](#)]
  126. Phillips, K.A.; Marshall, D.A.; Haas, J.S.; Elkin, E.B.; Liang, S.-Y.; Hassett, M.J.; Ferrusi, I.; Brock, J.E.; Van Bebbler, S.L. Clinical Practice Patterns and Cost Effectiveness of Human Epidermal Growth Receptor 2 Testing Strategies in Breast Cancer Patients. *Cancer* **2009**, *115*, 5166–5174. [[CrossRef](#)] [[PubMed](#)]
  127. Liu, M.; Yu, X.; Chen, Z.; Yang, T.; Yang, D.; Liu, Q.; Du, K.; Li, B.; Wang, Z.; Li, S.; et al. Aptamer Selection and Applications for Breast Cancer Diagnostics and Therapy. *J. Nanobiotechnol.* **2017**, *15*, 81. [[CrossRef](#)] [[PubMed](#)]
  128. Mathenge, E.G.; Dean, C.A.; Clements, D.; Vaghar-Kashani, A.; Photopoulos, S.; Coyle, K.M.; Giacomantonio, M.; Malueth, B.; Nunokawa, A.; Jordan, J.; et al. Core Needle Biopsy of Breast Cancer Tumors Increases Distant Metastases in a Mouse Model. *Neoplasia* **2014**, *16*, 950–960. [[CrossRef](#)]
  129. Castro-Giner, F.; Aceto, N. Tracking Cancer Progression: From Circulating Tumor Cells to Metastasis. *Genome Med.* **2020**, *12*, 31. [[CrossRef](#)]
  130. Chen, W.; Li, X.; Zhu, L.; Liu, J.; Xu, W.; Wang, P. Preclinical and Clinical Applications of Specific Molecular Imaging for HER2-Positive Breast Cancer. *Cancer Biol. Med.* **2017**, *14*, 271. [[CrossRef](#)]
  131. Gao, D.; Gao, J.; Xu, M.; Cao, Z.; Zhou, L.; Li, Y.; Xie, X.; Jiang, Q.; Wang, W.; Liu, J. Targeted Ultrasound-Triggered Phase Transition Nanodroplets for Her2-Overexpressing Breast Cancer Diagnosis and Gene Transfection. *Mol. Pharm.* **2017**, *14*, 984–998. [[CrossRef](#)]
  132. Busquets, M.A.; Estelrich, J.; Sánchez-Martín, M.J. Nanoparticles in Magnetic Resonance Imaging: From Simple to Dual Contrast Agents. *Int. J. Nanomed.* **2015**, *10*, 1727–1741. [[CrossRef](#)] [[PubMed](#)]
  133. Chen, Q.; Xu, L.; Liang, C.; Wang, C.; Peng, R.; Liu, Z. Photothermal Therapy with Immune-Adjuvant Nanoparticles Together with Checkpoint Blockade for Effective Cancer Immunotherapy. *Nat. Commun.* **2016**, *7*, 13193. [[CrossRef](#)] [[PubMed](#)]
  134. Pellico, J.; Llop, J.; Fernández-Barahona, I.; Bhavesh, R.; Ruiz-Cabello, J.; Herranz, F. Iron Oxide Nanoradiomaterials: Combining Nanoscale Properties with Radioisotopes for Enhanced Molecular Imaging. *Contrast Media Mol. Imaging* **2017**, *2017*, 1549580. [[CrossRef](#)] [[PubMed](#)]
  135. Chen, T.-J.; Cheng, T.-H.; Chen, C.-Y.; Hsu, S.C.N.; Cheng, T.-L.; Liu, G.-C.; Wang, Y.-M. Targeted Herceptin–Dextran Iron Oxide Nanoparticles for Noninvasive Imaging of HER2/Neu Receptors Using MRI. *J. Biol. Inorg. Chem.* **2009**, *14*, 253–260. [[CrossRef](#)]
  136. Alric, C.; Hervé-Aubert, K.; Aubrey, N.; Melouk, S.; Lajoie, L.; Mème, W.; Mème, S.; Courbebaisse, Y.; Ignatova, A.A.; Feofanov, A.V.; et al. Targeting HER2-Breast Tumors with ScFv-Decorated Bimodal Nanoparticles. *J. Nanobiotechnol.* **2018**, *16*, 18. [[CrossRef](#)]
  137. Zhang, Y.; Ni, Q.; Xu, C.; Wan, B.; Geng, Y.; Zheng, G.; Yang, Z.; Tao, J.; Zhao, Y.; Wen, J.; et al. Smart Bacterial Magnetic Nanoparticles for Tumor-Targeting Magnetic Resonance Imaging of HER2-Positive Breast Cancers. *ACS Appl. Mater. Interfaces* **2019**, *11*, 3654–3665. [[CrossRef](#)]
  138. Lim, E.-K.; Kim, T.; Paik, S.; Haam, S.; Huh, Y.-M.; Lee, K. Nanomaterials for Theranostics: Recent Advances and Future Challenges. *Chem. Rev.* **2015**, *115*, 327–394. [[CrossRef](#)]
  139. Hardman, R. A Toxicologic Review of Quantum Dots: Toxicity Depends on Physicochemical and Environmental Factors. *Environ. Health Perspect.* **2006**, *114*, 165–172. [[CrossRef](#)]
  140. Wei, T.; Xing, H.; Wang, H.; Zhang, Y.; Wang, J.; Shen, J.; Dai, Z. Bovine Serum Albumin Encapsulation of near Infrared Fluorescent Nano-Probe with Low Nonspecificity and Cytotoxicity for Imaging of HER2-Positive Breast Cancer Cells. *Talanta* **2020**, *210*, 120625. [[CrossRef](#)]
  141. Seifalian, A.; Rizvi, S.; Rouhi, S.; Taniguchi, S.; Yang, S.Y.; Green, M.; Keshtgar, M. Near-Infrared Quantum Dots for HER2 Localization and Imaging of Cancer Cells. *Int. J. Nanomed.* **2014**, *9*, 1323. [[CrossRef](#)]
  142. Wang, Z.; Wang, W.; Bu, X.; Wei, Z.; Geng, L.; Wu, Y.; Dong, C.; Li, L.; Zhang, D.; Yang, S.; et al. Microarray Based Screening of Peptide Nano Probes for HER2 Positive Tumor. *Anal. Chem.* **2015**, *87*, 8367–8372. [[CrossRef](#)] [[PubMed](#)]

143. Ramos-Gomes, F.; Bode, J.; Sukhanova, A.; Bozrova, S.V.; Saccomano, M.; Mitkovski, M.; Krueger, J.E.; Wege, A.K.; Stuehmer, W.; Samokhvalov, P.S.; et al. Single- and Two-Photon Imaging of Human Micrometastases and Disseminated Tumour Cells with Conjugates of Nanobodies and Quantum Dots. *Sci. Rep.* **2018**, *8*, 4595. [[CrossRef](#)] [[PubMed](#)]
144. Xavir, C.; Blykers, A.; Vaneycken, I.; D'Huyvetter, M.; Heemskerk, J.; Lahoutte, T.; Devoogdt, N.; Caveliers, V. 18F-Nanobody for PET Imaging of HER2 Overexpressing Tumors. *Nucl. Med. Biol.* **2016**, *43*, 247–252. [[CrossRef](#)] [[PubMed](#)]
145. Ahlgren, S.; Wällberg, H.; Tran, T.A.; Widström, C.; Hjertman, M.; Abrahmsén, L.; Berndorff, D.; Dinkelborg, L.M.; Cyr, J.E.; Feldwisch, J.; et al. Targeting of HER2-Expressing Tumors with a Site-Specifically 99m Tc-Labeled Recombinant Affibody Molecule, ZHER2: 2395, with C-Terminally Engineered Cysteine. *J. Nucl. Med.* **2009**, *50*, 781–789. [[CrossRef](#)] [[PubMed](#)]
146. Welch, M.J.; Hawker, C.J.; Wooley, K.L. The Advantages of Nanoparticles for PET. *J. Nucl. Med.* **2009**, *50*, 1743–1746. [[CrossRef](#)] [[PubMed](#)]
147. Lee, H.; Shields, A.F.; Siegel, B.A.; Miller, K.D.; Krop, I.; Ma, C.X.; LoRusso, P.M.; Munster, P.N.; Campbell, K.; Gaddy, D.F.; et al. 64Cu-MM-302 Positron Emission Tomography Quantifies Variability of Enhanced Permeability and Retention of Nanoparticles in Relation to Treatment Response in Patients with Metastatic Breast Cancer. *Clin. Cancer Res.* **2017**, *23*, 4190–4202. [[CrossRef](#)]
148. Rainone, P.; Riva, B.; Belloli, S.; Sudati, F.; Ripamonti, M.; Verderio, P.; Colombo, M.; Colzani, B.; Gilardi, M.C.; Moresco, R.M.; et al. Development of 99mTc-Radiolabeled Nanosilica for Targeted Detection of HER2-Positive Breast Cancer. *Int. J. Nanomed.* **2017**, *12*, 3447–3461. [[CrossRef](#)]
149. Lee, H.; Zheng, J.; Gaddy, D.; Orcutt, K.D.; Leonard, S.; Geretti, E.; Hesterman, J.; Harwell, C.; Hoppin, J.; Jaffray, D.A.; et al. A Gradient-Loadable 64Cu-Chelator for Quantifying Tumor Deposition Kinetics of Nanoliposomal Therapeutics by Positron Emission Tomography. *Nanomed. Nanotechnol. Biol. Med.* **2015**, *11*, 155–165. [[CrossRef](#)]
150. Rainone, P.; De Palma, A.; Sudati, F.; Roffia, V.; Rigamonti, V.; Salvioni, L.; Colombo, M.; Ripamonti, M.; Spinelli, A.E.; Mazza, D.; et al. 99mTc-Radiolabeled Silica Nanocarriers for Targeted Detection and Treatment of HER2-Positive Breast Cancer. *Int. J. Nanomed.* **2021**, *16*, 1943–1960. [[CrossRef](#)]
151. Jang, M.; Yoon, Y.I.; Kwon, Y.S.; Yoon, T.-J.; Lee, H.J.; Hwang, S.I.; Yun, B.L.; Kim, S.M. Trastuzumab-Conjugated Liposome-Coated Fluorescent Magnetic Nanoparticles to Target Breast Cancer. *Korean J. Radiol.* **2014**, *15*, 411. [[CrossRef](#)]
152. Jiang, Q.; Hao, S.; Xiao, X.; Yao, J.; Ou, B.; Zhao, Z.; Liu, F.; Pan, X.; Luo, B.; Zhi, H. Production and Characterization of a Novel Long-Acting Herceptin-Targeted Nanobubble Contrast Agent Specific for Her-2-Positive Breast Cancers. *Breast Cancer* **2016**, *23*, 445–455. [[CrossRef](#)] [[PubMed](#)]
153. Li, X.; Xia, S.; Zhou, W.; Ji, R.; Zhan, W. Targeted Fe-Doped Silica Nanoparticles as a Novel Ultrasound–Magnetic Resonance Dual-Mode Imaging Contrast Agent for HER2-Positive Breast Cancer. *Int. J. Nanomed.* **2019**, *14*, 2397–2413. [[CrossRef](#)] [[PubMed](#)]
154. Chen, J.S.; Chen, J.; Bhattacharjee, S.; Cao, Z.; Wang, H.; Swanson, S.D.; Zong, H.; Baker, J.R.; Wang, S.H. Functionalized Nanoparticles with Targeted Antibody to Enhance Imaging of Breast Cancer in Vivo. *J. Nanobiotechnol.* **2020**, *18*, 135. [[CrossRef](#)] [[PubMed](#)]
155. Chen, F.; Ma, K.; Madajewski, B.; Zhuang, L.; Zhang, L.; Rickert, K.; Marelli, M.; Yoo, B.; Turker, M.Z.; Overholtzer, M.; et al. Ultrasmall Targeted Nanoparticles with Engineered Antibody Fragments for Imaging Detection of HER2-Overexpressing Breast Cancer. *Nat. Commun.* **2018**, *9*, 4141. [[CrossRef](#)] [[PubMed](#)]
156. Wu, Y.; Meng, Q.; Yang, Z.; Shi, L.; Hu, R.; Zhang, P.; Wei, J.; Ren, J.; Leng, B.; Xu, D.; et al. Circulating HER-2 mRNA in the Peripheral Blood as a Potential Diagnostic and Prognostic Biomarker in Females with Breast Cancer. *Oncol. Lett.* **2018**, *16*, 3726–3734. [[CrossRef](#)] [[PubMed](#)]
157. Emami, M.; Shamsipur, M.; Saber, R.; Irajirad, R. An Electrochemical Immunosensor for Detection of a Breast Cancer Biomarker Based on AntiHER2–Iron Oxide Nanoparticle Bioconjugates. *Analyst* **2014**, *139*, 2858–2866. [[CrossRef](#)]
158. Villegas-Serralta, E.; Zavala, O.; Flores-Urquiza, I.A.; García-Casillas, P.E.; Chapa González, C. Detection of HER2 through Antibody Immobilization Is Influenced by the Properties of the Magnetite Nanoparticle Coating. *J. Nanomater.* **2018**, *2018*, 7571613. [[CrossRef](#)]
159. Yang, J.; Wang, Z.; Zong, S.; Song, C.; Zhang, R.; Cui, Y. Distinguishing Breast Cancer Cells Using Surface-Enhanced Raman Scattering. *Anal. Bioanal. Chem.* **2012**, *402*, 1093–1100. [[CrossRef](#)]
160. Tao, Y.; Li, M.; Kim, B.; Auguste, D.T. Incorporating Gold Nanoclusters and Target-Directed Liposomes as a Synergistic Amplified Colorimetric Sensor for HER2-Positive Breast Cancer Cell Detection. *Theranostics* **2017**, *7*, 899–911. [[CrossRef](#)]
161. Tabatabaei-Panah, A.-S.; Jeddi-Tehrani, M.; Ghods, R.; Akhondi, M.-M.; Mojtavavi, N.; Mahmoudi, A.-R.; Mirzadegan, E.; Shojaeian, S.; Zarnani, A.-H. Accurate Sensitivity of Quantum Dots for Detection of HER2 Expression in Breast Cancer Cells and Tissues. *J. Fluoresc.* **2013**, *23*, 293–302. [[CrossRef](#)]
162. Gijs, M.; Penner, G.; Blackler, G.; Impens, N.; Baatout, S.; Luxen, A.; Aerts, A. Improved Aptamers for the Diagnosis and Potential Treatment of HER2-Positive Breast Cancer. *Pharmaceuticals* **2016**, *9*, 29. [[CrossRef](#)] [[PubMed](#)]
163. Chu, M.; Kang, J.; Wang, W.; Li, H.; Feng, J.; Chu, Z.; Zhang, M.; Xu, L.; Wang, Y. Evaluation of Human Epidermal Growth Factor Receptor 2 in Breast Cancer with a Novel Specific Aptamer. *Cell. Mol. Immunol.* **2017**, *14*, 398–400. [[CrossRef](#)] [[PubMed](#)]
164. Kim, J.-H.; Suh, J.-S.; Yang, J. Labeling-Free Detection of ECD-HER2 Protein Using Aptamer-Based Nano-Plasmonic Sensor. *Nanotechnology* **2020**, *31*, 175501. [[CrossRef](#)] [[PubMed](#)]
165. Zheng, D.; Wan, C.; Yang, H.; Xu, L.; Dong, Q.; Du, C.; Du, J.; Li, F. Her2-Targeted Multifunctional Nano-Theranostic Platform Mediates Tumor Microenvironment Remodeling and Immune Activation for Breast Cancer Treatment. *Int. J. Nanomed.* **2020**, *15*, 10007–10028. [[CrossRef](#)] [[PubMed](#)]
166. Choi, W.I.; Lee, J.H.; Kim, J.-Y.; Heo, S.U.; Jeong, Y.Y.; Kim, Y.H.; Tae, G. Targeted Antitumor Efficacy and Imaging via Multifunctional Nano-Carrier Conjugated with Anti-HER2 Trastuzumab. *Nanomed. Nanotechnol. Biol. Med.* **2015**, *11*, 359–368. [[CrossRef](#)]

## Appendix 2



Review

# Protein-Based Nanoparticles for the Imaging and Treatment of Solid Tumors: The Case of Ferritin Nanocages, a Narrative Review

Francesco Mainini <sup>1</sup>, Arianna Bonizzi <sup>1</sup>, Marta Sevieri <sup>1</sup>, Leopoldo Sitia <sup>1</sup>, Marta Truffi <sup>2</sup>, Fabio Corsi <sup>1,2,\*</sup>, and Serena Mazzucchelli <sup>1,\*</sup>

<sup>1</sup> Dipartimento di Scienze Biomediche e Cliniche “L. Sacco”, Università di Milano, 20157 Milano, Italy; francesco.mainini@unimi.it (F.M.); arianna.bonizzi@unimi.it (A.B.); marta.sevieri@unimi.it (M.S.); leopoldo.sitia@unimi.it (L.S.)

<sup>2</sup> Istituti Clinici Scientifici Maugeri IRCCS, 27100 Pavia, Italy; marta.truffi@icsmaugeri.it

\*Correspondence: fabio.corsi@unimi.it (F.C.); serena.mazzucchelli@unimi.it (S.M.)

**Abstract:** Protein nanocages have been studied extensively, due to their unique architecture, exceptional biocompatibility and highly customization capabilities. In particular, ferritin nanocages (FNs) have been employed for the delivery of a vast array of molecules, ranging from chemotherapeutics to imaging agents, among others. One of the main favorable characteristics of FN is their intrinsic targeting efficiency toward the Transferrin Receptor 1, which is overexpressed in many tumors. Furthermore, genetic manipulation can be employed to introduce novel variants that are able to improve the loading capacity, targeting capabilities and bio-availability of this versatile drug delivery system. In this review, we discuss the main characteristics of FN and the most recent applications of this promising nanotechnology in the field of oncology with a particular emphasis on the imaging and treatment of solid tumors.

**Keywords:** ferritin; cancer; tumor targeting; drug delivery; imaging

## 1. Introduction

Nanoparticle-based drug delivery systems have the capacity to enhance the physico-chemical properties of a wide variety of drugs used in oncology to limit off-site side effects and improve their therapeutic efficacy [1–3]. The ideal nanocarrier should be bio-compatible and be able to avoid recognition by the reticuloendothelial system (RES), composed of tissue-resident macrophages and phagocytes in the bloodstream, capable of efficiently clearing exogenous nanoparticles (NP) from the circulation [4]. Natural proteins nanocages have a distinctive advantage in this regard, in comparison to synthetic NP (liposomes, polymeric NP, micelles and dendrimers), since they are virtually invisible to the immune system and display great biocompatibility coupled with minimal toxicity. An exception is represented by virus-like particles (VLPs), which are also composed of self-assembled proteins that are, in some cases, highly immunogenic [5].

Endogenous self-assembled NPs can be synthesized by many cell types and are primarily used to store and/or distribute to different tissues a wide variety of molecules, such as nutrients and biochemical signals. NPs of this kind are quite diverse in terms of size and physiological activity. Some examples are ferritin nanocages (FNs), heat-shock protein cages, vault ribonucleoproteins, the E2 protein of the pyruvate dehydrogenase multienzyme complex, chaperones, carboxysomes and other enzyme complexes [6]. Unfortunately, most of these protein-based NP are understudied and have, so far, limited applications in the field of oncology. However, FN have been studied extensively due to their intrinsic targeting capabilities toward the Transferrin Receptor 1 (TfR1), which is highly expressed in many tumors, making them very appealing for drug-delivery applications in oncology. Furthermore, the small size and high customization potential make them ideal candidates for the development of novel nanomedicines able to deliver a wide variety of drugs to the tumor microenvironment (TME). This review describes the structure and function of FN, modifications of the nanocages by chemical or genetic manipulation (Figure 1) and novel applications of this nanotechnology for the imaging and treatment of solid tumors (Figure 2).



**Citation:** Mainini, F.; Bonizzi, A.; Sevieri, M.; Sitia, L.; Truffi, M.; Corsi, F.; Mazzucchelli, S. Protein-Based Nanoparticles for the Imaging and Treatment of Solid Tumors: The Case of Ferritin Nanocages, a Narrative Review. *Pharmaceutics* **2021**, *13*, 2000. <https://doi.org/10.3390/pharmaceutics13122000>

Academic Editor: Xiangyang Shi

Received: 2 November 2021

Accepted: 19 November 2021

Published: 25 November 2021

**Publisher's Note:** MDPI stays neutral with regard to jurisdictional claims in published maps and institutional affiliations.



**Copyright:** © 2021 by the authors. Licensee MDPI, Basel, Switzerland. This article is an open access article distributed under the terms and conditions of the Creative Commons Attribution (CC BY) license (<https://creativecommons.org/licenses/by/4.0/>).



## Human Hc Ferritin Nanocages (FN) for the imaging and treatment of tumors

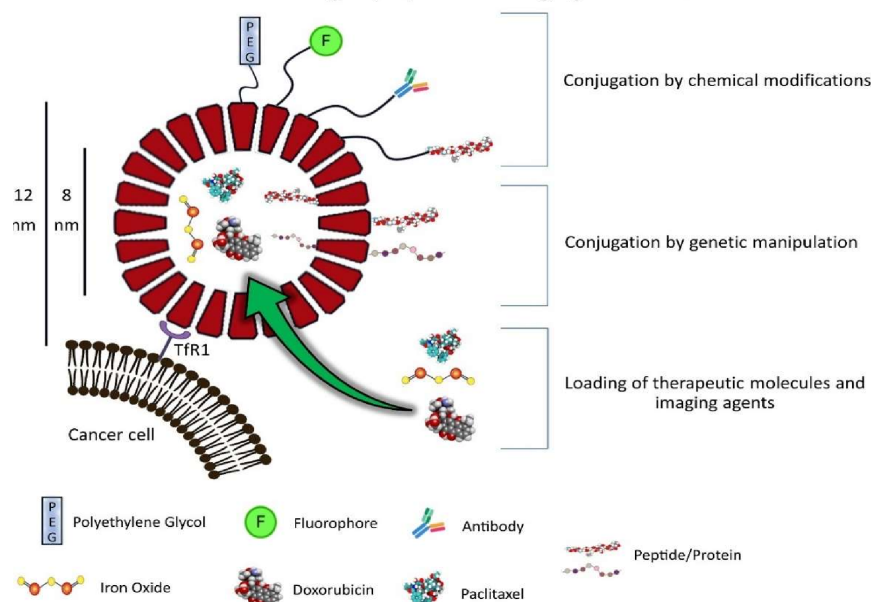


**Figure 1.** FN as a protein-based delivery system for oncological therapeutics and imaging agents. FNs are composed of 24 Hc subunits that can be chemically or genetically modified to couple a large variety of molecules (antibodies, peptides, fluorophores, polyethylene glycol (PEG) and others) to their surface (N-terminus) or internal cavity (C-terminus). Furthermore, FNs can be loaded with different drugs and imaging agents and have intrinsic targeting capabilities toward the receptor TfR1, which is overexpressed in many tumors. This cartoon was created by using BioRender (<https://biorender.com/>, accessed on 2 November 2021).

## Applications of FN in the field of oncology

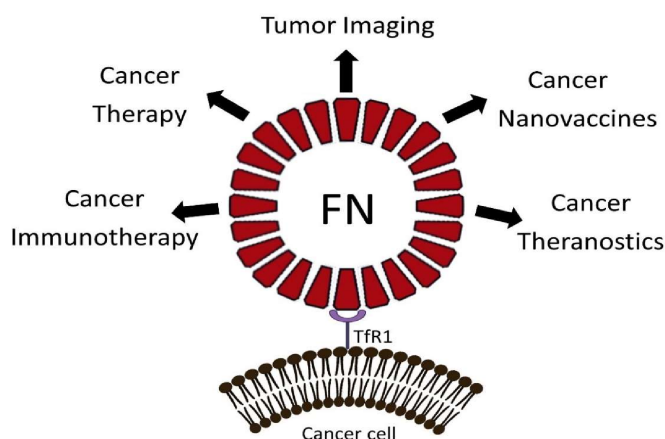


**Figure 2.** Applications of FNs in the field of oncology. FNs are versatile drug delivery systems. They can be loaded simultaneously with anticancer and imaging agents to provide effective antitumor therapy that can be monitored by different imaging modalities. In addition, FNs can be loaded with immunomodulatory drugs to remodel the TME or can be developed to incorporate tumor associated antigens to induce specific adaptive immune responses against cancer cells, in the case of nanovaccines. This cartoon was created by using BioRender (<https://biorender.com/>, accessed on 2 November 2021).

## 2. FN Structure and Properties

Ferritin self-assembles in hollow icosahedral-shaped nanocages with inner and outer dimensions of 8 and 12 nm, respectively [7]. In mammalian cells, ferritin is composed of heavy-chain (Hc, 21 kDa) and light-chain (Lc, 19 kDa) subunits (24 in total between the two) which are structurally similar. FN employed as a delivery device in cancer application are mostly constituted only by Hc subunits of human ferritin. Ferritin and FNs are remarkably stable in biological fluids and are resistant to denaturants, including high temperatures (>80 C) [8]. Each subunit is composed of four long helices, a short helix and a long loop [9]. The C-terminal of each subunit folds into the inner cavity, while the N-terminal is exposed on the outer surface of the nanocage. The ratio between Hc and Lc subunits is determined by ferritin's primary role in tissues. For example, in the heart and brain, the Hc is more abundant, while, in the liver and spleen, the Lc is predominant. The Hc subunit contains a dinuclear ferroxidase site that is located within the four-helix bundle, while the Lc provides efficient sites for iron nucleation and mineralization [10]. Ferritin and FN carry six C4 channels and eight C3 channels. The C3 channels have hydrophilic properties and allow the passage of Fe(II) ions and water molecules

in and out of the protein cage. On the other hand, the C4 channels allow the passage of small hydrophobic molecules [8].

Ferritin in the bloodstream is mainly composed of Lc subunits [8], which seem to be secreted primarily by macrophages [11]; however, their role in the serum is still highly debated. Nonetheless, high ferritin levels have been linked with ongoing infections and chronic inflammation, while its reduced levels have been correlated with iron deficiency [12–14]. Interestingly, it can be localized in cells both in the cytoplasm and in the nucleus. Iron stored in ferritin can be utilized by the cell in a process mediated by autophagy, where it is transported to the lysosomes and iron is released in a pH-dependent manner [15]. On the other hand, in conditions of oxidative stress, ferritin can convert DNA damaging Fe(II) to harmless Fe(III), thus limiting DNA damage mediated by the formation of hydroxyl radicals through the Fenton reaction [16–18]. Two proteins, poly(rC)-binding protein 1 (PCBP1) and nuclear receptor coactivator 4 (NCOA4), are involved in the transport of iron inside and outside ferritin [19]. Furthermore, it has been proposed that O-glycosylation of the Hc could be involved in the nuclear translocation of Ferritin, which maintains its intact structure during this process [20,21]. FNs share all structural features and properties with their physiological form, and they often have been demonstrated to be managed by the cells and the tissue as natural ferritin [21,22].

#### Strategies for Loading FN

Molecular cargoes can be loaded into the inner core of FN by different methodologies (Figure 3). Extreme pH (2 or 13) is used to transiently disassemble the protein nanocage into monomers that can reassemble by adjusting the pH toward neutrality. By employing this methodology, FN can be loaded with different chemotherapeutic drugs. Interestingly, only minor differences in the loading efficiency between doxorubicin (DOX), epirubicin (EPI), daunorubicin (DAU) and idarubicin (IDA) were seen, despite their differences in terms of hydrophobicity [23]. In addition, high concentrations of guanidine hydrochloride (GuHCl) or urea are able to disrupt the non-covalent forces which support FNs' structure, leading to their disassembly. This process can be reversed by dialysis to remove the excess of chaotropic agents, leading to the recovery of the original nanostructure with consequent loading of molecular cargoes in the inner cavity [24]. More recently, atmospheric cold plasma (ACP) technology was implemented to reduce the  $\alpha$ -helix/  $\beta$ -sheet contents and thermal stability of FN to allow disassembly at a pH of 4. This technique can be utilized to load molecules which are susceptible to extreme pH conditions and could be degraded during the loading procedure [25]. In addition, our group has showed that the loading of molecules sensitive to low pH can be achieved during the reassembly phase by adding the molecule of interest to the ferritin-containing solution after the adjustment of the pH toward neutrality [26]. In another report, Jiang and colleagues developed a methodology that is able to provide high loading of DOX and high recovery of FN by incubating DOX with FN at 60 °C for 4 h [27]. This loading methodology enables the opening of FN's channel to introduce DOX without disrupting FN's structure. Lastly, by taking advantage of the natural capacity of FNs to encapsulate iron in their cavity, several metal ions can be coupled to molecules of interest that can then be loaded into FNs. In this case, the final loading efficiency of the chosen drug depends on its binding affinity for the metal ion, the FN species used and preparation conditions. For example, Zhen and colleagues suggested that, between Cu(II), Mn(II), Zn(II) and Fe(III) metal ions, the use of copper resulted in the highest loading rate of DOX into FN [28]. A more detailed comparison of loading methodologies for DOX into FN has been reviewed by He and colleagues [29], while Zhang and colleagues provide specific protocols regarding the loading of various drugs into FNs by using different methodologies [30].

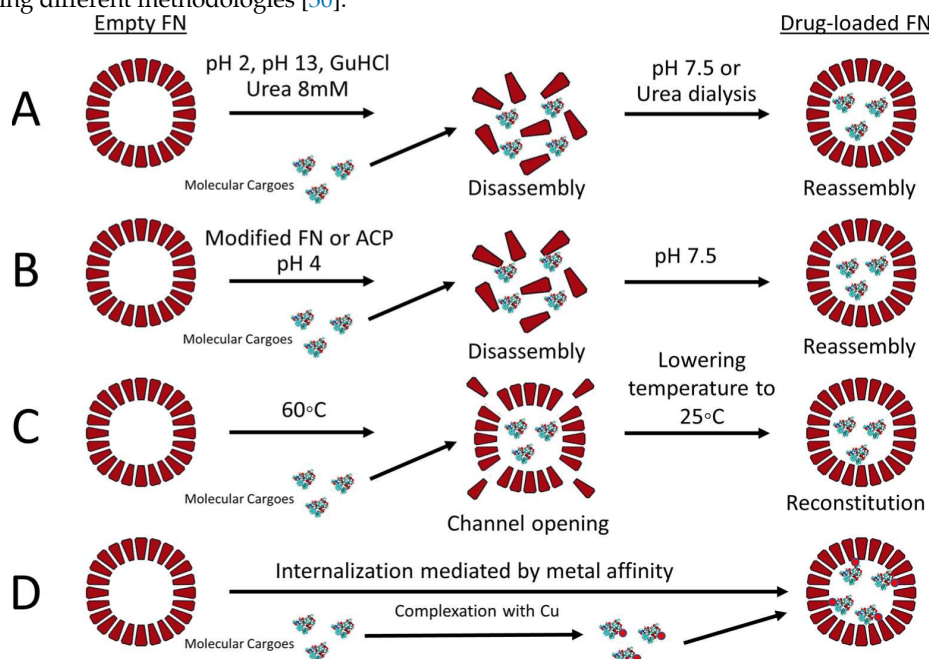


**Figure 3.** Biochemical strategies used to load different cargoes into FNs: (A) pH or urea-mediated disassembly–reassembly methodology; (B) modified ferritins or ACP can be utilized to disassemble FN at pH 4, and then pH 7.5 is used to reassemble FN; (C) high temperatures partially destabilize FN to allow channel openings with consequent drug loading, and then lowering the temperature can slowly reconstitute the natural conformation of FN; (D) molecular cargoes can be complexed with Cu(II) or other metal ions which have a high affinity for the internal cavity of FN. This methodology permits the loading of hydrophobic molecules with some limitations.

Overall, FNs' physicochemical properties (small size and negative Z potential), together with their intrinsic capacity to avoid recognition by RES and targeting capability toward TfR1-expressing tumor cells, make them an ideal candidate for the development of drug delivery systems for nanobiotechnological applications in the field of oncology (Table 1). Moreover, drug loading and targeting efficiency could be enhanced by chemical and genetic manipulations of FNs, as is discussed in the following section.

**Table 1.** FN-based NPs for the imaging and treatment of tumors.

FN Origin	Purpose	Modifications	Loaded with	In Vivo Tested?	Reference
Human Hc FN	Cancer therapy	BCP1 peptide	DOX	Yes	[31]
Human Hc FN	Cancer therapy	Mutations to enhance the binding of Cu <sup>2+</sup>	DOX	Yes	[32]
Human Hc FN	Cancer therapy	4 Lysines (C-terminus)	siRNA (EGFR)	Yes	[33]
Human Hc FN	Cancer therapy	PD-L1 binding peptide	DOX	Yes	[34]
Human Hc FN	Cancer therapy	tLyP-1 peptide	PTX	Yes	[35]
Human Hc FN	Cancer therapy	Trastuzumab	DOX	Yes	[36]
Human Hc FN	Cancer therapy	PEGylation (50% subunits)	DOX	Yes	[37]
Human Hc FN	Cancer therapy	PEGylation (75% subunits)	Acriflavine	Yes	[38]
Human Hc FN	Cancer therapy	None	Olaparib	No	[39]
Human Hc FN	Cancer therapy	None	Everolimus	No	[40]
Human Hc FN	Cancer therapy	None	Curcumin	No	[41]
Human Hc FN	Cancer therapy	Anti FAP antibody	Navitoclax	Yes	[42]
Human Hc FN	Cancer therapy	None	DOX	Yes	[43]
Human Hc FN	Cancer therapy	α2 1 targeting peptide	DOX	Yes	[44]
Human Hc FN	Cancer therapy	None	PTX	Yes	[45]
Human Hc FN	Cancer therapy	Trastuzumab or Cetuximab	Empty	No	[46]
Human Hc FN	Cancer therapy	Pout peptide (C terminus)	EPI, Camptothecin	Yes	[47]
<i>Pyrococcus furiosus</i> FN	Cancer therapy	SP94 peptide	DOX	Yes	[48]

**Table 1. Cont.**

FN Origin	Purpose	Modifications	Loaded with	In Vivo Tested?	Reference
Horse spleen FN	Cancer therapy	None	Mertansine	No	[49]
Horse spleen FN	Cancer therapy	None	Arsenoplatin-1	No	[50]
Horse spleen FN	Cancer therapy	Emulsified FN (size 78nm)	Rapamycin and Erastin	Yes	[51]
Horse spleen FN	Cancer therapy	GKRK peptide	Vincristine	Yes	[52]
Unspecified	Cancer therapy	PEG–Panitumumab	Oxaliplatin	Yes	[53]
Unspecified	Cancer therapy	RGD peptide	Resveratrol	Yes	[54]
Unspecified	Cancer therapy	None	Au(III) thiosemicarbazone	Yes	[55]
<i>Pyrococcus furiosus</i> FN	Cancer nanovaccine	SpyCatcher	SpyTagged peptides	Yes	[56]
Human Hc FN	Cancer Immunotherapy	M2pep peptide (N-terminus), cationic peptide (C-terminus)	CpG	Yes	[57]
Human Hc FN	Cancer Theranostic	None	Iron Oxide (core) and IRdye800 or DOX	Yes	[58]
Human Hc FN	Cancer Theranostic	Coated with RBC (functionalized with FA)	Iron Oxide, Cy5.5	Yes	[59]

Horse spleen FN	Cancer Theranostic	2-amino-2-deoxy-glucose	Gold NP	No	[60]
Horse spleen FN	Cancer Theranostic	None	Endogenous Iron	Yes	[61]
Unspecified	Cancer Theranostic	PEG-FA	Perfluoropentane	Yes (imaging only)	[62]
Human Hc FN	Tumor Imaging	None	ICG	Yes	[26,63]
Human Hc FN	Tumor Imaging	SDSSD peptide or hydroxyapatite binding peptide	Cy5	Yes	[64]
Human Hc FN	Tumor Imaging	None	Iron Oxide or Cy5.5	Yes	[65]

### 3. Production and Modifications of FN

FNs utilized in preclinical studies are usually produced as recombinant protein in *E. coli* strains engineered to express only the human Hc subunit. This procedure involves the transformation of bacteria with a plasmid containing the Hc sequence of interest, which is then purified by anion-exchanger columns after treatment at 70 °C. The resulting FNs are composed, in this case, of 100% Hc subunits [66]. Otherwise, FNs can be purified from the horse spleen, where the ratio between Hc and Lc subunits was found to be ~1/10 [67]. To ensure that purified FNs are not contaminated by endotoxins that could impact both in vitro and in vivo experiments, additional procedures to remove endotoxins might be required [68].

The genetic manipulation of the Hc-FN DNA sequence led to the development of more than one hundred variants to introduce novel functionalities that are able to improve the drug loading, biodistribution and targeting properties of FNs [69]. For example, the self-assembly properties of FNs can be altered to produce novel nanostructures comprising 8 or 48 subunits instead of 24 [70,71]. In addition, ferritin can be modified to produce nanocages that can disassemble at a pH of 4 or 6, instead of 2 [72–74]. Intriguingly, Gu and colleagues developed His-modified ferritins that do not self-assemble at neutral pH. However, metal ions or a pH of 10 induce self-assembly with consequent increases of the drug-loading efficiency, as compared to the standard pH methodology discussed previously [75]. Unfortunately, the stability in serum of His-modified ferritins was not evaluated, and it is unclear if these nanoconstructs are suitable for in vivo studies.

Different strategies have been recently employed to enhance the half-life of FNs in the circulation to provide higher tumor accumulation and reduce clearance by RES. For example, Wang and colleagues developed a novel FN that includes an albumin-binding domain that is able to increase FNs' half-life by 17 times, as compared to the standard FN [76]. In another report, an amino acid sequence rich in proline (P), serine (S) and alanine (A) residues (PAS polypeptide) was inserted by genetic manipulation into FN to increase blood half-life and DOX encapsulation efficiency [77,78]. Interestingly, the insertion of two glutamate residues in the PAS sequence (PASE) further improved FNs' accumulation to the tumor site [79]. In another report, Jin and colleagues introduced in the ferritin construct a blood circulation prolonging (BCP) peptide derived from the phage M13. The generated FN (BCP1-FN) showed improved circulation time compared to standard FN (20 h compared to 2 h). In addition, when loaded with DOX, BCP1-FN-DOX showed superior therapeutic efficacy in a mouse model of melanoma compared to FN-DOX and free DOX. Intriguingly, the authors suggested that the RGD portion of the BCP1 peptide could be responsible for the binding of BCP1-FN to peripheral blood cells, particularly platelets, which are able to protect the nanocages from RES recognition [31]. Nonetheless, blood cells' "hitchhiking" has recently emerged as one of the strategies that can be employed to enhance the delivery of NP to the tumor site [80,81].

Since FNs are composed of different subunits, novel FN-based nanostructures have been developed with combinations of different ferritins resulting in hybrid nanocages with interesting physicochemical properties. Ahn and colleague developed a hybrid FN composed of modified subunits (F160) and standard Hc in a ratio 1:1. F160 was devised to provide large pores to FN and was produced by removing the C-terminal channel forming E-helix from the Hc sequence. The resulting hybrid FN (nicked-FN) allows for the encapsulation of DOX by simple incubation, improving the loading of DOX and the recovery of the nicked-FN-DOX in comparison to encapsulation in unmodified FN or with the pH-mediated disassembly and reassembly methodology [82]. Another strategy to enhance DOX loading into FN was developed by producing a mutant FN that displays an enhanced affinity for copper ions [32]. In another report, FNs were modified with the addition of biotin accepted peptide, which resulted in biotinylated FN that can be more easily modified by the addition of streptavidin-tagged molecules [83]. These modified FN could be used in a variety of immunoassays based on streptavidin-tagged antibodies to increase the sensitivity. It is unsure if they can be employed for in vivo studies.

The delivery of nucleic acids by NP-based delivery systems has always been a primary goal of the research effort in the field of nanotechnology. Interestingly, modified FNs with the addition of a cationic polypeptide were developed to facilitate the incorporation of siRNAs in FNs' nanostructure [33,84]. However, it has also recently been shown that unmodified FNs could incorporate siRNAs by pH-mediated disassembly and reassembly methodology [85].

FNs can also be modified to include immunogenic peptides that are able to induce immune responses against specific antigens. As proof of principle, Kanekiyo and colleagues



developed a nanovaccine against the H1N1 virus based of FNs that were modified to include the viral hemagglutinin sequence. Preclinical testing of the developed nanoformulation showed induced protection of animal models to H1N1 infection [86]. More recently, FN-based anticancer nanovaccines have been developed and were tested successfully in preclinical models [56,87,88].

Interestingly, many FN variants have been developed to include novel targeting ligands. For example, Jiang and colleagues introduced, by genetic manipulation, a hepatocellular carcinoma (HCC)-targeting peptide to the FN's structure that was then loaded with DOX. This novel formulation showed superior activity compared to free DOX in reducing HCC tumor growth and metastases in preclinical models [48,89]. In another report, the PDL1 binding peptide 1 (PD-L1pep1, CLQKTPKQC) was introduced into ferritin's sequence to generate an FN targeted to PD-L1 [34]. Another well-studied tumor-targeting ligand is the tLyp-1 peptide, which binds the receptor Neuropilin 1 expressed in the stroma of many types of tumors [90]. Modified FNs were developed to include the tLyp-1 peptide in the external structure of the nanocage and were subsequently loaded with Paclitaxel (PTX). The resulting FNs (tLyp-FN-PTXs) showed enhanced uptake by tumor cells and were able to control tumor growth in vivo compared to free-PTX or FN, where the sequence of tLyp was mutated (m-tLyp-FN-PTX) [35].

Beyond genetic manipulation, FNs have available primary amines on their surface that can be exploited for chemical conjugation purposes. N-hydroxysuccinimide (NHS) ester or maleimide groups, in combination with 1-ethyl-3-(3-dimethylaminopropyl) carbodiimide (EDC), are often used to couple peptides, PEG, fluorophores or antibodies to FN in a buffered solution, without the use of organic solvents [42,91]. This coupling methodology is often employed to develop fluorescent versions of FNs that can be utilized in a variety of in vitro and in vivo assays, including flow cytometry, fluorescence microscopy and live imaging, which are critical techniques for NP characterization and for the evaluation of biodistribution and targeting capacity of novel formulations of FNs. In a recent report, FNs were modified with the addition of positively charged polyamine dendrimers (PAMAM) to allow efficient loading of nucleic acids. MiRNA-loaded FNs were successfully used to target leukemia cells and showed promising in vitro results [92].

Overall, both genetic and chemical manipulations can enhance multiple aspects of the intrinsic properties of FNs, such as targeting, loading and half-life. However, it is unknown if these modifications could induce the production of specific anti-ferritin antibodies when administered in humans. Interestingly, it has been shown that modifications such as PEGylation could result in the generation of anti-PEG antibodies [93]. Therefore, it is plausible that some of the developed modifications of the native human Hc subunit, by both genetic and chemical manipulation, could potentially reduce the effectiveness of FN after multiple administrations, limit their targeting capabilities and induce undesirable immunogenic reactions [93]. Furthermore, the FN's origin could be an important factor contributing to immunological side effect. These potential complications should be carefully taken in consideration to ensure the success of modified FNs in the prospect of clinical translation [94].

#### 4. FN-Based NPs for Cancer Treatment in Preclinical Models

One of the main issues in the delivery of chemotherapeutics for cancer treatment is the onset of off-site side effects, which can cause a wide spectrum of complications, such as infections, neuropathies, cytopenias, nephrotoxicity, cardiotoxicity and hepatotoxicity [95–98]. NP-based delivery systems are utilized in oncology primarily to reduce the severity of these side effects, improving drug accumulation at the tumor site. Examples of nanotherapeutics currently used in the clinical practice are Doxil™, Abraxane™, Marqibo™ and DaunoXome™, which are NP-based platforms for the delivery of DOX, PTX, Vincristine and DAU, respectively [1].

Interestingly, FNs have been extensively studied as nanocarriers for DOX, since this hydrophilic drug can be encapsulated efficiently into FNs and can be delivered to tumor cells by the TfR1-mediated intrinsic targeting capabilities of FNs. Our group and others have shown that not only are FN-DOX formulations superior to free DOX or Doxil™ in controlling tumor burden in preclinical models of cancer, but they also dramatically reduced drug cardiotoxic effects, as compared to the free DOX [48,99–101]. In another report, Huang and colleagues developed a hybrid FN-DOX formulation for the treatment of lung cancer. It is composed of PEGylated Hc subunits to provide stealth capabilities and non-PEGylated Hc subunits to allow the binding of the nanocage to TfR1. In vivo results showed that, after intratracheal administration of hybrid FN-DOX, the tumor burden in a orthotopic murine model of lung cancer (3LL) was dramatically reduced when compared to free DOX [37]. Apart from DOX, platinum-based chemotherapeutics (cisplatin, oxaliplatin, Pt(II) terpyridine and carboplatin) have been successfully encapsulated in FNs and have shown encouraging antitumor activity in preclinical models of cancer [53,102,103]. Recently, Ferraro and colleagues developed a novel FN loaded with Arsenoplatin-1 ( $\text{Pt}(\mu\text{NHC}(\text{CH}_3)\text{O})_2\text{ClAs}(\text{OH})_2$ ), which combines the cytotoxic effects of both cisplatin and arsenic trioxide. Preliminary in vitro results showed that this novel formulation provides selectivity toward cancer cells, but, unfortunately, it was not tested in vivo [50].

The development of drug resistance often occurs after treatment with standard chemotherapeutics, and it can be mediated by the activity of the transporter multidrug resistance protein 1 (MDR1), which is upregulated in the hypoxic areas of tumors and facilitates

the excretion of chemotherapeutics outside the tumor cell membrane [104]. Interestingly, hypoxia in the TME can induce the expression of TfR1 mediated by hypoxia-inducible factor-1 $\alpha$  (HIF-1 $\alpha$ ) in tumor cells [105]. Hence, FN-based NPs could be employed to specifically target hypoxic areas in tumors. For this purpose, Huang and colleagues developed a hybrid FN (composed of 75% PEGylated subunits) (Figure 4) for the delivery of the HIF-1 $\alpha$  inhibitor Acriflavine (AF). This nanoformulation was particularly effective when used in combination with cisplatin, since the delivery of AF to the TME was able to reduce the expression of MDR1 on tumor cells, thus reducing the development of resistance to cisplatin, which was not effective as standalone treatment in the 3LL lung cancer xenograft model [38].

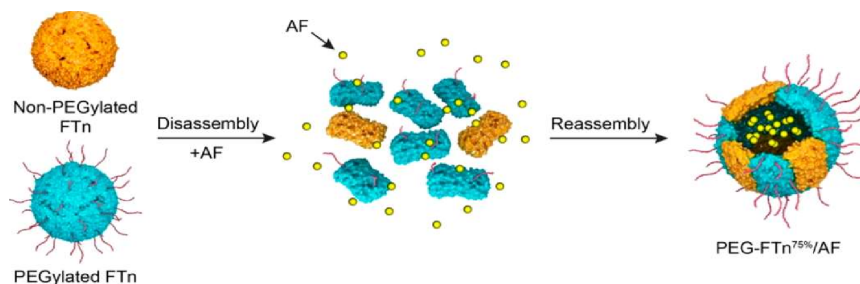


**Figure 4.** Structure and loading procedure for AF-loaded hybrid PEGylated FN. Hybrid FNs can be developed by utilizing the pH disassembly/reassembly methodology, starting from two different FNs (in this case, a PEGylated FN and non-PEGylated FN). In addition, prior to the reassembly phase, anticancer drugs can be added, resulting in their inclusion inside the FN nanostructure after reassembly. Adapted from [39], American Chemical Society, 2019.

Ferritin was also recently employed to develop a novel nanoformulation containing both Rapamycin, an mTOR inhibitor, and Erastin, a ferroptosis inducer. NPs were produced by the emulsification technique, which was shown to be superior compared to the standard pH disassembly–reassembly methodology in regards to drug loading. Interestingly, the size of the NP formed was 7-fold larger than standard FN (78 compared to 12 nm). Nonetheless, this novel formulation achieved impressive results in controlling the tumor growth in a murine model of breast cancer which recapitulates tumor relapse and metastases formation. Briefly, the primary tumor was allowed to grow, and it was excised to simulate surgery. Subsequently, NPs or the free drugs were included in a thermo-responsive F-127 hydrogel and injected into the tumor resection cavity to test the ability of the nanoformulation to prevent tumor recurrence [51]. Unfortunately, the authors did not evaluate the differences in uptake between standard a FN and the modified version developed. Furthermore, since NPs were not administered intravenously, their biodistribution was not evaluated.

FN has also been explored as a nanocarrier for a large variety of drugs for cancer therapy, such as Olaparib [39], Everolimus [40], Curcumin [41], Oxaliplatin + Panitumumab [53], Mertansine [49], Resveratrol [54] and Navitoclax [42].

#### 4.1. FN-Based NPs for Immunomodulation and Immunotherapy

Another therapeutic strategy which has recently emerged in cancer therapy is the immunomodulation of the TME, in particular, the reprogramming of tumor associated macrophages (TAMs). In solid tumors, TAMs constitute up to 50% of the tumor mass and have been shown to support local immunosuppression and metastases formation [106]. They are recruited from the bloodstream and surrounding tissues by growth factors and chemokines, including colony-stimulating factor 1, C-C motif ligand 2 and vascular endothelial growth factor [107,108]. Interestingly, TAMs are conventionally categorized as anti-inflammatory M2-like macrophages and express high levels of TfR1 compared to proinflammatory M1-like macrophages [109,110]. For this reason, TAMs could be effectively targeted by FN-based therapeutics. Of note, macrophages, in general, can be considered as “gate-keepers” of iron metabolism due to their involvement in the recycling of iron from dying erythrocytes [111]. In addition, TAMs-derived FNs have been shown to function as growth factors on malignant mammary epithelium in a process independent of iron [112]. In order to re-educate TAMs and promote a phenotype switch from M2-like to antitumoral M1-like, FNs have been developed to deliver the toll-like receptor 9 agonist CpG, a nucleic acid with M1-polarizing properties [57]. FNs were functionalized with the TAMs-targeting peptide M2pep (YEQDPWGVKWWY), which was combined with a cationic peptide to allow the attachment of the negatively charged CpG. Interestingly, this novel formulation was able to achieve reduction in tumor growth in a murine model of breast cancer. However, a similar effect was seen even when CpG was absent. The authors hypothesized that the antitumoral effect mediated by the M2pep-modified FN could be mediated by the intrinsic M1-polarizing activity of the cationic peptide included in the modified FN, since the unmodified FN showed only minor antitumor activity [57].

The discovery of the molecular mechanisms underpinning the immunosuppressive state in the TME led to the FDA approval of immune checkpoint inhibitors (ICIs) for cancer therapy, giving rise to novel immunotherapeutic options that are able to induce a strong infiltration of active immune cells in the TME, with consequent control of tumor growth [113]. ICIs currently used in the clinical setting are monoclonal antibodies (mAbs) that are able to block the activity of the programmed cell death protein 1 (PD-1)/PD-L1 interaction or cytotoxic T-lymphocyte

antigen-4 expressed by T cells. Recently, a DOX-loaded engineered FN displaying the PD-L1 binding peptide (PpNF) was developed by Seon and colleagues [34]. Interestingly, this novel nanoformulation was able to achieve enhanced tumor-growth reduction in the colon carcinoma CT26 xenograft model, as compared to anti-PD-L1 mAb and free DOX (Figure 5). In addition, the engineered FNs without DOX were shown to be superior to anti-PD-L1 mAb in enhancing the activity of T cells in vitro.

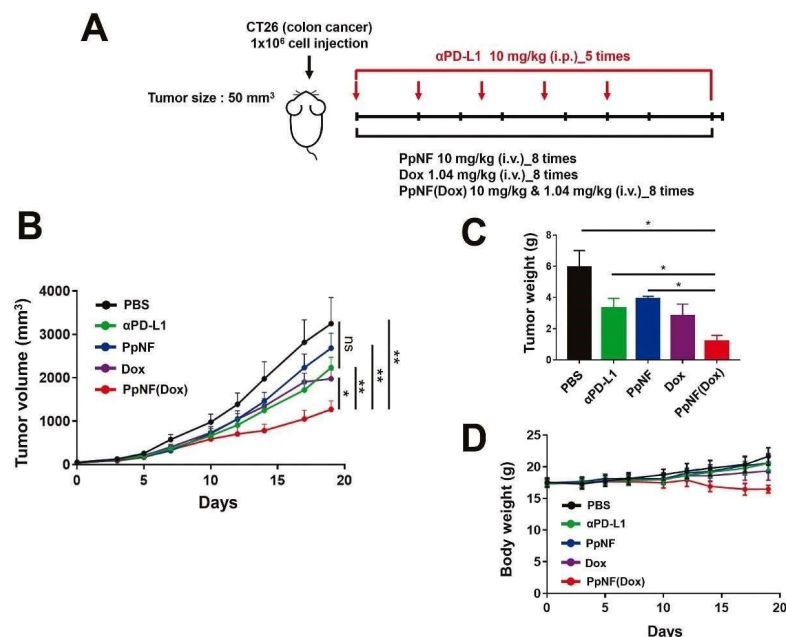


**Figure 5.** Antitumor activity of FNs displaying the PD-L1 binding peptide (PpNF). (A) Experimental schemes for antitumor treatments. Mice bearing s.c. CT26 syngeneic colon tumors were treated with DOX-loaded PpNF (PpNF(Dox)) or PpNF or Dox administered by i.v. injection three times per week. Anti-PD-L1 antibody was administered by i.p. injection twice per week. (B) Tumor volumes after treatment. (C) The weights of excised tumors from each group at the 19-day post-injection. (D) Body weights. The data represent means  $\pm$  SEM (\*  $p < 0.05$  and \*\*  $p < 0.01$ ;  $t$ -test). Reproduced with permission from [35], Elsevier, 2021.

We hypothesize that, in future years, novel FN-based delivery system will be employed to modulate the activity of immune cells, since a new paradigm for NP-based anticancer therapeutics is emerging [114]. In fact, the expanding arsenal of nanomedicines able to modulate the activity of TME-infiltrating immune cells could be utilized to support standard chemotherapeutics or immunotherapies in order to reactivate the antitumor immunity [115].

#### 4.2. FN-Based NPs for the Treatment of Brain Tumors

The blood–brain barrier (BBB) is a diffusion barrier that impedes the influx of most compounds from the bloodstream to the brain parenchyma and represents a protective interface between the central nervous system and peripheral blood circulation [116]. Interestingly, brain cells require iron for metabolic processes; thus, transferrin and ferritin have to bypass the BBB in a process mediated by ligand–receptor recognition. Within the brain, TfR1 was shown to be expressed by capillary endothelial cells, choroid plexus epithelial cells and neurons, which increase the expression of TfR1 in condition of iron deficiency [117]. In addition, TfR1 has been shown to be overexpressed in brain tumors, particularly in glioblastomas, and its overexpression is associated with worse prognosis [118]. Taking into consideration these experimental evidences, we see that FNs are promising candidates for effective brain tumor therapy, due to their intrinsic targeting capability toward TfR1.

Fan and colleagues demonstrated that DOX-loaded FNs are able to bypass the BBB and deliver DOX to brain tumors in mice, dramatically increasing their survival compared to mice treated with control treatments (free DOX and Doxil<sup>TM</sup>) [43]. Interestingly, FNs maintain their intact structure after crossing the BBB by transcytosis. This process is mediated by endothelial cells and allows the accumulation of FNs in the brain parenchyma in healthy mice. However, FNs co-localize with lysosomes after internalization in glioma cells. These results corroborate the idea that FNs traverse the BBB and effectively deliver therapeutics to brain tumors without affecting the surrounding tissues. The authors speculate that the different fate of FNs between endothelial and tumor cells could be due to the differences in expression of TfR1 [43]. More recently,  $\epsilon$ 2 1-targeted Dox-loaded FN ( $\epsilon$ 2-FN-DOX) was shown to have enhanced activity compared to FN-DOX in controlling the tumor growth of glioblastoma in an orthotopic model of brain tumor (U-87MG) [44].

Interestingly,  $\epsilon$ 2-FN-DOX had a higher drug-loading capacity compared to FN-DOX (60 vs. 15%, respectively). The authors speculate that this could be due to the modified integrin  $\epsilon$ 2 1 targeting sequence, which possesses multiple carboxyl groups that could have an impact in ionic interactions between DOX and  $\epsilon$ 2-FN.



In another report, PTX-loaded FNs were successfully developed by the disassembly and reassembly methodology and were used to treat C6 glioma bearing mice. The results showed enhanced activity of FN-PTX compared to the free drug in controlling tumor growth. Furthermore, treatment with FN-PTX showed no apparent signs of toxicity in the heart, liver, spleen, lung and kidneys of treated animals [45].

Other anticancer compounds, such as Au(III) thiosemicarbazone [55] and vincristine [52], have been successfully loaded into FNs and used to treat brain tumors in various murine models of cancer, achieving impressive results in controlling tumor growth. Interestingly, FNs can also facilitate the delivery of therapeutic mAb through the BBB. Our group has developed FNs coupled with Trastuzumab or Cetuximab, two FDA-approved mAbs that are able to target the human epidermal growth factor receptor 2 and the epidermal growth factor receptor, respectively [46]. In addition, our group has developed a methodology to specifically study the translocation of FNs (or potentially other nanocarriers) through the BBB. This *ex vivo* model is based on layers of primary rat brain microvascular endothelial cells and astrocytes, which are used as a surrogate of the BBB [119].

We speculate that the development of novel FN therapeutics for the treatment of brain tumors will be particularly prominent in the coming years, since FNs have shown to effectively bypass the BBB without disassembly, leading to the release of FN-loaded therapeutics directly to tumor cells and avoiding off-site side effects.

### 5. Preclinical Exploitation of FN-Based NPs for Tumor Imaging

There is an ever-growing need for novel imaging agents that are able to effectively identify the presence of very small tumors in the early stage of the pathology, when they can be successfully treated by surgery or anticancer therapies. In addition, after successful surgery, patients undergo routine diagnostic tests to reveal the insurgence of metastatic events that could occur even several years after the original diagnosis [120]. Unfortunately, metastatic tumors are often incurable, since they usually become resistant to standard therapies and account for 90% of total cancer death worldwide [121]. Hence, it is critical to identify the presence of metastases with the current imaging modalities (computerized tomography (CT), magnetic resonance imaging (MRI) and positron emission tomography (PET)) which are often utilized together with contrast agents that are able to accumulate specifically in the TME.

In regard to MRI, gadolinium-based contrast agents are widely used, since they are able to identify highly vascularized tissues, such as tumors [122]. However, these types of agents are not cancer-specific and can result in a high rate of false positives. In addition, standard MRI does not have the sufficient spatial resolution to detect micro-metastases, thus leading to possible misdiagnoses of oligometastatic disease [123]. On the other hand, the glucose analog 18F-Fluorodeoxyglucose is a contrast agent utilized in PET/CT imaging to detect tumors, allowing for the visualization of areas with high metabolic activity [124]. Unfortunately, other areas characterized by active metabolic activity (benign tumors, inflammation sites and areas of ongoing infections) can give rise to false-positive results. Lastly, PET scans are quite expensive and require the use of radioactive contrast agents based on glucose that cannot be utilized in pregnant women or diabetic patients, due to off-target side effects [125].

NP-based delivery systems have been employed to enhance the specificity of contrast agents for tumor cells [126–128]. FNs have also been explored as a delivery platform for imaging probes, particularly for metal-based contrast agents. For example, multimodal FNs loaded with superparamagnetic iron oxide (Magnetoferritins) and a near-infrared fluorescence dyes were developed to efficiently detect tumors by multiple imaging modalities [58,59,65]. Interestingly, Magnetoferritins can efficiently identify very small tumors (~1 mm) by MRI in murine models of cancer, thus dramatically increasing the limit of detection of current contrast agents for MRI. Iron-loaded FNs derived from equine spleen (HoS-FN, composed of 85% of Lc and 15% of Hc subunits) were also utilized for MRI visualization of tumors [61]. Interestingly, HoS-FN showed enhanced uptake by SCAR5-positive cells, due to the specific targeting of this receptor mediated by Lc subunits. Furthermore, HoS-FNs were also able to reduce tumor growth, as compared to apoferritin HoS-FN in a murine model of breast cancer.

Imaging agents are also used in fluorescence-guided oncological surgery to assist the surgeon in the identification of metastatic foci, particularly in lymph nodes [129]. Indocyanine-green (ICG) is one of the most used FDA-approved fluorescent dyes for this purpose, since it can be visualized avoiding background autofluorescence (mainly due to hemoglobin) and has a low risk of adverse events [130,131]. Our group has developed ICG-loaded FNs with improved fluorescence accumulation in tumors in comparison to free ICG in a murine model of breast cancer [26,63]. Since specific accumulation of FN-ICG in tumors can be detected up to 24 h after intravenous injection in mice, we speculate that FN-ICG could be administered prior to surgery, and it could be visualized during surgery by fluorescence-guided endoscopy. This methodology could potentially reduce surgery time and improve the detection of small metastases, particularly in lymph nodes.

FNs were also developed to specifically visualize bone metastases by genetic manipulation of ferritin to include osteoblast and hydroxyapatite-binding peptides [64]. In another report, folic acid-functionalized FNs were developed to target tumor cells and deliver perfluoropentane, a compound used for low-intensity focused ultrasound imaging and therapy [62]. Lastly, gold NPs were efficiently encapsulated into 2-amino-2-deoxyglucose-functionalized FNs to develop a tumor-targeted FN for CT imaging [60].

Overall, FN-based nanostructures can be utilized for the tumor-specific delivery of numerous contrast agents to improve their pharmacokinetic characteristics and enhance tumor accumulation.

### 6. Drawbacks and Future Perspective of FN

FNs are a versatile drug delivery system for chemotherapeutics and imaging agents. However, one of the major limitations of FNs in regards to drug loading is the low encapsulation capacity for hydrophobic compounds. This is primarily due to the leakage of the loaded hydrophobic drug from FN soon after encapsulation. Nonetheless, hydrophobic drugs can still be loaded inside FN by utilizing methodologies such as the pre-complexation with copper ions or the modification of native ferritin with hydrophobic amino acid sequences, that are able to enhance the affinity of hydrophobic compounds for ferritin. For this purpose, Wang and colleagues designed a novel FN construct (Am-PNCage) by linking the sequence of the Pout peptide (GRGDSKKHHHHHAFAFAFVVA) to the C terminus of Hc ferritin through a flexible amino acid sequence GGSG, which replaced the E helix amino acids of Hc. This novel FN was employed to achieve the co-loading of the hydrophilic anthracycline EPI and the hydrophobic topoisomerase inhibitor Camptothecin and showed impressive antitumor activity in different murine models of cancer [47]. This novel FN construct could pave the way for the development of sophisticated FN-based nanostructures that are able to integrate multiple drugs with different mechanisms of action. This combinatorial nanotherapy could synergistically strike solid tumors by taking advantage of specific chemosensitivities to limit the insurgence of resistance to single chemotherapeutics.

An important area that is currently understudied is the relevance of the various modifications of FNs in regards to uptake and toxicity, particularly toward immune cells and erythrocytes in the bloodstream. For example, RGD-modified NP (nano-emulsions and liposomes) have been shown to be taken up by phagocytes in the bloodstream that are then able to transport NPs to specific sites in the body where there is ongoing inflammation and/or angiogenesis, such as the TME [132,133]. In fact, a majority of research efforts have been focused on showing that FN-loaded drugs can induce fewer side effects as compared to the free drug. This has been shown extensively for DOX, since FN-DOXs have an encouraging minimal effect on cardiomyocytes when compared to DOX [99,100]. However, it remains unclear if FN modifications can impact their uptake on different cell types present in the bloodstream. This area of study could be particularly relevant to pursue since it has been recently speculated that the enhanced accumulation of nanotherapeutics in the TME could be mediated not only by the EPR effect but also by the phenomenon of NP hitchhiking [81,114,133,134].

Indeed, FNs have favorable and interesting characteristics as an NP-based delivery system. Their efficient loading capacity for different drugs used in oncology, intrinsic targeting toward TfR1 and biocompatibility make them an ideal nano-platform for the treatment and imaging of tumors. Unfortunately, to date, FNs have not yet reached the clinical stage. In fact, the current high cost of production somewhat limits their translational potential. However, we speculate that the recent advancement concerning drug-loading efficiency and customization capabilities could facilitate the interest of pharmaceutical industries in developing novel production protocols for FNs that are aimed at enhancing purity, while, at the same time, reducing the costs of production. Collectively, the number of experimental evidences in support of the use of FNs as nano-delivery systems are everincreasing, making their translation from bench to bedside a reasonable possibility. Lastly, the opportunity of co-encapsulating different drugs into FNs allows for the development of novel FN-based theranostic agents that are able to combine both imaging and therapeutic functionality in a fully biocompatible nanosystem. For these reasons, we believe that, in the near future, the clinical application of FNs could play a pivotal role in the diagnosis and treatment of solid tumors.

**Author Contributions:** F.C., F.M. and S.M. conceived of and designed the work; F.M., A.B., M.S., L.S., M.T., F.C. and S.M. wrote the manuscript; M.T., S.M., F.M. and F.C. revised the paper. All authors have read and agreed to the published version of the manuscript.

**Funding:** The research leading to these results has received funding from AIRC under IG 2017—ID. 20172 project—P.I. Corsi Fabio.

**Institutional Review Board Statement:** Not applicable.

**Informed Consent Statement:** Not applicable.

**Acknowledgments:** The authors acknowledge AIRC for F.M. postdoctoral fellowship and University of Milan for A.B., M.S. and L.S. doctoral and postdoctoral fellowship, respectively. Figures 1 and 2 were created with [BioRender.com](https://BioRender.com) (accessed on 2 November 2021).

**Conflicts of Interest:** The authors declare no conflict of interest.

### References

1. Anselmo, A.C.; Mitragotri, S. Nanoparticles in the clinic: An update. *Bioeng. Transl. Med.* **2019**, *4*, e10143. [[CrossRef](#)]

2. Wang, J.; Li, Y.; Nie, G. Multifunctional biomolecule nanostructures for cancer therapy. *Natl. Rev. Mater.* **2021**, *6*, 766–783. [[CrossRef](#)] [[PubMed](#)]
3. Wei, G.; Wang, Y.; Yang, G.; Wang, Y.; Ju, R. Recent progress in nanomedicine for enhanced cancer chemotherapy. *Theranostics* **2021**, *11*, 6370–6392. [[CrossRef](#)] [[PubMed](#)]
4. Gustafson, H.H.; Holt-Casper, D.; Grainger, D.W.; Ghandehari, H. Nanoparticle uptake: The phagocyte problem. *Nano Today* **2015**, *10*, 487–510. [[CrossRef](#)] [[PubMed](#)]
5. Nooraee, S.; Bahrololom, H.; Hoseini, Z.S.; Katalani, C.; Hajizade, A.; Easton, A.J.; Ahmadian, G. Virus-Like particles: Preparation, immunogenicity and their roles as nanovaccines and drug nanocarriers. *J. Nanobiotechnol.* **2021**, *19*, 59. [[CrossRef](#)]
6. Bhaskar, S.; Lim, S. Engineering protein nanocages as carriers for biomedical applications. *NPG Asia Mater.* **2017**, *9*, e371. [[CrossRef](#)]
7. Truffi, M.; Fiandra, L.; Sorrentino, L.; Monieri, M.; Corsi, F.; Mazzucchelli, S. Ferritin nanocages: A biological platform for drug delivery, imaging and theranostics in cancer. *Pharmacol. Res.* **2016**, *107*, 57–65. [[CrossRef](#)] [[PubMed](#)]
8. Arosio, P.; Ingrassia, R.; Cavadini, P. Ferritins: A family of molecules for iron storage, antioxidation and more. *Biochim. Biophys. Acta Gen. Subj.* **2009**, *1790*, 589–599. [[CrossRef](#)]
9. Harrison, P.M.; Arosio, P. The ferritins: Molecular properties, iron storage function and cellular regulation. *Biochim. Biophys. Acta Bioenerg.* **1996**, *1275*, 161–203. [[CrossRef](#)]
10. Chasteen, N.D.; Harrison, P.M. Mineralization in ferritin: An efficient means of iron storage. *J. Struct. Biol.* **1999**, *126*, 182–194. [[CrossRef](#)]
11. Cohen, L.A.; Gutierrez, L.; Weiss, A.; Leichtmann-Bardoogo, Y.; Zhang, D.L.; Crooks, D.R.; Sougrat, R.; Morgenstern, A.; Galy, B.; Hentze, M.W.; et al. Serum ferritin is derived primarily from macrophages through a nonclassical secretory pathway. *Blood* **2010**, *116*, 1574–1584. [[CrossRef](#)]
12. Moreira, A.C.; Mesquita, G.; Gomes, M.S. Ferritin: An inflammatory player keeping iron at the core of pathogen-host interactions. *Microorganisms* **2020**, *8*, 589. [[CrossRef](#)]
13. Cullis, J.O.; Fitzsimons, E.J.; Griffiths, W.J.H.; Tsochatzis, E.; Thomas, D.W. Investigation and management of a raised serum ferritin. *Br. J. Haematol.* **2018**, *181*, 331–340. [[CrossRef](#)]
14. Camaschella, C.; Girelli, D. The changing landscape of iron deficiency. *Mol. Asp. Med.* **2020**, *75*, 100861. [[CrossRef](#)]
15. Asano, T.; Komatsu, M.; Yamaguchi-Iwai, Y.; Ishikawa, F.; Mizushima, N.; Iwai, K. Distinct Mechanisms of Ferritin Delivery to Lysosomes in Iron-Depleted and Iron-Replete Cells. *Mol. Cell. Biol.* **2011**, *31*, 2040–2052. [[CrossRef](#)]
16. Cai, C.; Ching, A.; Lagace, C.; Linsenmayer, T. Nuclear ferritin-mediated protection of corneal epithelial cells from oxidative damage to DNA. *Dev. Dyn.* **2008**, *237*, 2676–2683. [[CrossRef](#)]
17. Ahmad, S.; Moriconi, F.; Naz, N.; Sultan, S.; Sheikh, N.; Ramadori, G.; Malik, I.A. Ferritin L and ferritin H are differentially located within hepatic and extra hepatic organs under physiological and acute phase conditions. *Int. J. Clin. Exp. Pathol.* **2013**, *6*, 622–629.
18. Darshan, D.; Vanoaica, L.; Richman, L.; Beermann, F.; Kühn, L.C. Conditional deletion of ferritin H in mice induces loss of iron storage and liver damage. *Hepatology* **2009**, *50*, 852–860. [[CrossRef](#)]
19. Ryu, M.S.; Zhang, D.; Protchenko, O.; Shakoury-Elizeh, M.; Philpott, C.C. PCB1 and NCOA4 regulate erythroid iron storage and heme biosynthesis. *J. Clin. Investig.* **2017**, *127*, 1786–1797. [[CrossRef](#)]
20. Surguladze, N.; Patton, S.; Cozzi, A.; Fried, M.G.; Connor, J.R. Characterization of nuclear ferritin and mechanism of translocation. *Biochem. J.* **2005**, *388*, 731–740. [[CrossRef](#)]
21. Zhang, L.; Li, L.; Di Penta, A.; Carmona, U.; Yang, F.; Schöps, R.; Brandsch, M.; Zugaza, J.L.; Knez, M. H-Chain Ferritin: A Natural Nuclei Targeting and Bioactive Delivery Nanovector. *Adv. Healthc. Mater.* **2015**, *4*, 1305–1310. [[CrossRef](#)]
22. Bellini, M.; Mazzucchelli, S.; Galbiati, E.; Sommaruga, S.; Fiandra, L.; Truffi, M.; Rizzuto, M.A.; Colombo, M.; Tortora, P.; Corsi, F.; et al. Protein nanocages for self-triggered nuclear delivery of DNA-targeted chemotherapeutics in Cancer Cells. *J. Control. Release* **2014**, *196*, 184–196. [[CrossRef](#)]
23. Kurza tkowska, K.; Pazos, M.A., II; Herschkowitz, J.I.; Hepel, M. Cancer-Targeted Controlled Delivery of Chemotherapeutic Anthracycline Derivatives Using Apoferritin Nanocage Carriers. *Int. J. Mol. Sci.* **2021**, *22*, 1362. [[CrossRef](#)]
24. Santambrogio, P.; Levi, S.; Arosio, P.; Palagi, L.; Vecchio, G.; Lawson, D.M.; Yewdall, S.J.; Artymiuk, P.J.; Harrison, P.M.; Jappelli, R.; et al. Evidence that a salt bridge in the light chain contributes to the physical stability difference between heavy and light human ferritins. *J. Biol. Chem.* **1992**, *267*, 14077–14083. [[CrossRef](#)]
25. Yang, R.; Liu, Y.; Meng, D.; Wang, D.; Blanchard, C.L.; Zhou, Z. Effect of atmospheric cold plasma on structure, activity, and reversible assembly of the phytoferritin. *Food Chem.* **2018**, *264*, 41–48. [[CrossRef](#)]
26. Sitia, L.; Sevieri, M.; Bonizzi, A.; Allevi, R.; Morasso, C.; Foschi, D.; Corsi, F.; Mazzucchelli, S. Development of Tumor Targeted Indocyanine Green-Loaded Ferritin Nanoparticles for Intraoperative Detection of Cancers. *ACS Omega* **2020**, *5*, 12035–12045. [[CrossRef](#)] [[PubMed](#)]
27. Jiang, B.; Chen, X.; Sun, G.; Chen, X.; Yin, Y.; Jin, Y.; Mi, Q.; Ma, L.; Yang, Y.; Yan, X.; et al. A natural drug entry channel in the ferritin nanocage. *Nano Today* **2020**, *35*, 100948. [[CrossRef](#)]
28. Zhen, Z.; Tang, W.; Chen, H.; Lin, X.; Todd, T.; Wang, G.; Cowger, T.; Chen, X.; Xie, J. RGD-Modified Apoferritin Nanoparticles for Efficient Drug Delivery to Tumors. *ACS Nano* **2013**, *7*, 4830–4837. [[CrossRef](#)]
29. He, J.; Fan, K.; Yan, X. Ferritin drug carrier (FDC) for tumor targeting therapy. *J. Control. Release* **2019**, *311–312*, 288–300. [[CrossRef](#)] [[PubMed](#)]
30. Zhang, J.; Cheng, D.; He, J.; Hong, J.; Yuan, C.; Liang, M. Cargo loading within ferritin nanocages in preparation for tumor-targeted delivery. *Nat. Protoc.* **2021**, *16*, 4878–4896. [[CrossRef](#)]
31. Jin, P.; Sha, R.; Zhang, Y.; Liu, L.; Bian, Y.; Qian, J.; Qian, J.; Lin, J.; Ishimwe, N.; Hu, Y.; et al. Blood Circulation-Prolonging Peptides for Engineered Nanoparticles Identified via Phage Display. *Nano Lett.* **2019**, *19*, 1467–1478. [[CrossRef](#)]
32. Wang, Z.; Dai, Y.; Wang, Z.; Jacobson, O.; Zhang, F.; Yung, B.C.; Zhang, P.; Gao, H.; Niu, G.; Liu, G.; et al. Metal ion assisted interface re-engineering of a ferritin nanocage for enhanced biofunctions and cancer therapy. *Nanoscale* **2018**, *10*, 1135–1144. [[CrossRef](#)]
33. Huang, H.; Yuan, S.; Ma, Z.; Ji, P.; Ma, X.; Wu, Z.; Qi, X. Genetic recombination of poly(l-lysine) functionalized apoferritin nanocages that resemble viral capsid nanometer-sized platforms for gene therapy. *Biomater. Sci.* **2020**, *8*, 1759–1770. [[CrossRef](#)]
34. Jeon, I.S.; Yoo, J.D.; Gurung, S.; Kim, M.; Lee, C.; Park, E.J.; Park, R.W.; Lee, B.; Kim, S. Anticancer nanocage platforms for combined immunotherapy designed to harness immune checkpoints and deliver anticancer drugs. *Biomaterials* **2021**, *270*, 120685. [[CrossRef](#)]
35. Ma, Y.; Li, R.; Dong, Y.; You, C.; Huang, S.; Li, X.; Wang, F.; Zhang, Y. tLyP-1 peptide functionalized human H chain ferritin for targeted delivery of paclitaxel. *Int. J. Nanomed.* **2021**, *16*, 789–802. [[CrossRef](#)]



36. Andreato, F.; Bonizzi, A.; Sevieri, M.; Truffi, M.; Monieri, M.; Sitia, L.; Silva, F.; Sorrentino, L.; Allevi, R.; Zerbi, P.; et al. CoAdministration of H-ferritin-doxorubicin and Trastuzumab in neoadjuvant setting improves efficacy and prevents cardiotoxicity in HER2 + murine breast cancer model. *Sci. Rep.* **2020**, *10*, 11425. [[CrossRef](#)]
37. Huang, X.; Chisholm, J.; Zhuang, J.; Xiao, Y.; Duncan, G.; Chen, X.; Suk, J.S.; Hanes, J. Protein nanocages that penetrate airway mucus and tumor tissue. *Proc. Natl. Acad. Sci. USA* **2017**, *114*, E6595–E6602. [[CrossRef](#)]
38. Huang, X.; Zhuang, J.; Chung, S.W.; Huang, B.; Halpert, G.; Negron, K.; Sun, X.; Yang, J.; Oh, Y.; Hwang, P.M.; et al. Hypoxia-tropic Protein Nanocages for Modulation of Tumor- and Chemotherapy-Associated Hypoxia. *ACS Nano* **2019**, *13*, 236–247. [[CrossRef](#)]
39. Mazzucchelli, S.; Truffi, M.; Baccarini, F.; Beretta, M.; Sorrentino, L.; Bellini, M.; Rizzuto, M.A.; Ottria, R.; Ravelli, A.; Ciuffreda, P.; et al. H-Ferritin-nanocaged olaparib: A promising choice for both BRCA-mutated and sporadic triple negative breast cancer. *Sci. Rep.* **2017**, *7*, 7505. [[CrossRef](#)]
40. Bonizzi, A.; Truffi, M.; Sevieri, M.; Allevi, R.; Sitia, L.; Ottria, R.; Sorrentino, L.; Sottani, C.; Negri, S.; Grignani, E.; et al. Everolimus nanoformulation in biological nanoparticles increases drug responsiveness in resistant and low-responsive breast cancer cell lines. *Pharmaceutics* **2019**, *11*, 384. [[CrossRef](#)]
41. Pandolfi, L.; Bellini, M.; Vanna, R.; Morasso, C.; Zago, A.; Carcano, S.; Avvakumova, S.; Bertolini, J.; Rizzuto, M.; Colombo, M.; et al. H-Ferritin Enriches the Curcumin Uptake and Improves the Therapeutic Efficacy in Triple Negative Breast Cancer Cells. *Biomacromolecules* **2017**, *18*, 3318–3330. [[CrossRef](#)]
42. Sitia, L.; Bonizzi, A.; Mazzucchelli, S.; Negri, S.; Sottani, C.; Grignani, E.; Rizzuto, M.A.; Prosperi, D.; Sorrentino, L.; Morasso, C.; et al. Selective Targeting of Cancer-Associated Fibroblasts by Engineered H-Ferritin Nanocages Loaded with Navitoclax. *Cells* **2021**, *10*, 328. [[CrossRef](#)]
43. Fan, K.; Jia, X.; Zhou, M.; Wang, K.; Conde, J.; He, J.; Tian, J.; Yan, X. Ferritin Nanocarrier Traverses the Blood Brain Barrier and Kills Glioma. *ACS Nano* **2018**, *12*, 4105–4115. [[CrossRef](#)] [[PubMed](#)]
44. Huang, C.-W.; Chuang, C.-P.; Chen, Y.-J.; Wang, H.-Y.; Lin, J.-J.; Huang, C.-Y.; Wei, K.-C.; Huang, F.-T. Integrin  $\alpha 2$  1-targeting ferritin nanocarrier traverses the blood–brain barrier for effective glioma chemotherapy. *J. Nanobiotechnol.* **2021**, *19*, 180. [[CrossRef](#)]
45. Liu, W.; Lin, Q.; Fu, Y.; Huang, S.; Guo, C.; Li, L.; Wang, L.; Zhang, Z.; Zhang, L. Target delivering paclitaxel by ferritin heavy chain nanocages for glioma treatment. *J. Control. Release* **2020**, *323*, 191–202. [[CrossRef](#)]
46. Rizzuto, M.A.; Magro, R.D.; Barbieri, L.; Pandolfi, L.; Sguazzini-Viscontini, A.; Truffi, M.; Salvioni, L.; Corsi, F.; Colombo, M.; Re, F.; et al. H-Ferritin nanoparticle-mediated delivery of antibodies across a BBB in vitro model for treatment of brain malignancies. *Biomater. Sci.* **2021**, *9*, 2032–2042. [[CrossRef](#)]
47. Wang, Z.; Zhang, S.; Zhang, R.; Chen, X.; Sun, G.; Zhou, M.; Han, Q.; Zhang, B.; Zhao, Y.; Jiang, B.; et al. Bioengineered DualTargeting Protein Nanocage for Stereoscopic Loading of Synergistic Hydrophilic/Hydrophobic Drugs to Enhance Anticancer Efficacy. *Adv. Funct. Mater.* **2021**, *31*, 2102004. [[CrossRef](#)]
48. Jiang, B.; Zhang, R.; Zhang, J.; Hou, Y.; Chen, X.; Zhou, M.; Tian, X.; Hao, C.; Fan, K.; Yan, X. GRP78-targeted ferritin nanocaged ultra-high dose of doxorubicin for hepatocellular carcinoma therapy. *Theranostics* **2019**, *9*, 2167–2182. [[CrossRef](#)] [[PubMed](#)]
49. Tan, T.; Wang, Y.; Wang, H.; Cao, H.; Wang, Z.; Wang, J.; Li, J.; Li, Y.; Zhang, Z.; Wang, S. Apoferritin nanocages loading mertansine enable effective eradication of cancer stem-like cells in vitro. *Int. J. Pharm.* **2018**, *553*, 201–209. [[CrossRef](#)]
50. Ferraro, G.; Pratesi, A.; Cirri, D.; Imbimbo, P.; Monti, D.M.; Messori, L.; Merlino, A. Arsenoplatin-Ferritin nanocage: Structure and cytotoxicity. *Int. J. Mol. Sci.* **2021**, *22*, 1874. [[CrossRef](#)] [[PubMed](#)]
51. Li, Y.; Wang, X.; Yan, J.; Liu, Y.; Yang, R.; Pan, D.; Wang, L.; Xu, Y.; Li, X.; Yang, M. Nanoparticle ferritin-bound erastin and rapamycin: A nanodrug combining autophagy and ferroptosis for anticancer therapy. *Biomater. Sci.* **2019**, *7*, 3779–3787. [[CrossRef](#)]
52. Zhai, M.; Wang, Y.; Zhang, L.; Liang, M.; Fu, S.; Cui, L.; Yang, M.; Gong, W.; Li, Z.; Yu, L.; et al. Glioma targeting peptide modified apoferritin nanocage. *Drug Deliv.* **2018**, *25*, 1013–1024. [[CrossRef](#)] [[PubMed](#)]
53. Lin, C.Y.; Yang, S.J.; Peng, C.L.; Shieh, M.J. Panitumumab-Conjugated and Platinum-Cored pH-Sensitive Apoferritin Nanocages for Colorectal Cancer-Targeted Therapy. *ACS Appl. Mater. Interfaces* **2018**, *10*, 6096–6106. [[CrossRef](#)] [[PubMed](#)]
54. Zheng, Q.; Cheng, W.; Zhang, X.; Shao, R.; Li, Z. A pH-Induced Reversible Assembly System with Resveratrol-Controllable Loading and Release for Enhanced Tumor-Targeting Chemotherapy. *Nanoscale Res. Lett.* **2019**, *14*, 305. [[CrossRef](#)]
55. Zhang, J.; Zhang, Z.; Jiang, M.; Li, S.; Yuan, H.; Sun, H.; Yang, F.; Liang, H. Developing a Novel Gold(III) Agent to Treat Glioma Based on the Unique Properties of Apoferritin Nanoparticles: Inducing Lethal Autophagy and Apoptosis. *J. Med. Chem.* **2020**, *63*, 13695–13708. [[CrossRef](#)]
56. Wang, W.; Liu, Z.; Zhou, X.; Guo, Z.; Zhang, J.; Zhu, P.; Yao, S.; Zhu, M. Ferritin nanoparticle-based SpyTag/SpyCatcher-enabled click vaccine for tumor immunotherapy. *Nanomed. Nanotechnol. Biol. Med.* **2019**, *16*, 69–78. [[CrossRef](#)]
57. Shan, H.; Dou, W.; Zhang, Y.; Qi, M. Targeted ferritin nanoparticle encapsulating CpG oligodeoxynucleotides induces tumor-associated macrophage M2 phenotype polarization into M1 phenotype and inhibits tumor growth. *Nanoscale* **2020**, *12*, 22268–22280. [[CrossRef](#)]
58. Jiang, B.; Jia, X.; Ji, T.; Zhou, M.; He, J.; Wang, K.; Tian, J.; Yan, X.; Fan, K. Ferritin nanocages for early theranostics of tumors via inflammation-enhanced active targeting. *Sci. China Life Sci.* **2021**. online ahead of print. [[CrossRef](#)]
59. Song, R.; Ruan, M.; Dai, J.; Xue, W. Biomimetic magnetofluorescent ferritin nanoclusters for magnetic resonance and fluorescence modal imaging and targeted tumor therapy. *J. Mater. Chem. B* **2021**, *9*, 2494–2504. [[CrossRef](#)]
60. Aslan, T.N.; Asık, E.; Güray, N.T.; Volkan, M. The potential application of gold-apoferritin nanocages conjugated with 2-amino-2deoxyglucose for imaging of breast cancer cells. *JBIC J. Biol. Inorg. Chem.* **2020**, *25*, 1139–1152. [[CrossRef](#)]
61. Bitonto, V.; Alberti, D.; Ruiu, R.; Aime, S.; Geninatti Crich, S.; Cutrin, J.C. L-ferritin: A theranostic agent of natural origin for MRI visualization and treatment of breast cancer. *J. Control. Release* **2020**, *319*, 300–310. [[CrossRef](#)]
62. Li, J.; Ji, H.; Jing, Y.; Wang, S. pH- and acoustic-responsive platforms based on perfluoropentane-loaded protein nanoparticles for ovarian tumor-targeted ultrasound imaging and therapy. *Nanoscale Res. Lett.* **2020**, *15*, 31. [[CrossRef](#)]
63. Sevieri, M.; Sitia, L.; Bonizzi, A.; Truffi, M.; Mazzucchelli, S.; Corsi, F. Tumor Accumulation and Off-Target Biodistribution of an Indocyanine-Green Fluorescent Nanotracer: An Ex Vivo Study on an Orthotopic Murine Model of Breast Cancer. *Int. J. Mol. Sci.* **2021**, *22*, 1601. [[CrossRef](#)]
64. Kim, J.-W.; Lee, K.-K.; Park, K.-W.; Kim, M.; Lee, C.-S. Genetically Modified Ferritin Nanoparticles with Bone-Targeting Peptides for Bone Imaging. *Int. J. Mol. Sci.* **2021**, *22*, 4854. [[CrossRef](#)]
65. Cao, C.; Wang, X.; Cai, Y.; Sun, L.; Tian, L.; Wu, H.; He, X.; Lei, H.; Liu, W.; Chen, G.; et al. Targeted In Vivo Imaging of Microscopic Tumors with Ferritin-based Nanoprobes Across Biological Barriers. *Adv. Mater.* **2014**, *26*, 2566–2571. [[CrossRef](#)]
66. Zhang, C.; Zhang, X.; Zhao, G. Ferritin nanocage: A versatile nanocarrier utilized in the field of food, nutrition, and medicine. *Nanomaterials* **2020**, *10*, 1894. [[CrossRef](#)]

67. Plath, L.D.; Ozdemir, A.; Aksenov, A.A.; Bier, M.E. Determination of Iron Content and Dispersity of Intact Ferritin by Superconducting Tunnel Junction Cryodetection Mass Spectrometry. *Anal. Chem.* **2015**, *87*, 8985–8993. [CrossRef]
68. Silva, F.; Sitia, L.; Allevi, R.; Bonizzi, A.; Sevieri, M.; Morasso, C.; Truffi, M.; Corsi, F.; Mazzucchelli, S. Combined method to remove endotoxins from protein nanocages for drug delivery applications: The case of human ferritin. *Pharmaceutics* **2021**, *13*, 229. [CrossRef]
69. Jin, Y.; He, J.; Fan, K.; Yan, X. Ferritin variants: Inspirations for rationally designing protein nanocarriers. *Nanoscale* **2019**, *11*, 12449–12459. [CrossRef]
70. Zhang, S.; Zang, J.; Zhang, X.; Chen, H.; Mikami, B.; Zhao, G. “Silent” Amino Acid Residues at Key Subunit Interfaces Regulate the Geometry of Protein Nanocages. *ACS Nano* **2016**, *10*, 10382–10388. [CrossRef]
71. Wang, W.; Wang, L.; Chen, H.; Zang, J.; Zhao, X.; Zhao, G.; Wang, H. Selective Elimination of the Key Subunit Interfaces Facilitates Conversion of Native 24-mer Protein Nanocage into 8-mer Nanorings. *J. Am. Chem. Soc.* **2018**, *140*, 14078–14081. [CrossRef]
72. Choi, S.H.; Choi, K.; Chan Kwon, I.; Ahn, H.J. The incorporation of GALA peptide into a protein cage for an acid-inducible molecular switch. *Biomaterials* **2010**, *31*, 5191–5198. [CrossRef]
73. Wang, W.; Wang, L.; Li, G.; Zhao, G.; Zhao, X.; Wang, H. AB loop engineered ferritin nanocages for drug loading under benign experimental conditions. *Chem. Commun.* **2019**, *55*, 12344–12347. [CrossRef]
74. Zang, J.; Chen, H.; Zhang, X.; Zhang, C.; Guo, J.; Du, M.; Zhao, G. Disulfide-Mediated conversion of 8-mer bowl-like protein architecture into three different nanocages. *Nat. Commun.* **2019**, *10*, 778. [CrossRef] [PubMed]
75. Gu, C.; Zhang, T.; Lv, C.; Liu, Y.; Wang, Y.; Zhao, G. His-Mediated Reversible Self-Assembly of Ferritin Nanocages through Two Different Switches for Encapsulation of Cargo Molecules. *ACS Nano* **2020**, *14*, 17080–17090. [CrossRef]
76. Wang, C.; Zhang, C.; Li, Z.; Yin, S.; Wang, Q.; Guo, F.; Zhang, Y.; Yu, R.; Liu, Y.; Su, Z. Extending Half Life of H-Ferritin Nanoparticle by Fusing Albumin Binding Domain for Doxorubicin Encapsulation. *Biomacromolecules* **2018**, *19*, 773–781. [CrossRef]
77. Falvo, E.; Tremante, E.; Arcovito, A.; Papi, M.; Elad, N.; Boffi, A.; Morea, V.; Conti, G.; Toffoli, G.; Fracasso, G.; et al. Improved Doxorubicin Encapsulation and Pharmacokinetics of Ferritin-Fusion Protein Nanocarriers Bearing Proline, Serine, and Alanine Elements. *Biomacromolecules* **2016**, *17*, 514–522. [CrossRef]
78. Yin, S.; Wang, Y.; Zhang, B.; Qu, Y.; Liu, Y.G.; Dai, S.; Zhang, Y.; Wang, Y.; Bi, J. Engineered human heavy-chain ferritin with half-life extension and tumor targeting by PAS and YGDK peptide functionalization. *Pharmaceutics* **2021**, *13*, 521. [CrossRef]
79. Falvo, E.; Malagrì, F.; Arcovito, A.; Fazi, F.; Colotti, G.; Tremante, E.; Di Micco, P.; Braca, A.; Opri, R.; Giuffrè, A.; et al. The presence of glutamate residues on the PAS sequence of the stimuli-sensitive nano-ferritin improves in vivo biodistribution and mitoxantrone encapsulation homogeneity. *J. Control. Release* **2018**, *275*, 177–185. [CrossRef]
80. Zheng, L.; Hu, X.; Wu, H.; Mo, L.; Xie, S.; Li, J.; Peng, C.; Xu, S.; Qiu, L.; Tan, W. In Vivo Monocyte/Macrophage-Hitchhiked Intratumoral Accumulation of Nanomedicines for Enhanced Tumor Therapy. *J. Am. Chem. Soc.* **2020**, *142*, 382–391. [CrossRef]
81. Zelepukin, I.V.; Yaremenko, A.V.; Shipunova, V.O.; Babenyshev, A.V.; Balalaeva, I.V.; Nikitin, P.I.; Deyev, S.M.; Nikitin, M.P. Nanoparticle-Based drug delivery via RBC-hitchhiking for the inhibition of lung metastases growth. *Nanoscale* **2019**, *11*, 1636–1646. [CrossRef] [PubMed]
82. Ahn, B.; Lee, S.G.; Yoon, H.R.; Lee, J.M.; Oh, H.J.; Kim, H.M.; Jung, Y. Four-Fold Channel-Nicked Human Ferritin Nanocages for Active Drug Loading and pH-Responsive Drug Release. *Angew. Chem. Int. Ed.* **2018**, *57*, 2909–2913. [CrossRef]
83. Men, D.; Zhang, T.-T.; Hou, L.-W.; Zhou, J.; Zhang, Z.-P.; Shi, Y.-Y.; Zhang, J.-L.; Cui, Z.-Q.; Deng, J.-Y.; Wang, D.-B.; et al. Self-Assembly of Ferritin Nanoparticles into an Enzyme Nanocomposite with Tunable Size for Ultrasensitive Immunoassay. *ACS Nano* **2015**, *9*, 10852–10860. [CrossRef] [PubMed]
84. Lee, E.J.; Lee, S.J.; Kang, Y.S.; Ryu, J.H.; Kwon, K.C.; Jo, E.; Yhee, J.Y.; Kwon, I.C.; Kim, K.; Lee, J. Engineered proteinicles for targeted delivery of siRNA to cancer cells. *Adv. Funct. Mater.* **2015**, *25*, 1279–1286. [CrossRef]
85. Li, L.; Muñoz-Culla, M.; Carmona, U.; Lopez, M.P.; Yang, F.; Trigueros, C.; Otaegui, D.; Zhang, L.; Knez, M. Ferritin-Mediated siRNA delivery and gene silencing in human tumor and primary cells. *Biomaterials* **2016**, *98*, 143–151. [CrossRef]
86. Kanekiyo, M.; Wei, C.J.; Yassine, H.M.; McTamney, P.M.; Boyington, J.C.; Whittle, J.R.R.; Rao, S.S.; Kong, W.P.; Wang, L.; Nabel, G.J. Self-Assembling influenza nanoparticle vaccines elicit broadly neutralizing H1N1 antibodies. *Nature* **2013**, *499*, 102–106. [CrossRef]
87. Lee, B.-R.; Ko, H.K.; Ryu, J.H.; Ahn, K.Y.; Lee, Y.-H.; Oh, S.J.; Na, J.H.; Kim, T.W.; Byun, Y.; Kwon, I.C.; et al. Engineered Human Ferritin Nanoparticles for Direct Delivery of Tumor Antigens to Lymph Node and Cancer Immunotherapy. *Sci. Rep.* **2016**, *6*, 35182. [CrossRef] [PubMed]
88. Han, J.A.; Kang, Y.J.; Shin, C.; Ra, J.S.; Shin, H.H.; Hong, S.Y.; Do, Y.; Kang, S. Ferritin protein cage nanoparticles as versatile antigen delivery nanoplatforams for dendritic cell (DC)-based vaccine development. *Nanomed. Nanotechnol. Biol. Med.* **2014**, *10*, 561–569. [CrossRef]
89. Jiang, B.; Yan, L.; Zhang, J.; Zhou, M.; Shi, G.; Tian, X.; Fan, K.; Hao, C.; Yan, X. Biomaterialization Synthesis of the Cobalt Nanozyme in SP94-Ferritin Nanocages for Prognostic Diagnosis of Hepatocellular Carcinoma. *ACS Appl. Mater. Interfaces* **2019**, *11*, 9747–9755. [CrossRef]
90. Chuckran, C.A.; Liu, C.; Bruno, T.C.; Workman, C.J.; Vignali, D.A. Neuropilin-1: A checkpoint target with unique implications for cancer immunology and immunotherapy. *J. Immunother. Cancer* **2020**, *8*, e000967. [CrossRef]
91. Khoshnejad, M.; Greineder, C.F.; Pulsipher, K.W.; Villa, C.H.; Altun, B.; Pan, D.C.; Tsourkas, A.; Dmochowski, I.J.; Muzykantov, V.R. Ferritin Nanocages with Biologically Orthogonal Conjugation for Vascular Targeting and Imaging. *Bioconjug. Chem.* **2018**, *29*, 1209–1218. [CrossRef]
92. Palombarini, F.; Masciarelli, S.; Incocciati, A.; Liccardo, F.; Di Fabio, E.; Iazzetti, A.; Fabrizi, G.; Fazi, F.; Maccone, A.; Bonamore, A.; et al. Self-Assembling ferritin-dendrimer nanoparticles for targeted delivery of nucleic acids to myeloid leukemia cells. *J. Nanobiotechnol.* **2021**, *19*, 172. [CrossRef]
93. Suk, J.S.; Xu, Q.; Kim, N.; Hanes, J.; Ensign, L.M. PEGylation as a strategy for improving nanoparticle-based drug and gene delivery. *Adv. Drug Deliv. Rev.* **2016**, *99*, 28–51. [CrossRef] [PubMed]
94. Tosi, G.; Belletti, D.; Pederzoli, F.; Ruozzi, B. Apoferritin nanocage as drug reservoir: Is it a reliable drug delivery system? *Expert Opin. Drug Deliv.* **2016**, *13*, 1341–1343. [CrossRef] [PubMed]
95. Ramadori, G.; Cameron, S. Effects of systemic chemotherapy on the liver. *Ann. Hepatol.* **2010**, *9*, 133–143. [CrossRef]
96. Oun, R.; Moussa, Y.E.; Wheate, N.J. The side effects of platinum-based chemotherapy drugs: A review for chemists. *Dalt. Trans.* **2018**, *47*, 6645–6653. [CrossRef]
97. Branca, J.J.V.; Carrino, D.; Gulisano, M.; Ghelardini, C.; Di Cesare Mannelli, L.; Pacini, A. Oxaliplatin-Induced Neuropathy: Genetic and Epigenetic Profile to Better Understand How to Ameliorate This Side Effect. *Front. Mol. Biosci.* **2021**, *8*, 643824. [CrossRef]
98. Jagiela, J.; Bartnicki, P.; Rysz, J. Nephrotoxicity as a Complication of Chemotherapy and Immunotherapy in the Treatment of Colorectal Cancer, Melanoma and Non-Small Cell Lung Cancer. *Int. J. Mol. Sci.* **2021**, *22*, 4618. [CrossRef]

99. Mazzucchelli, S.; Bellini, M.; Fiandra, L.; Truffi, M.; Rizzuto, M.A.; Sorrentino, L.; Longhi, E.; Nebuloni, M.; Prosperi, D.; Corsi, F.; et al. Nanometronomic treatment of 4T1 breast cancer with nanocaged doxorubicin prevents drug resistance and circumvents cardiotoxicity. *Oncotarget* **2016**, *8*, 8383–8396. [[CrossRef](#)]
100. Liang, M.; Fan, K.; Zhou, M.; Duan, D.; Zheng, J.; Yang, D.; Feng, J.; Yan, X. H-ferritin-nanocaged doxorubicin nanoparticles specifically target and kill tumors with a single-dose injection. *Proc. Natl. Acad. Sci. USA* **2014**, *111*, 14900–14905. [[CrossRef](#)]
101. Yang, Z.; Wang, X.; Diao, H.; Zhang, J.; Li, H.; Sun, H.; Guo, Z. Encapsulation of platinum anticancer drugs by apoferritin. *Chem. Commun.* **2007**, *33*, 3453–3455. [[CrossRef](#)]
102. Ferraro, G.; Pica, A.; Petruk, G.; Pane, F.; Amoresano, A.; Cilibrizzi, A.; Vilar, R.; Monti, D.M.; Merlino, A. Preparation, structure, cytotoxicity and mechanism of action of ferritin-Pt(II) terpyridine compound nanocomposites. *Nanomedicine* **2018**, *13*, 2995–3007. [[CrossRef](#)]
103. Comerford, K.M.; Wallace, T.J.; Karhausen, J.; Louis, N.A.; Montalto, M.C.; Colgan, S.P. Hypoxia-Inducible factor-1-dependent regulation of the multidrug resistance (MDR1) gene. *Cancer Res.* **2002**, *62*, 3387–3394.
104. Tacchini, L.; Bianchi, L.; Bernelli-Zazzera, A.; Cairo, G. Transferrin Receptor Induction by Hypoxia: HIF-1-mediated transcriptional activation and cell-specific post-transcriptional regulation. *J. Biol. Chem.* **1999**, *274*, 24142–24146. [[CrossRef](#)]
105. Vitale, I.; Manic, G.; Coussens, L.M.; Kroemer, G.; Galluzzi, L. Macrophages and Metabolism in the Tumor Microenvironment. *Cell Metab.* **2019**, *30*, 36–50. [[CrossRef](#)]
106. Allavena, P.; Anfray, C.; Ummano, A.; Andón, F.T. Therapeutic manipulation of tumor-associated macrophages: Facts and hopes from a clinical and translational perspective. *Clin. Cancer Res.* **2021**, *27*, 3291–3297. [[CrossRef](#)]
107. Malfitano, A.M.; Pisanti, S.; Napolitano, F.; Di Somma, S.; Martinelli, R.; Portella, G. Tumor-Associated macrophage status in cancer treatment. *Cancers* **2020**, *12*, 1987. [[CrossRef](#)]
108. Corna, G.; Campana, L.; Pignatti, E.; Castiglioni, A.; Tagliafico, E.; Bosurgi, L.; Campanella, A.; Brunelli, S.; Manfredi, A.A.; Apostoli, P.; et al. Polarization dictates iron handling by inflammatory and alternatively activated macrophages. *Haematologica* **2010**, *95*, 1814. [[CrossRef](#)]
109. Marques, O.; Porto, G.; Rêma, A.; Faria, F.; Paula, A.C.; Gomez-Lazaro, M.; Silva, P.; da Silva, B.M.; Lopes, C. Local iron homeostasis in the breast ductal carcinoma microenvironment. *BMC Cancer* **2016**, *16*, 187. [[CrossRef](#)]
110. Cairo, G.; Recalcati, S.; Mantovani, A.; Locati, M. Iron trafficking and metabolism in macrophages: Contribution to the polarized phenotype. *Trends Immunol.* **2011**, *32*, 241–247. [[CrossRef](#)]
111. Alkhateeb, A.A.; Han, B.; Connor, J.R. Ferritin stimulates breast cancer cells through an iron-independent mechanism and is localized within tumor-associated macrophages. *Breast Cancer Res. Treat.* **2013**, *137*, 733–744. [[CrossRef](#)]
112. Wei, S.C.; Duffy, C.R.; Allison, J.P. Fundamental mechanisms of immune checkpoint blockade therapy. *Cancer Discov.* **2018**, *8*, 1069–1086. [[CrossRef](#)]
113. Sofias, A.M.; Combes, F.; Koschmieder, S.; Storm, G.; Lammers, T. A paradigm shift in cancer nanomedicine: From traditional tumor targeting to leveraging the immune system. *Drug Discov. Today* **2021**, *26*, 1482–1489. [[CrossRef](#)]
114. Mainini, F.; De Santis, F.; Fucà, G.; Di Nicola, M.; Rivoltini, L.; Eccles, M. Nanobiotechnology and Immunotherapy: Two Powerful and Cooperative Allies against Cancer. *Cancers* **2021**, *13*, 3765. [[CrossRef](#)]
115. Sweeney, M.D.; Zhao, Z.; Montagne, A.; Nelson, A.R.; Zlokovic, B.V. Blood-Brain Barrier: From Physiology to Disease and Back. *Physiol. Rev.* **2019**, *99*, 21–78. [[CrossRef](#)]
116. Moos, T.; Morgan, E.H. Transferrin and Transferrin Receptor Function in Brain Barrier Systems. *Cell. Mol. Neurobiol.* **2000**, *20*, 77–95. [[CrossRef](#)]
117. Rosager, A.M.; Sørensen, M.D.; Dahlrot, R.H.; Hansen, S.; Schonberg, D.L.; Rich, J.N.; Lathia, J.D.; Kristensen, B.W. Transferrin receptor-1 and ferritin heavy and light chains in astrocytic brain tumors: Expression and prognostic value. *PLoS ONE* **2017**, *12*, e0182954. [[CrossRef](#)]
118. Fiandra, L.; Mazzucchelli, S.; Truffi, M.; Bellini, M.; Sorrentino, L.; Corsi, F. In Vitro Permeation of FITC-loaded Ferritins Across a Rat Blood-brain Barrier: A Model to Study the Delivery of Nanoformulated Molecules. *J. Vis. Exp.* **2016**, *2016*, 54279. [[CrossRef](#)]
119. Phan, T.G.; Croucher, P.I. The dormant cancer cell life cycle. *Nat. Rev. Cancer* **2020**, *20*, 398–411. [[CrossRef](#)]
120. Pienta, K.J.; Hammarlund, E.U.; Axelrod, R.; Amend, S.R.; Brown, J.S. Convergent Evolution, Evolving Evolvability, and the Origins of Lethal Cancer. *Mol. Cancer Res.* **2020**, *18*, 801–810. [[CrossRef](#)]
121. Jeong, Y.; Hwang, H.S.; Na, K. Theranostics and contrast agents for magnetic resonance imaging. *Biomater. Res.* **2018**, *22*, 20. [[CrossRef](#)]
122. Millet, I.; Pages, E.; Hoa, D.; Merigeaud, S.; Doyon, F.C.; Prat, X.; Taourel, P. Pearls and pitfalls in breast MRI. *Br. J. Radiol.* **2012**, *85*, 197–207. [[CrossRef](#)]
123. Farwell, M.D.; Pryma, D.A.; Mankoff, D.A. PET/CT imaging in cancer: Current applications and future directions. *Cancer* **2014**, *120*, 3433–3445. [[CrossRef](#)] [[PubMed](#)]
124. Kikano, E.G.; Avril, S.; Marshall, H.; Jones, R.S.; Montero, A.J.; Avril, N. PET/CT Variants and Pitfalls in Breast Cancers. *Semin. Nucl. Med.* **2021**, *51*, 474–484. [[CrossRef](#)] [[PubMed](#)]
125. Ma, T.; Zhang, P.; Hou, Y.; Ning, H.; Wang, Z.; Huang, J.; Gao, M. “Smart” Nanoprobes for Visualization of Tumor Microenvironments. *Adv. Healthc. Mater.* **2018**, *7*, e1800391. [[CrossRef](#)] [[PubMed](#)]
126. Li, Y.; Zhou, Y.; Yue, X.; Dai, Z. Cyanine Conjugate-Based Biomedical Imaging Probes. *Adv. Healthc. Mater.* **2020**, *9*, e2001327. [[CrossRef](#)] [[PubMed](#)]
127. Morato, Y.L.; Paredes, K.O.; Chamizo, L.L.; Marciello, M.; Filice, M. Recent Advances in Multimodal Molecular Imaging of Cancer Mediated by Hybrid Magnetic Nanoparticles. *Polymers* **2021**, *13*, 2989. [[CrossRef](#)] [[PubMed](#)]
128. Thammineedi, S.R.; Saksena, A.R.; Nusra, S.; Iyer, R.R.; Shukla, S.; Patnaik, S.C.; Reddy, R.P.; Bolneni, N.; Sharma, R.M.; Smith, L.; et al. Fluorescence-Guided cancer surgery—A new paradigm. *J. Surg. Oncol.* **2021**, *123*, 1679–1698. [[CrossRef](#)] [[PubMed](#)]
129. Son, G.M.; Ahn, H.-M.; Lee, I.Y.; Ha, G.W. Multifunctional Indocyanine Green Applications for Fluorescence-Guided Laparoscopic Colorectal Surgery. *Ann. Coloproctol.* **2021**, *37*, 133–140. [[CrossRef](#)] [[PubMed](#)]
130. Eglhoff-Juras, C.; Bezdetsnaya, L.; Dolivet, G.; Lassalle, H.-P. NIR fluorescence-guided tumor surgery: New strategies for the use of indocyanine green. *Int. J. Nanomed.* **2019**, *14*, 7823–7838. [[CrossRef](#)]
131. Sofias, A.M.; Bjørkøy, G.; Ochando, J.; Sønsteve, L.; Hegvik, M.; Davies, C.d.L.; Haraldseth, O.; Lammers, T.; Mulder, W.J.M.; Hak, S. Cyclic Arginine–Glycine–Aspartate-Decorated Lipid Nanoparticle Targeting toward Inflammatory Lesions Involves Hitchhiking with Phagocytes. *Adv. Sci.* **2021**, *8*, 2100370. [[CrossRef](#)]
132. Sofias, A.M.; Toner, Y.C.; Meerwaldt, A.E.; van Leent, M.M.T.; Soultanidis, G.; Elschot, M.; Gonai, H.; Grendstad, K.; Flobak, Å.; Neckmann, U.; et al. Tumor Targeting by  $\alpha$  v  $\beta$  3-Integrin-Specific Lipid Nanoparticles Occurs via Phagocyte Hitchhiking. *ACS Nano* **2020**, *14*, 7832–7846. [[CrossRef](#)]

133. Dong, X.; Chu, D.; Wang, Z. Leukocyte-Mediated Delivery of Nanotherapeutics in Inflammatory and Tumor Sites. *Theranostics* **2017**, *7*, 751–763. [[CrossRef](#)] [[PubMed](#)]
134. Moore, T.L.; Hauser, D.; Gruber, T.; Rothen-Rutishauser, B.; Lattuada, M.; Petri-Fink, A.; Lyck, R. Cellular Shuttles: Monocytes/Macrophages Exhibit Transendothelial Transport of Nanoparticles under Physiological Flow. *ACS Appl. Mater. Interfaces* **2017**, *9*, 18501–18511. [[CrossRe](#)]



## Appendix 3



<http://pubs.acs.org/journal/acsofd>

Mini-Review

## Novel Bioengineering Strategies to Improve Bioavailability and *In Vivo* Circulation of H-Ferritin Nanocages by Surface Functionalization

Marta Sevieri, Mattia Pinori, Arianna Chesi, Arianna Bonizzi, Leopoldo Sitia, Marta Truffi, Carlo Morasso, Fabio Corsi,\* and Serena Mazzucchelli\*

Cite This: <https://doi.org/10.1021/acsomega.2c07794>

Read Online



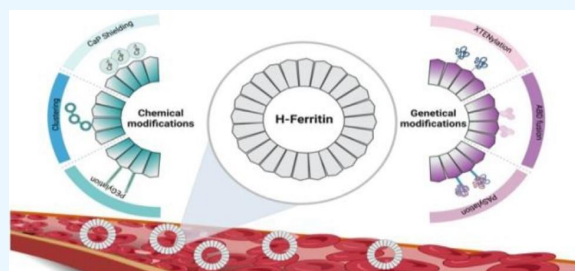
ACCESS |

Metrics & More



Article Recommendations |

**ABSTRACT:** Due to its unique architecture and innate capability to specifically target cancer cells, ferritin has emerged as an attractive class of biomaterials for drug delivery. In many studies, various chemotherapeutics have been loaded into ferritin nanocages constituted by H-chains of ferritin (HF<sub>n</sub>), and their related antitumor efficacy has been explored by employing different strategies. Despite the multiple advantages and the versatility of HF<sub>n</sub>-based nanocages, there are still many challenges to face for their reliable implementation as drug nanocarriers in the process of clinical translation. This review aims at providing an overview of the significant efforts expended during recent years to maximize the features of HF<sub>n</sub> in terms of increased stability and *in vivo* circulation. The most considerable modification strategies explored to improve bioavailability and pharmacokinetics profiles of HF<sub>n</sub>-based nanosystems will be discussed herein.



### 1. INTRODUCTION

Over the past 20 years, there has been a growing interest in the study of nanomedicine due to its potential to address some of the issues of traditional drug delivery therapy in oncology.<sup>1</sup> Although in preclinical settings many strategies based on nanoparticles demonstrate efficacy in tackling tumor growth and expanding survival, they unfortunately translate into a relatively low number of nanoformulations from which patients can effectively benefit.<sup>2</sup>

Considering that the success rate of clinical translation of many nanotechnological solutions, often too complicated, remains relatively low, the strategy of taking advantage of simpler nanomedicine platforms could be a winning choice. Indeed, leveraging biocompatible nanostrategies

presenting high bloodstream stability and natural tumor homing could tackle safety issues and the translational challenges of traditional nanomedicines, closing the gap for real clinical applications. In this context, nanocages made from ferritin have attracted considerable attention in the biomedical and bioengineering fields by virtue of their unique features.<sup>3</sup>

Ferritin (Fn) is one of the most studied proteins and in nature is responsible first for the maintenance of intracellular iron concentrations and also for protection from oxidative stress.<sup>3</sup> Human Fn is a globular multimeric protein made from 24 subunits of H (heavy) and L (light) Fn chains which can self-assemble in a cave-sphere quaternary structure, forming a stable nanocage of 12 nm diameter with an internal cavity 8 nm in diameter.<sup>3</sup> Moreover, the

salt bridges and hydrogen bonds that link subunits allow Fn to tolerate pH and temperature variations. This protein remains stable also in the presence of denaturing agents, which enables Fn to disassemble in extremely acidic (pH 2–3) or basic (pH 10–12) conditions and reassemble in a shape-memory manner when the pH returns to neutrality.<sup>4</sup>

By taking advantage from these unique structural and physicochemical features, nanotechnologists have exploited nanocages constituted only by H-chains of Fn (HF<sub>n</sub>) for drug delivery, accomplishing the loading of different types of compounds, like chemotherapeutics or fluorescent dyes.<sup>5</sup> More importantly, the ability to directly target the human transferrin receptor 1 (TfR1), which is overexpressed in several cancer types, increases the attractiveness of HF<sub>n</sub> in the context of cancer treatment.<sup>3</sup>

## 2. H-FERRITIN NANOCAGES FOR DRUG DELIVERY

The applications of HF<sub>n</sub> in the biomedical field are multiple. Referring to the nanotechnology field, it can be exploited as a reaction chamber to produce metal or semiconductor nanoparticles (NPs). Indeed, the unique cavity of this type of nanocages is extensively exploited for the biomineralization of metal oxides (iron, manganese, cobalt, chromium, and nickel) to assemble semiconductor inorganic NPs with interesting fluorescent properties related to their size and shape.<sup>3</sup> In addition to that, cancer treatment and vaccines development are two emerging dominant fields where HF<sub>n</sub> can be applied. In particular, the nanomedicine scenario has developed fast due to the global need for new therapeutic approaches and technologies against the ongoing pandemic of coronavirus disease 2019 (COVID-19).

An example is the nanoparticle vaccine based on ferritin designed against the SARS-CoV-2 Omicron variant. The ferritin structure was exploited to incorporate in the N-terminal position a protein A tag as a structural scaffold. Then, as an immunogen, the receptor binding domain (RBD) of SARS-CoV-2 Omicron spike protein was fused with an Fc tag at the C-terminus. Once purified, the RBD was assembled onto nanoparticles by the interaction of Fc and the protein A tag. This is a new design strategy for vaccines which can enhance the neutralizing immune responses.<sup>6</sup>

To date, HF<sub>n</sub> has found wider application in the oncological field, where it is employed especially as a delivery system for the diagnosis and treatment of tumors. Within HF<sub>n</sub> it is possible to encapsulate different compounds and chemotherapeutic drugs for oncological therapy. Some examples of drugs that can be easily entrapped in the HF<sub>n</sub> shell are cisplatin,

carboplatin, and desferrioxamine B, since they have an innate tendency to bind metals. HF<sub>n</sub> containing cisplatin has been extensively studied and demonstrated to be important in tumor treatment in different applications, including the study of the apoptotic process and the treatment of melanoma.<sup>7</sup> To date, a plethora of therapeutic drugs, e.g., paclitaxel, curcumin, daunomycin, doxorubicin, epirubicin, etc., have been loaded into the inner cavity of ferritin nanocages.<sup>8,9</sup>

Among the HF<sub>n</sub>-based nanoformulates, one the most studied in the literature involves the encapsulation of doxorubicin (DOX), a cytotoxic drug broadly used in anti-cancer therapy. Indeed, it has been widely demonstrated that DOX nanoformulation in HF<sub>n</sub> is able to improve efficacy and accumulation to the tumor and, above all, is decisive in reducing its cardiotoxicity as well as the serious side effects associated with this type of treatment.<sup>4,10,11</sup>

Another important chemotherapeutic drug that can be encapsulated in HF<sub>n</sub> is paclitaxel (PTX), employed for the treatment of advanced ovarian cancer and AIDS-related Kaposi sarcoma. Unfortunately, the clinical applications of PTX are limited due to its poor solubility and the lack of targeting. Loading this drug into HF<sub>n</sub> makes it possible to overcome the lack of targeting and demonstrates higher therapeutic efficacy and decreased systemic toxicity *in vivo*.<sup>12</sup>

Encapsulation in HF<sub>n</sub> is also reported to stabilize lipophilic drugs like curcumin. Indeed, once loaded into HF<sub>n</sub>, curcumin is found to be more stable and bioavailable, which reduces the premature degradation that occurs when it is used in free form. Although *in vitro* studies have demonstrated an effect of HF<sub>n</sub>curcumin in controlling the proliferative activity on tumor cells, the low solubility of this drug that leads to a poor encapsulation efficacy prevented it from proceeding to further *in vivo* assessments.<sup>13</sup>

HF<sub>n</sub>-based systems have been employed also as carriers of miRNA and/or siRNA, due to their ability to protect their cargo from nuclease activity and to achieve tumor-targeted delivery. These short noncoding RNA molecules related with tumor progression and/or resistance can be delivered into HF<sub>n</sub> in combination with other standard treatments.<sup>14</sup> HF<sub>n</sub> nanocages hold promise to also promote diagnostic imaging tools. One example is the HF<sub>n</sub> formulations enclosing indocyanine green (ICG), a fluorescent dye widely used in clinics for different purposes (e.g., lymph node mapping). HF<sub>n</sub>ICG nanocages are reported to address the issues of rapid degradation and lack of specificity related to ICG, providing a suitable nanotracer for fluorescence-guided detection of cancer tissues.<sup>5</sup>

### 3. LIMITATIONS OF H-FERRITIN NANOCAGES

As previously reported, HF<sub>n</sub> nanocages have been studied with outstanding results as delivery systems in terms of specific tumor recognition and increased activity with lower side effects.<sup>10,11</sup> Properties such as high biocompatibility and good biodegradability put HF<sub>n</sub> ahead of conventional materials in clinical translation for imaging and drug delivery purposes. Unfortunately, despite their many undeniable benefits, HF<sub>n</sub>-based nanosystems also have important vulnerabilities.

First, it is necessary to consider the short plasma half-life after systemic injection displayed by HF<sub>n</sub>, which leads to poor accumulation at tumor sites.<sup>4,15</sup> Indeed, according to the results obtained by Yin et al., the 2–3 h half-life of human HF<sub>n</sub> in circulation as obtained for an HF<sub>n</sub>/DOX formulation is unsatisfactory, considering that this circulation time is shorter than those of the majority of other drug nanocarriers due to its relatively small particle size.<sup>16</sup> In light of this, many efforts have been made toward the exploration of functionalization strategies for a broader application of HF<sub>n</sub> and improvement in treatment outcomes. Second, often the drug-binding ability of HF<sub>n</sub> is not completely satisfactory. Overall, both the yields and stability of the HF<sub>n</sub>–drug complexes might not meet the necessary requirements for its potential pharmaceutical applications.<sup>15</sup>

In this review, we summarize actions proposed recently by researchers with the aim of addressing the short half-life that characterizes HF<sub>n</sub> to maximize its intrinsic capability to target specific tumor sites (Figure 1).

### 4. CHEMICAL MODIFICATIONS OF H-FERRITIN NANOCAGES

**4.1. Conjugation of H-Ferritin Nanocages with Polyethylene Glycol (PEG) Molecules.** It is worth noting that surface modifications of nanomaterials can strongly influence their performance as drug delivery vehicles by improving their biocompatibility, selectivity, and circulation in the bloodstream. Among the different approaches developed for the improvement of HF<sub>n</sub>'s features, multiple chemical modifications have been proposed, including conjugation with polyethylene glycol (PEG), reported to enhance the *in vivo* circulation time. Indeed, this strategy, named PEGylation, has been extensively employed to improve systemic circulation time and decrease immunogenicity, thus increasing the efficiency of drug and gene delivery to target cells and tissues.<sup>17,18</sup> However, it has also been reported that PEGylation may interfere with the intrinsic ability of HF<sub>n</sub> to recognize TfR1 and target cancer cells.<sup>19</sup> As a consequence, it has become necessary to introduce further adaptations to the classic PEGylation strategies.

An interesting PEG-masked HF<sub>n</sub> nanoplatform was developed for the treatment of melanoma. After performing a controlled modification of the HF<sub>n</sub> protein surface with a precise number of PEG molecules, the authors inserted a selective targeting moiety for melanoma cells, named  $\alpha$ -MSH peptide. This targeting strategy was successful in improving the circulation half-life of HF<sub>n</sub> and achieving selective internalization by melanoma cells.<sup>20</sup>

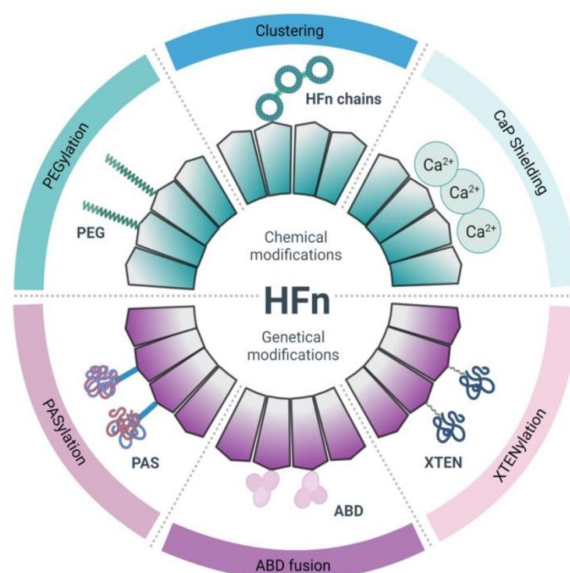


Figure 1. Scheme of chemical and genetical modifications of HF<sub>n</sub> aimed at improving stability and *in vivo* circulation.

However, it is worth noting that the PEGylation process presents several disadvantages, including increased costs and reduced yields.<sup>15,21</sup> In addition, PEG, which has been considered non-antigenic for years, may be responsible for immunogenicity, as well as not being biodegradable, thus bringing possible issues in biosafety which cannot be neglected.<sup>17</sup>

**4.2. Clustering of H-Ferritin Nanocages with PEG Molecules.** Recently, an interesting strategy to precisely assemble nanostructures in a controlled manner has been proposed. More specifically, it uses a “bottom-up” hierarchical incorporation of protein building blocks in order to obtain highly ordered nanostructures by means of PEG chemical conjugation. In particular, the strategy of assembling more HF<sub>n</sub> via PEG chemical conjugation to achieve the multivalent binding of HF<sub>n</sub>, thus facilitating prolonged circulation time and accumulation within tumor cells, has been investigated. Two-armed PEG molecules were used to link free –NH<sub>2</sub> groups of HF<sub>n</sub> in order to achieve nanostructured assemblies, named oligomeric nanozymes, composed by monomers, dimers, and multimers. After a detailed *in vitro* characterization, the behavior of different HF<sub>n</sub> nano-assemblies was evaluated in a murine model of colorectal cancer. It was observed that the assembly of four HF<sub>n</sub> nanocages displayed improved blood pharmacokinetics and circulation time compared to the mono- and bi-assemblies, as well as enhanced tumor uptake.<sup>22</sup>

**4.3. Shielding of H-Ferritin Nanocages with Calcium Phosphate.** It is known that the high expression of TfR1 in the liver may interfere with HF<sub>n</sub> accumulation in tumors. Indeed, it has been observed that a co-culture with liver cells may cause reduced uptake efficiency by tumor cells, thus negatively affecting HF<sub>n</sub>'s delivery to the tumor.<sup>23</sup> To overcome this limitation, a biomineralization strategy of shielding HF<sub>n</sub> with a calcium phosphate (CaP) shell has been proposed.

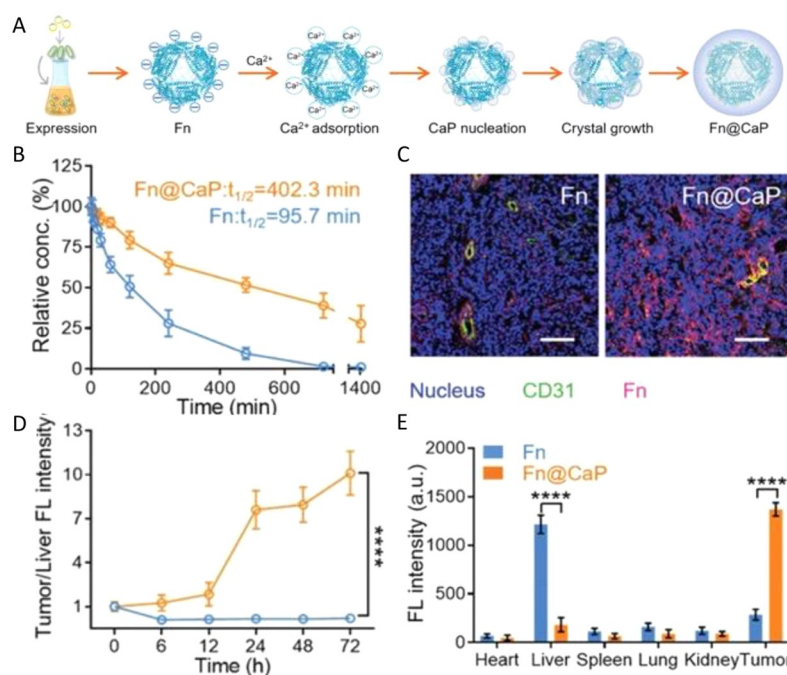


Figure 2. Fabrication and characterization of a biominerallized ferritin nanoplatform and evaluation of its *in vivo* distribution. (A) Schematic illustration of the preparation of the Fn@CaP nanoplatform. (B) Comparative analysis of blood half-life of Fn and Fn@CaP in HeLa tumor-bearing mice. (C) CLSM images of Fn and Fn@CaP accumulated in tumor tissues. (D) Comparative analysis of dynamic tumor versus liver fluorescence intensity of Cy7-labeled Fn and Fn@CaP in mice given the indicated treatments. (E) Comparative analysis of the fluorescence intensity of Cy7-labeled Fn and Fn@CaP at 24 h. Data represent the mean  $\pm$  s.d. Statistical significance was calculated via a two-tailed Student's *t* test (D, E). \*\*\* $p < 0.001$ , \*\*\*\* $p < 0.0001$ . Reproduced with permission from ref 23. Copyright 2021 Wiley-VCH GmbH.

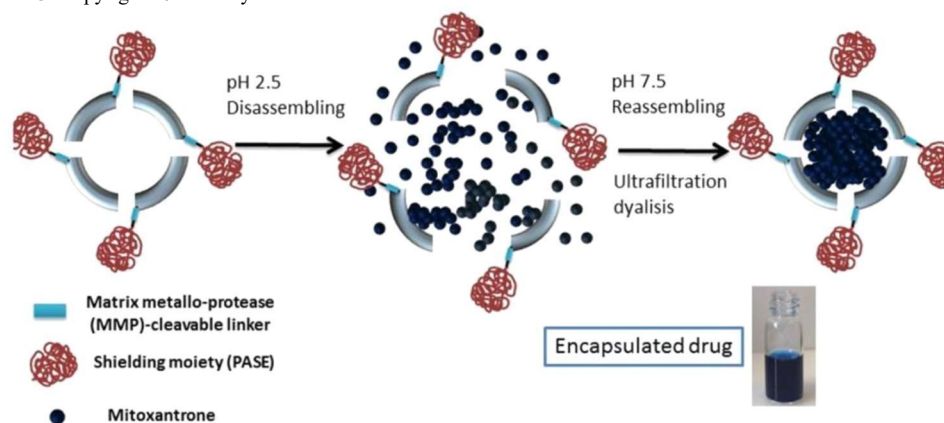


Figure 3. Scheme of HFn-PASE loading strategy. Reproduced with permission from ref 28. Copyright 2022 Elsevier B.V.



Indeed, the presence of a mineral-reinforced coating is expected to enhance HF<sub>n</sub>'s serum stability, as likewise observed for CaP-mineralized micelles.<sup>24</sup> Wang et al. developed ferritin nanoparticles coated with CaP aimed at maintaining stability in the liver (pH 7.4) while re-exposing it in the weakly acidic tumor microenvironment (Figure 2A). This strategy is conceived therefore to protect the nanoparticle from hepatic TfR1 recognition and at the same time ensure selective dissolution of the CaP shell in the tumor to allow specific binding and uptake by tumor cells. Overall, the biomineralization method to encapsulate nanomaterials is beneficial for the improvement of the serum half-life of HF<sub>n</sub> in comparison to the nonmineralized control HF<sub>n</sub> (Figure 2B). In addition, mice administered with CaP-coated HF<sub>n</sub> nanocages showed a dramatic reduction of liver accumulation and a 12-fold larger efficiency of tumor-specific HF<sub>n</sub> delivery (Figure 2C–E). Ultimately, extensive evaluations performed on multiple cell lines and patient-derived xenograft models supported the relevance of this nanopatforms as an efficient nanostrategy for promoting tumor targeting and accumulation (Figure 2).<sup>23</sup>

## 5. GENETICAL MODIFICATIONS OF H-FERRITIN NANOCAGES

**5.1. PASylation of H-Ferritin Nanocages.** Over the years, genetic engineering techniques have been applied for the development of modified ferritin nanoparticles, as a complement to the chemical modifications previously discussed. Among the genetic modifications proposed, an important role is played by the modification known as PASylation.<sup>25</sup> This modification, which is based on the genetic fusion of biopharmaceuticals such as proteins, peptides, and lowmolecular-weight drugs with a sequence rich in proline (P), alanine (A), and serine (S), was designed by Schlapschy with the aim of mimicking PEG while gaining advantages in biocompatibility and biodegradability as well as in increasing circulation time.<sup>16</sup>

Moreover, PAS sequences show high solubility in physiological solution and adopt stable random coil conformations, leading to expanded hydrodynamic volumes. Consequently, PAS conjugates show retarded kidney filtration and prolonged pharmacokinetics *in vivo*.<sup>26</sup>

This strategy has been applied to HF<sub>n</sub> by genetically fusing PAS sequences to the N-terminal portion of H-Ferritin subunits. In particular, two HF<sub>n</sub> constructs were designed inserting in the N-terminal position PAS sequences of different lengths: 40 (HF<sub>n</sub>-PAS40) and 75 (HF<sub>n</sub>-PAS75) amino acids, respectively. The PAS40 and PAS75 polypeptides were both genetically fused to HF<sub>n</sub> throughout a linker sequence consisting of three glycine residues that ensures proper PAS exposure on the outer

surface of HF<sub>n</sub>. Both HF<sub>n</sub> mutants displayed high stability in plasma and outstanding efficiency in the encapsulation of doxorubicin. Indeed, the stability and circulation time of HF<sub>n</sub>-PAS-DOXO complexes were dramatically increased with respect to those of wild-type protein.<sup>15</sup>

Moreover, with the aim of increasing both half-life and tumortargeting ability, H-Ferritin nanocages were genetically fused with the PAS sequence via two different linker sequences (GFLG and PLGLAG) and with the tumor-targeting peptide RGDK (Arg-Gly-Asp-Lys). In particular, GFLG and PLGLAG constitute cleavable sites that are recognized by cathepsin B and matrix metalloproteinase-2/9, respectively. The *in vivo* pharmacokinetics study revealed the positive impact of this strategy on HF<sub>n</sub>'s half-life. Indeed, approximately 4.9-fold longer circulation time was observed in comparison to the wildtype form, thus allowing enhanced retention time at the tumor site. The addition of RGDK, on the other hand, was successful in improving biodistribution, uptake efficiency, and targeting ability at the tumor site by specifically binding to integrin  $\alpha v\beta 3/5$  and neuropilin-1, which are expressed at high levels in different tumor types.<sup>16</sup>

In another work, a different variant of PASylated H-Ferritin nanocages was designed with the aim of preventing healthy cells' internalization while ensuring specific tumor targeting. The authors genetically inserted, between the sequence encoding for H-Ferritin and the PAS sequence, a linker sequence named MP recognized by tumor matrix metalloproteases (MMPs). Thus, while the presence of the PAS shield promotes the extension of the *in vivo* stability, the recognition of the MP sequence by MMPs enables the unmasked HF<sub>n</sub> to freely interact with TfR1 overexpressed in cancer cells, triggering tumor-specific accumulation. Again, these H-Ferritin constructs displayed a longer half-life and greater drug encapsulation efficiency compared to the wild type HF<sub>n</sub>.<sup>27</sup>

Based on the evidence that negatively charged nanocages can have different behaviors in terms of circulation time, HF<sub>n</sub>-MPPAS was redesigned by adding two glutamic acid (E) residues, resulting in a new construct called HF<sub>n</sub>-MP-PASE. Through this modification, increased circulation time and longer accumulation at the tumor site of HF<sub>n</sub> nanocages were observed compared with the previously assessed nanocages thanks to the reduced undesired interaction with healthy tissues (Figure 3).<sup>28</sup>

**Table 1. Summary of All Significant Efforts Involving Surface Functionalization Aimed at Improving *In Vivo* Circulation Time of Ferritin Nanocages**

Modification Strategy	Material	Achievements
Chemical Modifications		
PEGylation	PEG sequences + $\alpha$ -MSH peptide	<ul style="list-style-type: none"> <li>Extended circulation time up to 24 h</li> <li>Specific recognition and internalization into melanoma cells</li> </ul>
Clustering into oligomers	PEG sequences	<ul style="list-style-type: none"> <li>Prolonged circulation time and enhanced tumor uptake with the nanostructure consisting of 4 HF<sub>n</sub> monomers</li> </ul>
Biom mineralization	CaP shielding	<ul style="list-style-type: none"> <li>Increased <i>in vivo</i> half-life</li> <li>Reduced uptake by liver cells</li> <li>Enhanced accumulation at the tumor</li> </ul>
Genetical Modifications		
PASylation	PAS sequence	Enhanced stability in plasma Improved encapsulation efficiency of doxorubicin
	PAS sequence + RGDK targeting peptide	Prolonged half-life (4.9-fold increase) Improved tumor targeting ability
	PAS sequence + cleavable linker recognized by tumor metalloproteases	Extension of the <i>in vivo</i> stability promoted by PAS sequences Specific tumor interaction thanks to the unmasking of PAS sequences at the tumor microenvironment Enhanced drug encapsulation efficiency
	PASE sequence + cleavable linker recognized by tumor metalloproteases	<ul style="list-style-type: none"> <li>Increased circulation time thanks to the addition of acidic residues</li> <li>Longer accumulation at the tumor site and reduced undesired interaction with healthy tissues</li> </ul>
	PAS sequence	Increased accumulation at the tumor Reduced uptake by healthy tissues
Fusion with albumin binding domains	Coating with albumin	<ul style="list-style-type: none"> <li>Extended circulation time and improved pharmacokinetic profile</li> </ul>
XTENylation	XTEN polypeptides	<ul style="list-style-type: none"> <li>Improved half-life in relation to the length of the XTEN polymer</li> </ul>
	XTEN polypeptides	Improved half-life in relation to the length of the XTEN polymer High bioavailability and very low immunogenicity

Tesarova et al. proposed novel HF<sub>n</sub>-based nanoconstructs modified on the surface with PAS sequences of 10 and 20 amino acids, respectively. Here, to enable functionalization of the surface with PAS peptides, the surface of H-Ferritin nanocages was first decorated with gold nanoparticles, and subsequently PAS sequences were incubated, obtaining the final nanoconstruct. HF<sub>n</sub> nanocages modified with PAS10 and loaded with the cytostatic drug ellipticine displayed increased accumulation at the tumor, while its uptake into off-target tissues was hampered in a murine model of triple-negative breast cancer.<sup>29</sup>

**5.2. Modification of H-Ferritin Nanocages with Albumin Binding Domain (ABD).** Another

interesting modification that has been proposed to improve the performance of H-Ferritins as drug delivery vehicles involves their genetic functionalization with a variant of the ABD. This strategy is intended to exploit the high affinity that ABD has for human serum albumin (HSA), the most abundant protein found in plasma. Thus, by coating the outer surface of HF<sub>n</sub>

nanocages with ABD, an increase in circulation time is expected to occur.

In order to study the pharmacokinetic profile *in vivo*, HF<sub>n</sub> nanocages were loaded with doxorubicin, and the half-life was evaluated by monitoring the drug's concentration at different time points subsequent to

the intravenous administration of ABD-HFn/DOX, HFn/DOX, and DOX. As a result, ABDHFn/DOX displayed an extended half-life compared to both the free drug (19-fold longer) and HFn/DOX (12-fold longer). Furthermore, it was observed that ABD does not affect cellular uptake, as genetically modified nanocages showed results comparable to those obtained with wild-type HFn nanoparticles.<sup>30</sup>

### 5.3. XTENylation of H-Ferritin Nanocages.

Another approach studied to mask the surface of nanocages with the aim of improving their stability is the method known as XTENylation. XTEN represents a class of unstructured polymers consisting of six repeating hydrophilic amino acids (A, E, G, P, S, and T) that can be genetically fused to obtain XTENylated proteins. The circulation time of XTEN polymers increases proportionally to their length since longer polypeptides confer larger hydrodynamic volumes, resulting in slower renal clearance. It has been observed that conjugation of XTEN polymers of the same length with therapeutic peptides or proteins can alter the half-life times of individual drugs differently. In any case, the half-life of each individual molecule can be altered depending on the length of the XTEN polymer.<sup>17</sup>

In another work, long-circulating ferritin nanocages (LCFNs) using intrinsically disordered proteins called “IDP cloud” were designed through 3D modeling with the purpose of shielding the nanoparticles and increasing the half-life time. Based on 3D modeling, ferritin monomers were genetically functionalized with XTEN polymers of different lengths (LCFN36, LCFN72, LCFN144, LCFN288), consisting of only hydrophilic amino acids (P, A, T, G, E, S), with the aim of understanding which length was optimal to give a longer half-life time. The results showed that increasing the length of the peptide achieved an increment in the half-life time compared to the wild-type form, thus showing a correlation between the two factors, while no significant difference was observed between LCFN144 and LCFN288.<sup>21</sup>

In addition, XTEN polymers have been observed to exhibit high biodegradability (thus avoiding accumulation in tissues following prolonged treatment), high bioavailability, and low or absent immunogenicity, making XTENylation a promising modification strategy.<sup>17</sup>

All significant efforts involving surface functionalization aimed at improving *in vivo* circulation time of ferritin nanocages, discussed herein, are summarized in Table 1.

## 6. CONCLUSIONS

In the past decade, hundreds of nanodrug delivery systems based on HFn have been proposed. Several studies have demonstrated that ferritin nanocarriers can not only improve the bioavailability of soluble drugs and drive a specific accumulation at the tumor

but also mitigate the side effects of toxic drugs on healthy tissues. However, some key challenges need to be addressed, including the relatively low stability and short *in vivo* half-life of ferritin. At present, different methods that include chemical and genetical modifications have been proposed as functionalization strategies to optimize the employment of ferritin nanosystems. Many of them hold great potential in tumor therapy and seem promising in tackling the major challenges described.


Clearly, considering the growing number of related publications, the PASylation strategy is one of the most compelling. Indeed, in the face of a relatively easy production, this functionalization strategy is reported to help overcome many of the current difficulties in the use of ferritin-based assemblies for *in vivo* applications. Overall, also biomineralization of HFn nanocages with calcium phosphate presents itself as a very new and promising strategy to tackle the above-discussed limitations and to advance toward the development of proteinbased nanoplatforms for effective diagnostic and therapeutic applications.

In conclusion, further translational efforts based on ferritin nanoparticles as fine-tuned anti-tumor drug delivery platforms are expected in the near future.

## ■ AUTHOR INFORMATION

Corresponding Authors

**Fabio Corsi** – *Nanomedicine Laboratory, Department of Biomedical and Clinical Sciences, Università degli Studi di Milano, 20157 Milan, Italy; Breast Unit, Istituti Clinici Scientifici Maugeri IRCCS, 27100 Pavia, Italy; Nanomedicine and Molecular Imaging Lab, Istituti Clinici Scientifici Maugeri IRCCS, 27100 Pavia, Italy; Email: [fabio.corsi@unimi.it](mailto:fabio.corsi@unimi.it)*

**Serena Mazzucchelli** – *Nanomedicine Laboratory, Department of Biomedical and Clinical Sciences, Università degli Studi di Milano, 20157 Milan, Italy;  [orcid.org/0000-0001-6904-8895](https://orcid.org/0000-0001-6904-8895); Email: [serena.mazzucchelli@unimi.it](mailto:serena.mazzucchelli@unimi.it)*

Authors

**Marta Sevieri** – *Nanomedicine Laboratory, Department of Biomedical and Clinical Sciences, Università degli Studi di Milano, 20157 Milan, Italy*

**Mattia Pinori** – *Nanomedicine Laboratory, Department of Biomedical and Clinical Sciences, Università degli Studi di Milano, 20157 Milan, Italy*

**Arianna Chesi** – *Nanomedicine Laboratory, Department of Biomedical and Clinical Sciences, Università degli Studi di Milano, 20157 Milan, Italy*

**Arianna Bonizzi** – *Nanomedicine Laboratory, Department of Biomedical and Clinical Sciences, Università degli Studi di Milano, 20157 Milan, Italy*



**Leopoldo Sitia** – *Nanomedicine Laboratory, Department of Biomedical and Clinical Sciences, Università degli Studi di Milano, 20157 Milan, Italy*

**Marta Truffi** – *Nanomedicine and Molecular Imaging Lab, Istituti Clinici Scientifici Maugeri IRCCS, 27100 Pavia, Italy*

**Carlo Morasso** – *Nanomedicine and Molecular Imaging Lab, Istituti Clinici Scientifici Maugeri IRCCS, 27100 Pavia, Italy*; [orcid.org/0000-0001-9185-0198](https://orcid.org/0000-0001-9185-0198)

Complete contact information is available at: <https://pubs.acs.org/10.1021/acsomega.2c07794>

#### Author Contributions

Writing original draft preparation, A.B., A.C., M.P., M.S., L.S., M.T., C.M., and S.M.; writing review and editing, M.P., M.S., S.M., and F.C. All authors have read and agreed to the published version of the manuscript.

#### Notes

The authors declare no competing financial interest.

#### Biographies

Marta Sevieri received her Master's degree in Industrial Biotechnology at the University of Milan-Bicocca, Italy, in 2018 and is now a Ph.D. student at the University of Milan, Italy. Her research interest is in the evaluation of ferritin-based nanoparticles for fluorescence-guided surgery. She has published 20 SCI-cited papers with more than 100 citations (h index of 7).

Mattia Pinori received his Master's degree in Experimental and Applied Biology in 2022 at the University of Pavia, Italy. His research interests include studies on the expression of heterologous proteins in *E. coli* and protein purification.

Arianna Chesi obtained her Master's degree in Pharmaceutical Biotechnology in 2021 at the University of Milan, Italy. Her research interests include studies on the development of a biological nanoparticle platform for the delivery of anti-cancer therapies.

Arianna Bonizzi received her Master's degree in Neurobiology in 2015 at the University of Pavia, Italy, and is now a Ph.D. student at the University of Milan, Italy. Her research activities are focused on nanobiotechnology, breast cancer nanomedicine, and the integration of Raman spectroscopy with biochemical assay for the noninvasive study of metabolic disorders. She has published 26 SCI-cited papers with more than 250 citations (h index of 9).

Leopoldo Sitia received his Ph.D. in Nanopharmacology in 2015 at the Mario Negri Institute for Pharmacological Research in Milan, Italy. His research activities are focused on nanotechnology, nano-biointeractions, and breast cancer nanomedicine. He has published 29 SCI-cited papers with more than 500 citations (h index of 14).

Marta Truffi received her Ph.D. in Biomolecules, Structural Biology, Pathology and Biotherapy at the University of Paris VII - Denis Diderot, France. She is currently a Research Scientist at the Istituti Clinici Scientifici Maugeri IRCCS in Pavia, Italy. Her research interests are mainly focused on the study of diagnostic and prognostic biomarkers of disease and their exploitation for the development of targeted/nanotargeted approaches. She has published more than 50 SCI-cited papers with more than 900 citations (h index of 18).

Carlo Morasso got a Ph.D. in Medicinal Chemistry at the University of Milan, Italy. Currently, he works as a Senior Research Scientist at the Istituti Clinici Scientifici Maugeri IRCCS in Pavia, Italy. His research interests mainly focus on using nano-structured materials for healthcare applications and advanced optical spectroscopies in biomedical research. He is the author of more than 60 peer-reviewed articles with more than 900 citations (h index of 21).

Fabio Corsi obtained his specialization in general medicine at the University of Milan, Italy, in 1999. He is head of the Nanomedicine Laboratory at the Department of Biomedical and Clinical Sciences, University of Milan, Italy, and of the Laboratory of Nanomedicine and Molecular Imaging at Maugeri Clinical Scientific Institutes IRCCS, Pavia, Italy. Moreover, he is the director of the Breast Surgical Unit at Maugeri Clinical Scientific Institutes IRCCS, Pavia, Italy. His current research interests include the study of protein-based nanoparticles and their applications in anti-cancer therapy. He has published over 160 SCI-cited papers with more than 3000 citations (h index of 32).

Serena Mazzucchelli received her Ph.D. in Biology in 2010 at the University of Milan-Bicocca, Italy. Her research interest focuses on the development of ferritin-based nanoparticles as targeted delivery systems for cancer diagnosis and treatment. She has published over 70 SCI-cited papers with more than 1600 citations (h index of 23).

#### ■ ACKNOWLEDGMENTS

We thank AIRC for funding M.P.'s research fellowship (AIRC IG 2017ID20172-P.I. Corsi Fabio) The research leading to these results has

received funding from AIRC IG (2017 ID20172-P.I. Corsi Fabio and 2022ID27107-P.I. Mazzucchelli Serena). We also acknowledge the University of Milan for a post-doctoral fellowship to L.S. and for fellowships to A.C., M.S., and A.B. Figure 1 and the TOC graphic were created with [BioRender.com](https://www.biorender.com). ■

## REFERENCES

- (1) Sun, X.; Hong, Y.; Gong, Y.; Zheng, S.; Xie, D. Bioengineered Ferritin Nanocarriers for Cancer Therapy. *Int. J. Mol. Sci.* 2021, 22 (13), 7023.
- (2) van der Meel, R.; Sulheim, E.; Shi, Y.; Kiessling, F.; Mulder, W. J. M.; Lammers, T. Smart Cancer Nanomedicine. *Nat. Nanotechnol.* 2019, 14 (11), 1007–1017.
- (3) Truffi, M.; Fiandra, L.; Sorrentino, L.; Monieri, M.; Corsi, F.; Mazzucchelli, S. Ferritin Nanocages: A Biological Platform for Drug Delivery, Imaging and Theranostics in Cancer. *Pharmacol. Res.* 2016, 107, 57–65.
- (4) Mazzucchelli, S.; Bellini, M.; Fiandra, L.; Truffi, M.; Rizzuto, M. A.; Sorrentino, L.; Longhi, E.; Nebuloni, M.; Prospero, D.; Corsi, F. Nanometronomic Treatment of 4T1 Breast Cancer with Nanocaged Doxorubicin Prevents Drug Resistance and Circumvents Cardiotoxicity. *Oncotarget* 2017, 8 (5), 8383–8396.
- (5) Sitia, L.; Sevieri, M.; Bonizzi, A.; Allevi, R.; Morasso, C.; Foschi, D.; Corsi, F.; Mazzucchelli, S. Development of Tumor-Targeted Indocyanine Green-Loaded Ferritin Nanoparticles for Intraoperative Detection of Cancers. *ACS Omega* 2020, 5 (21), 12035–12045.
- (6) Falvo, E.; Tremante, E.; Arcovito, A.; Papi, M.; Elad, N.; Boffi, A.; Morea, V.; Conti, G.; Toffoli, G.; Fracasso, G.; Giacomini, P.; Ceci, P. Improved Doxorubicin Encapsulation and Pharmacokinetics of Ferritin-Fusion Protein Nanocarriers Bearing Proline, Serine, and Alanine Elements. *Biomacromolecules* 2016, 17 (2), 514–522.
- (7) Yin, S.; Wang, Y.; Zhang, B.; Qu, Y.; Liu, Y.; Dai, S.; Zhang, Y.; Wang, Y.; Bi, J. Engineered Human Heavy-Chain Ferritin with Half-Life Extension and Tumor Targeting by PAS and RGDK Peptide Functionalization. *Pharmaceutics* 2021, 13 (4), 521.
- (8) Podust, V. N.; Balan, S.; Sim, B.-C.; Coyle, M. P.; Ernst, U.; Peters, R. T.; Schellenberger, V. Extension of in Vivo Half-Life of Biologically Active Molecules by XTEN Protein Polymers. *J. Controlled Release* 2016, 240, 52–66.
- (9) Suk, J. S.; Xu, Q.; Kim, N.; Hanes, J.; Ensign, L. M. PEGylation as a Strategy for Improving Nanoparticle-Based Drug and Gene Delivery. *Adv. Drug Delivery Rev.* 2016, 99 (Pt A), 28–51.
- (10) Huang, X.; Chisholm, J.; Zhuang, J.; Xiao, Y.; Duncan, G.; Chen, X.; Suk, J. S.; Hanes, J. Protein Nanocages That Penetrate Airway Mucus and Tumor Tissue. *Proc. Natl. Acad. Sci. U. S. A.* 2017, 114 (32), E6595–E6602.
- (11) Vannucci, L.; Falvo, E.; Fornara, M.; De Micco, P.; Benada, O.; Krizan, J.; Svoboda, J.; Hulikova-Capkova, K.; Morea, V.; Boffi, A.; Ceci, P. Selective Targeting of Melanoma by PEG-Masked Protein-Based Multifunctional Nanoparticles. *Int. J. Nanomedicine* 2012, 7, 1489–1509.
- (12) Lee, N. K.; Lee, E. J.; Kim, S.; Nam, G.; Kih, M.; Hong, Y.; Jeong, C.; Yang, Y.; Byun, Y.; Kim, I.-S. Ferritin Nanocage with Intrinsically Disordered Proteins and Affibody: A Platform for Tumor Targeting with Extended Pharmacokinetics. *J. Controlled Release* 2017, 267, 172–180.
- (13) Liu, Q.; Tian, J.; Liu, J.; Zhu, M.; Gao, Z.; Hu, X.; Midgley, A. C.; Wu, J.; Wang, X.; Kong, D.; Zhuang, J.; Liu, J.; Yan, X.; Huang, X. Modular Assembly of Tumor-Penetrating and Oligomeric Nanozyme Based on Intrinsically Self-Assembling Protein Nanocages. *Adv. Mater.* 2021, 33 (39), 2103128.
- (14) Wang, C.; Wang, X.; Zhang, W.; Ma, D.; Li, F.; Jia, R.; Shi, M.; Wang, Y.; Ma, G.; Wei, W. Shielding Ferritin with a Biomineralized Shell Enables Efficient Modulation of Tumor Microenvironment and Targeted Delivery of Diverse Therapeutic Agents. *Adv. Mater.* 2022, 34 (5), 2107150.
- (15) Min, K. H.; Lee, H. J.; Kim, K.; Kwon, I. C.; Jeong, S. Y.; Lee, S. C. The Tumor Accumulation and Therapeutic Efficacy of Doxorubicin Carried in Calcium Phosphate-Reinforced Polymer Nanoparticles. *Biomaterials* 2012, 33 (23), 5788–5797.
- (16) Ahmadpour, S.; Hosseinimehr, S. J. PASylation as a Powerful Technology for Improving the Pharmacokinetic Properties of Biopharmaceuticals. *Curr. Drug Delivery* 2018, 15 (3), 331–341.
- (17) Binder, U.; Skerra, A. PASylation®: A Versatile Technology to Extend Drug Delivery. *Curr. Opin. Colloid Interface Sci.* 2017, 31, 10–17.
- (18) Fracasso, G.; Falvo, E.; Colotti, G.; Fazi, F.; Ingegnere, T.; Amalfitano, A.; Doglietto, G. B.; Alfieri, S.; Boffi, A.; Morea, V.; Conti, G.; Tremante, E.; Giacomini, P.; Arcovito, A.; Ceci, P. Selective Delivery of Doxorubicin by Novel Stimuli-Sensitive Nano-Ferritins Overcomes Tumor Refractoriness. *J. Controlled Release* 2016, 239, 10–18.
- (19) Falvo, E.; Malagrino, F.; Arcovito, A.; Fazi, F.; Colotti, G.;

- Tremante, E.; Di Micco, P.; Braca, A.; Opri, R.; Giuffrè, A.; Fracasso, G.; Ceci, P. The Presence of Glutamate Residues on the PAS Sequence of the Stimuli-Sensitive Nano-Ferritin Improves in Vivo Biodistribution and Mitoxantrone Encapsulation Homogeneity. *J. Controlled Release* 2018, 275, 177–185.
- (20) Tesarova, B.; Dostalova, S.; Smidova, V.; Goliasova, Z.; Skubalova, Z.; Michalkova, H.; Hynek, D.; Michalek, P.; Polanska, H.; Vaculovicova, M.; Hacek, J.; Eckschlager, T.; Stiborova, M.; Pires, A. S.; Neves, A. R. M.; Abrantes, A. M.; Rodrigues, T.; Matafome, P.; Botelho, M. F.; Teixeira, P.; Mendes, F.; Heger, Z. Surface-PASylation of Ferritin to Form Stealth Nanovehicles Enhances in Vivo Therapeutic Performance of Encapsulated Ellipticine. *Appl. Mater. Today* 2020, 18, 100501.
- (21) Wang, C.; Zhang, C.; Li, Z.; Yin, S.; Wang, Q.; Guo, F.; Zhang, Y.; Yu, R.; Liu, Y.; Su, Z. Extending Half Life of H-Ferritin Nanoparticle by Fusing Albumin Binding Domain for Doxorubicin Encapsulation. *Biomacromolecules* 2018, 19 (3), 773–781.

## Appendix 4

International Journal of  
*Molecular Science*

## Article

# Tumor Accumulation and Off-Target Biodistribution of an Indocyanine-Green Fluorescent Nanotracer: An Ex Vivo Study on an Orthotopic Murine Model of Breast Cancer

- <sup>1</sup> Dipartimento di Scienze Biomediche e cliniche "L. Sacco", Università di Milano, 20157 Milan, Italy; marta.sevieri@unimi.it (M.S.); leopoldo.sitia@unimi.it (L.S.); arianna.bonizzi@unimi.it (A.B.)
- <sup>2</sup> Istituti Clinici Scientifici Maugeri IRCCS, 27100 Pavia, Italy; marta.truffi@icsmaugeri.it
- \* Correspondence: serena.mazzucchelli@unimi.it (S.M.); fabio.corsi@unimi.it (F.C.)

**Abstract:** Indocyanine green (ICG) is a near infrared fluorescent tracer used in image-guided surgery to assist surgeons during resection. Despite appearing as a very promising tool for surgical oncology, its employment in this area is limited to lymph node mapping or to laparoscopic surgery, as it lacks tumor targeting specificity. Recently, a nanoformulation of this dye has been proposed with the aim toward tumor targeting specificity in order to expand its employment in surgical oncology. This nanosystem is constituted by 24 monomers of H-Ferritin (HF<sub>n</sub>), which self-assemble into a spherical cage structure enclosing the indocyanine green fluorescent tracer. These HF<sub>n</sub> nanocages were demonstrated to display tumor homing due to the specific interaction between the HF<sub>n</sub> nanocage and transferrin receptor 1, which is overexpressed in most tumor tissues. Here, we provide an ex vivo detailed comparison between the biodistribution of this nanotracer and free ICG, combining the results obtained with the Karl Storz endoscope that is currently used in clinical practice and the quantification of the ICG signal derived from the fluorescence imaging system IVIS Lumina II. These insights demonstrate the suitability of this novel HF<sub>n</sub>-based nanosystem in fluorescence-guided oncological surgery.

**Keywords:** ferritin nanoparticles; ICG; tumor targeting; nanomedicine; ex vivo imaging; fluorescence-guided surgery; fluorescence



**Citation:** Sevieri, M.; Sitia, L.; Bonizzi, A.; Truffi, M.; Mazzucchelli, S.; Corsi, F. Tumor Accumulation and Off-Target Biodistribution of an Indocyanine-Green Fluorescent Nanotracer: An Ex Vivo Study on an Orthotopic Murine Model of Breast Cancer. *Int. J. Mol. Sci.* **2021**, *22*, 1601. <https://doi.org/10.3390/ijms22041601>

Academic Editor: Paola Manini  
Received: 29 December 2020  
Accepted: 2 February 2021  
Published: 5 February 2021

**Publisher's Note:** MDPI stays neutral with regard to jurisdictional claims in published maps and institutional affiliations.



**Copyright:** © 2021 by the authors. Licensee MDPI, Basel, Switzerland. This article is an open access article distributed under the terms and conditions of the Creative Commons Attribution (CC BY) license (<https://creativecommons.org/licenses/by/4.0/>).

## 1. Introduction

Fluorescence-guided surgery (FGS) is an intraoperative medical procedure that provides real-time fluorescence images of the operating field [1]. It is gaining interest in surgical oncology due to its potential to improve tumor margin visualization and the identification of tumor deposits. Indeed, a more precise anatomic localization of cancer tissues during resection would be crucial for the success of any oncological surgery and decisive in maximizing the benefits for patients [2–4].

The implementation of FGS requires the development of more accurate and sensitive imaging devices and of an effective fluorescence contrast agent [5,6]. Among different probes that may assist this technique, indocyanine green (ICG) is one of the most used and well known [1,7–9], despite other near-infrared (NIR) fluorophores being approved by the Food and Drug Administration (FDA), including Methylene Blue, 5-Aminolevulinic acid (5-ALA), and Fluorescein, which are also suitable for FGS applications but are much less frequently employed [10,11].

ICG is a tricarbocyanine, water-soluble fluorescent dye with substantial fluorescence emission in the near-infrared (NIR) wavelength region (700–900 nm) [8,12–14]. Due to its fluorescent characteristics and safety, ICG is currently used for several cancer-related surgical applications, including sentinel lymph node (SLN) mapping, the identification of

solid tumors, lymphography, angiography, and anatomical imaging during surgery [14–18]. However, since it lacks specific tumor targeting and suffers from rapid degradation and blood-stream elimination [19,20], the potential for its use in oncological FGS still has certain limitations [3,21,22].

ICG is a passive tumor-targeted probe and its performance in ensuring the unambiguous identification of cancer tissue is still modest and insufficient in providing a trustworthy exploitation of this technique [1]. Therefore, most research focuses on designing nanocarriers as delivery systems for ICG with the aim of tackling some of its current issues and to expand its possible applications in cancer diagnosis and treatment [22,23]. Hence, the overall goal would be to develop systems with high specificity for tumors able to provide enhanced contrast between cancer tissues or affected lymph nodes and healthy tissue, in order to tailor specific surgeries [22,24,25].

In the last 15 years, several studies have been carried out using ferritin bionanoparticles [26]. These nanoparticles, thanks to their protein nature, show an excellent biocompatibility profile, great solubility in biological fluids and good stability at high temperatures and in the presence of denaturing agents [27,28]. H-Ferritin (HF<sub>n</sub>) nanoparticles appear as cave spheres consisting of 24 monomers of human ferritin H chains with an external diameter of 12 nm.

They demonstrate a natural homing toward cancer cells due to the specific recognition of the transferrin receptor-1 (TfR1), which is overexpressed in all tumor subtypes and represents a universal molecule for tumor targeting as its expression in cancer is higher than that seen in other healthy cells [29–31]. Their physiological features and their capacity to encapsulate drugs or fluorescent probes, makes ferritin nanocages ideal platforms for oncological applications, such as drug delivery and diagnostics [32].

Several HF<sub>n</sub>-based nanodrugs have been proposed for drug delivery with excellent results in terms of specific tumor recognition and increased activity with lower side effects [33–35]; however, ferritin nanoparticles suggested for diagnostic purposes are restricted to magnetic resonance imaging [27,32,36] and there are only a few examples of optical imaging applications [37] that do not include FGS or ICG exploitation. In light of this, we have proposed ICG loaded HF<sub>n</sub> nanocages as an *in vivo* system for FGS that will allow the surgeon to perform a more accurate surgical resection of the tumor with the ultimate goal of improving surgical outcomes [38].

Preliminary studies have demonstrated *in vitro* the tumor-targeted recognition of ICG upon nanoformulation in HF<sub>n</sub> nanocages. These studies have demonstrated that nanoformulation also affects the fluorescence stability, improving it, and resulting in better fluorescence signal in tumors [38]. Here, we performed an *ex vivo* analysis of HF<sub>n</sub>-ICG tumor accumulation and biodistribution to better elucidate the differences in ICG behavior *in vivo* upon nanoformulation.

## 2. Results and Discussion

### 2.1. HF<sub>n</sub>-ICG Displayed a Higher Intratumor Accumulation Compared to Free ICG

To further study the suitability of HF<sub>n</sub>-ICG as tumor-targeted nanotracer for *in vivo* image-guided surgery [38], we decided to perform an *ex vivo* study on a syngeneic orthotopic murine model of breast cancer. Starting from the *in vivo* pilot experiment that provided evidence regarding the potential of HF<sub>n</sub>-ICG to target the tumor mass [38], in this study, we evaluated the tumor accumulation and the biodistribution of both free and nano-formulated ICG *ex vivo* with the aim to demonstrate the improved performances and the potential of HF<sub>n</sub>-ICG as a nano-tracer for fluorescence tumor detection.

HF<sub>n</sub> displayed natural tumor homing due to its capability to specifically bind the transferrin 1 receptor (TfR1) and be internalized through receptor-mediated endocytosis. These features have been fully explored in tumor-targeted drug delivery, using HF<sub>n</sub> to treat different kinds of cancers. Many drugs have been encapsulated and tested, including Olaparib, Everolimus, Cis-Platinum, Curcumin, and Mitoxantrone [26,39–43], and the most interesting results were obtained with doxorubicin [33–35,44–46].

Despite the HF<sub>n</sub>-based nanosystems being applied to cancer detection were well studied with positron emission tomography application, magnetic resonance, and multimodal imaging, their application in fluorescence image-guided surgery is almost unexplored [38]. We used a model of murine breast cancer, obtained by the injection of 4T1 cells into the mammary fat pad of *Balb/C* female mice. Tumor-bearing mice were divided into two experimental groups and injected with 3.8 mg/kg of free ICG or nano-formulated ICG.

After 6 and 24 h mice were sacrificed, the tumors were collected and imaged by the KARL STORZ NIR/ICG endoscopic system, as reported in Video S1–S5.

This represents one of the main systems used in *in vivo* surgery and allowed us to really test the suitability of our nanoconstruct. As shown in Figure 1a, an intense blue fluorescent signal was localized in the tumor mass of mice treated with HF<sub>n</sub>-ICG at 6 h, while mice injected with ICG displayed a barely noticeable signal, more similar to a dark blue shade. At 24 h after injection, the tumors harvested from mice treated with HF<sub>n</sub>-ICG showed a fluorescent signal lower than the one detected at 6 h but still evident, while, in the group injected with free ICG, the fluorescence signal was hardly visible (Supplementary Material, video S2–S4).



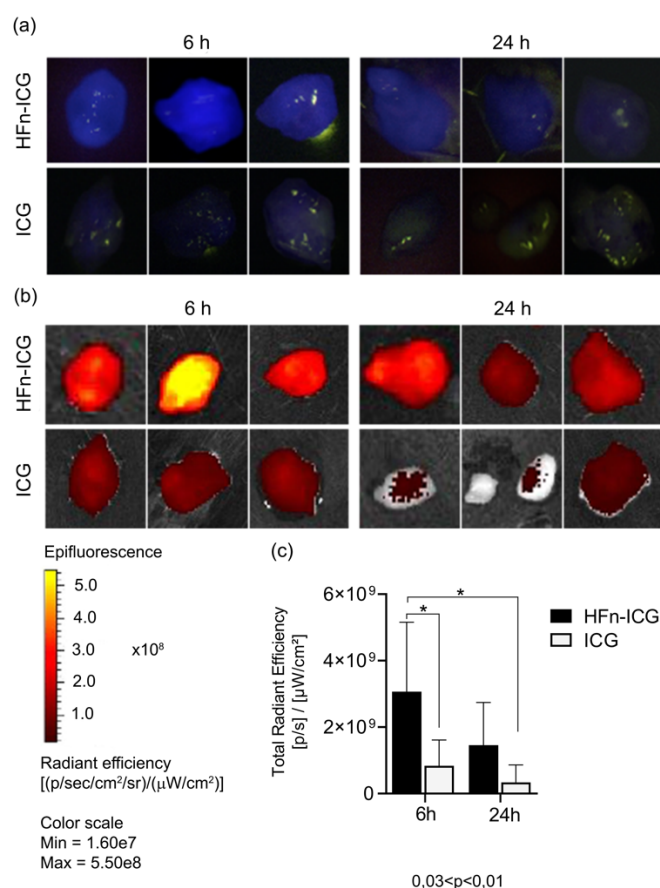


**Figure 1.** The tumor targeting of H-Ferritin (HFn)–indocyanine green (ICG) and free ICG was evaluated in 4T1 tumor-bearing mice, 6 and 24 h after intravenous administration with a KARL STORZ near-infrared (NIR)/ICG endoscopic system ((a), blue signal) and a IVIS Lumina II system (b). In (a,b) images of three representative tumors of each group are shown. Imaging analysis of data obtained by IVIS Lumina II allowed us to quantify the dye in the tumor (c). The fluorescence was higher in HFn–ICG-treated mice than in free ICG-treated mice at both 6 and 24 h. There is a statistical significance between HFn–ICG and free ICG at 6 h ( $p$ -value = 0.0345) and between HFn–ICG at 6 h and free ICG detected at 24 h ( $p$ -value = 0.0112). Color scale expressed as the total radiant efficiency ( $\times 10^8$ ),  $n = 6$ . \*  $p < 0.05$ .

To confirm and obtain a quantitative analysis of these observations, we coupled the imaging from the KARL STORZ NIR/ICG endoscopic system to the imaging performed by the IVIS Lumina II system, which allowed us also to quantify the fluorescence due to the software for analysis. The IVIS lumina II acquisitions corroborated that the HFn-ICG tumor accumulation at 6 h was still visible at 24 h, while the free ICG did not accumulate and was rapidly cleared (Figure 1b,c). Indeed, there was a significant difference in the levels of fluorescence between HFn-ICG and free ICG at 6 h as well as with ICG at 24 h. Therefore, in mice injected with HFn-ICG it was possible to detect a higher fluorescence signal compared to the signal visible at 6 h for free ICG.

## 2.2. HFn Encapsulation Improves Tumor Uptake of ICG

To assess if the higher accumulation in cancer was really due to improved HFn-ICG performances related to a better uptake of the ICG, we performed a histological evaluation of tumors collected at 6 and 24 h from both groups to localize the signal. We obtained confocal microscopy images of the tumor (Figure 2), where the red signal associated with ICG was higher in samples treated with the nanoformulation and showed a different distribution compared to that observed with free ICG both at 6 and at 24 h.

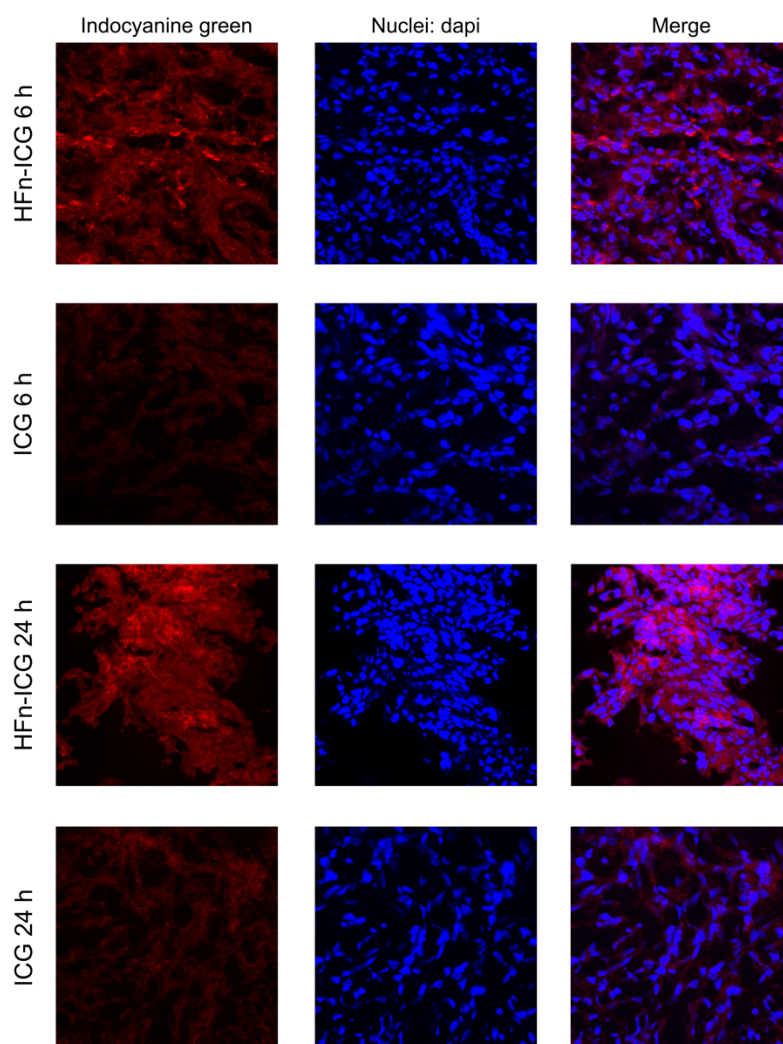


**Figure 2.** Confocal images of tumor cryosections collected from mice injected with HFn-ICG or free ICG (red) and sacrificed at 6 and 24 h. Nuclei were stained with 4',6-Diamidino-2-phenylindole dihydrochloride (dapi; blue). Scale bar = 50  $\mu$ m.

Different to the dotted distribution of intracellular HFn-ICG that is due to the vesicle-mediated uptake mechanism, as demonstrated by the colocalization between the ICG signal and TfR1 reported in Figure 3, the uptake pattern observed for free ICG was less intense and specific (Figures 2 and 3). This might be due to the specific and low uptake of free ICG in cancer cells and to a fast degradation of the molecule that leads to a fluorescence loss. In light of this, HFn encapsulation could significantly improve the intracellular uptake of ICG and preserve its fluorescence, as already previously suggested [38], therefore ensuring a more precise identification of the tumor.



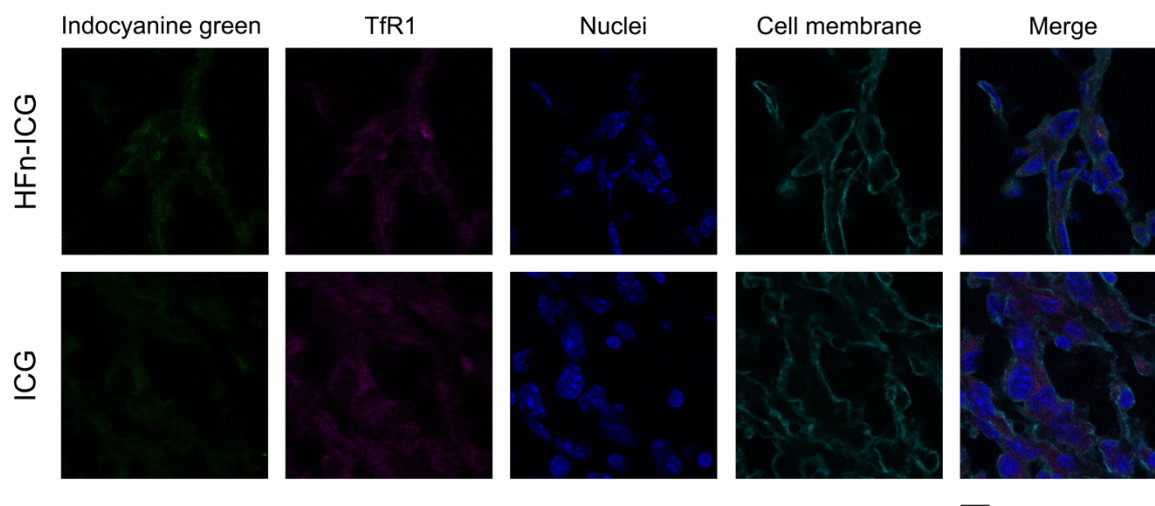


**Figure 3.** Colocalization between the transferrin receptor-1 (TfR1) receptor and ICG upon HFn-mediated internalization. Tumors collected from mice injected with HFn-ICG or free ICG (green) and sacrificed at 6 h, were cryosectioned and labelled to study the colocalization with TfR1 (purple). Nuclei and cell membranes were stained with dapi (blue) and Wheat Germ Agglutinin-Alexa Fluor 488 (cyan), respectively. Scale bar = 10  $\mu$ m.

### 2.3. HFn Encapsulation Markedly Improved the ICG Kinetics of Biodistribution

As previously described with the tumor analysis, the major organs were also examined by the KARL STORZ NIR/ICG endoscopic system to evaluate the off-target biodistribution of fluorescence in each district (Figure 4a). In this case, there was also a significant difference between the mice injected with HFn-ICG and free ICG. HFn-ICG was detectable at 6 h in the tumor (Figure 1a, blue signal) and also at the liver, kidneys, and at the gastrointestinal tract. Additionally, even with a lower intensity, it is observed at the axillary lymph nodes, heart, and lungs.

This biodistribution profile is consistent with the ICG metabolism. This occurs in the liver, where it is accumulated into bile salts and released in the intestines, allowing its excretion with feces. As expected, when ICG is administered as a free dye it is rapidly metabolized. A weak fluorescence signal was observed at 6 h in the liver and in the last part of the intestinal tract. At 24 h after injection, there was a noticeable decrease in the fluorescence levels compared to the 6 h time point. However, in the organs from mice injected with free ICG, there was an almost complete washout of the dye, while in those from mice injected with HFn-ICG, the fluorescence signal (blue) was still present in the liver, kidneys, stomach, and in the distal part of the gut, in addition to the already discussed accumulation at the tumor (Figure 1a).

While the detection of the ICG signal in the gut, liver, and kidneys was consistent with its metabolism, the signal in the stomach was surprising, as the HFn-ICG was administered by parenteral injection. However, the reason was easily attributable to the sphincter relaxation occurring upon sacrifice that allowed the diffusion of ICG-rich bile salts into the stomach. These results overall suggested the crucial role of the HFn nanocage in protecting ICG from rapid metabolism and degradation, which instead represents the destiny of the free dye.

Figure 4b shows an overview of the distribution of the signal associated with ICG in the same organs observed in Figure 4a. These representative imaging scans performed by the IVIS Lumina II reflect what is reported by Figure 4a and the analysis of the imaging scans described in Figure 5 reveal a striking difference between the two formulations in terms of the kinetics of biodistribution. ICG is rapidly metabolized and it was unable to accumulate specifically at any organ.

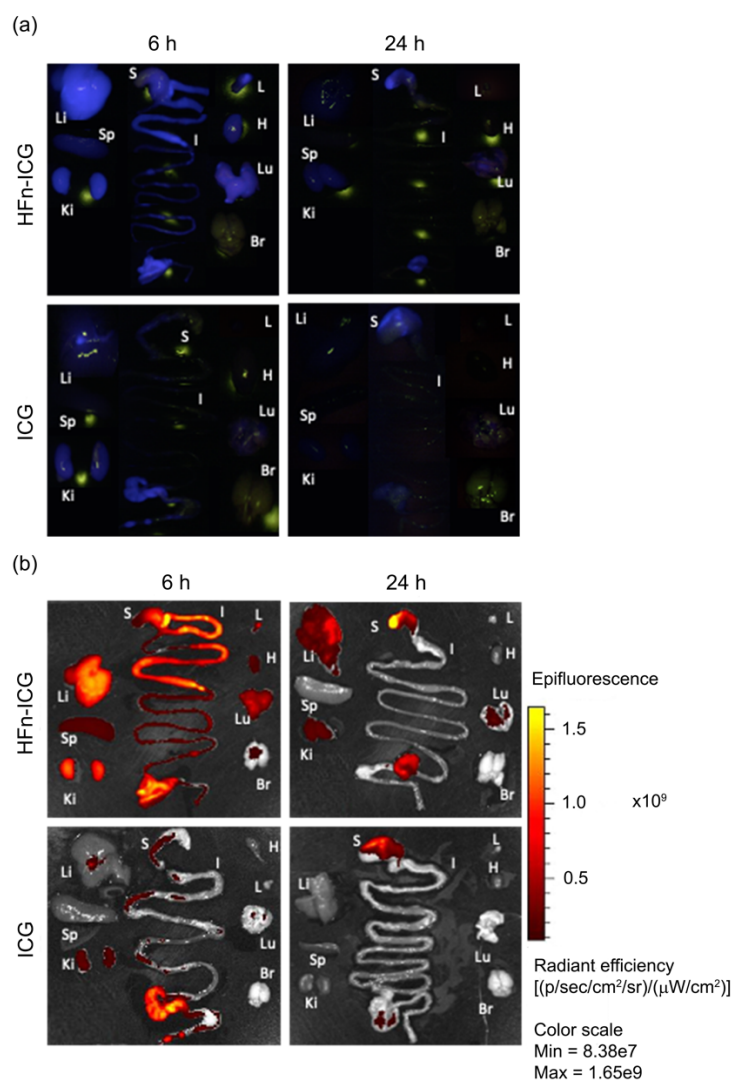


**Figure 4.** Representative images of organs collected from tumor-bearing mice, 6 and 24 h after I.V. administration of HFn-ICG and free ICG obtained with the KARL STORZ NIR/ICG endoscopic system (a, blue signal) and IVIS Lumina II system (b). In each panel, it is possible to observe the following organs: Liver (Li), Spleen (Sp), Kidneys (Ki), Stomach (S), Intestine (I), Lymph node (L), Heart (H), Lung (Lu), and Brain (Br)). Color scale expressed as the total radiant efficiency ( $\times 10^9$ ).

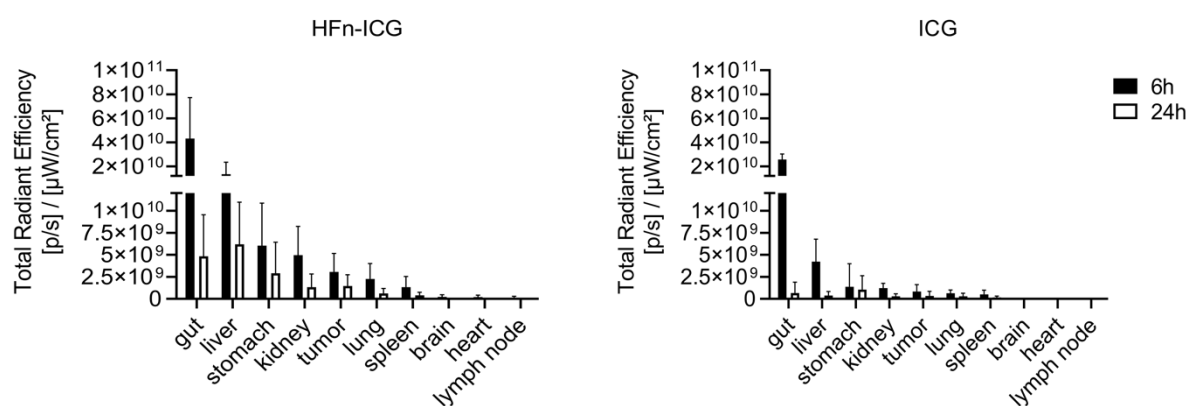


**Figure 5.** Imaging analysis of data obtained by IVIS Lumina II allowed us to quantify the signal associated with ICG by drawing regions of interest (ROIs) around each of the individual tissues. The histograms show the mean value measured in each organ of the mice treated with HFn-ICG (left panel) and with free ICG (right panel) and sacrificed 6 and 24 h after the injection. The bars are the mean value  $\pm$  standard deviation (SD),  $n = 6$ .

At 6 h, as previously mentioned, when administered as a free dye, ICG was found in the liver and the gut but was then promptly excreted as no fluorescent signal is visible at either location at 24 h. On the contrary, HF<sub>n</sub>-ICG allowed us to detect higher signals in all the organs and appeared to preserve the dye's fluorescence up to 24 h in the gut, liver, stomach, and at the tumor, which is our focus.

In Figure 6, we report the quantification of the signal for each individual organ. The gut, which exhibited the highest signal compared to the other organs, displayed, at 6 h, an accumulation of ICG comparable between the two formulations. Afterward, in both groups, there was a progressive decay of the signal. However, in mice treated with HF<sub>n</sub>-ICG, the presence of the dye was persistent at 24 h. The fluorescence signal in the gut was not located in the intestinal wall but was only restricted to the chyle, and then to the feces. In the liver, it was possible to see an accumulation of the signal in favor of HF<sub>n</sub>-ICG still visible at the last time point and more intense compared to the free ICG.

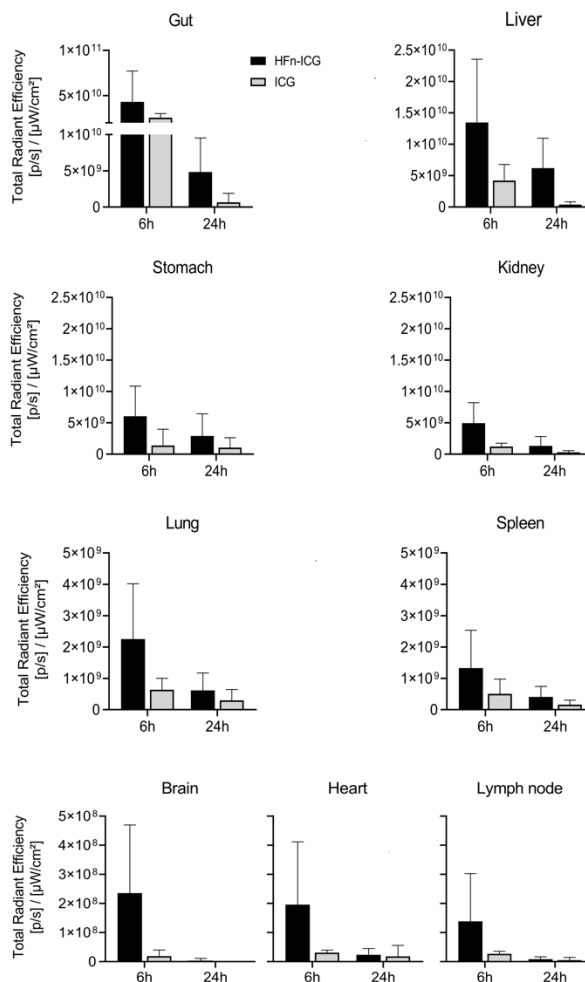


**Figure 6.** Imaging analysis of the ICG signal obtained by IVIS Lumina II and associated to different organs. Quantification of the signal associated with ICG was performed by drawing ROIs around each of the individual tissues. The histograms show the mean value measured in each organ of mice treated with HF<sub>n</sub>-ICG (left panel) and with free ICG (right panel) and sacrificed 6 and 24 h after the injection. The bars are the mean value  $\pm$  SD,  $n = 6$ .

Presumably, ICG, which has a quicker clearance, accumulated in the liver at an earlier time and, at 6 h, was already completely excreted into the bile (Figure 6). The fluorescence intensity registered in the stomach had a similar trend to that in the kidney in both groups. The fluorescence signal appeared attenuated at 24 h for HF<sub>n</sub>-ICG, while it was visible at lower levels for ICG even at 6 h. With regard to the lungs, spleen, brain, heart, and axillary lymph nodes, the signal was far lower, with an order of magnitude of  $10^8$ – $10^9$ , compared to the fluorescence at the gut, liver, stomach, and kidney ( $10^{10}$ – $10^{11}$ ).

The fluorescence signal of HF<sub>n</sub>-ICG was higher compared to the free ICG at each time point in every organ of this second group. In the brain, heart, and lymph nodes, the fluorescence of ICG was hardly observable. Overall, the ability of targeting the tumor mass with improved fluorescence accumulation in tumor, as confirmed by this ex vivo study, makes HF<sub>n</sub>-ICG a powerful system for the delivery of ICG. Further studies with mass spectrometry should be performed to elucidate if the increased fluorescence signal observed in cancer tissue and also in off-target organs is due to a better profile of the biodistribution or to the increased stability of the fluorescence signal acquired upon nanoformulation.

### 3. Materials and Methods

#### 3.1. Development of ICG-Loaded-HFn Nanoparticles

HFn was purchased from MoLiRom s.r.l. (Rome, Italy). The ICG was nano-formulated exploiting the ability of HFn to disassemble and reassemble its quaternary structure in response to changes in the pH, as previously reported [38].

#### 3.2. Animals

The animals were managed according to procedures approved by the Italian Ministry of Health (Protocol Number 611/2019-PR, 6 August 2019). All procedures involving animals and their health were conducted in accordance with the 3R principles to minimize the number of mice used and their collateral suffering. The animals were housed in specific pathogen-free conditions and were kept in cages with free access to water and food.

#### 3.3. Tumor Targeting and Biodistribution

For the biodistribution studies, we recruited six animals for each experimental time point. Seven-week-old female BALB/c mice were injected into the mammary fat pad with 100,000 4T1-Luc cells (Bioware Ultra, PerkinElmer, Waltham, MA, USA). After 21 days, the mice were intravenously injected in the tail vein with ICG or HFn-ICG at a concentration of 3.8 mg/Kg. Subsequently, the mice were sacrificed by cervical dislocation at 6 or 24 h to follow the biodistribution of the two administered formulations. Immediately after the sacrifice, we performed an accurate autopsy by means of the KARL STORZ NIR/ICG endoscopic system (OPAL1 Technology, equipped with a high-end full HD camera IMAGE 1 SPIES and a xenon light source D-light P SCB; KARL STORZ GmbH & Co. KG, Tuttlingen, Germany).

This allowed us to detect the fluorescent signal observable in blue at the tumor site and in terms of the organ distribution. The tumor and the major organs, i.e., the liver, stomach, gut, kidneys, spleen, heart, lung, brain, and lymph nodes were collected and imaged with an IVIS Lumina II imaging system (PerkinElmer, Waltham, MA, USA). Ex vivo scans of organs were performed with the following acquisition parameters: Excitation filter: 745 nm, emission filter: ICG, exposure time: 2 s, binning factor: Medium, f/Stop: 2, Field of View: D.

The Living Image Software 4.3.1 (Perkin Elmer, Waltham, MA, USA) conjugated with the Image Math tool was used to separate the ICG signal from the tissue autofluorescence, image processing, and fluorescence signal quantification analysis. In detail, the Image Math tool offered together with Living Image® 4.3.1 software allowed the subtraction of the tissue autofluorescence background from the signal. Due to the acquisition of an imaging scan with a background filter (i.e., green fluorescent protein filter), it was possible to separate the ICG signal from the tissue autofluorescence and perform the correct image processing and quantification. Tables reporting Signal to noise (SNR) and Signal to Background (SBR) ratios have been provided as Supplementary Material (Tables S1 and S2, respectively).

Finally, all the tumors were frozen at  $-80^{\circ}\text{C}$  for cryosectioning and histological analysis.

#### 3.4. Confocal Laser Scanning Microscopy

Cryosections of  $9\ \mu\text{m}$  were obtained from each 4T1 tumor and, after adhesion in glass slides, were counterstained with  $0.2\ \mu\text{g}/\text{mL}$  dapi ( $4^{\circ},6$ -diamino-2-phenylindole; Thermo Fisher Scientific Inc., Waltham, MA, USA) for 10 min at room temperature, washed thrice, and mounted with Prolong Gold (Life technology; #P10144, Thermo Fisher Scientific Inc., Waltham, MA, USA). Microscopy analyses of cryosections were performed with a Leica SP8 microscope confocal system equipped with lasers at 405, 488, 513, and 633 nm (Leica, Wetzlar, Germany). Tumor images were acquired at a  $512 \times 512$  pixel resolution using a  $63\times$  immersion oil lens.

To assess the colocalization between nanoformulated ICG and Tfr1, we labelled the tumor cryosection as follows. The cryosections were air dried at room temperature (RT) for 15 min, rinsed with phosphate saline buffer (PBS), and fixed for 5 min with 2% paraformaldehyde (Sigma-Aldrich, Merck Life Science, Milano, Italy). They were then permeabilized for 10 min at RT with 0.1% Triton X-100 (Sigma-Aldrich, Merck Life Science, Saint Louis, MO, USA) in PBS. Afterward, the samples were incubated for 1 h at RT with a solution containing 2% Bovine Serum Albumin (BSA; Sigma-Aldrich, Merck Life Science, Saint Louis, MO, USA) and 2% goat serum (Euroclone, Pero, Italy) in PBS. Tfr1 labelling was performed with the anti-Tfr1 antibody (1:200; ab84036; Abcam, Cambridge, UK) by overnight incubation at  $4^{\circ}\text{C}$ .

After three washes in PBS, the anti-Tfr1 antibody was recognized by Alexa Fluor 488-conjugated antibody against rabbit Immunoglobulins G (IgGs; Thermo Fisher Scientific Inc., Waltham, MA, USA) at a 1:300 dilution by incubating for 2 h at RT in PBS, 2% BSA, 2% goat serum, and  $0.2\ \mu\text{g}/\text{mL}$  dapi ( $4^{\circ},6$ -diamino-2-phenylindole; Thermo Fisher Scientific Inc., Waltham, MA, USA). Finally, the samples were counterstained with wheat germ agglutinin and Alexa Fluor™ 488 Conjugate incubating for 1 h at RT in PBS (1:200; W11261; Thermo Fisher Scientific Inc., Waltham, MA, USA) for visualization of the cell membranes. A single plane image of the tumor section was acquired at a  $512 \times 512$  pixel resolution using a  $63\times$  immersion oil lens and applying a digital zoom of three times.

### 3.5. Statistical Analysis

All data were expressed as the mean  $\pm$  SD. Student's *t*-test and the *p* values were evaluated using the GraphPad Prism version 6.00 for Windows (Graph-Pad Software, San Diego, CA, USA). The sample size was calculated referring to [47], using the Power and Sample Size Calculator program with a statistical power of 80% and an alpha error of 5% calculated.

## 4. Conclusions

Intraoperative visualization of tumors by means of fluorescence-guided surgery (FGS) may not only allow more accurate tumor resections but also improve safety by reducing unnecessary damage to normal tissues with benefits for both the surgeons and cancer patients. Therefore, practical methods for improving the surgeon's ability to resect tumors are needed. Here, we provided a strict comparison in terms of the tumor accumulation, off-target biodistribution and kinetics of clearance prodromic to in vivo assess tracking capability of HFn-ICG. These results support the suitability of HFn-ICG for the FGS application; however, our future endeavors will be focused on the improvement of the HFn circulation time in order to maximize its capability to localize at a tumor for longer to thereby allow its application in other kinds of tumors.

**Supplementary Materials:** Supplementary materials can be found at <https://www.mdpi.com/14-22-0067/22/4/1601/s1>. Video S1. Non-treated mouse imaged by the KARL STORZ NIR/ICG endoscopic system. The ICG signal is absent, and the tissue autofluorescence is evidenced by green light. Video S2. Mouse injected with HFn-ICG and imaged after 24 h by the KARL STORZ NIR/ICG endoscopic system in vivo. This video displays how the fluorescent signal of ICG, visible in blue, allowed us to easily detect the tumor mass and was clearly distinguishable from the background, which is visualized in green. Video S3. Mouse injected with HFn-ICG and imaged after 24 h by the KARL STORZ NIR/ICG endoscopic system during the surgical intervention. Here, it is possible to observe the labelled tumor mass during the surgical intervention. The tumor mass is clearly distinguishable from the surrounding tissue. Video S4. Mouse injected with free ICG and imaged after 24 h by the KARL STORZ NIR/ICG endoscopic system during the surgical intervention. Here, it is possible to observe the labelled tumor mass during the surgery. The tumor mass of the mouse injected with free ICG does not appear as fluorescent. Video S5. Mouse injected with HFn-ICG and imaged after 2 h by the KARL STORZ NIR/ICG endoscopic system. Here, it is possible to see the ICG signal before the achievement of complete organ distribution. Indeed, until 2 h after injection, the ICG, free or nanoformulated, is mainly present in the bloodstream, resulting in a blurred visualization of the anatomical compartments. Table S1. SNR obtained from the ratio between the mean total radiant efficiency of signal acquired with ICG filter and the mean total radiant efficiency of signal acquired with GFP filter ( $n = 6$ ). Table S2. SBR obtained from the ratio between the mean total radiant efficiency of signal acquired with ICG filter in a ROI drawn on target organ and the mean total radiant efficiency of signal acquired with ICG filter in a ROI drawn on background ( $n = 6$ ).

**Author Contributions:** Conceptualization, S.M. and F.C.; investigation, S.M., M.S., L.S. and A.B.; writing—original draft preparation, M.S. and S.M.; writing—review and editing, M.T. and F.C.; supervision, F.C. and S.M.; funding acquisition, F.C. All authors have read and agreed to the published version of the manuscript.

**Funding:** This research received no external funding. The APC was funded by University of Milan.

**Institutional Review Board Statement:** The study was conducted according to the guidelines of the Declaration of Helsinki, and approved by the Italian Ministry of Health (611/2019-PR, approved on 6th August 2019).

**Informed Consent Statement:** Not applicable.

**Data Availability Statement:** Data available in a publicly accessible repository [https://doi.org/10.13130/RD\\_UNIMI/ZKBQFS](https://doi.org/10.13130/RD_UNIMI/ZKBQFS), after publication.

**Acknowledgments:** We thank KARL STORZ GmbH & Co for the complimentary use of the NIR/ICG endoscopic system, Diego Foschi (University of Milan) for the helpful discussion, the Pediatric Clinical Research Center "Romeo and Enrica Invernizzi" at the University of Milan for S.M. position and for the imaging facility, and the University of Milan for L.S.'s post-doctoral position and the PhD fellowships of M.S. and A.B.

**Conflicts of Interest:** The authors declare no conflict of interest.

### Abbreviations

ICG	Indocyanine Green
HFn	H-Ferritin
HFn-ICG	H-Ferritin loaded with ICG
FGS	Fluorescence-guided surgery
FDA	Food and Drug Administration
NIR	Near-infrared
SLN	Sentinel lymph node
TfR1	Transferrin receptor 1



DAPI	4',6-Diamidino-2-phenylindole dihydrochloride
ROI	Region of interest
SD	Standard deviation
PBS	Phosphate saline buffer
BSA	Bovine serum albumin
IgG	Immunoglobulin G
SNR	Signal to noise ratio
SBR	Signal to background ratio

## References

- Zheng, Y.; Yang, H.; Wang, H.; Kang, K.; Zhang, W.; Ma, G.; Du, S. Fluorescence-guided surgery in cancer treatment: Current status and future perspectives. *Ann. Transl. Med.* **2019**, *7*, S6. [[CrossRef](#)] [[PubMed](#)]
- Tringale, K.R.; Pang, J.; Nguyen, Q.T. Image-guided surgery in cancer: A strategy to reduce incidence of positive surgical margins. *WIREs Syst. Biol. Med.* **2018**, *10*, e1412. [[CrossRef](#)]
- Mondal, S.B.; Gao, S.; Zhu, N.; Liang, R.; Gruev, V.; Achilefu, S. Real-time fluorescence image-guided oncologic surgery. In *Advances in Cancer Research*; Elsevier: Amsterdam, The Netherlands, 2014; Volume 124, pp. 171–211, ISBN 978-0-12-411638-2.
- Sorrentino, L.; Sartani, A.; Pietropaolo, G.; Bossi, D.; Mazzucchelli, S.; Truffi, M.; Foschi, D.; Corsi, F. A novel indocyanine green fluorescence-guided video-assisted technique for sentinel node biopsy in breast cancer. *World J. Surg.* **2018**, *42*, 2815–2824. [[CrossRef](#)]
- Okusanya, O.T.; Madajewski, B.; Segal, E.; Judy, B.F.; Venegas, O.G.; Judy, R.P.; Quatromoni, J.G.; Wang, M.D.; Nie, S.; Singhal, S. Small portable interchangeable imager of fluorescence for fluorescence guided surgery and research. *Technol. Cancer Res. Treat.* **2015**, *14*, 213–220. [[CrossRef](#)]
- Chi, C.; Du, Y.; Ye, J.; Kou, D.; Qiu, J.; Wang, J.; Tian, J.; Chen, X. Intraoperative imaging-guided cancer surgery: From current fluorescence molecular imaging methods to future multi-modality imaging technology. *Theranostics* **2014**, *4*, 1072–1084. [[CrossRef](#)] [[PubMed](#)]
- Alander, J.T.; Kaartinen, I.; Laakso, A.; Pätälä, T.; Spillmann, T.; Tuchin, V.V.; Venermo, M.; Välisuo, P. A review of indocyanine green fluorescent imaging in surgery. *Int. J. Biomed. Imaging* **2012**, *2012*, 1–26. [[CrossRef](#)]
- Schaafsma, B.E.; Mieog, J.S.D.; Hutteman, M.; van der Vorst, J.R.; Kuppen, P.J.K.; Löwik, C.W.G.M.; Frangioni, J.V.; van de Velde, C.J.H.; Vahrmeijer, A.L. The clinical use of indocyanine green as a near-infrared fluorescent contrast agent for image-guided oncologic surgery. *J. Surg. Oncol.* **2011**, *104*, 323–332. [[CrossRef](#)]
- DSouza, A.V.; Lin, H.; Henderson, E.R.; Samkoe, K.S.; Pogue, B.W. Review of fluorescence guided surgery systems: Identification of key performance capabilities beyond indocyanine green imaging. *J. Biomed. Opt.* **2016**, *21*, 80901. [[CrossRef](#)] [[PubMed](#)]
- Barth, C.W.; Gibbs, S. Fluorescence image-guided surgery: A perspective on contrast agent development. *Proc. SPIE* **2020**, 11222. [[CrossRef](#)]
- Low, P.S.; Singhal, S.; Srinivasarao, M. Fluorescence-guided surgery of cancer: Applications, tools and perspectives. *Curr. Opin. Chem. Biol.* **2018**, *45*, 64–72. [[CrossRef](#)]
- Hill, T.K.; Abdulahad, A.; Kelkar, S.S.; Marini, F.C.; Long, T.E.; Provenzale, J.M.; Mohs, A.M. Indocyanine green-loaded nanoparticles for image-guided tumor surgery. *Bioconjugate Chem.* **2015**, *26*, 294–303. [[CrossRef](#)] [[PubMed](#)]
- Zhao, P.; Zheng, M.; Yue, C.; Luo, Z.; Gong, P.; Gao, G.; Sheng, Z.; Zheng, C.; Cai, L. Improving drug accumulation and photothermal efficacy in tumor depending on size of ICG loaded lipid-polymer nanoparticles. *Biomaterials* **2014**, *35*, 6037–6046. [[CrossRef](#)]
- Nagaya, T.; Nakamura, Y.A.; Choyke, P.L.; Kobayashi, H. Fluorescence-guided surgery. *Front. Oncol.* **2017**, *7*, 314. [[CrossRef](#)]
- Muhanna, N.; Chan, H.H.L.; Douglas, C.M.; Daly, M.J.; Jaidka, A.; Eu, D.; Bernstein, J.; Townson, J.L.; Irish, J.C. Sentinel lymph node mapping using ICG fluorescence and cone beam CT—A feasibility study in a rabbit model of oral cancer. *BMC Med. Imaging* **2020**, *20*, 106. [[CrossRef](#)] [[PubMed](#)]
- Starosolski, Z.; Bhavane, R.; Ghaghada, K.B.; Vasudevan, S.A.; Kaay, A.; Annapragada, A. Indocyanine green fluorescence in second near-infrared (NIR-II) window. *PLoS ONE* **2017**, *12*, e0187563. [[CrossRef](#)]
- Alius, C.; Oprescu, S.; Balalau, C.; Elena Nica, A. Indocyanine green enhanced surgery; principle, clinical applications and future research directions. *J. Clin. Investig. Surg.* **2018**, *3*, 1–8. [[CrossRef](#)]
- Verbeek, F.P.R.; Troyan, S.L.; Mieog, J.S.D.; Liefers, G.-J.; Moffitt, L.A.; Rosenberg, M.; Hirshfield-Bartek, J.; Gioux, S.; van de Velde, C.J.H.; Vahrmeijer, A.L.; et al. Near-infrared fluorescence sentinel lymph node mapping in breast cancer: A multicenter experience. *Breast Cancer Res. Treat.* **2014**, *143*, 333–342. [[CrossRef](#)]
- Saxena, V.; Sadoqi, M.; Shao, J. Degradation kinetics of indocyanine green in aqueous solution. *J. Pharm. Sci.* **2003**, *92*, 2090–2097. [[CrossRef](#)]
- Muckle, T.J. Plasma proteins binding of indocyanine green. *Biochem. Med.* **1976**, *15*, 17–21. [[CrossRef](#)]
- Veys, I.; Pop, C.-F.; Barbieux, R.; Moreau, M.; Noterman, D.; De Neubourg, F.; Nogaret, J.-M.; Liberale, G.; Larsimont, D.; Bourgeois, P. ICG fluorescence imaging as a new tool for optimization of pathological evaluation in breast cancer tumors after neoadjuvant chemotherapy. *PLoS ONE* **2018**, *13*, e0197857. [[CrossRef](#)]

22. Wang, H.; Li, X.; Tse, B.W.-C.; Yang, H.; Thorling, C.A.; Liu, Y.; Touraud, M.; Chouane, J.B.; Liu, X.; Roberts, M.S.; et al. Indocyanine green-incorporating nanoparticles for cancer theranostics. *Theranostics* **2018**, *8*, 1227–1242. [[CrossRef](#)]
23. Sevieri, M.; Silva, F.; Bonizzi, A.; Sitia, L.; Truffi, M.; Mazzucchelli, S.; Corsi, F. Indocyanine green nanoparticles: Are they compelling for cancer treatment? *Front. Chem.* **2020**, *8*, 535. [[CrossRef](#)]
24. Eglhoff-Juras, C.; Bezdetsnaya, L.; Dolivet, G.; Lassalle, H.-P. NIR fluorescence-guided tumor surgery: New strategies for the use of indocyanine green. *IJN* **2019**, *14*, 7823–7838. [[CrossRef](#)] [[PubMed](#)]
25. Xi, L.; Jiang, H. Image-guided surgery using multimodality strategy and molecular probes: Image-guided surgery using multimodality strategy and molecular probes. *WIREs Nanomed. Nanobiotechnol.* **2016**, *8*, 46–60. [[CrossRef](#)] [[PubMed](#)]
26. Truffi, M.; Fiandra, L.; Sorrentino, L.; Monieri, M.; Corsi, F.; Mazzucchelli, S. Ferritin nanocages: A biological platform for drug delivery, imaging and theranostics in cancer. *Pharmacol. Res.* **2016**, *107*, 57–65. [[CrossRef](#)]
27. Wang, Z.; Gao, H.; Zhang, Y.; Liu, G.; Niu, G.; Chen, X. Functional ferritin nanoparticles for biomedical applications. *Front. Chem. Sci. Eng.* **2017**, *11*, 633–646. [[CrossRef](#)] [[PubMed](#)]
28. Lee, B.-R.; Ko, H.K.; Ryu, J.H.; Ahn, K.Y.; Lee, Y.-H.; Oh, S.J.; Na, J.H.; Kim, T.W.; Byun, Y.; Kwon, I.C.; et al. Engineered human ferritin nanoparticles for direct delivery of tumor antigens to lymph node and cancer immunotherapy. *Sci. Rep.* **2016**, *6*, 35182. [[CrossRef](#)] [[PubMed](#)]
29. Li, L.; Fang, C.J.; Ryan, J.C.; Niemi, E.C.; Lebrón, J.A.; Björkman, P.J.; Arase, H.; Torti, F.M.; Torti, S.V.; Nakamura, M.C.; et al. Binding and uptake of H-ferritin are mediated by human transferrin receptor-1. *Proc. Natl. Acad. Sci. USA* **2010**, *107*, 3505–3510. [[CrossRef](#)]
30. Fan, K.; Cao, C.; Pan, Y.; Lu, D.; Yang, D.; Feng, J.; Song, L.; Liang, M.; Yan, X. Magnetoferritin nanoparticles for targeting and visualizing tumour tissues. *Nat. Nanotechnol.* **2012**, *7*, 459–464. [[CrossRef](#)]
31. Cheng, X.; Fan, K.; Wang, L.; Ying, X.; Sanders, A.J.; Guo, T.; Xing, X.; Zhou, M.; Du, H.; Hu, Y.; et al. TfR1 binding with H-ferritin nanocarrier achieves prognostic diagnosis and enhances the therapeutic efficacy in clinical gastric cancer. *Cell Death Dis.* **2020**, *11*, 92. [[CrossRef](#)]
32. Fan, K.; Yan, X. Bioengineered ferritin nanoprobe for cancer theranostics. In *Handbook of Nanomaterials for Cancer Theranostics*; Elsevier: Amsterdam, The Netherlands, 2018; pp. 143–175, ISBN 978-0-12-813339-2.
33. Liang, M.; Fan, K.; Zhou, M.; Duan, D.; Zheng, J.; Yang, D.; Feng, J.; Yan, X. H-ferritin-nanocaged doxorubicin nanoparticles specifically target and kill tumors with a single-dose injection. *Proc. Natl. Acad. Sci. USA* **2014**, *111*, 14900–14905. [[CrossRef](#)]
34. Mazzucchelli, S.; Bellini, M.; Fiandra, L.; Truffi, M.; Rizzuto, M.A.; Sorrentino, L.; Longhi, E.; Nebuloni, M.; Prosperi, D.; Corsi, F. Nanometronomic treatment of 4T1 breast cancer with nanocaged doxorubicin prevents drug resistance and circumvents cardiotoxicity. *Oncotarget* **2017**, *8*, 8383–8396. [[CrossRef](#)] [[PubMed](#)]
35. Andreato, F.; Bonizzi, A.; Sevieri, M.; Truffi, M.; Monieri, M.; Sitia, L.; Silva, F.; Sorrentino, L.; Allevi, R.; Zerbi, P.; et al. Coadministration of H-ferritin-doxorubicin and trastuzumab in neoadjuvant setting improves efficacy and prevents cardiotoxicity in HER2 + murine breast cancer model. *Sci. Rep.* **2020**, *10*, 11425. [[CrossRef](#)]
36. Ruggiero, M.; Alberti, D.; Bitonto, V.; Geninatti Crich, S. Ferritin: A platform for MRI contrast agents delivery. *Inorganics* **2019**, *7*, 33. [[CrossRef](#)]
37. Zhen, Z.; Tang, W.; Todd, T.; Xie, J. Ferritins as nanoplatforms for imaging and drug delivery. *Expert Opin. Drug Deliv.* **2014**, *11*, 1913–1922. [[CrossRef](#)] [[PubMed](#)]
38. Sitia, L.; Sevieri, M.; Bonizzi, A.; Allevi, R.; Morasso, C.; Foschi, D.; Corsi, F.; Mazzucchelli, S. Development of tumor-targeted indocyanine green-loaded ferritin nanoparticles for intraoperative detection of cancers. *ACS Omega* **2020**, *5*, 12035–12045. [[CrossRef](#)]
39. Mazzucchelli, S.; Truffi, M.; Baccarini, F.; Beretta, M.; Sorrentino, L.; Bellini, M.; Rizzuto, M.A.; Ottria, R.; Ravelli, A.; Ciuffreda, P.; et al. H-ferritin-nanocaged olaparib: A promising choice for both BRCA-mutated and sporadic triple negative breast cancer. *Sci. Rep.* **2017**, *7*, 7505. [[CrossRef](#)]
40. Bonizzi, A.; Truffi, M.; Sevieri, M.; Allevi, R.; Sitia, L.; Ottria, R.; Sorrentino, L.; Sottani, C.; Negri, S.; Grignani, E.; et al. Everolimus nanoformulation in biological nanoparticles increases drug responsiveness in resistant and low-responsive breast cancer cell lines. *Pharmaceutics* **2019**, *11*, 384. [[CrossRef](#)]
41. Falvo, E.; Tremante, E.; Fraioli, R.; Leonetti, C.; Zamparelli, C.; Boffi, A.; Morea, V.; Ceci, P.; Giacomini, P. Antibody-drug conjugates: Targeting melanoma with cisplatin encapsulated in protein-cage nanoparticles based on human ferritin. *Nanoscale* **2013**, *5*, 12278–12285. [[CrossRef](#)]
42. Pandolfi, L.; Bellini, M.; Vanna, R.; Morasso, C.; Zago, A.; Carcano, S.; Avvakumova, S.; Bertolini, J.A.; Rizzuto, M.A.; Colombo, M.; et al. H-ferritin enriches the curcumin uptake and improves the therapeutic efficacy in triple negative breast cancer cells. *Biomacromolecules* **2017**, *18*, 3318–3330. [[CrossRef](#)]
43. Falvo, E.; Malagrì, F.; Arcovito, A.; Fazi, F.; Colotti, G.; Tremante, E.; Di Micco, P.; Braca, A.; Opri, R.; Giuffrè, A.; et al. The presence of glutamate residues on the PAS sequence of the stimuli-sensitive nano-ferritin improves in vivo biodistribution and mitoxantrone encapsulation homogeneity. *J. Control. Release* **2018**, *275*, 177–185. [[CrossRef](#)] [[PubMed](#)]
44. Damiani, V.; Falvo, E.; Fracasso, G.; Federici, L.; Pitea, M.; De Laurenzi, V.; Sala, G.; Ceci, P. Therapeutic efficacy of the novel stimuli-sensitive nano-ferritins containing doxorubicin in a head and neck cancer model. *Int. J. Mol. Sci.* **2017**, *18*, 1555. [[CrossRef](#)] [[PubMed](#)]
45. Fracasso, G.; Falvo, E.; Colotti, G.; Fazi, F.; Ingegnere, T.; Amalfitano, A.; Doglietto, G.B.; Alfieri, S.; Boffi, A.; Morea, V.; et al. Selective delivery of doxorubicin by novel stimuli-sensitive nano-ferritins overcomes tumor refractoriness. *J. Control. Release* **2016**, *239*, 10–18. [[CrossRef](#)] [[PubMed](#)]
46. Zhang, L.; Li, L.; Di Penta, A.; Carmona, U.; Yang, F.; Schöps, R.; Brandsch, M.; Zugaza, J.L.; Knez, M. H-chain ferritin: A natural nuclei targeting and bioactive delivery nanovector. *Adv. Healthcare Mater.* **2015**, *4*, 1305–1310. [[CrossRef](#)] [[PubMed](#)]



47. Fiandra, L.; Mazzucchelli, S.; De Palma, C.; Colombo, M.; Allevi, R.; Sommaruga, S.; Clementi, E.; Bellini, M.; Prosperi, D.; Corsi, F. Assessing the in vivo targeting efficiency of multifunctional nanoconstructs bearing antibody-derived ligands. *ACS Nano* **2013**, *7*, 6092–6102. [[CrossRef](#)]

**Other publications produced and related with this PhD thesis:**

**Sevieri M.**, Sottani C., Chesi A., Bonizzi A., Sitia L., Robustelli della Cuna F. S., Grignani E., Corsi F., Mazzucchelli S. *Deciphering the role of H-ferritin nanocages in improving tumor-targeted delivery of Indocyanine Green: combined analysis of murine tissue homogenates with UHPLC-MS/MS and fluorescence.* ACS Omega 2023 (Under review).

**Appendix 6:** Sottani C, Grignani E, Cottica D, Mazzucchelli S, **Sevieri M**, Chesi A, Corsi F, Galfrè S, Robustelli Della Cuna FS, Calleri E. *Development and Validation of a Bioanalytical UHPLC-MS/MS Method Applied to Murine Liver Tissue for the Determination of Indocyanine Green Loaded in H-Ferritin Nanoparticles.* Front. Chem. 9:784123. doi: 10.3389/fchem.2021.784123

**Attachment 7** Silva, F., Sitia, L., Allevi, R., Bonizzi, A., **Sevieri, M.**, Morasso, C., Truffi, M., Corsi, F., & Mazzucchelli, S. (2021). *Combined Method to Remove Endotoxins from Protein Nanocages for Drug Delivery Applications: The Case of Human Ferritin.* Pharmaceutics, 13(2), 229. doi:10.3390/pharmaceutics13020229;



# Development and Validation of a Bioanalytical UHPLC-MS/MS Method Applied to Murine Liver Tissue for the Determination of Indocyanine Green Loaded in H-Ferritin Nanoparticles

## OPEN ACCESS

### Edited by:

Eugenia Gallardo,  
Universidade da Beira Interior,  
Portugal

### Reviewed by:

Christian Fernandes,  
Federal University of Minas Gerais,  
Brazil

Alvaro Jose Dos Santos Neto,  
University of São Paulo, Brazil  
Andras Szeitz,  
University of British Columbia, Canada  
Tanveer A. Wani,  
King Saud University, Saudi Arabia

### \*Correspondence:

Cristina Sottani  
Cristina.sottani@icmauger.it

### Specialty section:

This article was submitted to  
Analytical Chemistry,  
a section of the journal  
Frontiers in Chemistry

**Received:** 27 September 2021

**Accepted:** 19 November 2021

**Published:** 03 January 2022

### Citation:

Sottani C, Grignani E, Cottica D,  
Mazzucchelli S, Sevieri M, Chesi A,  
Corsi F, Galfrè S,  
Robustelli della Cuna FS and Calleri E  
(2022) Development and Validation of  
a Bioanalytical UHPLC-MS/MS  
Method Applied to Murine Liver Tissue  
for the Determination of Indocyanine  
Green Loaded in H-  
Ferritin Nanoparticles.  
Front. Chem. 9:784123.  
doi: 10.3389/fchem.2021.784123

Cristina Sottani<sup>1\*</sup>, Elena Grignani<sup>1</sup>, Danilo Cottica<sup>1</sup>, Serena Mazzucchelli<sup>2</sup>, Marta Sevieri<sup>2</sup>, Arianna Chesi<sup>2</sup>, Fabio Corsi<sup>2,3</sup>, Sarah Galfrè<sup>4</sup>, Francesco Saverio Robustelli della Cuna<sup>4</sup> and Enrica Calleri<sup>4</sup>

<sup>1</sup>Environmental Research Center, Istituti Clinici Scientifici Maugeri IRCCS, Pavia, Italy, <sup>2</sup>Nanomedicine Laboratory, Department of Biomedical and Clinical Sciences "Luigi Sacco", Milano University, Milan, Italy, <sup>3</sup>Breast Unit, Istituti Clinici Scientifici Maugeri IRCCS, Pavia, Italy, <sup>4</sup>Department of Drug Sciences, University of Pavia, Pavia, Italy

Indocyanine green (ICG) is one of the most commonly used fluorophores in near-infrared fluorescence-guided techniques. However, the molecule is prone to form aggregates in saline solution with a limited photostability and a moderate fluorescence yield. ICG was thus formulated using protein-based nanoparticles of H-ferritin (HFn) in order to generate a new nanostructure, HFn-ICG. In this study, an ultrahigh performance liquid chromatography-tandem mass spectrometry (UHPLC-MS/MS) system was employed to develop and validate the quantitative analysis of ICG in liver tissue samples from HFn-ICG-treated mice. To precipitate HFn, cold acetone in acidic solution at pH 5.0 was used. The processed liver samples were injected into the UHPLC-MS/MS system for analysis using the positive electrospray ionization mode. Chromatographic separation was achieved on a Waters Acquity UPLC<sup>®</sup> HSS T3 Column (1.8 μm, 2.1 × 100 mm) with 0.1% formic acid and acetonitrile as the mobile phase with gradient elution. The selected reaction monitoring transitions of  $m/z$  753 →  $m/z$  330 and  $m/z$  827 →  $m/z$  330 were applied for ICG and IR-820 (the internal standard, IS), respectively. The method was selective and linear over a concentration range of 50–1,500 ng/ml. The method was validated for sensitivity, accuracy, precision, extraction recovery, matrix effect, and stability in liver tissue homogenates. ICG extraction recoveries ranged between 85 and 108%. The intra- and inter-day precisions were less than 6.28%. The method was applied to a bio-distribution study to compare the amount of ICG levels from mice treated with HFn-ICG and free ICG. The analyses of the homogenate samples from the two types of treatment showed that the concentration levels of ICG is approximately six-fold higher than those of free ICG (1,411 ± 7.62 ng/ml vs. 235 ± 26.0 ng/ml) at 2 h post injection.

**Keywords:** indocyanine green, liver tissue, UHPLC-MS/MS, FDA validation, biodistribution study

Article

# Combined Method to Remove Endotoxins from Protein Nanocages for Drug Delivery Applications: The Case of Human Ferritin

Filippo Silva <sup>1,†</sup>, Leopoldo Sitia <sup>1,†</sup>, Raffaele Allevi <sup>1</sup>, Arianna Bonizzi <sup>1</sup>, Marta Sevieri <sup>1</sup>, Carlo Morasso <sup>2</sup>, Marta Truffi <sup>2</sup>, Fabio Corsi <sup>1,2,\*</sup> and Serena Mazzucchelli <sup>1,\*</sup>

- <sup>1</sup> Dipartimento di Scienze Biomediche e Cliniche "L. Sacco", Università di Milano, 20157 Milano, Italy; filippo.silva@unimi.it (F.S.); leopoldo.sitia@unimi.it (L.S.); raffaele.allevi@unimi.it (R.A.); arianna.bonizzi@unimi.it (A.B.); marta.sevieri@unimi.it (M.S.)  
<sup>2</sup> Istituti Clinici Scientifici Maugeri IRCCS, 27100 Pavia, Italy; carlo.morasso@icsmaugeri.it (C.M.); marta.truffi@icsmaugeri.it (M.T.)  
 \* Correspondence: fabio.corsi@unimi.it (F.C.); serena.mazzucchelli@unimi.it (S.M.)  
 † These authors contributed equally to this work.



**Citation:** Silva, F.; Sitia, L.; Allevi, R.; Bonizzi, A.; Sevieri, M.; Morasso, C.; Truffi, M.; Corsi, F.; Mazzucchelli, S. Combined Method to Remove Endotoxins from Protein Nanocages for Drug Delivery Applications: The Case of Human Ferritin. *Pharmaceutics* **2021**, *13*, 229. <https://doi.org/10.3390/pharmaceutics13020229>

Academic Editor:  
Eduardo Ruiz-Hernandez  
Received: 31 December 2020  
Accepted: 28 January 2021  
Published: 6 February 2021

**Publisher's Note:** MDPI stays neutral with regard to jurisdictional claims in published maps and institutional affiliations.



Copyright: © 2021 by the authors. Licensee MDPI, Basel, Switzerland. This article is an open access article distributed under the terms and conditions of the Creative Commons Attribution (CC BY) license (<https://creativecommons.org/licenses/by/4.0/>).

**Abstract:** Protein nanocages represent an emerging candidate among nanoscaled delivery systems. Indeed, they display unique features that proved to be very interesting from the nanotechnological point of view such as uniform structure, stability in biological fluids, suitability for surface modification to insert targeting moieties and loading with different drugs and dyes. However, one of the main concerns regards the production as recombinant proteins in *E. coli*, which leads to a product with high endotoxin contamination, resulting in nanocage immunogenicity and pyrogenicity. Indeed, a main challenge in the development of protein-based nanoparticles is finding effective procedures to remove endotoxins without affecting protein stability, since every intravenous injectable formulation that should be assessed in preclinical and clinical phase studies should display endotoxins concentration below the admitted limit of 5 EU/kg. Different strategies could be employed to achieve such a result, either by using affinity chromatography or detergents. However, these strategies are not applicable to protein nanocages as such and require implementations. Here we propose a combined protocol to remove bacterial endotoxins from nanocages of human H-ferritin, which is one of the most studied and most promising protein-based drug delivery systems. This protocol couples the affinity purification with the Endotrap HD resin to a treatment with Triton X-114. Exploiting this protocol, we were able to obtain excellent levels of purity maintaining good protein recovery rates, without affecting nanocage interactions with target cells. Indeed, binding assay and confocal microscopy experiments confirm that purified H-ferritin retains its capability to specifically recognize cancer cells. This procedure allowed to obtain injectable formulations, which is preliminary to move to a clinical trial.

**Keywords:** drug delivery; protein nanocages; endotoxin purification; ferritin

## 1. Introduction

Interest in protein nanocages (P-NCs) has been growing over the past years since they turn out to be fascinating drug delivery systems. Their appeal relies mainly on their minimal toxicity, good biocompatibility and easy metabolism, since they can be degraded following physiological protein degradation routes [1]. Indeed, P-NCs are constituted by protein monomers that self-assemble in hollow structures [1]. P-NCs constitutive monomers can be chemically or genetically modified by inserting surface functionalities, in order to tune surface charge, ligand display, stability and drug loading [2]. Different P-NCs have been developed in the last twenty years such as Vault, viral capsids and Heat-shock proteins, but the H-ferritin nanocage (HFn) represents "The Golden boy" of P-NCs developed for drug delivery [3,4].

## Acknowledgments

Firstly, I truly and deeply thank my supervisor, Dr. Serena Mazzucchelli for always believing in me and in everything I did during these three years. Her enthusiasm for research is an example for me, increasing and growing in me the curiosity and desire for this area. Under her guidance, I had the opportunity to grow in a stimulating environment, both from a professional and personal point of view, for which I will be forever grateful.

I thank Prof. Fabio Corsi for its rigorous scientific advice and for its precious academic guidance, for giving me the opportunity to become part of the team and giving me access to the laboratory and research facilities and for supporting my training and education.

My strong gratitude goes also to the coordinator of the PhD Program in Translational Medicine, Prof.ssa Chiarella Sforza for her support during these three years.

A precious help to our project derives from the important collaborations with the groups of Prof.ssa Francesca Baldelli Bombelli (Politecnico di Milano) and Dr. Cristina Sottani (Istituti Scientifici Maugeri). Moreover, my acknowledgments are also for the people belonging to the group of Prof. Fabian Kiessling (Aachen University, Germany) for their hospitality during my Erasmus Traineeship and valuable help for the experiments performed in its research center.

I also would like to thank all the members of the Nanomedicine team: Leo, Ari and Marta T. for working alongside me all these years and supporting me in all the projects I took part in. This work has led us to become friends and I am very proud of what we achieved as a team.

Last but not least, thanks to my future husband Mirko, my family and my friends for their love and continuous support.

This thesis is dedicated to those who do not give up in the face of difficulties but find the strength to go forward with a smile and determination, because if you refuse to accept anything but the best, you very often get it.